

**SENSING THE MICRO-MOTION OF AN ORTHOPAEDIC IMPLANT:
SENSOR HEAD AND ANTENNA DEVELOPMENT**

by

Rajas Prakash Khokle



Dissertation submitted in fulfilment of the requirements

for the degree of

DOCTOR OF PHILOSOPHY

School of Engineering
Faculty of Science and Engineering
Macquarie University
Sydney, Australia

14th of April 2018

ABSTRACT

Every year millions of people undergo orthopaedic surgeries that help them live a better life. About 10% of them require revision due to implant loosening. In this thesis, a small millimetre sized non-contact electromagnetic sensor is explored that can detect the micro-motion of the implant and therefore predict the impending implant failure. The research focuses on two parts namely, development of an eddy current sensor head implanted inside the bone and the design of a bone implantable antenna to facilitate the data telemetry.

This research explores the use of eddy current sensors in the human body through extensive electromagnetic simulations and experiments for monitoring the micro-motion of an orthopaedic (tibial) implant. A statistical curve fitting technique is established to find the sensitivity, range and optimal frequency of operation. The effect of the human body is mitigated by exploiting E-Field confinement due to the dielectric contrast. This helps in increasing the sensitivity and range and robustness of the sensor.

The simulations are verified experimentally by using a femur bone from cow. A quantum tunnelling effect based Tunnelling Magneto Resistor is integrated with an eddy current loop for magnetic field detection. A heterodyne detection technique is developed to convert the signal to low

frequency. This increases the sensitivity of the displacement sensor by an order of magnitude as compared to the traditional eddy current sensor.

The sensor should be immune to the changes in the structure and properties of the human tissue. For this purpose, a detailed analysis of the effect of variation in complex tissue permittivity of bone is carried out and recommendations are made. The effect of positioning error on the sensing characteristics is examined closely and maximum tolerances at different stand-off distances are provided. The optimal geometry of the sensor is also determined for obtaining the high sensitivity and range of operation.

A highly miniaturized antenna implanted inside the bone and operating at 2.4 GHz ISM band is developed. Complementary Archimedean spirals printed in two layers and connected with a shorting pin are designed on a high dielectric permittivity substrate to achieve miniaturization. The location of the shorting pin is varied to tune the resonant frequency and impedance matching. A detail parametric analysis with respect to the geometric parameters and the tissue parameters is performed.

A new family of fractal geometries, named 'Family of M Segment Quadratic Fractal Curves', is proposed. It offers a design flexibility in terms of miniaturization, form factor and antenna complexity. This new fractal is used to design two miniaturized implantable slot antennas - one narrow band and one wideband. An empirical expression for the design of slot antennas on substrates of varying thickness is also developed. A complete step by step process for designing an implantable CPW fed slot antenna operating at the desired resonant frequency is detailed.

STATEMENT OF CANDIDATE

I certify that the work in this thesis has not previously been submitted for a degree nor has it been submitted as part of the requirements for a degree to any other university or institution other than Macquarie University.

I also certify that the thesis is an original piece of research and it has been written by me.

In addition, I certify that all information sources and literature used are indicated in the thesis.

Rajas Khokle

ACKNOWLEDGMENTS

First and foremost I would like to acknowledge my parents and wife for encouraging me to pursue my ideas and dream. They have shown immense support as I sailed through my PhD journey and I would always be grateful to them.

Macquarie University started an initiative of bringing people from medicine and engineering together under the umbrella of WiMed research group. When I started my PhD, I attended one the WiMed meetings. In this meeting, Dr. Desmond Bokor from Australian School of Advanced Medicine, (Macquarie University) made a presentation on revision of orthopaedic implants. I picked up the problem from this meeting and started to address the issue with Prof. Michael Heimlich and Prof. Karu Eselle. Therefore, I would like to acknowledge Prof. Desmond Bokor for providing a strong motivation and his expertise in medicine.

I would like to thank my principle supervisor Prof. Karu Esselle who provided me with an opportunity to work towards my PhD at Macquarie University. His encouragement and supervision helped me in becoming a competent and independent researcher. My co-supervisor Prof. Michael Heimlich provided valuable inputs during experiments and I am grateful for his time and advice.

I would like to express my gratitude towards Prof. Susana Cardoso de

Freitas from INESC - Microsistemas e Nanotecnologias, Lisbon, Portugal who provided me an opportunity to explore Magnetic Tunnel Junction devices for magnetic field sensing. I would also like to thank Fernando Franco and Marilia De Silva for fabricating TMR and GMR sensor heads and helping me with the testing setup.

I would also like to thank Mr. Renato Morosin from Lintek Pty. Ltd. for fabricating the tiny sensors PCB panels. Thanks are also due to Mr. Walther Adendorff, Vivek Hedge and Ken Yuen from Macquarie Engineering and Technical Services for fabricating the titanium tibial implant plate. Thanks are also due to the Macquarie library and librarians in providing excellent literature resources for starting my research. I would also like to acknowledge WiMed grants for fabrication of sensors and antennas. Acknowledgements are also due to Synthes Australia Pty. Ltd. for Support For Research Grant (number - 13335/00).

Finally, last but not the least, I would like to thank my fellow doctoral students Usman Afzal, Roy Simorangkir and Maria Kovaleva for providing excellent and stimulating company and for listening to my ideas. Maria did an excellent job with the fine soldering of tiniest sensor heads to the SMA connectors. Her feedback on the writing of this thesis has been invaluable.

To Sadhguru Jaggi Vasudev

Contents

Table of Contents	ix
List of Figures	xv
List of Tables	xxix
1 Introduction	1
1.1 Motivation	1
1.2 Scope of the Dissertation	10
1.3 Organization of the Thesis	11
1.4 Thesis Contribution	14
1.5 Publications	15
2 Overview	17
2.1 Introduction	17
2.2 Sensor System Design	20
2.3 Eddy Current Sensors	28
2.3.1 Operating Principle of Eddy Current Sensing	28
2.4 Analytical Modelling of Inductor	30

2.4.1	Electromagnetic Response of a Rectangular Current Loop . . .	33
2.4.2	Aim of the Research on Sensor	37
2.5	Implantable Antenna	37
2.5.1	Antennas Available in the Literature	37
2.5.2	Aim of Research on Implantable Antenna	42
2.5.3	Summary	42
I	Micromotion Sensor	43
3	Eddy Current Sensors: Effect of The Human Body	45
3.1	Introduction	45
3.2	Numerical Modelling of Sensor	46
3.2.1	Frequency Response of An Eddy Current Sensor	55
3.3	EC Sensor Inside Human Body	61
3.4	Mitigation of the Effect of Human Body	69
3.5	Evaluation of the Sensitivity of EC sensor	75
3.6	Definition of The Sensor Parameters	79
3.7	Summary	83
4	Eddy Current Sensors: Experimental Setup and Results	85
4.1	Introduction	85
4.2	Experimental Setup for EC Sensor Characterization	86
4.2.1	Experimental Procedure	91
4.2.2	Experimental Results	94
4.3	Eddy Current-Tunnelling Magneto Resistive Sensor	104
4.4	Introduction	104

4.5	Magnetic Tunnel Junction Sensors	105
4.6	EC-TMR Sensor Integration	107
4.7	Experimental Results	109
4.8	Summary	112
5	Investigation of Changes in Sensor and Human Body	113
5.1	Introduction	113
5.2	Effect of Variation in Permittivity of Tibial Bone	114
5.3	Effect of Rotation of The Sensor	118
5.4	Different Configuration of the Eddy Current Sensor	125
5.5	Summary	133
II	Data Telemetry Antenna	135
6	Miniaturized Implantable Antenna for Data Telemetry	137
6.1	Introduction	137
6.2	Antenna Design	138
6.3	Parametric Analysis	142
6.4	Tissue Parametric Analysis	153
6.5	Summary	159
7	Implantable M-Segment Quadratic Fractal Slot Antenna	161
7.1	Introduction	161
7.2	M-Segment Quadratic Fractal Curve	165
7.2.1	Generation and Characterization of Fractals	166
7.2.2	Fractal Monopole Design	171

7.2.3	EM Analysis of The Fractal	172
7.3	Design of the Implantable CPW fed M-Segment Quadratic Fractal Slot Antenna	180
7.3.1	Calculation of the Effective Permittivity for Slot Antenna . .	181
7.3.2	Design of the Slot Antenna	185
7.4	Experimental Setup and Results	189
7.5	Parametric Analysis	192
7.5.1	Effect of Slot and CPW Line Parameters	192
7.5.2	Effect of Biocompatible PDMS Coating	195
7.5.3	Effect of the Muscle Tissue Parameters	200
7.6	Summary	203
8	Design of Wideband Fractal Slot Antenna	205
8.1	Introduction	205
8.2	Design of Wideband Antenna	207
8.3	Parametric Analysis	211
8.3.1	Effect of CPW Line Parameters	211
8.3.2	Effect of Coupling Distance	214
8.3.3	Effect of Ground Plane	216
8.3.4	Effect of PDMS Thickness	219
8.3.5	Effect of Muscle Dimensions	221
8.4	Summary	222
9	Conclusion and Future Work	223
9.1	Summary of the Research Work	223
9.2	Future Work	224

A Curve Fit Analysis	229
A.1 Effect of Changing Permittivity of Bone	229
A.2 Effect of Rotation of the Sensor	234
A.3 Different Eddy Current Loops	239
B MATLAB Codes	245
Bibliography	273

List of Figures

1.1	(a) Anatomy of a healthy knee.(b) Comparison of a healthy and damaged knee [1]	2
1.2	Different stages of Total Knee Arthroplasty.	3
2.1	Block diagram of the wireless orthopaedic implant micromotion detection.	22
2.2	3 degrees of freedom of the orthopaedic implant.	23
2.3	Multiple sensor placement for hip, knee and shoulder joint [54]. . .	24
2.4	Sensor area plan.	28
2.5	(a) Physical model and (b) Equivalent circuit of the Eddy Current sensor.	29
2.6	Geometry parameters of a inductive line.	31
2.7	Geometry of a thin rectangular loop in x - y plane with the location of point $P(x,y,z)$ at which the magnetic field is evaluated.	34
2.8	Various miniature antennas reported in the literature [91,114–116].	39
2.9	Different designs of the implantable antenna designed in proximity of bones [118–121,123].	40

2.10	Real and imaginary part of permittivity of bone and muscle tissue [124].	41
3.1	Making a tibial implant from bone.	47
3.2	Orientation and placement of sensor and the orthopaedic tibial im- plant.	48
3.3	Result of simulations with default simulation settings.	50
3.4	Effect of setting convergence $ \Delta S < 0.001$ and $\angle S < 0.1$	51
3.5	Effect of order of basis function on the distance parametric.	52
3.6	Effect of order of basis function on the convergence rate.	53
3.7	Effect of setting convergence $ \Delta S < 0.001$ and $\angle S < 0.1$, mesh size < 0.5 mm, and using second order basis function.	53
3.8	Comparison of simulated and measured relative L, R and Q quan- tities for a two turn loop.	55
3.9	Frequency response of one turn loop eddy current sensor.	56
3.10	Direction of current in a loop at low and high frequency.	57
3.11	Variation of inductance of loop with frequency.	58
3.12	Current distribution on the loop at different frequencies.	59
3.13	Magnetic field along a line perpendicular to the loop and passing through the titanium orthopaedic implant for different frequencies of excitation.	60
3.14	Magnetic field distribution from a two turn planar loop at 10 KHz, 1 MHz and 100 MHz frequency showing the depth of penetration.	60
3.15	Dielectric properties of bone and muscle tissue.	62

3.16 Design of a two turn loop implanted inside the tibial bone with orthopaedic implant.	64
3.17 Comparison of the free space and in body impedance properties of the two turn eddy current sensor.	65
3.18 Power dissipation in the different objects as a function of frequency.	66
3.19 Relative power dissipation in different objects as a function of frequency.	68
3.20 Comparison of impedance properties of a two turn eddy current sensor coated with different dielectric materials.	71
3.21 Comparison of relative power loss for a two turn eddy current sensor coated with different dielectric materials.	72
3.22 E-Field distribution along the line passing through the centre of EC loop.	74
3.23 H-Field distribution along the line passing through the centre of EC loop.	74
3.24 (a) Power dissipation in target and tissue as a function of frequency and standoff distance. (b) Curve fit for FT_{max} and standoff distance.	75
3.25 Variation of the impedance parameters as a function of the stand-off distance.	76
3.26 Variation of impedance parameters - L, R, and Q as a function of the stand-off distance and frequency.	77
3.27 Curve fit analysis of the L, R and Q factor.	80
3.28 Resistance - distance curves at three frequencies $f_1 < F_{Worst}$, $f = F_{Worst}$ and $f_2 > F_{Worst}$	81
3.29 Sensitivity Analysis for Inductance, Resistance and Q factor.	82

3.30	Sensitivity Range for Inductance, Resistance and Q factor.	84
4.1	Tibial implant cut from the titanium sheet of thickness of 4 mm. . .	86
4.2	SMA connectorized eddy current sensors.	87
4.3	Micromotion stage with controller and 3 DOF assembly.	88
4.4	Schematics of the entire experimental setup showing micromotion stage, micromotion controller, VNA and PC.	89
4.5	Cow bone preparation for experimental validation. (a) Bone cleaved to create a flat surface. (b) Hole drilled at three distances, 5 mm, 10 mm and 15 mm. (c) Placement of bone and titanium implant. (d) Bone covered with wet towel to avoid dessication.	90
4.6	Experimental setup for moving the implant, capturing measurements from VNA and saving the results in a file for further analysis.	91
4.7	Flowchart for controlling the micromotion stage and acquiring measurements from VNA.	92
4.8	CST simulation of SMA connector with 10 mm wire.	93
4.9	(a) Frequency response of the sensor before de-embedding. (b) Frequency response of the sensor after de-embedding.	95
4.10	Exponential curve fit of the de-embedded resistance data.	96
4.11	Comparison of simulated and measured R, L and Q parameters. . .	97
4.12	Comparison of simulated and measured inductance, resistance and Q factor.	99
4.13	Comparison of simulated and measured adjusted R^2 inductance, resistance and Q factor.	100

4.14 Comparison of simulated and measured sensitivities for inductance, resistance and Q factor.	101
4.15 Comparison of simulated and measured ranges for inductance, resistance and Q factor.	102
4.16 change in inductance, resistance and Q Factor with 10 μm motion of the implant at stand off distance of 5 mm, 10 mm and 15 mm.	103
4.17 Pad schematic of the fabricated chip.	106
4.18 Fabricated TMR sensor chip.	106
4.19 Resistance of the fabricated TMR sensor as a function of applied magnetic field.	107
4.20 EC-TMR sensor integration.	108
4.21 Schematic of the heterodyne detection technique for displacement measurement using EC-TMR sensor.	109
4.22 Experimental setup of EC-TMR sensor for heterodyne detection of micromotion sensor.	110
4.23 Exponential curve fit for the measured inductance and resistance of the eddy current loop.	110
4.24 Output of TMR sensor and Eddy current sensor expressed as relative percentage change.	111
5.1 Current distribution on the target for different stand-off distances and rotation angles.	121
5.2 Percent error in inductance, resistance and Q Factor sensitivity as a function of rotation angle.	124

5.3	Relative power dissipation in the target and the tissue for different rotation angles.	125
5.4	Different configurations for rectangular loops.	126
5.5	(a)Impedance parameters (L, R and Q-Factor) as a function of frequency for different loop configurations.	127
5.6	(b)Relative power dissipation in tissue, target and loop for different loop configurations.	128
6.1	(a) Top layer of the complimentary spiral antenna showing the position of via, feed point, outer radius of spiral and line width of 0.1 mm. (b) Bottom layer of the antenna with the complimentary arms shorted at the centre. (c) Side view of the antenna showing the stacking of the alumina substrate and metal traces. (d) Antenna assembly enclosed in the PDMS cover.	139
6.2	Placement of antenna inside the tibial bone near the titanium implant.	141
6.3	Frequency response of the optimized antenna.	141
6.4	Effect of changing the outer radius of the spiral on the resonant frequency.	144
6.5	Effect of changing the width of the spiral trace on the resonant frequency.	145
6.6	Effect of changing the width of the spiral trace on the impedance of the antenna.	146
6.7	Effect of changing the position of the shorting pin on the resonant frequency.	147

6.8	Effect of changing the thickness of the substrate on the resonant frequency.	148
6.9	Effect of changing the thickness of the substrate on the impedance characteristics of the antenna.	149
6.10	(a) Geometry of one turn, two turn and three turn loop geometries alongside the designed antenna.(b) Effect of the different loop geometries on the resonance of the antenna.	150
6.11	Effect of one turn, two turn and three turn loop geometries on the S parameters of the system.	151
6.12	Effect of the antenna on the frequency response of the one turn, two turn and three turn loop geometries.	151
6.13	Relative change in the impedance of the eddy current loops due to the antenna.	152
6.14	(a) Effect of the leg size variation on the frequency response. (b) Effect of leg size variation on the gain, radiation efficiency, and the directivity of antenna.	153
6.15	E-Field Distribution for different sizes of leg.	154
6.16	(a) Effect of the leg size variation on the frequency response of the antenna without PDMS coating. (b) Effect of the leg size variation on the gain ,and radiation efficiency of the antenna without PDMS coating.	155
6.17	Comparison of the E-Field distribution with and without the PDMS Coating.	155
6.18	Effect of changing the permittivity of bone on radiation efficiency. .	157
6.19	Effect of changing the muscle radius on the resonant frequency. . .	158

6.20	Effect of changing the muscle radius on the radiation parameters.	159
6.21	Effect of changing the muscle permittivity and conductivity on the antenna radiation parameters.	160
7.1	Placement of new antenna perpendicular to the sensor PCB showing wire bonds.	162
7.2	(a) Generating fractal iterations for even and odd value of m , using the operations 'p' and 'q'. (b)First 4 fractal iteration stages for $m=2$ and $m=3$ family.	167
7.3	Example of different types of geometries possible with proposed fractal construct	167
7.4	(a) Orientation of ($m=2,n=4$) antenna in Co-ordinate system. (b)Photograph of the fabricated fractal antennas.	171
7.5	Measured Input impedance of the fabricated fractal antennas.	173
7.6	(a) Simulated input impedance of the first five iterations of the Koch fractal curve (inset: Orientation of Koch fractal antenna in HFSS. (b) Comparison of the measured normalized resonances for the different iterations of antennas ($n = 0$ to $n = 4$) of different families ($m = 2$ to $m = 5$) of proposed curve, with iterations of Koch fractal curve.	175
7.7	Average lacunarity as a function of the iteration number.	177
7.8	Radiation patterns of the four families ($m = 2$ to $m = 5$) of proposed fractal curves.	178
7.9	Dipole printed on a thin dielectric substrate.	182

7.10 Effective Permittivity as a function of dielectric permittivity and height.	184
7.11 Resonant frequency shift for a slot antenna implanted inside human knee.	185
7.12 Response of the $m=2$, $n=2$ antenna designed for initial length of 18.2 mm.	187
7.13 Current distribution on designed fractal antenna.	187
7.14 Effect of extending the CPW line beyond slot dipole on current distribution.	188
7.15 Effect of extending the CPW line beyond slot dipole on reflection coefficient.	188
7.16 Final design of the fractal antenna with dimensions.	189
7.17 Frequency response of impedance matched antenna.	190
7.18 Fabricated Single band fractal antenna with and without PDMS. . .	190
7.19 Antenna connected with the VNA, top and side view.	191
7.20 Antenna covered with the muscle tissue.	191
7.21 Comparison of the frequency response of the simulated and measured antenna.	192
7.22 Effect of changing the width of the slot on the impedance matching and the resonant frequency of the antenna.	193
7.23 Effect of changing the width of the CPW line on the reflection coefficient of the slot fractal antenna.	194
7.24 Effect of changing the gap between the CPW line and ground on the impedance matching and the resonant frequency of the slot fractal antenna.	194

7.25	Effect of changing the Gap between the CPW line and ground on the impedance of the slot fractal antenna.	195
7.26	Effect of changing the thickness of the coating on the impedance matching and resonant frequency of the fractal slot antenna.	196
7.27	Effect of changing the thickness of the coating on the gain and radiation efficiency of the antenna.	197
7.28	Effect of changing the thickness of the coating on the radiation pattern of the antenna in $\Phi = 0^0$ and $\Phi = 90^0$ planes at 2.4 GHz.	198
7.29	Effect of changing the permittivity of the coating on the impedance matching and the resonant frequency of the fractal slot antenna.	198
7.30	Effect of changing the muscle radius on the frequency response of fractal antenna.	201
7.31	Effect of changing the muscle radius on the gain of the fractal slot antenna in three principle planes.	202
7.32	Gain and radiation efficiency as a function of muscle radius at the resonant frequency of the antenna.	202
7.33	Effect of changing the muscle permittivity on the frequency response of the fractal slot antenna.	203
8.1	Three different configurations of the wideband antenna design.	208
8.2	Frequency response of the three different configurations of the wideband antenna design.	209
8.3	Fabricated wideband antennas with and without PDMS coating.	209
8.4	Comparison of the simulated and fabricated wideband fractal antenna.	210

8.5	Effect of changing the width of the CPW line for different values of gap between line and ground plane (a)Gap = 0.3 mm (b)Gap = 0.5 mm (c)Gap = 0.7 mm	212
8.6	Effect of changing the length of the CPW line on the frequency response of the wideband fractal slot antenna.	213
8.7	Design of criss cross antenna showing different coupling distances. .	214
8.8	Effect of changing the coupling distance between two resonators on the frequency response of the wideband fractal slot antenna.	215
8.9	Current distribution on the wideband fractal slot antenna at 2.25 GHz and 2.43 GHz for CD = 3.5 mm shows the spreading of current at the edge of antenna.	215
8.10	Effect of changing the coupling distance between two resonators on the imaginary part of the impedance of the wideband fractal slot antenna.	216
8.11	Effect of changing the length of the ground plane on the frequency response of antenna.	217
8.12	Effect of changing the length of the ground plane on the resistance of the antenna.	217
8.13	(a) Effect of the ground length variation on the peak gain and the radiation efficiency. (b) Effect of the ground length variation on the radiation pattern in $\Theta = 90$ plane	218
8.14	Effect of changing the thickness of the PDMS cover on the reflection co-efficient of the wideband fractal slot antenna.	219

8.15 (a) Effect of PDMS cover thickness variation on peak gain and radiation efficiency. (b) Effect of PDMS cover thickness variation on radiation pattern in $\Phi = 90$ plane.	220
8.16 (a) Effect of changing the radius of the muscle on the reflection coefficient of the wideband fractal slot antenna. (b) Effect of changing the radius of the muscle on the peak gain and radiation efficiency of the wideband fractal antenna.	221
9.1 High level system architecture of the wireless orthopaedic implant micro-motion device.	226
A.1 Curve fit analysis for a two turn loop without PDMS coating with +25 % change in bone complex permittivity.	230
A.2 Curve fit analysis for a two turn loop without PDMS coating with -25 % change in bone complex permittivity.	231
A.3 Curve fit analysis for a two turn loop with PDMS coating with +25 % change in bone complex permittivity.	232
A.4 Curve fit analysis for a two turn loop with PDMS coating with -25 % change in bone complex permittivity.	233
A.5 rotation Angle = 0^0	235
A.6 rotation Angle = 45^0	236
A.7 rotation Angle = 60^0	237
A.8 rotation Angle = 90^0	238
A.9 Curve fit analysis for a one turn loop.	240
A.10 Curve fit analysis for a two turn wide trace loop.	241
A.11 Curve fit analysis for a three turn loop.	242

A.12 Curve fit analysis for a three turn asymmetric loop.	243
A.13 Curve fit analysis for a three turn two layer loop.	244

List of Tables

1.1	Number of orthopaedic surgeries from the registers of different countries.	6
2.1	Comparison of different sensor technologies for displacement sensing [63].	27
2.2	Analytical low-frequency electrical parameters of the inductor coil.	33
2.3	Comparison of implantable antenna in literature near bone.	40
3.1	Comparison of the resources required for two different solution frequencies.	49
3.2	Effect of Order of Basis function on System Resources	53
3.3	Comparison of the impedance parameters of a two turn eddy current loop in human body and free space. Frequency in GHz, inductance in nH and resistance in Ω s.	65
3.4	Limiting frequencies for a two turn eddy current sensor in human body.	69
3.5	Limiting frequencies for the different dielectric coatings.	73

5.1	Effect of the variation of complex permittivity of the bone on the sensitivity of a two turn EC sensor directly implanted in bone without PDMS coating.	115
5.2	Effect of the variation of the complex permittivity of the bone on the sensitivity of a two turn EC sensor directly implanted in the bone with the PDMS coating.	116
5.3	Sensitivity (in ppm) as a function of stand-off distance and rotation.	119
5.4	Maximum range as a function of sensitivity level (in ppm) and angle of rotation in degrees.	123
5.5	Maximum angle of rotation allowed for $\pm 10\%$ error limit.	123
5.6	Electrical characteristics of different eddy current loop geometries in free space. Frequencies are in GHz, inductance is in nH and resistance is in Ω	126
5.7	Electrical characteristics of different eddy current loop geometries inside human body. Frequencies are in GHz, Inductance is in nH and resistance is in Ω	129
5.8	Comparison of the range of the sensor with different eddy current loop geometries.	130
5.9	Sensitivities of different configurations of eddy current loops at different stand-off distances.	131
5.10	Different useful frequencies for the different loop configurations. . .	132
6.1	Comparison of the performance of present antenna with other published work.	143
6.2	Effect of changing the outer radius of spiral.	144

6.3	Antenna parameters for varying the trace width.	145
6.4	Radiation performance of antenna in presence of the eddy current loop.	150
7.1	Effect of changing the permittivity of the coating on the antenna performance.	199
8.1	Final dimensions of the wideband fractal antenna.	210

Chapter 1

Introduction

1.1 Motivation

Anatomy of Joints and Total Knee Replacement

In the human anatomy, bones provide the structure, stability and support for the body. An adult human body has 206 bones. The places where two bones meet are known as joints. The joints provide flexibility to the skeleton and enable motion. The knee is one of the largest and complex joints in the body and as such is important to perform all the day to day activities. Human locomotion largely depends on the health of this knee joint. Figure 1.1 shows the anatomical structure of a knee joint. It consists of the lower end of femur (thigh bone), the upper end of tibia (shin bone) and patella (knee cap). Cartilage, ligaments and tendons surround this joint that provide protection, stability and smooth operation. The surface of the knee is covered by a thin lining known as synovial membrane, which releases a lubricating fluid that reduces friction and wear. Thigh muscles and quadriceps provide strength to the joint. In a healthy knee, all these parts work

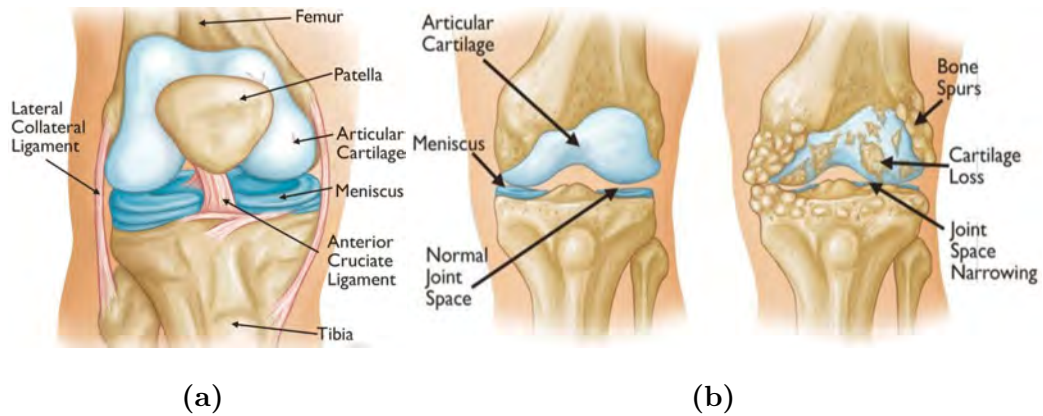


Figure 1.1: (a) Anatomy of a healthy knee.(b) Comparison of a healthy and damaged knee [1]

in perfect harmony.

When a person has a disease like arthritis or suffers from injuries and accidents, this balance is disturbed, and the person experiences discomfort, pain and reduced mobility. The difference between a healthy and a damaged knee is shown in Fig. 1.1b. Cartilage loss, bone spurs and narrow joint space are the common features of a damaged knee.

When a disease or injury is in an advanced state, it is not possible to cure it using any medicine or physiotherapy. In such cases, knee replacement or knee arthroplasty is the only solution. The knee replacement surgery or Total Knee Arthroplasty (TKA) aims to resurface the damaged knee parts to improve the joint condition that reduces the pain and increases mobility of the person. It is possible to have either total or partial knee replacement. The different steps a surgeon performs during a total knee arthroplasty are shown in Fig. 1.2. They can be grouped into 5 stages.

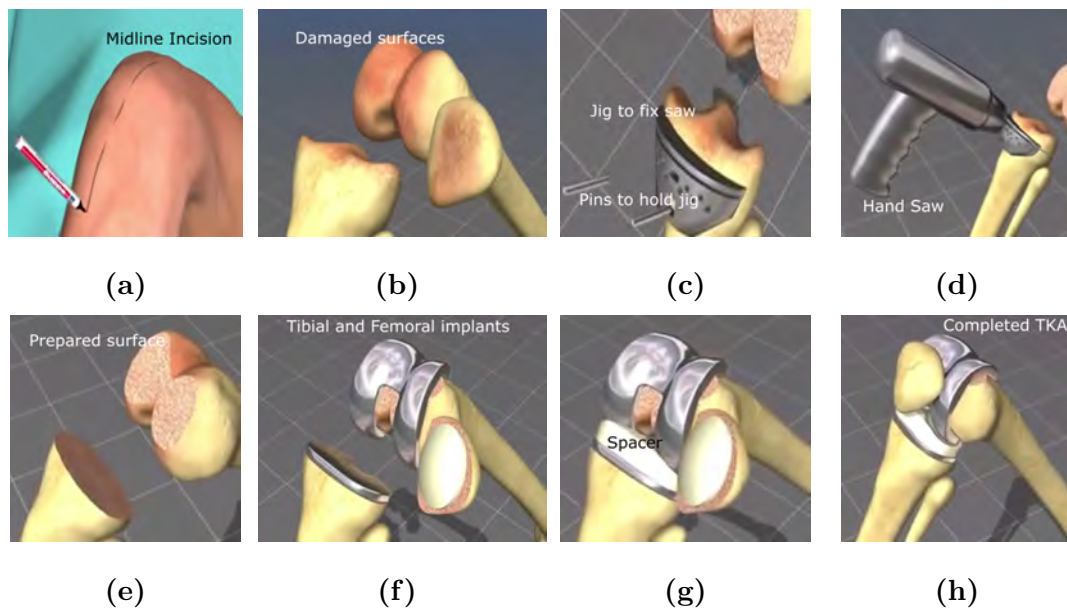


Figure 1.2: Different stages of Total Knee Arthroplasty.

1. Bone preparation: First a midline incision is made to get an access to the knee joint. Then, the patella is removed and the damaged surfaces of the tibial and femoral bones are exposed. To resurface the damaged parts, a motorized hand saw is used. To have a stable and clean cut, a metallic jig is positioned on the bone and fixed using the pins that go into the holes drilled by a power drill. These holes are left unfilled even after surgery is completed.
2. Fixing metallic implants: The metallic implants are then carefully positioned on the prepared surface. Bone cement is applied on the surface of the implants to promote the adhesion to the bone. Alternatively, they are press-fit in the cement-less surgeries.
3. Resurfacing the patella: The under surface of the patella (kneecap) is cut and resurfaced with a plastic button. Some surgeons do not resurface the

patella, depending upon the case.

4. Spacer insertion: A medical-grade plastic spacer, usually made from high density polymer like PMMA, is inserted between the metal components to create a smooth gliding surface.
5. Verification and closing: Finally, the full range of the motion is checked and corrective steps are performed, if necessary, followed by the closing of the incision. Patient is then moved for rehabilitation and recovery.

Revision Arthroplasty - A World Overview

Worldwide, over sixteen major countries maintain some form of the orthopaedic register. Table 1.1 collates the data from the registers of eight major countries viz. Australia [2, 3], United Kingdom [4], United States of America [5], New Zealand [6], Portugal [7], Netherlands[8], Switzerland[9], and Belgium [10]. The key point from the data of all these registers is that globally, around 10% of the orthopaedic surgeries are the revision surgeries. While the number of primary revisions is high, some cases also require a second or even third revision. Other countries also provide similar data for the shoulder, wrist, hip, knee or ankle arthroplasties.

Sweden reports that out of 379,550 THA's performed, 38,670 were revision surgeries with 9.24% revision burden [11]. Canadian arthroplasty registers show 44,910 Total Hip Arthroplasties (THA) with 4408 resurgeries, giving a revision rate of 9.8 %. While degenerative arthritis is observed as a major cause for revision, 36.6% cases were due to the aseptic loosening or instability of the implant according to the Canadian register [12]. South African register from 2015 [13], mentions 2956 THA's and 2835 TKA's out of which 9.8% and 4.7% were revision surgeries with

major cause identified as aseptic loosening (64.4%) and instability (33.3%). In [14], data from the worldwide registers were compiled. It was reported that the most common causes for the revisions in THA were aseptic loosening (55.2%), dislocation (11.8 %), septic loosening (7.5%), and periprosthetic fractures (6%). The most common causes in TKA were aseptic loosening (29.8%), septic loosening (14.8%), pain (9.5%), and wear (8.2%). The most common causes in TAA (Total Ankle Arthroplasty) were aseptic loosening (38%), technical errors (15%), pain (12%), and septic loosening (9.8%). The authors of [15] report the revision rate of 6.8% for TKA between period 2011-2013 in Isfahan, Iran. About 56% of these are attributed to mechanical failure, aseptic loosening, instability and periprosthetic fracture.

With the increasing sanitation and cleanliness standards, the amount of infection related revisions is expected to come down. However, the revisions due to mechanical instability, aseptic loosening, wear and periprosthetic fractures cannot be avoided till a mechanism to detect the early failure is in place. Besides causing pain and discomfort to the person, the revision surgery also puts economic strain on the Medicare services (or the people themselves). Hence, it is necessary to have a modality that can detect the micromotion of an orthopaedic implant at an early stage so that the revision surgery can be avoided.

Therefore, the process of osseo-integration, implant stability and micro motion is discussed next.

Table 1.1: Number of orthopaedic surgeries from the registers of different countries.

	AU	UK	Holland	NZ	Portugal	USA	Swiss	Belgium	Total
Hip Primary	440841	800683	125391	110208	4384	151880	18066	9529	1651453
Hip Revision	57819	89023	16991	16251	648	17180	2148	1028	200060
Burden %	11.59	10.00	11.93	12.85	12.87	10.16	10.62	9.73	10.80
Knee Primary	544075	875585	116780	95821	4110	235718	14501	9048	1886590
Knee Revision	48502	54278	10360	6739	291	22403	1484	733	144057
Burden %	8.18	5.83	8.14	6.57	6.61	8.67	9.28	7.49	7.09
Shoulder Primary	29068	17300	2077	7305	111	NA	NA	NA	55861
Shoulder Revision	3338	2045	203	571	9	NA	NA	NA	6166
Burden %	10.30	10.57	8.90	7.24	7.5	NA	NA	NA	9.94
Ankle Primary	1662	3185	122	1261	17	NA	NA	NA	6247
Ankle Revision	376	358	15	179	1	NA	NA	NA	929
Burden %	18.44	10.10	10.94	12.43	5.55	NA	NA	NA	12.94
Elbow Primary	2738	1639	107	476	66	NA	NA	NA	5026
Elbow Revision	536	507	38	81	4	NA	NA	NA	1166
Burden %	16.37	23.62	26.20	14.54	5.71	NA	NA	NA	18.83

Osseointegration, Implant Stability, and Micromotion

Osseointegration is the term used to denote an intimate contact between the bone and the metallic implants. The principles and process of osteointegration are well known and well understood in the literature [16–19]. After the surgery, the newly formed tissues start occupying the voids and spaces of the microporous surface of the implant. The cuts and drills in the tibial or femoral bones are repaired by hematoma formation and mesenchymal tissue. These are later replaced by the woven bone tissues. This is followed by the lamellar bone remodelling and the growth of the bone marrow.

There is an evidence that the high relative motion between the implant and the host bone leads to the ingrowth of the fibrous tissues rather than bone [20]. Thus, the success of good fixation of the implant by osseointegration depends upon a stable interface between the implant surface and the bone. Different studies [21–23] conducted until now, corroborate this phenomenon. In [24], a study of the stability of femoral components having non-porous distal stem was done in the canine model. It was found that the relative micromotion was $34 \mu\text{m}$ just after the surgery which decreased to $5 \mu\text{m}$ within a year that indicated extensive bone regrowth and excellent stability. It was concluded that the proximally porous uncemented femoral components are crucial in providing the initial stability to the implant. This research led to the development of the porous implants. Further, in [25] a computational model was developed that explored the implant design features that resisted loosening. The finite element analysis of the contact mechanics of the press-fit hip implants also showed that minimizing the micromotion, especially during the post-operative situation, should provide an adequate stability for the

implant to promote the osseointegration [26].

In [27], it was found that the bone ingrowth was inhibited by the intermittent micro motion of the implants in rabbits. About 20 cycles of 0.5 mm motion were applied once a day. Due to this, there was formation of the vascularised fibrous tissues instead of the bone. The motion induced shear strain that caused the fibrous tissue formation. In [28], Osseointegration under the biomechanical stress-strain and the bone formation and resorption was studied in the beagle dogs. Their investigations showed that the micromotion of less than 30 microns at the bone implant interface does not interfere with the bone growth. In [29], local micromotion measurement on the femoral stem for Total Hip Replacement (THR) is reported. The failure of the cementless THR is mainly attributed to the aseptic loosening and stability of the implants [30,31]. About 150 μm of micromotion has been considered as the limit for avoiding the fibrous tissue formation and promote the bone ingrowth [29,31].

In [32], micromotion generation as an effect of applied stress and torque on the bone (dental implants) of different densities was studied. It was found that a mean force of 62.7 N shows the maximum displacement of 71.9 μm . Thus, the micromotion of the implant, specially during the early stages of recovery, makes osseointegration difficult and gives rise to the implant instability. This, in due course of time, creates painful situation for the patient and later warrants a re-surgery.

A detailed procedure to obtain the micromotion information in the lab settings is described in [33]. It utilizes X-ray opaque markers made from tantalum, inserted at specific locations in the bone followed by the X-ray imaging at regular intervals. Recently, in [34] a new technique based on micro computed tomography

(micro-CT) and radiopaque markers is proposed to provide a full field micromotion measurement at the entire bone-implant interface. This study has been performed for the cementless femoral stem implants in a human cadaver. It had a standard deviation of $4 \mu\text{m}$ and accuracy of $20\mu\text{m}$.

Another system based on the differential variable reluctance transducer (DVRT) has been developed in [35]. In this setup, the commercially available DVRT sensors from Microstrain Inc. were used in contact-based configuration. These sensors also had to be calibrated frequently to account for the frequency dependant hysteresis. Moreover, the electronics for motion detection was outside the body.

In [36], various techniques currently employed to detect the micromotion of the implant are discussed. They are classified into two groups: imaging based and implant integrated sensor based. Imaging techniques include radiography [37], computed tomography[38], Magnetic Resonance Imaging [38, 39], and FDG-PET [40]. While radiography is a 2D assessment of a 3D process, computed tomography offers better quantification of osteolysis. MRI is more useful for the evaluation of the periprosthetic tissue (as MRI provides an excellent soft tissue contrast). FDG-PET is quite cost intensive and provides accuracy only when combined with other modalities. Moreover, PDG-PET and CT have very high radiation doses involving high risk of cancers and it is recommended that they should be used only with strong clinical justification [41].

Implant integrated sensors involve the use of accelerometers and vibrometry. Well fixed implants show linear behaviour, while loosened ones show an acoustic behaviour. However, the specificity and sensitivity of vibrometry is estimated to be only 20% higher than the radiographs [42], and they are contact based devices.

However, these systems cannot be used for a prolonged monitoring of the or-

thopaedic implant. It is not possible to utilize the X-ray techniques as it would mean a visit by the patient to a radiologist everyday. Also, the daily radiation dose from these methods would be detrimental to the patient's health. The contact based configuration is not suitable for an implantable micromotion sensor as it would mean changing the design of an orthopaedic implant, which has been optimised through years of research.

Therefore, a sensor that can sense the micromotion of an orthopaedic implant remotely (without modifying or touching the implant) can be very useful from the application point of view. First, it can help the healthcare professional to advise the patient suitably, such that the bone growth and osseointegration takes place sufficiently. This should prolong the life of the implant and relieve the person from pain and discomfort. On the other hand, the data collected from such sensors can be used for studies of the bone densities, forces acting on different parts of bones and effect of different activities on the bone growth and stability of the implant. Equipped with this research, better implants optimized by person's physiology can be developed. With the advances in 3D printing, one day a very customized orthopaedic implant may be made that can last the lifetime of a person without any causing pain or discomfort.

1.2 Scope of the Dissertation

A displacement sensor is the heart of this implantable wireless implant monitoring device. Also, to send the measured data outside the body, an antenna is another important component of the system. Therefore, focus of this thesis is on the electromagnetic considerations of the orthopaedic implant micromotion sensor.

Therefore the questions that this thesis answers are

1. What is the impact of human body on displacement sensor characteristics?
2. What is the possible range and sensitivity for such a sensor?
3. What is the most suitable frequency of operation for this sensor?
4. Is it possible to increase the sensitivity of the micromotion sensor? If yes, then how?
5. What is the effect of tissue variability on the sensor performance?
6. What could be a miniaturized antenna geometry for data telemetry?
7. What could be the suitable frequency of operation?
8. What could be the effect of manufacturing tolerances on antenna parameters?
9. What could be effect of tissue parameter variability on antenna parameters?
10. Is it possible to minimize the effect of manufacturing tolerances and tissue variability? If yes, then how?

1.3 Organization of the Thesis

The thesis is organised into 9 chapters. First two chapters provide the motivation and the overview of the research. Chapter 3, 4 and 5 discuss the displacement sensor implanted inside the human body. Chapter 6, 7 and 8 are based on the design and development of an implantable antenna for the data telemetry. Chapter 9 presents the conclusion and future direction of the research. The detailed synopsis is given below.

- *Chapter 1* - This chapter discusses the motivation behind the research, scope and organization of the thesis.
- *Chapter 2* - In this chapter, a preliminary sensor system design is presented. It discusses various sensors and their applicability to the present research problem. It is found that eddy current sensors are most suitable displacement sensors. Then, different ways of analysing the eddy current sensor found in the literature are discussed. It is followed by the literature review of the implantable antennas.
- *Chapter 3* - This chapter explores the simulation strategies for getting an accurate and physically viable results. Then, it analyses the effect of a human body on the sensor characteristics based on the power absorbed by the human tissue, orthopaedic implant and the loop itself. A way to mitigate the effect of human body is presented. Sensitivity and range of the sensor is defined in a new way which would be useful for an integrated circuit designer. The curve fit analysis method for evaluating sensor performance as a function of frequency and stand-off distance is discussed at length.
- *Chapter 4* - The experimental setup for evaluating the eddy current sensor is explained in this chapter. Magnetic Tunnel Junction (MTJ) based sensors integrated with the traditional eddy current loops are explored, and an order of magnitude higher sensitivity is obtained.
- *Chapter 5* - This chapter deals with the robustness analysis of the sensor. The effect of changing the tissue parameters, effect of rotation of the sensor and changing the geometry of the eddy current loop is evaluated.

- *Chapter 6* - A highly miniaturized antenna using complementary archimedean spirals in two layers is designed. An extensive parametric analysis is done that explains the tuning of the resonant frequency and impedance matching. Tissue variability is also considered for determining the robustness of the antenna.
- *Chapter 7* - A new fractal construct is proposed that gives designer a flexibility to choose between form factor, miniaturization and complexity of the antenna. It has two parameters,- ‘ m ’ which controls the Housdorff dimension and ‘ n ’ which controls the iteration number. A CPW-fed implantable slot antenna is designed using this fractal. A new empirical expression for designing the slot antennas is also given. This is followed by a step by step design process for the proposed antenna. A detailed parametric analysis is also performed.
- *Chapter 8* - In this chapter, coupled fractal resonators are designed to create a wideband antenna. This antenna is also subjected to the parametric analysis and the robustness against the tissue variability is evaluated.
- *Chapter 9* - The summary of the thesis is presented followed by a discussion on the future work.
- *Appendix A* - Graphs from the curve fit analysis of changing the complex permittivity of the tibial bone, rotation of the sensor and different sensor configurations.
- *Appendix B* - Matlab codes for performing the curve fit analysis on the frequency-distance data, and controlling the VNA and micromotion stage.

1.4 Thesis Contribution

This thesis, for the first time, explores the use of eddy current sensors in human body through extensive electromagnetic simulations and experiments for monitoring the micro-motion of an orthopaedic (tibial) implant. A statistical curve fitting technique is established to find the sensitivity, range and optimal frequency of operation. The effect of human body is mitigated by exploiting E-Field confinement due to the dielectric contrast. This helps in increasing the sensitivity, range and robustness of the sensor. Further, an eddy current - tunnelling magneto resistor integration is done and heterodyne detection technique is developed that increases the sensitivity of the sensor by an order of magnitude.

The sensor should be immune to changes in the structure and properties of the human tissue. For this purpose a detail analysis of the effect of variation in complex tissue permittivity of bone is carried out and recommendations are made. The effect of positioning error on the sensing characteristics is examined closely and maximum tolerances for different stand-off distance is provided. The optimal geometry of the sensor is also determined for obtaining high sensitivity and range of operation.

A highly miniaturized antenna implanted inside the bone and operating at 2.4 GHz ISM band is developed. A new family of fractal geometries, christened ‘Family of M segment Quadratic Fractal Curves’, is proposed. This fractal construct offers a design flexibility in terms of miniaturization, form factor and antenna complexity. This new fractal is used to design two miniaturized implantable slot antennas - one narrow band and one wideband. An empirical expression for the design of slot antennas on substrates of varying thickness is also developed. A complete step

by step process for designing an implantable CPW fed slot antenna operating at desired resonant frequency is detailed. This eliminates the use of cut and trial methods as well as optimization methods which are computationally expensive to perform for the in-body simulations.

1.5 Publications

This research led to the filing of an international patent in August, 2017. This is being pursued for further commercial exploitation. After the publication of the patent, the research output of the work is disseminated in following publications.

1. Rajas Khokle, Fernando Franco, Susana Cardoso de Freitas, Karu Esselle, Michael Heimlich, and Desmond Bokor, “Eddy Current – TMR Sensor For Micro-Motion Detection Of Orthopaedic Implants ”, accepted for *IEEE Intermag Conference*, Singapore, 2018.
2. Rajas Khokle, Karu Esselle, Michael Heimlich, Desmond Bokor, “Orthopaedic Implant Micromotion Sensing Using An Eddy Current Sensor,” *IEEE Life Science Conference*, Sydney, Dec. 2017.
3. Rajas Khokle, Karu Esselle, Michael Heimlich and Desmond Bokor, “Design of A Miniaturized Bone Implantable Antenna for A Wireless Implant Monitoring Device”, *Loughborough Antenna and Propagation Conference*, Nov. 2017.
4. Michael Heimlich, Desmond Bokor, Rajas Khokle and Karu Esselle, “ Implanted Sensing System for Joint Replacement”, *WO 2017 /143400A1*, August 2017.

5. Rajas Khokle, “Generation, Application and Analysis of a Novel Family of M-Segment Quadratic Fractal Curves to Antennas”, *Progress in Electromagnetic Research C*, Vol. 65, 191–200, 2016.

The following publications are communicated or under preparation for publication in journals:

1. Rajas Khokle, Fernando Franco, Susana Cardoso de Freitas, Karu Esselle, Michael Heimlich, and Desmond Bokor, “Integrated Eddy Current – TMR Sensor For Improved Micromotion Detection of the Orthopaedic Implants ”, *under review in IEEE Transactions on Magnetics*.
2. Rajas Khokle, Karu Esselle, Michael Heimlich, Desmond Bokor, “Investigation of An Eddy current Sensor Implanted in Human Body for Micro-Motion Detection of an Orthopaedic Implant”, *manuscript under preparation for communication in IEEE Transactions on Biomedical Engineering*.

Apart from this, my other publications during my PhD tenure are listed below:

1. Nainu Chaudhari, Rajas Khokle, Karu Esselle, and Anand Verma, “Improved stopband characteristics of microstrip lowpass filter using linearly distributed transmission zeros ”, *URSI Asia-Pacific Radio Science Conference*, Seoul, Korea, October 2016.
2. Maria Kovaleva, David Bulger, Rajas Khokle, Karu Esselle, “Application of The Cross-Entropy Method to Electromagnetic Optimisation Problems”, accepted in *IEEE International Symposium on Antennas and Propagation*, Boston, USA, July 2018,.

Chapter 2

Overview

2.1 Introduction

Implantable biomedical systems are coming of age since last decade. Many distinguished researchers have written excellent books on this topic [43–52] that cover various aspects such as sensing principles, data telemetry, bio-compatible materials, body area networks, energy harvesting, low power devices and ultra miniaturized components. This list of books can neither be considered exhaustive nor sufficient but merely a representative of different aspects of the implantable biomedical system design. These handbooks provide a dense source of information at a single place and can act as a starting point for any research and development activity in this field.

The sensors and sensor systems that can be deployed in human or animal body are discussed in [44,45]. In [44], the sensor-tissue interface and packaging materials are discussed in detail. It also covers various sensor systems such as MEMS based sensors, retinal implants, neuroprosthesis implants and wireless body area networks.

The use of invasive biosensors for chemical sensing and microdialysis is explored in [45].

In [43,47], design principles of an implantable device are discussed in detail. The electronics of implantable system is analysed and presented comprehensively in [47]. It systematically presents the entire system of implantable (as well as external communicating device) devices and considers issues like powering of implant, operation of sensor, collection or analysis of data from sensor (using Analog to Digital Converter and Micro-controllers) and data telemetry using transceivers and antenna system. The system level design of the proposed sensor is based on these design principles and guidelines.

Various biocompatible materials and especially, bioceramics that can be used in orthopaedic implants and for bone tissue reconstruction are described in [48]. It lists Zirconia and Alumina as the two most prominent bio-inert ceramics that are widely used. Other composite materials (natural and artificial) employing biocompatible polymers are found to be usually biodegradable and bioresorbable. These are primarily used in regenerative medical applications. The cutting-edge research in this area is towards creating ceramic-polymer composites which exhibit bio-activity that can promote bone bonding and even cancer treatment. Since, the proposed sensor is supposed to last for the lifetime of the patient, Alumina is chosen as the preferred material for substrate. Correspondingly, LTCC fabrication may be chosen for the final design of the sensor.

Remote powering of the implantable devices is considered in depth in [50]. It describes practical examples of battery-less implantable systems employing different energy harvesting and power transfer methods like optimized inductive links, midfield power transfer and electro-mechanical methods. Especially it describes

an implantable microsystem of mm scale which is powered by a remote powering inductive link with 21% efficiency over 30 mm distance by driving it using a class E Power amplifier at 13.56 MHz. However, due to extremely limited space available for the proposed application, remote powering by inductive links will not be possible and therefore is not considered .

The data telemetry challenges and subsequent antenna design are explored in [46]. It discusses link budgeting and the interaction of electromagnetic waves with human body. Telemetry requirements in terms data rates, frequency of operation, required and allowed power levels and antenna miniaturization is treated elucidated in this handbook. Various applications like retinal implants, ingestible capsules, and nerve implants are also discussed. The techniques described for the antenna miniaturization will be used in the proposed sensor system. The same antenna will also be utilized for powering up the sensor.

The manufacturing technologies for biomedical devices are described in [49]. It focuses on computer aided manufacturing and additive manufacturing techniques for biomedical devices. It also describes how Finite Element Method (FEM) can be used for evaluating mechanical, fluidic, thermal and dynamic properties of the implants.

Finally, the security aspect of the wireless implants is explored in [51,52]. When the implants interact wirelessly for power and data transfer to external devices, it can inadvertently transmit data to the unexpected recipients. This is especially true for the devices operating at 2.4 GHz ISM band where many different electronic equipments operate. This can cause theft of sensitive data. More importantly, it can cause malfunctioning of implants as it can receive unintentional commands of operation. This has to be handled through proper encryption and placing proper

security policies.

In this chapter, first the sensor system is designed. This is followed by the discussion on the choice of sensor and its evaluation based on available literature. The aims of the research on the sensor part are then detailed. Then the literature is reviewed for the implantable antenna design and subsequently the design requirements are fixed.

2.2 Sensor System Design

Using the information from the above handbooks and reference, the implantable system for orthopaedic implant micro-motion detection is designed. First the functional requirements are established as follows.

1. There should be a non-contact displacement sensor that can resolve tens of micrometer of motion of the orthopaedic metallic implants.
2. There should be an electronic integrated circuit that can convert the sensed parameter into the appropriate digital format after initial signal processing like low noise amplification. This may require design of an ADC with adequate bit resolution. Considering 360° motion (for example shoulder joint [53]) and capturing the distance for each 0.1° (which ensures that enough data points are collected to make a meaningful deduction), the ADC should have at least 3.6 KSPS ($360/0.1 = 3600$) speed.
3. There should be an adequate memory to hold the data of one entire cycle of motion. Considering one sample of 16 bits, this translates to about 7200 bytes or nearly 8 KB memory.

4. There should be a transceiver system to modulate the digital data onto carrier waves for transmission outside the body. OOK is often the choice of modulation for low power requirement. Alternatively, PSK or FSK may be used to reduce the interference.
5. There should be an antenna to transmit the signal outside the body. This antenna can also be used to derive the clock and power required for the device.

To fulfil these requirements, the sensor system is designed as shown in Fig. 2.1. The block diagram is explained along with the flow of measurement process as follows.

1. An external system (not shown) sends the wake up signal to start the measurement process. The implantable antenna receives the signal and extracts the clock from it using appropriate sine to square wave converter and/or frequency dividers. The extracted clock provides the timing signals for microcontroller as well as ADC.
2. The RF signal is then rectified to extract DC power. It is then provided to the power management section that divides the power appropriately between microcontroller (μC), transceiver circuit, Low Noise Amplifier (LNA), ADC and sensor.
3. The μC then verifies the identity of the external transmitter and sends its own identity. This ensures the safety and privacy of the patient by avoiding the unwanted interference and inadvertent signalling.

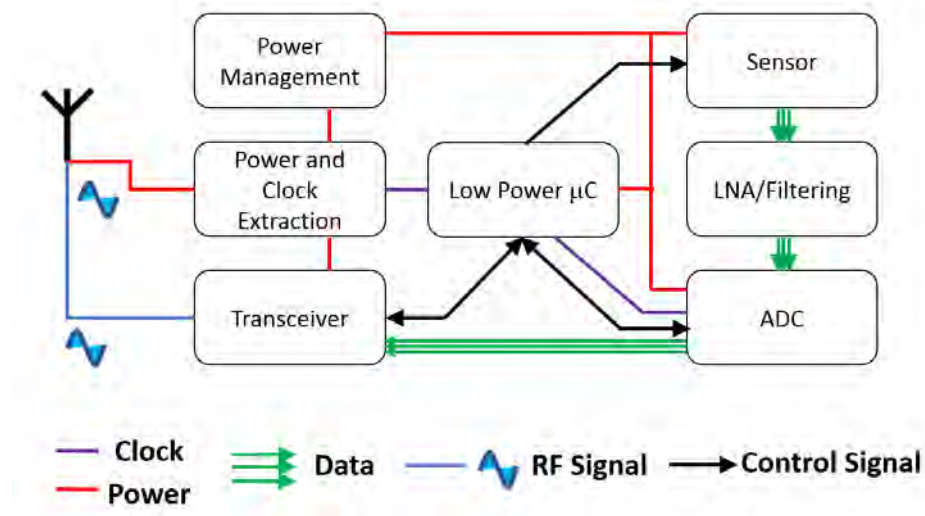


Figure 2.1: Block diagram of the wireless orthopaedic implant micromotion detection.

4. The sensor is then activated and the data is digitized using ADC after signal conditioning through the low noise front end amplifier and filter.
5. The data may be sent to the μC for storage or directly to the transceiver circuit for transmission to an external device.

Position of Sensors in Body

The tibial orthopaedic implant can have three degrees of freedom for motion as shown in Fig. 2.2. It can have translation along the perpendicular axis (z) or tilt or rotation along the in plane axes (x and y). The actual motion of the implant will depend upon the gait of the walking person. The knowledge of the implant motion as the person walks can give a valuable information about the stress points on the implant. The healthcare professional can therefore correct the gait of the person



Figure 2.2: 3 degrees of freedom of the orthopaedic implant.

based on this input which will lead to better life of implant as well as comfort to the patient. Therefore, it is needed to position at least 3 sensors in the vicinity of implant. The positioning of multiple of these sensors for hip joint, knee joint and shoulder joint are shown in Fig. 2.3 [54].

Comparison of the Different Micromotion Sensors

There are a number of sensors that can sense the spatial position of the target without touching them. They are classified as proximity sensors, displacement sensors, position sensors and vibration sensors. Proximity sensors simply provide an on-off output, based on the presence and absence of the target. Position sensor provides position of the target with respect to a fixed co-ordinate system. Displacement sensor provides the information of the relative motion of the target. Finally, the vibration sensor provides the amplitude and frequency of the target having an oscillatory motion. For detecting the micromotion of the orthopaedic implant, a displacement sensor is required.

There are primarily four types of displacement sensors based on 4 different kinds of sensing mechanisms. They are ultrasonic sensors, optical sensors, capacitive sensors, and inductive sensors.

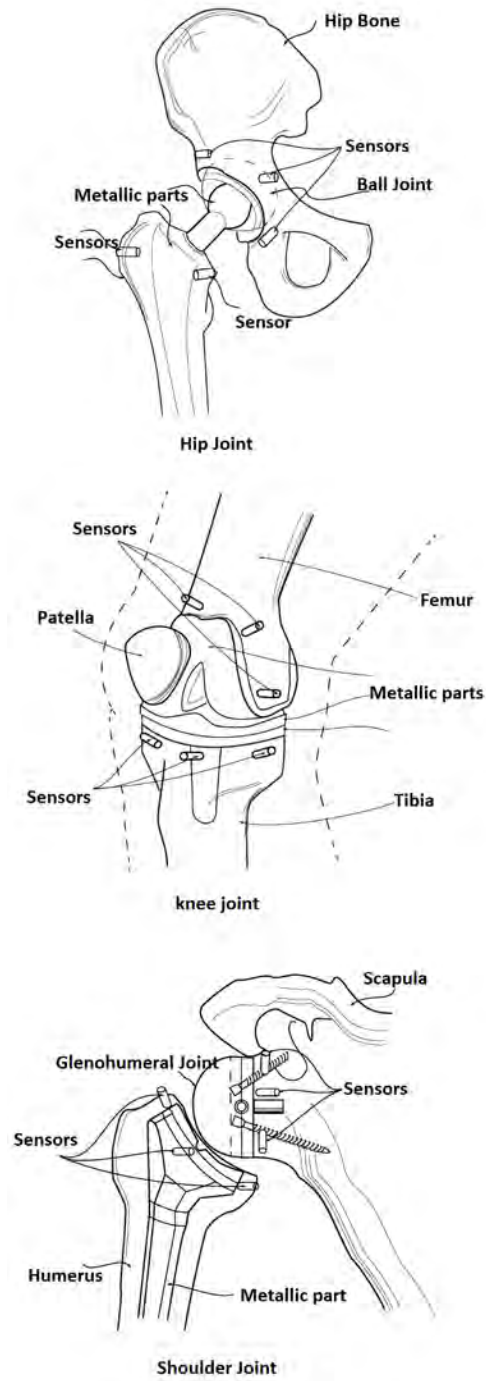


Figure 2.3: Multiple sensor placement for hip, knee and shoulder joint [54].

For the applications that involve bones and cartilages, ultrasound techniques are not suitable because of large ultrasound loss inside the bone and large reflection from the bone - soft tissue boundary. Moreover, it is also dependent upon the bone structure and geometry [55]. This makes it quite unsuitable for the present application.

Optical sensors routinely reach micron and sub-micron resolution using the Light Emitting Diodes (LEDs) and Laser Diodes (LDs). These are generally pulsed systems with time of flight measurement or interference based system with phase difference mapped to the displacement[56]. However, they cannot work inside the human body as such extremely high frequency electromagnetic waves are attenuated substantially within few microns of propagation inside the lossy human body[57, 58]. Also, their detection circuit is bulky and is not amenable to the miniaturization by designing specialized ICs. Therefore, they cannot be implanted inside the body.

The capacitance between a pair of electrodes is given by $C = \epsilon G$ where ϵ is the permittivity of the medium and G is the geometry factor. For a parallel plate capacitor the geometry factor is given by the area of plates (a) divided by the distance between the plates (d). When d changes, the capacitance also changes, which can be detected and mapped.

The capacitive sensors having very high resolution have been reported in literature [59, 60]. This option therefore is very attractive for micromotion sensing. However, the response also depends on the permittivity of the material between two electrodes. Since the permittivity of the human body is non-homogeneous, dispersive and changes with time, the response of sensor may not be repeatable. Hence, such sensors cannot work well in the environment with varying electric

properties of the medium. Further, the range of such sensors is very small.

Inductive sensors work on the principle of eddy currents generated in the metallic targets. The alternating current through an inductive loop produces a primary magnetic field. When a conducting material comes in its proximity, the eddy currents flow into it in such a way as to create a secondary magnetic field which opposes the primary field. The impedance characteristics of the loop change due to this. This change in impedance is mapped to the change in the position of the metal target [61,62]. These sensors are very suitable for electrically inhomogeneous material environment as their response ideally does not depend upon the dielectric constant of the material. They are only affected by the magnetic materials having $\mu_r > 1$. However, human body is non-magnetic in nature. Consequently, these sensors form a suitable choice for the detection of micro-motion of the orthopaedic implants.

The comparison of the different displacement sensors discussed above are summarized in Table 2.1 from the point of view of suitability for detection of micro motion of the orthopaedic implants.

Induction coil sensors and their design methods are reviewed in depth in [64] by Tumanski. He also reviewed the readout electronics systems used for exciting and measuring the AC magnetic fields by using the eddy current (EC) sensors. The output signal of an EC sensor increases linearly with frequency. However due to the factors like resistance, internal inductance and self capacitance of the coil which themselves depend on the frequency, the absolute frequency response of the EC sensor is more complex. Also, the self capacitance of the coil strongly depends upon the geometry of the coil, surrounding medium and shielding layers. Cavoit [65], developed a sensor system that could measure the signals from 0.1 to 50 MHz

Table 2.1: Comparison of different sensor technologies for displacement sensing [63].

Sensor	Advantages	Disadvantages
Ultrasonic	High Range, Can work inside body.	High losses in bone.
Optical	Very high resolution.	Line of sight. Very short range.
Capacitive	High resolution.	Cannot work inside body. Short range.
Inductive	Long range.	Moderate Resolution.

range. Yabukami [66] and Yamaguchi[67] have demonstrated that the magnetic pick up coils can be used at frequencies as high as 3.5 GHz. Thus, it is possible to use eddy current sensors for micromotion detection using very high frequency signals.

A system on chip for eddy current sensors is developed in [68], that included a 12 bit Sigma-Delta analog to digital converter (10 bit effective) with DSP compatible serial interface. A signal to noise plus distortion ratio (SNDR) of 60 dB was achieved in that design. The IC was fabricated in a standard 0.6 μm technology and consumed 10 mW at 2.7 V power supply. The die size was 3.5 mm \times 4 mm. The circuit integration techniques have evolved greatly since 2002 and much better performance and size reduction can be achieved with 180 nm or better IC technologies. Nonetheless these numbers are considered as the reference values and give a confidence that a complete implantable system is indeed possible.

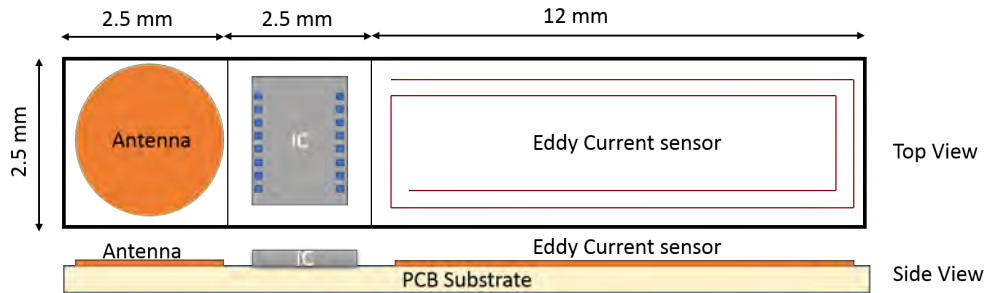


Figure 2.4: Sensor area plan.

Sensor Area Planning

Since the available space is limited, it is crucial to define and plan the board area use. The sensor has to fit in a cylindrical hole of diameter 3.5 mm and length of about 15 - 17 mm. Therefore, the stack of PCB boards that can fit into this volume will have the maximum dimension of $2.5 \text{ mm} \times 2.5 \text{ mm} \times 15 \text{ mm}$. On the PCB, therefore, the eddy current sensor can take about 10 mm to 12 mm of space, a chip containing the different circuits can have about $2.5 \text{ mm} \times 2.5 \text{ mm}$ dimensions and the antenna can have about $2.5 \text{ mm} \times 2.5 \text{ mm}$ of board area. The entire system may be powered wirelessly using the miniaturized antenna. The entire setup is shown in Fig. 2.4.

2.3 Eddy Current Sensors

2.3.1 Operating Principle of Eddy Current Sensing

In 1831, Michael Faraday discovered that a changing magnetic field induces voltage in a conductor which is proportional to the rate of change of magnetic field. Later, Heinrich Lenz, found that this induction is in opposite direction to the applied field.

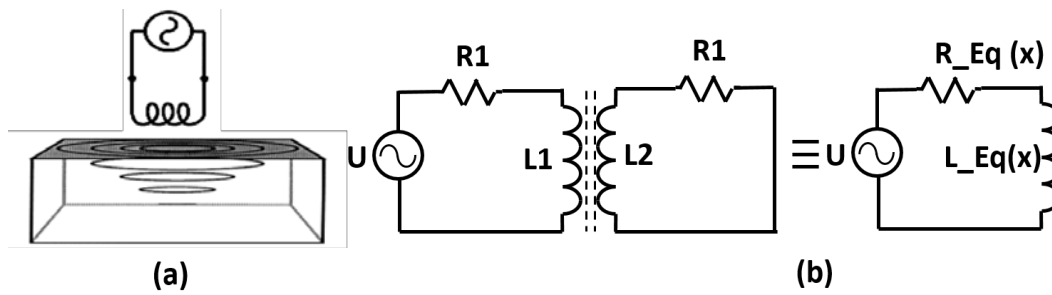


Figure 2.5: (a) Physical model and (b) Equivalent circuit of the Eddy Current sensor.

In other words, the current is induced in the conducting object such that it opposes the primary magnetic field. This is termed as Lenz's law. The Faraday's law of electromagnetic induction is therefore summarized in the expression $E = -d\phi/dt$ where E is EMF, and $d\phi/dt$ is the rate of change of magnetic flux.

For the displacement measurement, the physical model and an equivalent circuit model is shown in Fig. 2.5. The alternating current in the primary coil generates the alternating magnetic field. This induces eddy currents in the metallic target such that secondary magnetic field opposes the primary magnetic field. Consequently, the inductance of the primary coil decreases. The coil and the target are considered as weakly coupled primary coil and shorted secondary coil respectively. This makes the equivalent circuit model as shown in Fig. 2.5b. The primary coil has its own resistance, whereas for induced eddy currents that constitute secondary coil in the equivalent circuit, the power dissipation gives rise to its own secondary resistance. If the target moves away from the coil, the amount of eddy current induced decreases therefore the resistance reflected to the primary coil decreases while the inductance increases. This impedance change is utilized for the displacement measurement.

The equivalent inductance, resistance and Q factor of the this simple model can be given by the Eq. 2.1 to 2.3 [63,69].

$$L_{eq} = L_1 - \frac{\omega^2 M^2 L_2}{R_2^2 + \omega^2 L_2^2} \quad (2.1)$$

$$R_{eq} = R_1 + \frac{\omega^2 M^2 R_2}{R_2^2 + \omega^2 L_2^2} \quad (2.2)$$

$$Q_{eq} = \frac{\omega L}{R} = \frac{\omega \left(L_1 - \frac{\omega^2 M^2 L_2}{R_2^2 + \omega^2 L_2^2} \right)}{R_1 + \frac{\omega^2 M^2 R_2}{R_2^2 + \omega^2 L_2^2}} \quad (2.3)$$

Here R1 and L1 are the resistance and self-inductance of the sensor coil depending on the material and structure of the coil; R2 and L2 are the equivalent resistance and self-inductance of the target depending on the eddy current path, conductivity σ and relative permeability μ_r of the target; and ω is the exciting angular frequency of the power source, and M is the mutual inductance between the sensor coil and the target that depends on the relative position x between the sensor and target.

2.4 Analytical Modelling of Inductor

A printed inductor also has resistance and capacitance. Due to the small cross section and narrow width of the printed line, the inductor has a power loss which can be modelled as resistance in series with the inductor. Further, the capacitance between two traces and capacitance due to the charge accumulation at the corners of the rectangular coil gives rise to the self capacitance. This self capacitance is the reason for the coil to exhibit a self resonance frequency (SRF). An accurate circuit model will therefore have a capacitance in parallel with the inductor. Analytically,

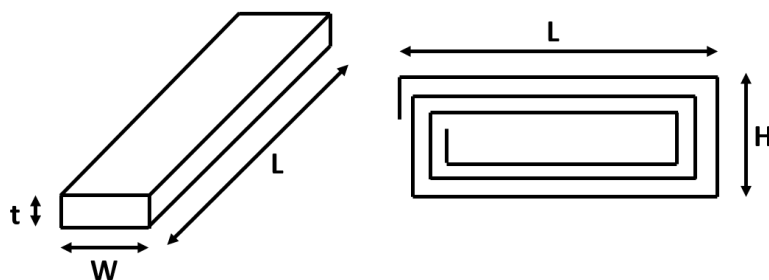


Figure 2.6: Geometry parameters of an inductive line.

the inductance, resistance and capacitance of the coil is calculated in the following sections.

Inductance Calculation

The equation to calculate the inductance of a N turn rectangular printed coil is given by Eq. 2.4 [70]. The loop geometry as well as trace dimensions are shown in Fig. 2.6. L is the length of the loop, H is the width of the loop, w is the width of the trace and t is its thickness.

$$L = \frac{N^2 \mu_0}{\pi} \left[-2(L + H) + 2\sqrt{H^2 + L^2} - H \ln\left(\frac{H + \sqrt{H^2 + L^2}}{L}\right) - L \ln\left(\frac{L + \sqrt{H^2 + L^2}}{H}\right) + H \ln\left(\frac{2H}{w}\right) + L \ln\left(\frac{2L}{w}\right) \right] \quad (2.4)$$

DC Resistance Calculation

The basic equation for resistance calculation of a conductor is given by Eq. 2.5. The material used is silver with resistivity $1.6e - 8 \Omega m$. The total unwound length of the coil is calculated for the different turns of coil. Here w is the width of the coil and t is the thickness of the coil.

$$R = \frac{\rho l}{A} = \frac{\rho l}{wt} \quad (2.5)$$

Capacitance Calculation

The capacitance between the two parallel plate capacitors is given by Eq. 2.6. Here l is the length of the line whereas t is the thickness and d is the distance between two lines. It can be noted that since the line is printed on the top of substrate, it experiences both air and substrate as the dielectric medium. To the first approximation, an average of the permittivity of substrate and air may be taken.

$$C = \frac{\epsilon_0 \epsilon_r A}{D} = \frac{\epsilon_0 \epsilon_r l t}{d} \quad (2.6)$$

Using these formulae, the inductance, capacitance and DC resistance of one turn, two turn and three turn copper loops of length 12 mm and width 2 mm with linewidth of 0.2 mm are calculated and tabulated in table 2.2. Based on inductance (L) and capacitance (C), the SRF is calculated using Eq. 2.7.

$$f_{SRF} = \frac{1}{2\pi\sqrt{LC}} \quad (2.7)$$

It could be noted that the formula for N turn loop does not account for the decrease in the length of the inner lines which is inevitable while printing the loop. Also, it neglects the mutual inductances between two lines on the opposite ends. Further, the formula is developed for the linewidth that is much smaller than the dimensions of the loop. For this particular rectangular geometry, this ratio is just 1:5 to 1:10. This also introduces errors substantially. So the predicted values scale exactly with N but are erroneous (From the analysis done in chapter 5, it could be noted that the error between the inductance value calculated using above formula and simulations for a three turn loop in free space at low frequencies is over 55%).

Table 2.2: Analytical low-frequency electrical parameters of the inductor coil.

Design	L in nH	R in Ω	C in pF	SRF in GHz
1 Turn Loop	15.69	0.109	0.42	1.97
2 Turn Loop	62.7	0.219	0.83	0.695
3 Turn Loop	141.28	0.329	1.25	0.378

Moreover, it does not take into account any frequency dependence or effect of human tissue surrounding. Therefore, only full wave analysis can predict the loop parameters accurately.

2.4.1 Electromagnetic Response of a Rectangular Current Loop

Using principles of electromagnetics, the impedance characteristics and the field distribution of a rectangular current loop can be determined. Such analysis has been done for electrically small loop in [71, 72]. Their method and results are explained next with a discussion on their applicability to the present research.

Magnetic Fields From a Rectangular Loop

Magnetic fields at a point at a distance 'r' in space due to the rectangular loop of length $2a$ and width $2b$ in the quasi-static regime ($l \ll \lambda/10$) are evaluated in [71]. First the vector potential A_x and A_y are calculated from Eq. 2.8 and 2.9 followed by the calculation of the vector components of the magnetic flux density B using Eq. 2.10 [73]. The parameters r_1, r_2, r_3 and r_4 are respective distances of point $P(x, y, z)$ from the corners of the loop as shown in Fig. 2.7.

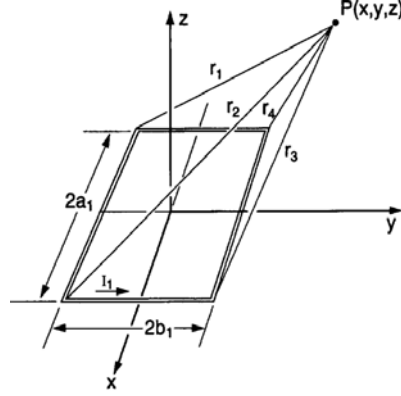


Figure 2.7: Geometry of a thin rectangular loop in x - y plane with the location of point $P(x, y, z)$ at which the magnetic field is evaluated.

$$A_x = \frac{\mu_0 I}{4\pi} \ln \left[\frac{r_1 + a_1 + x}{r_2 - a_1 + x} \cdot \frac{r_3 - a_1 + x}{r_4 + a_1 + x} \right], \quad (2.8)$$

$$A_y = \frac{\mu_0 I}{4\pi} \ln \left[\frac{r_2 + b_1 + y}{r_3 - b_1 + y} \cdot \frac{r_3 - b_1 + y}{r_4 + b_1 + y} \right], \quad (2.9)$$

$$B_x = -\frac{\partial A_y}{\partial z}, \quad B_y = -\frac{\partial A_x}{\partial z}, \quad B_z = \frac{\partial A_y}{\partial z} - \frac{\partial A_x}{\partial z}. \quad (2.10)$$

From Eq. 2.8, 2.9 and 2.10, the components of magnetic field density (B_x , B_y and B_z) are given by Eq. 2.11, 2.12, and 2.13.

$$B_x = \frac{\mu_0 I}{4\pi} \sum_{\alpha=1}^4 \left[\frac{(-1)^{\alpha+1} z}{r_\alpha [r_\alpha + d_\alpha]} \right], \quad (2.11)$$

$$B_y = \frac{\mu_0 I}{4\pi} \sum_{\alpha=1}^4 \left[\frac{(-1)^{\alpha+1} z}{r_\alpha [r_\alpha + (-1)^{\alpha+1} C_\alpha]} \right], \quad (2.12)$$

$$B_z = \frac{\mu_0 I}{4\pi} \sum_{\alpha=1}^4 \left[\frac{(-1)^\alpha d_\alpha}{r_\alpha [r_\alpha + (-1)^{\alpha+1} C_\alpha]} - \frac{C_\alpha}{r_\alpha [r_\alpha + d_\alpha]} \right], \quad (2.13)$$

The values of C_α and d_α are given by the Eq. 2.14.

$$C_1 = -C_4 = a_1 + x, \quad C_2 = -C_3 = a_1 - x, \quad d_1 = d_2 = y + b_1, \quad d_3 = d_4 = y - b_1. \quad (2.14)$$

Impedance of the Rectangular Current Loop

In [72], Cho and Itakuara have evaluated the input impedance of electrically small rectangular loop having perimeter ($p = 0.2\lambda$) by using moment method for different aspect ratios. The expression for real and imaginary part of the impedance is reproduced in Eq. 2.15 and 2.16. Here n is the aspect ratio of the rectangle, R_0 is the resistance of the square loop having area A , l_a and l_b are the lengths of the longer and shorter sides, $l_c = \sqrt{(l_a^2 + l_b^2)}$ and a is the radius of the wire. However, these expressions become increasingly inaccurate for narrow rectangular loops. Also, it considers that the loop is made from the wires having a circular cross section that is negligible with respect to the either dimension of the rectangle.

$$R_0 = \frac{320\pi^4}{\lambda^4} A^2, \quad R_n = \frac{16n^2}{(n+1)^4} R_0, \quad (2.15)$$

$$X_{in} = \frac{\mu_0}{\pi} \left[l_a \ln \frac{2A}{a(l_a + l_c)} + l_b \ln \frac{2A}{a(l_b + l_c)} + 2a + l_c - (l_a + l_b) \right]. \quad (2.16)$$

A numerical modelling approach for the design of EC sensors is described in [74]. It introduced new free space Green's functions and subsequent matrix method using the Method of Moments. It also considered the coating material on target by

using discreet step material profile. However, as listed by the authors themselves, the method assumes no self capacitance of the loop and assumes that constant current. Further, it has been applied for a circular loop geometry and not rectangular and human body does not have step material profile. So this approach cannot be used in the present application.

While all the above methods and equations are suitable for calculating the fields and input impedance of the loop, they do not account for the effect of frequency and the dispersive and inhomogeneous nature of the human body. Further, the loop is printed on a dielectric substrate and has a rectangular cross section which may not be negligible with respect to the shorter dimension of the loop. Thus, all these analytical methods are not suitable for investigating the response of an eddy current sensor implanted inside the human body.

Therefore, full wave analysis by numerical methods is frequently employed. For example Method of Moments (MOM) and Coupled Integral Equations (CIE) are used for numerically evaluating a superquadric loop antenna on the wrist of numerical human body phantom at 280MHz, 900MHz and 1800 MHz [75,76]. A similar work is done in [77] to evaluate the performance of a pager near human body. The effect of human body coupling to the loop antennas is investigated in [78]. In [79,80] rectangular loops in body are explored for inductive power transfer at 6.78 MHz and data telemetry at 866 MHz. There the inductance and resistance of the loop embedded in the agar jelly used as a tissue phantom is evaluated by using IE3D MOM based simulator.

Therefore, for the micromotion detection using eddy current sensors deeply implanted inside human body, numerical methods of evaluation are chosen for the research in this thesis.

2.4.2 Aim of the Research on Sensor

Eddy current sensor embedded inside the bone offers the best possibility of detecting the micromotion of the orthopaedic implant. The aims of the research on eddy current sensors are, therefore, formulated in following manner.

1. Since the direct human testing is not possible, set up a correct simulation model for detecting the micromotion of the knee implant.
2. Evaluate the impedance characteristics of the designed eddy current sensors.
3. Evaluate the sensitivity and range in terms of the loop parameters.
4. Design suitable experimental setup for validation of simulations.
5. Investigate the effect of loop parameters as well as human tissue parameters on the eddy current sensors. In other words, perform Monte Carlo analysis for evaluating the robustness of the sensor.

2.5 Implantable Antenna

2.5.1 Antennas Available in the Literature

First article on implantable antennas appeared in Journal of Applied Physiology in 1967 the dealt with the use of implantable device used to monitor temperature and heart rate [81]. Since then a lot of research has been done in this area. A quick search on google scholar shows a list of about 1100 articles published in various journals and conferences with more than 600 published by IEEE. In this section,

the published literature is reviewed in context of designing the antenna for the present application of the Wireless Orthopaedic Implant Monitoring Device.

The available literature so far caters to various applications such as neural implants [82–85], cardiac implants [86–88], retinal implants [89–92], dental implants [93–95], glucose monitoring [96–99], capsule endoscopy [100,101], and animal implants [102–105]. A review of various implantable antennas developed in last decade is done in [106–108], while the challenges and requirements of such antennas are discussed in various conference articles [109–113]. This list and the references are not exhaustive, however, they represent a substantial work conducted in the field of implantable antennas till date.

Some of the highly miniaturized implantable antenna are designed for retinal prosthesis [91,114] and brain machine interface [115,116]. In [91], rectangular and triangular spiral dipoles arranged in 2D and 3D space are used for miniaturization. In [114], on chip monopole antenna with inductive loading and parasitic elements is designed to operate at 2.4 GHz and 5.2 GHz. In [115], a 3D antenna occupying 1 mm^3 volume was designed using dielectric as well as magnetic material loading. In [116], a wireless link between an external loop and a $1 \text{ mm} \times 1 \text{ mm}$ loop implanted inside the brain (without encapsulation) was analysed using Ansys HFSS in the MICS (402-405 MHz) band. It was capacitively matched to get efficient power transfer. These antenna structures are shown in Fig. 2.8.

The antennas that are specifically designed to be deeply implanted in the proximity of bone are investigated in [117–123]. The geometry of these antennas is given in Fig. 2.9. In [117], a U shaped antenna with optimized distance between the two arms is utilized for creating a cylindrical loop. In [118], circular meandering is used to create a resonance at 400 MHz. In [120], similar design with more circu-

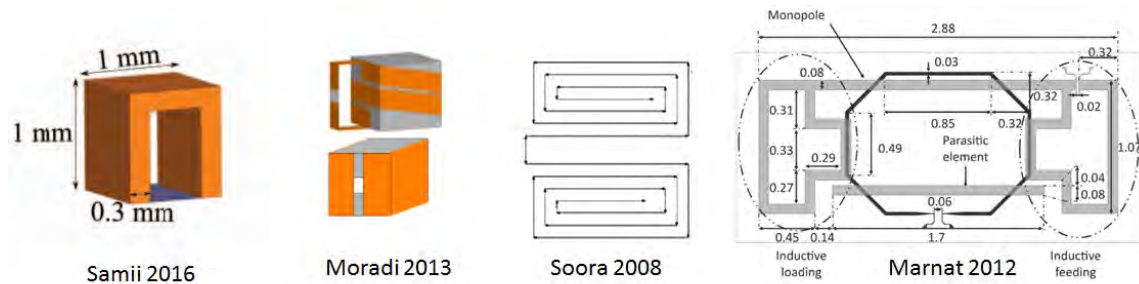


Figure 2.8: Various miniature antennas reported in the literature [91, 114–116].

lar meandering is used to decrease the size of the antenna, but the bandwidth is also reduced. In [119], a rectangular loop with complementary split ring resonator (CSRR) is used for miniaturization. Two such CSRRs are nested to obtain broad band operation. In [121], a cylindrical pin with slotted waveguides is used to create a resonance at 21 GHz. However, the loss of the order of 41 dB is also predicted at this frequency.

All these designs are bent in the cylindrical shape for ease of implanting inside body. Their performances are compared in Table 2.3. The first value in size column shows the diameter ϕ while second value shows the length of the cylinder. It can be seen that all of these designs except [121] work in the 400 - 405 MHz MICS band. All of them have very low gains due to miniaturization and absorption of power in human tissue.

As observed by these authors, the antennas that work near the bone have following properties

1. They require more miniaturization than the muscle implanted antenna as the relative permittivity of the bone is lower than the muscle tissue.
2. They have lower SAR compared to the muscle implanted antenna.

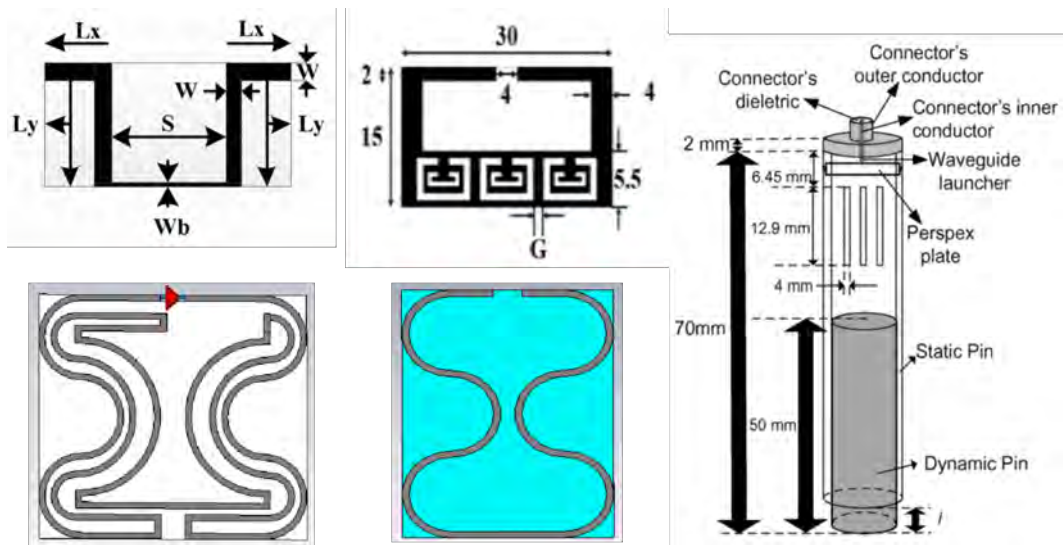


Figure 2.9: Different designs of the implantable antenna designed in proximity of bones [118–121, 123].

Table 2.3: Comparison of implantable antenna in literature near bone.

Reference	(ϕ , height)	Frequency	Bandwidth	Gain
[117]	10mm \times 15mm	400 MHz	200 MHz	-35.44 dBi
[118]	10mm \times 40mm	410 MHz	92 MHz	-27.6 dBi
[119]	6mm \times 15mm	400 MHz	2.4GHz	-36 dBi
[120]	5mm \times 40mm	400 MHz	40 MHz	-21 dBi
[121]	70 \times 10mm	21 GHz	NA	NA

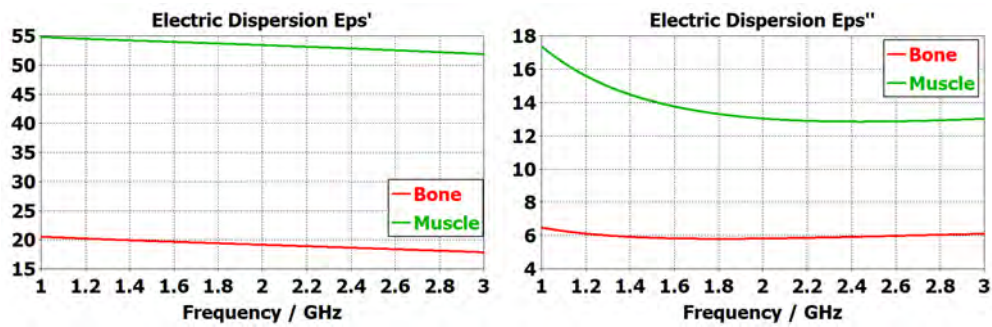


Figure 2.10: Real and imaginary part of permittivity of bone and muscle tissue [124].

3. They have higher losses and lower radiation efficiency because the wave has to propagate through lossy muscle tissue as well as due to the reflections between the bone and muscle tissue interface.

These observations can be understood with the help of the dielectric properties of the muscle and bone tissue plotted in Fig. 2.10. The dielectric constant ϵ' of bone is about 20, while that of muscle is in the range of 50. Similarly, ϵ'' is higher for the muscle ($\epsilon''_{Muscle} = 15$) than the bone ($\epsilon''_{Bone} = 6$). The amount of the E-fields absorbed, depends on the antenna structure and the tissue surrounding the antenna. If muscle tissue surrounds the antenna predominantly, then more E-fields will be absorbed increasing the SAR. Also, if the antenna has a structure in which E fields are concentrated, then the peak SAR value increases.

In most of these designs, therefore, the loop like structures are used. This is because, loops are magnetic dipoles, rather than electric dipoles and so have more magnetic field component than electric in their near field region. This is also seen when CSRR are used in [119] which provided broadband behaviour as well as reduction in SAR value. The slot like structure of the CSRR is nothing but a

magnetic dipole which assists in lowering the E field concentration that results in lower SAR value.

Based on the literature review, following requirements can be formulated for the antenna that can work for implantable wireless orthopaedic implant micromotion sensor.

2.5.2 Aim of Research on Implantable Antenna

1. Design a miniaturized antenna that can work in 2.4 GHz ISM band.
2. Evaluate the effect of design variation, manufacturing tolerance as well as human tissue variability.
3. Provide systematic design methodology.
4. Verify the design experimentally.

2.5.3 Summary

First, the system level design of the micromotion is done based on the established technologies and methods. Then the different sensing techniques are explored and eddy current based distance sensor is chosen. This is followed by the discussion on different analysis methods to determine the impedance characteristics of the EC sensors and the need to perform full wave numerical analysis is established for the purpose of measuring the micromotion of the orthopaedic implants. The design requirements for the eddy current sensor are fixed. Further, the implantable antennas available in the literature are reviewed and the requirements of the implantable antenna design are established.

Part I

Micromotion Sensor

Subtle motion is captured only when the E-Fields are confined.

Chapter 3

Eddy Current Sensors: Effect of Human Body

3.1 Introduction

An Eddy Current (EC) coil has three impedance parameter - resistance (R), inductance (L), and Q factor. All these three characteristics are frequency dependent and their calculation inside the human body is a non-trivial task. Furthermore, with the increase in frequency, the current on the loop does not remain constant. Thus, a phase difference arises between different points on the loop. This gives rise to the E-fields. From a circuit point of view, this is modelled as capacitance. Since, the amount of phase difference depends on frequency, the capacitive reactance also depends on frequency. In fact, this combination of inductance and capacitance gives rise to the self resonant frequency of the loop.

At this self resonant frequency, the reactance becomes zero while resistance becomes infinite. This happens at the frequency at which the length of loop =

$\lambda/2$. At this frequency, the spatial phase between two input terminals of loop is 180 degrees. Therefore, no current flows through the loop no matter how high the voltage is applied. Consequently, the loop resistance is seen as infinite.

For the purpose of displacement sensing, the EC inductor coil should have *high inductance, low capacitance and low resistance*. High inductance ensures that strong magnetic fields are generated which facilitate the measurements. Since the sensor is supposed to be embedded inside the human bone, smaller electric fields are preferable in order to decrease damage to the tissue by localized heating and ensure the robustness of the sensor from changes in body. This translates into the requirement of having low capacitance. Lower resistance of the coil means lesser power dissipation and wastage and so a desirable characteristic.

In this chapter, the numerical modelling of the eddy current sensor is presented. First, the simulation is done in the free space. For such simulations, in order to obtain a physically correct solution, a proper simulation strategy is developed. Then, the minimum frequency of operation is determined based on the skin effect. Then the eddy current sensor is implanted inside the tibial bone and the effect of the human body is discussed. Then a technique to mitigate the effect of the human body is described. This is followed by definition of sensitivity and range at defined sensitivity. These performance parameters for the proposed eddy current sensor are evaluated by the curve fit analysis of the frequency-distance data.

3.2 Numerical Modelling of Sensor

Ansys High Frequency Structure Simulator (HFSS) that uses Finite Element Method to solve the Maxwell's Equations numerically, is exclusively used for the numerical

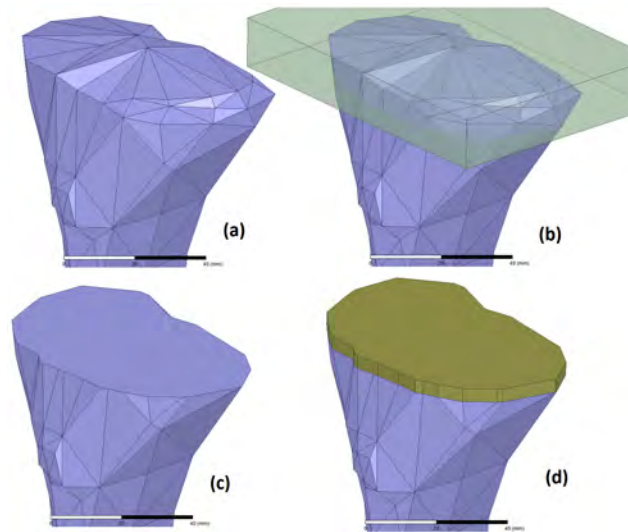


Figure 3.1: Making a tibial implant from bone.

modelling of the implantable eddy current sensor. First, the simulation is set up to evaluate the impedance characteristics of the eddy current sensor in free space. The free space simulation serves two purposes. Firstly, a proper simulation setting is evaluated to ensure that the obtained data is correct. Secondly, it acts as a reference for comparison of the effect of human body on the EC sensor. This section deals with the proper simulation setup.

First a single turn loop of length 10 mm and width 2 mm with the linewidth of 0.2 mm on Rogers 6010 substrate is designed in the XY plane. Then, the tibial bone from Ansys Human body model is imported as shown in Fig. 3.1 (a). A rectangular box is defined on the top side of this tibia (b). On boolean subtraction, a flat surface on top of the bone is obtained (c). This surface is thickened to form an object that acts as an orthopaedic tibial implant (d). One can notice similarity of this to the actual surgical procedure. Once the metallic tibial implant is obtained, the bone is removed to allow free space simulations. Then, the sensor is arranged

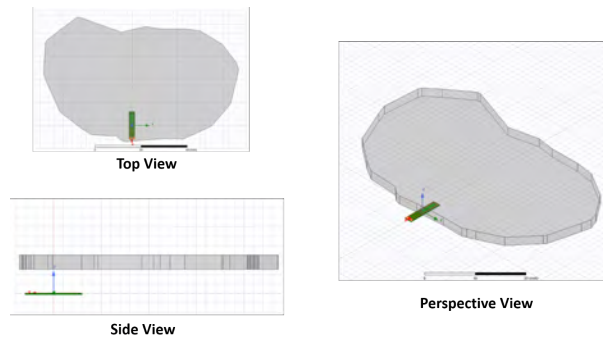


Figure 3.2: Orientation and placement of sensor and the orthopaedic tibial implant.

below the tibial implant. The orientation of the sensor and the implant is shown in Fig. 3.2

Solution Frequency

Generally, in FEM simulations, the solution frequency is set at the highest value of interest. Since the eddy current sensor cannot be operated above the self-resonant frequency, the SRF is provided as the solution frequency. The SRF for a loop in free space occurs at a frequency for which $P = \lambda_0/2$, where P is the perimeter of the loop. For a rectangular loop of length 12 mm and width 2 mm, the perimeter is 28 mm. Therefore, the λ_0 is 56 mm which corresponds to 5.35 GHz. Since the loop is printed on a very thin dielectric substrate having high permittivity, the actual SRF will be lower than this. However, since highest value of frequency is of interest, this value is set as solution frequency in the first design iteration.

To avoid the larger mesh, the target is not included in the simulation and the convergence criteria is set to the default value of $\Delta S < 0.02$. A fast frequency sweep is defined from 1 GHz to 6 GHz and the geometry is simulated. This gave

Table 3.1: Comparison of the resources required for two different solution frequencies.

<i>Solⁿ Freq.</i>	CPU	Mesh	RAM	SRF	R @ 2 GHz	L @ 2 GHz
3.3 GHz	57 Sec	2586	547 MB	3.331 GHz	3.02 Ω	21.86 nH
5.35 GHz	68 Sec	3718	804 MB	3.334 GHz	2.88 Ω	22.34 nH

the SRF at 3.3 GHz. For all further simulations, this frequency is used as the solution frequency. The advantage is that now, the number of mesh elements will be smaller than directly using 5.35 GHz, thereby reducing the required RAM and time for simulation. Table 3.1 shows the difference between the mesh size, RAM used, CPU time for the two solution frequencies along with the calculated SRF and resistance and inductance at a sample frequency of 2 GHz. While the change in SRF, resistance and inductance is 0.9%, 4.8% and 2.1% respectively, about 47% more RAM and 20% more CPU Time is used when the solution frequency is set higher than the SRF.

Motion of Implant

Once the solution frequency is set, it is important to get physically viable results. For this purpose the tibial implant is displaced in Z direction and the impedance characteristics of the loop are evaluated. Therefore, the impedance needs to be evaluated by displacing the tibial plate in the Z direction. The tibial plate is displaced from 0.5 mm to 10 mm in steps of 0.5 mm and resistance and inductance are evaluated at 100 MHz.

Setting up the correct simulation for the proposed eddy current sensor is a

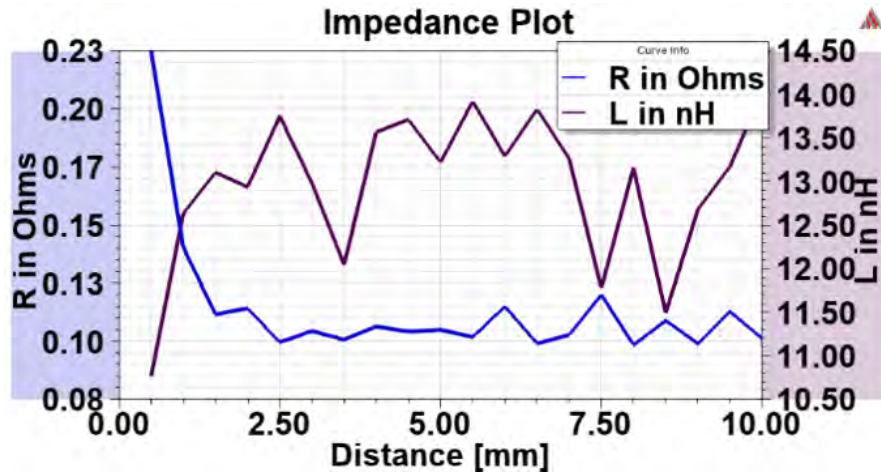


Figure 3.3: Result of simulations with default simulation settings.

non-trivial task as the default solver settings do not produce physically correct results. Since, many different configurations will be simulated, it is necessary to ensure that the simulation produces converged and physically correct solution. The most important simulation settings that affect the accuracy of simulation are convergence criteria, meshing, and the order of the basis functions used. These settings are evaluated against the memory required, the CPU time and the convergence of the results.

Convergence Criteria

The convergence criteria is important for obtaining the physically consistent results. For this, the solution frequency is set at 3.3 GHz. When the default convergence criteria $\Delta S_{max} < 0.02$ is used, Fig. 3.3 shows that it does not produce any consistent result for the inductance or resistance of the eddy current loop, especially at higher distances.

It is found that reducing this criteria to $|\Delta S_{max}| < 0.001$ and $\angle s < 0.1$, gives

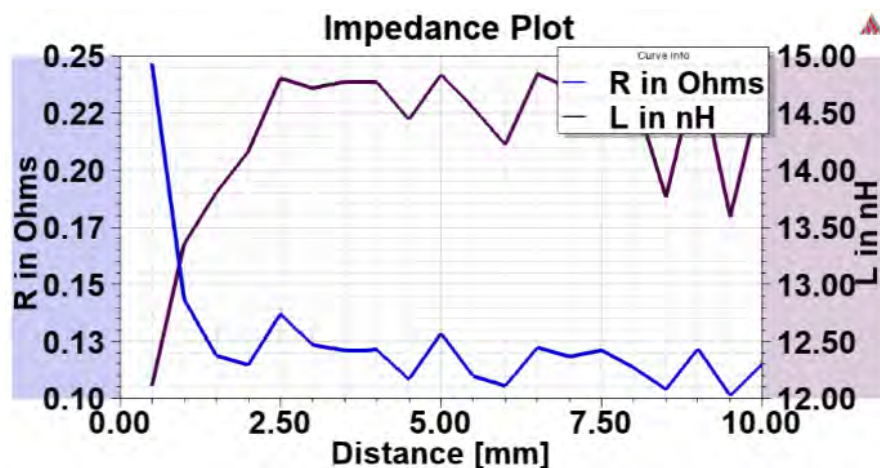


Figure 3.4: Effect of setting convergence $|\Delta S| < 0.001$ and $\angle S < 0.1$.

a slightly smoother curves (Fig. 3.4). Also, it is seen that only tightening $|\Delta S_{max}|$ does not ensure smoothing of resistance curves. However, it is found that defining convergence on magnitude and phase of S-parameter separately, ensures the consistent results for resistance and inductance. Also further tightening of convergence criteria does not improve the result despite the increase in the solution time. Hence, order of basis function and meshing are considered for the further improvement.

Order of Basis functions

In the next simulation, second order basis functions were used with 30 % of mesh refinement per pass. These settings ensure quicker convergence of the results. The convergence criteria are set as $\text{Max } |\Delta S| = 0.001$ and $\angle \Delta S = 0.1$. Such a tight convergence criteria is necessary to ensure that the field convergence and that even the smallest change is captured when the tibial implant moves away from the sensor. The result of distance variation is shown in Fig. 3.5. These settings are

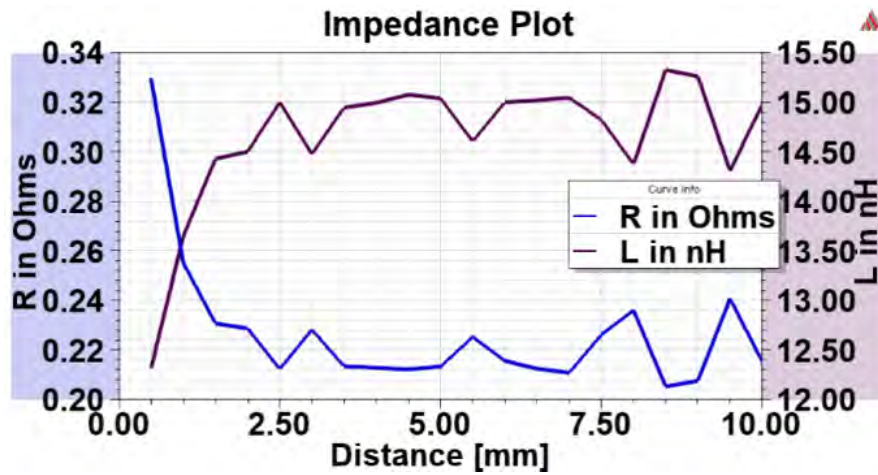


Figure 3.5: Effect of order of basis function on the distance parametric.

chosen carefully after studying several combinations of the simulation settings.

Fig. 3.6 shows the comparison of the convergence of the solution by using first order of basis functions versus second order. Table 3.2 compares other parameters such as time taken, number of mesh cells and memory used. This simulation is performed on Core i7 4770 CPU clocked at 3.4 GHz with 32 GB RAM and 64-bit Windows 8 operating system. The simulation is performed one after the other with no other program running. It can be seen that the use of second order basis functions has clear advantage in terms of number of passes required to reach the convergence criteria. Also, the number of mesh elements is reduced. While it consumes more memory, it is still faster with lower CPU time. It consumes almost 47% more RAM and but saves on 37% of CPU time. Since the project will involve huge number of simulations, the time is an important factor provided that the machine has enough RAM.

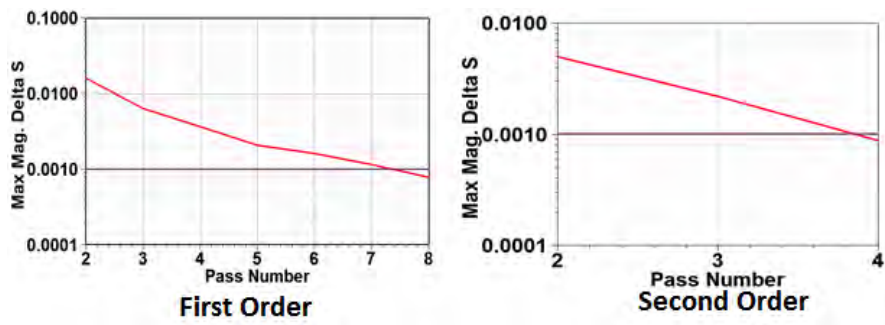


Figure 3.6: Effect of order of basis function on the convergence rate.

Table 3.2: Effect of Order of Basis function on System Resources

Order	Number of Passes	Mesh Elements	RAM	CPU Time (Min:Sec)
First Order	8	76719	4.81 GB	56:31
Second Order	4	28400	7.08 GB	35:52

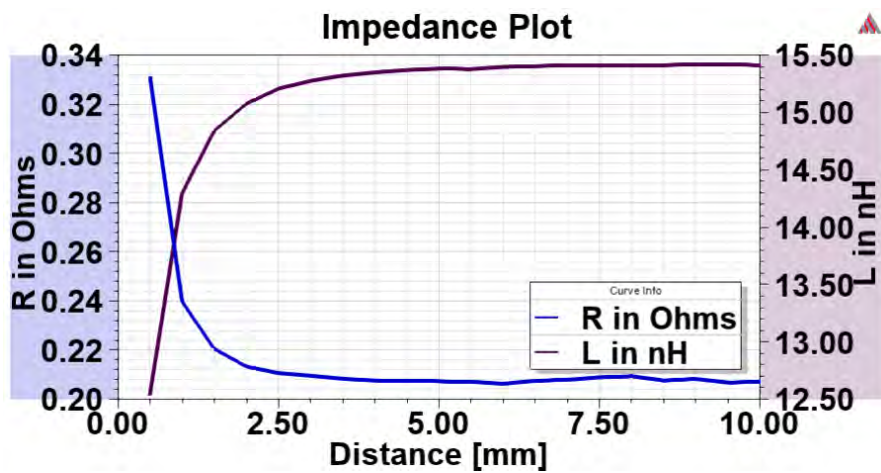


Figure 3.7: Effect of setting convergence $|\Delta S| < 0.001$ and $\angle S < 0.1$, mesh size < 0.5 mm, and using second order basis function.

Meshing

Since the field values at various locations of the sensor affect the impedance parameters, it is necessary to compute the fields at those locations. The default setup converges with less number of mesh elements on substrate. Consequently, the fields are interpolated at many positions. The interpolation error gives rise to the mesh noise which is found to be more than the reflected field due to eddy currents, especially at the high stand-off distance. Moreover, even if the S-parameters are converged, the field data still gives inaccurate results.

Therefore, to ensure that the field at the point of interest is calculated by the solver directly rather than by interpolation, the maximum length of any side of tetrahedron on the substrate is limited to 0.5 mm. This setting also has the advantage of reaching convergence in low number of passes as the initial mesh is much denser than the automatic mesh generated by the solver. Fig. 3.7 shows the smooth variation in resistance and reactance when meshing criteria is used along with the use of tight convergence criteria. It is also seen that the number of adaptive passes also reduce by the use of second order basis function.

To test the validity of the proposed simulation settings, a two turn loop is designed, simulated, fabricated and tested. The testing is done by using the setup and procedure described in Chapter 4. The measured values of the inductance is about 2.2% higher than the simulated one (measured 38.7 nH and simulated is 37.5 nH measured at 10 mm stand off distance). It can be due to the de-embedding or calibration or simulation inaccuracies as explained in Chapter 4. Nonetheless, to verify the sensitivity, the L,R and Q factor values are normalized with respect to their maximum values and the results are plotted in Fig. 3.8. The simulated

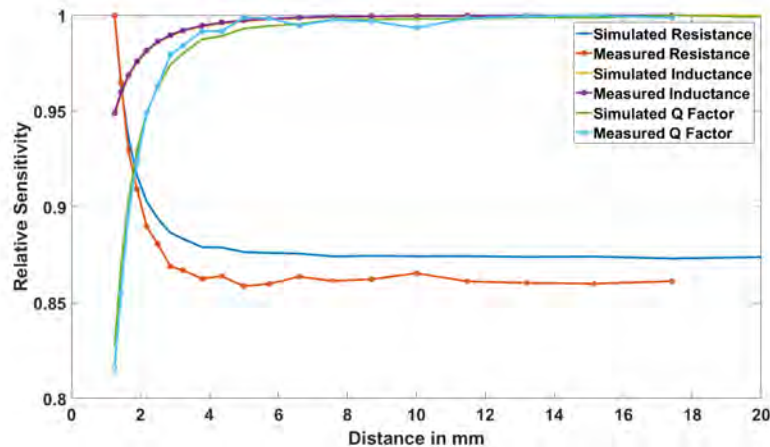


Figure 3.8: Comparison of simulated and measured relative L, R and Q quantities for a two turn loop.

and measured results show excellent agreement. The measured resistance shows more ripples than the simulated results. This validates the simulation settings and creates confidence in the further analysis.

3.2.1 Frequency Response of An Eddy Current Sensor

The inductance and resistance of a loop are not absolute parameters. They change with the frequency. A one turn loop EC sensor (same as designed in previous section) is used to look at the frequency response as shown in Fig. 3.9. It can be seen that both the inductance and resistance increase with frequency although not at the same rate. Inductance increases gradually with higher rate, whereas the resistance increases slowly at first and then increases rapidly near the self resonant frequency. This phenomenon is captured beautifully by the Q factor. Consequently, there is a frequency value for which Q factor is maximum. In this section, we look into this phenomenon in great detail creating a good understanding

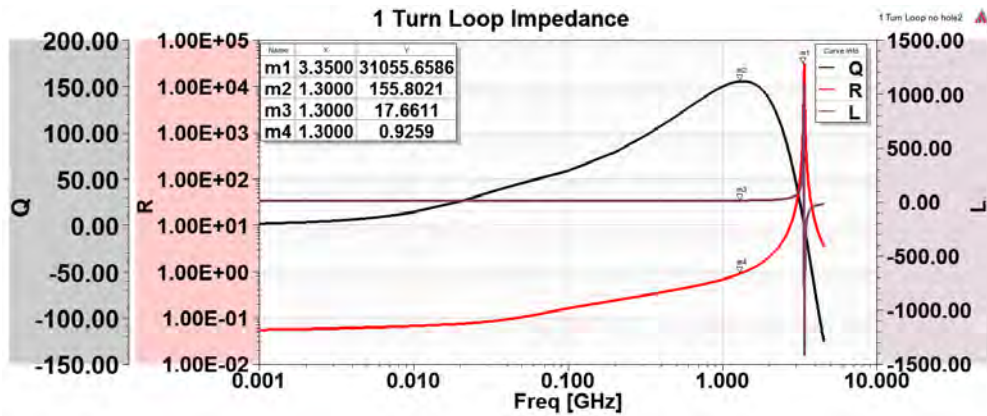


Figure 3.9: Frequency response of one turn loop eddy current sensor.

of underlying physical process.

At very low frequencies, the current is constant on both arms of the loop. As the frequency increases, the spatial variation in current starts appearing. when the length of the loop becomes equal to half wavelength, at that frequency, the spatial variation of current between the two end of loop becomes 180° . This can be seen in Fig. 3.10, in which the currents in two arms of the loop are opposite in direction at 1 MHz but they become same at 3.3 GHz. This seem to violate physics as there is no sink for current. Hence, the current cannot flow. Thus, at $\lambda/2$, the resistance of the loop is seen as infinite by the source.

When the current between two arms are exactly equal (which is strictly true only for DC), the rate of electron flowing in one direction equals the opposite direction. So no net electric field is seen. However, as the frequency increases, the phase difference starts appearing as explained above. This leads to generation of the E-fields which also oscillate at same frequency. This oscillating E field gives rise to the additional magnetic field. This adds to the original magnetic field of the loop. Consequently, the inductance of the loop seems to increase.

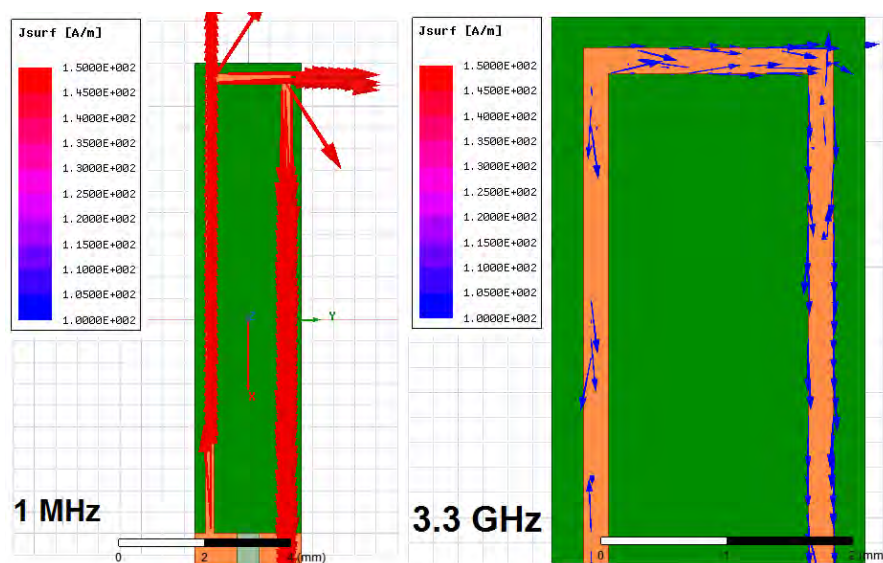


Figure 3.10: Direction of current in a loop at low and high frequency.

This continues until half wavelength ($\lambda/2$) frequency. Beyond this frequency, the E-fields dominate the H-field and the loop starts to look like a capacitor which explains the abrupt change in the reactance of the loop.

Fig. 3.11 shows the close up view of the behaviour of inductance with respect to the frequency. It is seen that the inductance first reduces till a certain frequency and then starts increasing. This seems contrary to the physics based explanation given above. To investigate further, the current on the loop is plotted at different frequencies, shown in Fig. 3.12. Current is also evaluated across the cross section of the loop line. Both these figures show that at lower frequencies, the current is uniformly distributed across the cross section of the line. As the frequency increases, the current starts collecting on the inner edges of the line. This effect is synonymous to the internal inductance of the circular wires and skin effect. There are two consequences of this phenomenon. One is that the current path reduces by about 0.2 mm from 2 mm loop width. Another is the change in the mutual

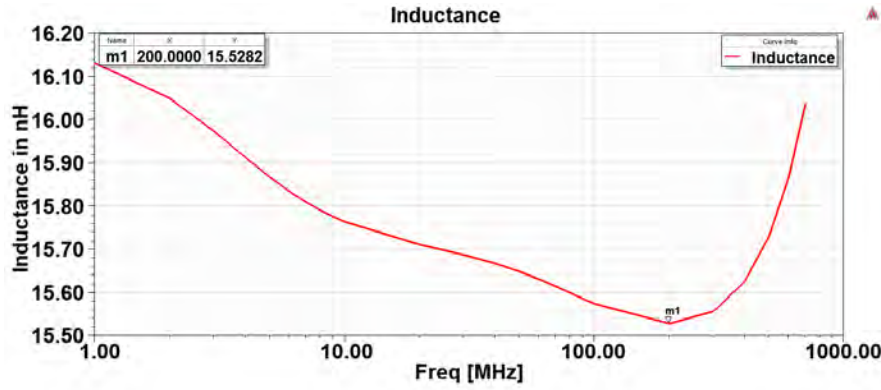


Figure 3.11: Variation of inductance of loop with frequency.

inductance between the two lines of the loop. This effect is more pronounced because of the rectangular form factor of the loop with 1:5 ratio.

Effect of Frequency on Magnetic Field Penetration in Target

The orthopaedic implants are usually made from titanium and titanium alloy - Ti-6Al-4V due to their attractive properties such as high tensile strength, rigidity and bio-compatibility [125]. The electrical conductivity of titanium and titanium alloys ranges between 1% to 3 % of IACS (conductivity of standard copper). The conductivity of titanium is 182000 S/m, while that of Ti-6Al-4V is 588235 S/m ($\rho = 170\mu\Omega - cm$) as reported in the literature. [126,127].

A high-frequency magnetic field attenuates inside the conducting medium. This attenuation depends upon the conductivity of the material and the frequency of the magnetic field. The distance at which the field strength reduces to $1/e$, is known as skin depth δ and can be found by Eq. 3.1, where f is the frequency of operation, μ is the permeability and σ is the conductivity of the medium.

$$\delta = \sqrt{\frac{1}{\pi f \mu \sigma}} \quad (3.1)$$

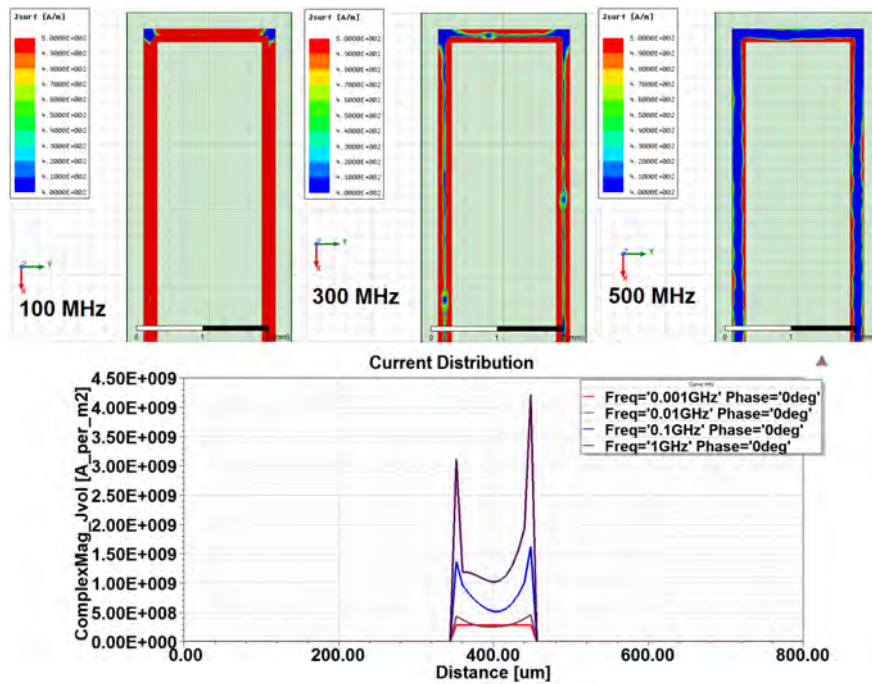


Figure 3.12: Current distribution on the loop at different frequencies.

Using Eq. 3.1, the skin depth for titanium and Ti-6Al-4V is calculated to be 4.3 mm and 1.4 mm, respectively at 1 KHz. It reduces to 4.3 μm and 1.4 μm at 1 MHz. In order to detect the the motion of the implant, it is necessary that the fields remain confined to the surface and should not emerge on the other side.

The numerical simulation of a two turn rectangular loop with the target in vicinity is performed for the excitation frequency is variation from 1 KHz to 100 MHz. The magnetic field along the Z direction at the centre of the loop is plotted in Fig. 3.13. The inset shows the geometry of the simulation. It can be seen that at the lower frequencies, the magnetic field passes through the target implant. However at 1 MHz, the field is negligible at a depth of about 1 mm. For 10 MHz and beyond, the fields are practically confined very near to the surface as calculated by the skin depth equation. The 2D magnetic field strength as a function of

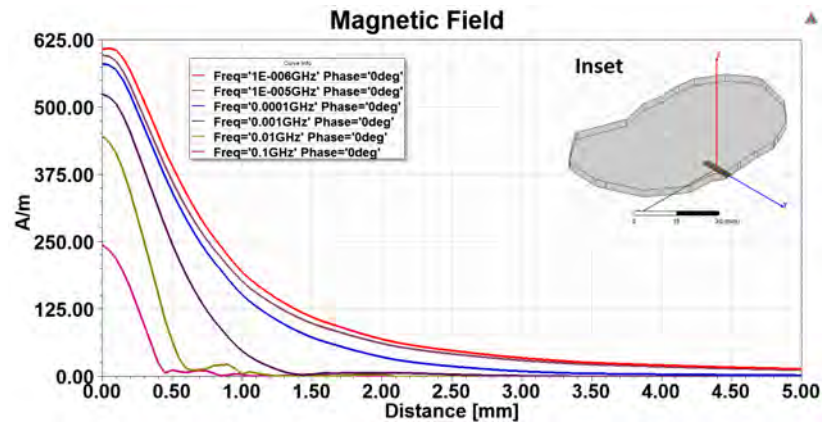


Figure 3.13: Magnetic field along a line perpendicular to the loop and passing through the titanium orthopaedic implant for different frequencies of excitation.

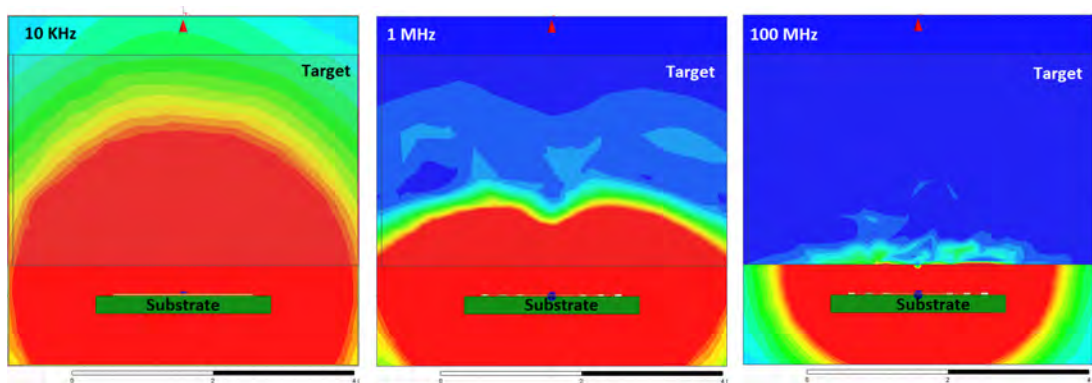


Figure 3.14: Magnetic field distribution from a two turn planar loop at 10 KHz, 1 MHz and 100 MHz frequency showing the depth of penetration.

frequency is shown in the Fig. 3.14 confirms the phenomenon. From this analysis, the subsequent simulations are performed for frequencies beyond 1 MHz.

3.3 EC Sensor Inside Human Body

As shown previously, the inductance, resistance and so the Q factor of the loop depend on the frequency. With the increasing frequency both the resistance and inductance increase. However the rate of increase is different which depends upon the geometry of the loop. The more the inductance, the better is the eddy current effect. Therefore, higher frequency is preferred to get better sensitivity and resolution. However, the increasing resistance (with frequency) decreases the amount of the current flowing through the loop. This behaviour is captured accurately by the Q factor. Q factor first increases with frequency, reaches to a peak (at F_{Qpeak}) and then starts decreasing.

Thus, F_{Qpeak} is the frequency beyond which increasing the frequency will not be helpful as increase in the resistance dominates. Therefore, F_{Qpeak} is generally considered as an ideal frequency of operation. However, when implanted inside the human tissue, its effects have to be considered which can substantially change the frequency response.

In the next section, electromagnetic properties of human body tissue are discussed followed by the evaluation of a two turn eddy current loop implanted inside a knee implant.

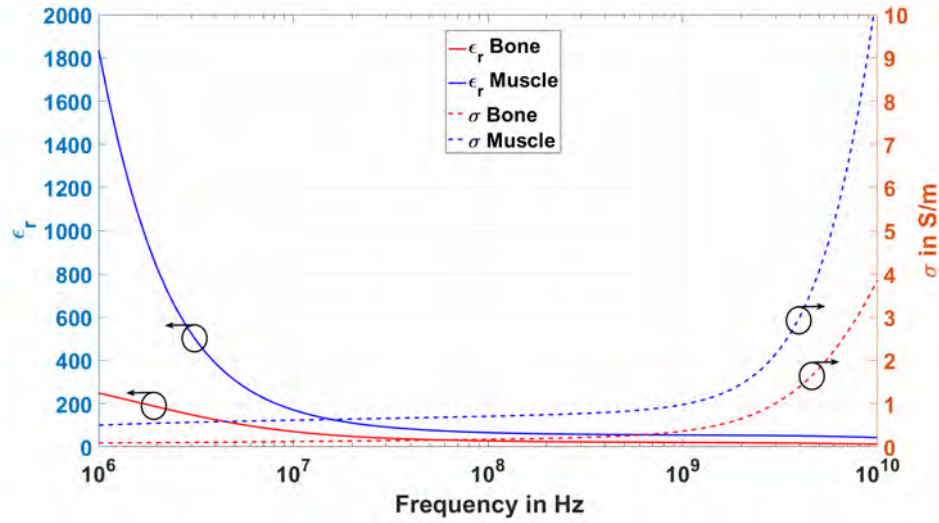


Figure 3.15: Dielectric properties of bone and muscle tissue.

EM properties of the Human Knee

The human knee is composed of two main tissues - tibial bone and muscle tissues. The skin layer being very thin, can be neglected. These tissues can be characterised electromagnetically by their relative permittivity ϵ_r and loss tangent $\tan \delta$. The human tissues are characterised in the range from 10 Hz to 20 GHz by [128] and modelled using Cole-Cole model [129]. The ϵ_r and conductivity σ for the tibial bone and muscle tissues from 1 MHz to 10 GHz are shown in the Fig. 3.15.

It can be seen that, both the tissues have similar response. However, the relative permittivity and the conductivity of the muscle tissue is higher than that of the tibial bone. Higher conductivity directly results in more power loss in the tissue whereas higher permittivity lowers the self resonant frequency. Also, the permittivity rises exponentially with the decrease in frequency below 10 MHz. The conductivity rises exponentially beyond 1 GHz. Since, conductivity is most detrimental to the sensor performance, it can be assumed that operating the sensor

beyond 1 GHz may not be very suitable unless it has any substantial benefit.

Eddy Current Sensor in Tibia

The eddy current loop can be fabricated on the PCB and inserted inside the cylindrical holes in the bone. Over the time, the bone grows around it sealing it from all the sides. This situation is simulated as follows. A two turn loop is designed on Rogers 6010 PCB with ϵ_r 10.2 and height 0.254mm. It is placed at a nominal distance of 5 mm away from the orthopaedic implant. The geometry is subtracted from the numerical tibial bone. Different muscle tissues like shin, quadriceps, hamstrings and calf are united and a homogeneous muscle medium is created.

Lower the frequency, lower is the Electro Magnetic power absorption by the human tissue. This makes the sensor safer for human use. Since the power loss in body is less, a low power, high efficiency sensor can be developed. However, the sensitivity increases with higher frequencies, hence frequencies up to 1 GHz (or self-resonant frequency) are explored. Conversely Frequencies below 1 MHz are not explored based on the skin depth analysis in the titanium implant. Therefore, to find optimal operational frequency, a broadband simulation spanning 3 decades of frequencies from 1 MHz to 1 GHz is performed with causality enforced in the simulation settings. Since the simulation domain becomes huge, a server class Intel Xeon CPU E6-2630 with two processors each with 8 cores clocked at 2.4 GHz with 128 GB RAM is used. The arrangement of the sensor implanted inside the human tibia is shown in Fig. 3.16. To utilize all the cores efficiently, 'HPC pool' license of HFSS is used that allows parallel processing of frequency samples and parametric variations.

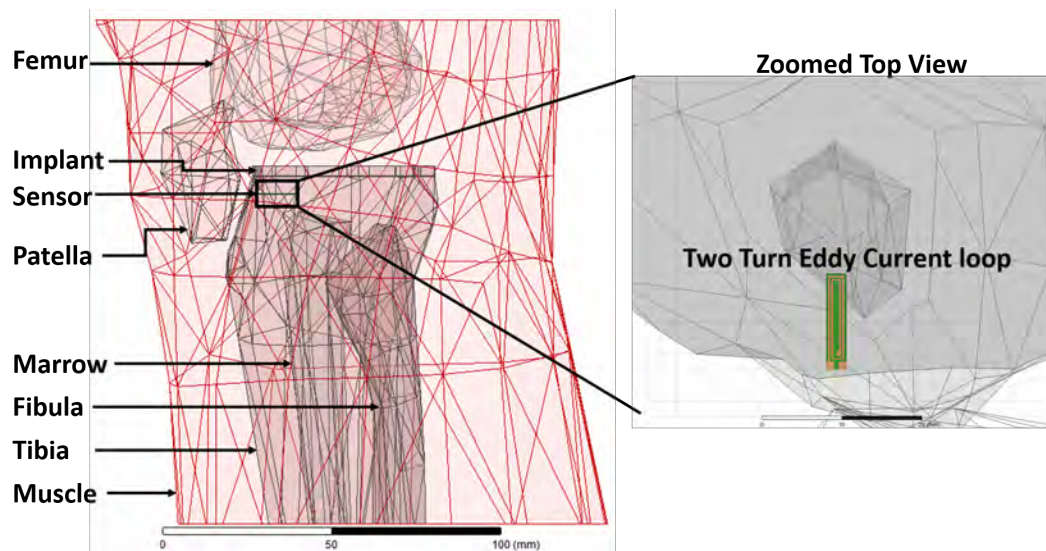


Figure 3.16: Design of a two turn loop implanted inside the tibial bone with orthopaedic implant.

The impedance properties, i.e. resistance, inductance, and Q factor as a function of frequency are shown and compared with the free space case in Fig. 3.17. The results of this comparison are tabulated in Table 3.3. Due to the presence of the bone the self resonant frequency (SRF) shifted from 1.14 GHz to 0.52 GHz. The frequency at which the Q factor peaks, is reduced to 40 MHz from 440 MHz. Also, the maximum Q factor is reduced to 28.8 from 97.7. This is because of the power lost in the human tissue. This also reflects as the increase in the resistance of the loop as seen in Fig. 3.17.

To further investigate the effect, the power lost in the tissue is evaluated by using the field calculator tool in Ansys HFSS. The field quantity volume power loss density is evaluated in each mesh cell and integrated over the entire volume of the object (see Eq. 3.2). In case of the loop, since it is modelled by a surface mesh, surface volume loss density is used (see Eq. 3.3). Similarly, for the calculation of

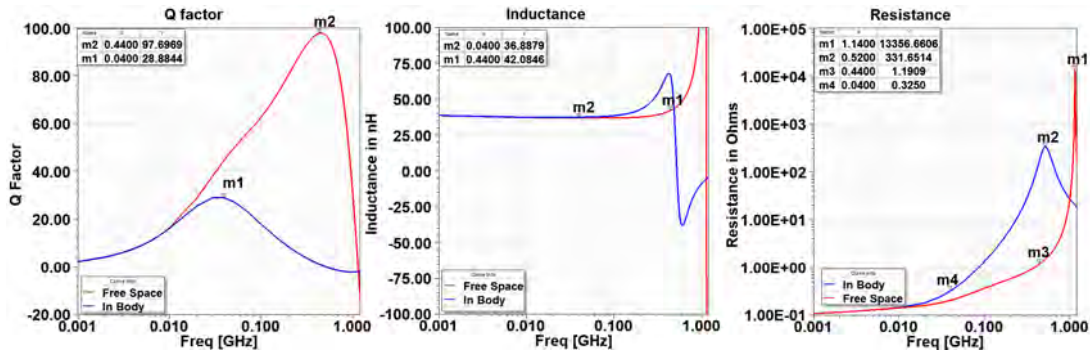


Figure 3.17: Comparison of the free space and in body impedance properties of the two turn eddy current sensor.

Table 3.3: Comparison of the impedance parameters of a two turn eddy current loop in human body and free space. Frequency in GHz, inductance in nH and resistance in Ω s.

Design	F_{SRF}	F_{Qpeak}	$Q @ F_{QPeak}$	$L @ F_{SRF}$	$R @ F_{SRF}$
Free Space	1.14	0.44	97.7	66.37	1.19
In Body	0.52	0.04	28.8	36.9	0.325

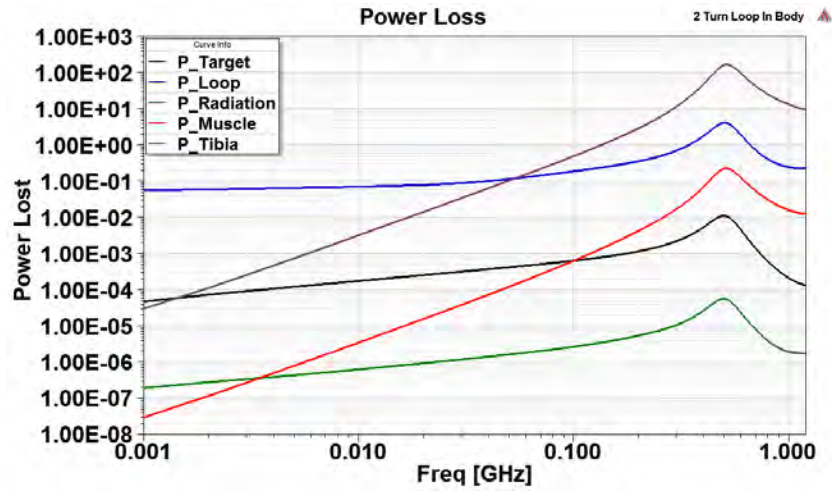


Figure 3.18: Power dissipation in the different objects as a function of frequency.

radiation loss, the surface loss density is integrated over the surface of the bounding box with an absorbing boundary condition.

$$P_{VolLoss} = \int_V (\rho_{vl}) dv \quad (3.2)$$

$$P_{SurfLoss} = \int_S (\rho_{sl}) ds \quad (3.3)$$

Since the loop is not matched to the 50Ω power source, to remove the effect of mismatch in field power calculations, the model is dynamically linked to the Ansys Circuit Simulator where it is excited by a constant 1 A current source. The excitation is then pushed back to the HFSS model to recalculate the fields. The power dissipation so obtained in target (P_Target), loop (P_Loop), radiation (P_Radiation), Muscle tissue (P_Muscle) and Tibial bone (P_Tibia) is shown in Fig. 3.18.

Following observations can be made from this figure.

1. Power dissipation increases with the frequency until SRF.
2. Power loss in the loop dominates at lower frequencies. Beyond about 50 MHz, the power loss in body tissue dominates.
3. Power lost in the tibial bone is higher than in the muscle tissue by at least 2 orders of magnitude despite the conductivity of the muscle is more than the bone. This is because the loop is embedded inside the bone and so maximum near field is confined to it.
4. Radiated power is very low and can be neglected. This is expected as the loop is electrically very small.
5. Power loss in the titanium target is almost 3 order of magnitude less than the power in the loop. This is because of the smaller conductivity (2 % IACS) of the titanium due to which smaller amount of current is induced. Also, the distance of the target from the loop is almost half of the maximum dimension of the loop.

The primary effect of the human tissue is that it absorbs the power due the presence of E fields. The higher the frequency, the higher is the conductivity of the tibial tissue and the muscles surrounding it (Fig. 3.15). Also with the increasing frequency, the currents on the parallel arms of the loops get increasingly out of phase. Consequently, the E-fields are developed between these two arms. Since, human body is lossy dielectric, it absorbs the energy in the E-field. This further adds to the losses in the human tissue. Therefore, we define another frequency FL_{max} . At this frequency, the power lost in tissue is more than the power dissipated in the loop. Operating the eddy current sensor beyond this

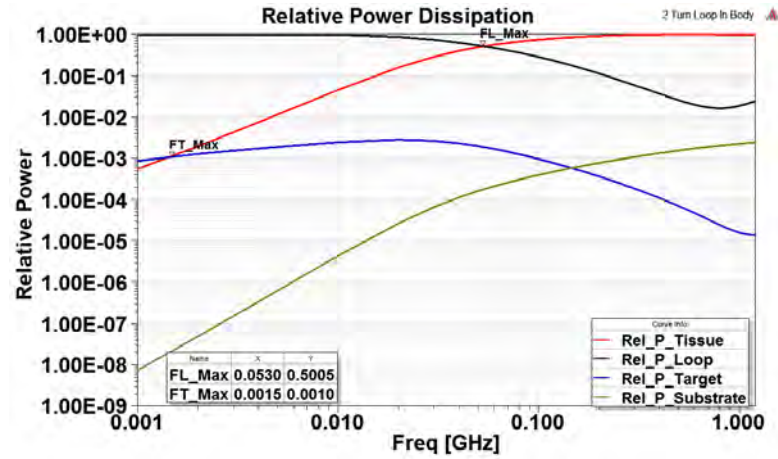


Figure 3.19: Relative power dissipation in different objects as a function of frequency.

frequency would mean that the more power is lost in the tissue than the loop itself and so it may not be advisable to do so.

Further, the energy is lost in the titanium orthopaedic target. There is a frequency at which power lost in tissue becomes greater than the titanium implant. This frequency can be termed as FT_{max} . Exciting the loop below this frequency may allow for implant motion be more effectively detected than the changes in the surrounding tissue. For evaluating these two frequency limits the relative power loss evaluation is necessary. Power lost in each object is therefore, normalized with respect to the total power loss. The results are shown in Fig. 3.19. Since, the power dissipation is normalized i.e. relative to the total power loss, the legend shows the power lost in tissue, loop, target and substrate as Rel_P_Tissue, Rel_P_Loop, Rel_P_Target and Rel_P_substrate respectively. From the Fig. 3.19, the FL_{max} is 53 MHz while FT_{max} is about 1.5 MHz.

These two frequencies have a distinct meaning. FL_{max} is the frequency beyond

Table 3.4: Limiting frequencies for a two turn eddy current sensor in human body.

F_{SRF}	F_{QPeak}	FL_{max}	FT_{max}
520 MHz	40 MHz	53 MHz	1.5 MHz

which if the sensor is operated, more power is lost in the tissue than the loop itself and so will lead to higher power requirement. FT_{max} is the maximum frequency, beyond which power lost in tissue is more than that in the target, so the variation in tissue parameter may dominate the micro-motion of the implant. This would affect the resolution of the sensor.

The sensor may still be operated beyond this frequency but the measurements may not be precise when done after long periods of time as tissue parameters may change either due to growth or change in the density and water /ion content of the tissue. Therefore, the limiting frequencies of operation in order of decreasing importance are F_{SRF} - F_{Qpeak} - FL_{max} - FT_{max} . Beyond F_{SRF} , inductor will start working as capacitor. Beyond F_{Qpeak} more power is lost in resistance than creating additional magnetic field. Beyond FL_{max} , more power is lost in tissue than the eddy current loop. Beyond FT_{max} , more power is lost in tissue than the target and so may decrease the precision of the measurement. For a two turn eddy current loop implanted inside the tibial bone, these frequencies are tabulated in 3.4.

3.4 Mitigation of the Effect of Human Body

It can be seen that the limiting frequencies are very low when the eddy current loop is directly inserted inside the tibial bone. In order to reduce the effect of human

tissue on the loop, the PCB printed eddy current loop can be coated by a dielectric material. There are various types of bio compatible dielectric materials. The most commonly used materials are Polydimethylsiloxane (PDMS) with $\epsilon_r = 2.7$, Polyether ether ketone (PEEK) with $\epsilon_r = 3.2$, Alumina with $\epsilon_r = 9.2$ and Zirconia with $\epsilon_r = 23$. Out of these, PDMS and PEEK are organic chemicals, whereas Alumina and Zirconia are ceramic materials.

A cylindrical coating of these materials is applied on the PCB, and it is inserted into tibial numerical phantom and simulations are performed. The effect of dielectric coating on the impedance characteristics of the eddy current loop is shown in Fig. 3.20. It can be seen that lower the ϵ_r of the dielectric cover, higher is the SRF and Q factor.

The relative power dissipation in various components is then plotted according to the above described process. The results are plotted in Fig. 3.21. The maximum operating frequency in terms of loop (FL_{Max}) and in terms of target (FT_{Max}) for different dielectric covers are given in table 3.5 along with F_{SRF} and F_{QPeak} . With the increasing dielectric constant, both the FL_{Max} and FT_{Max} decrease.

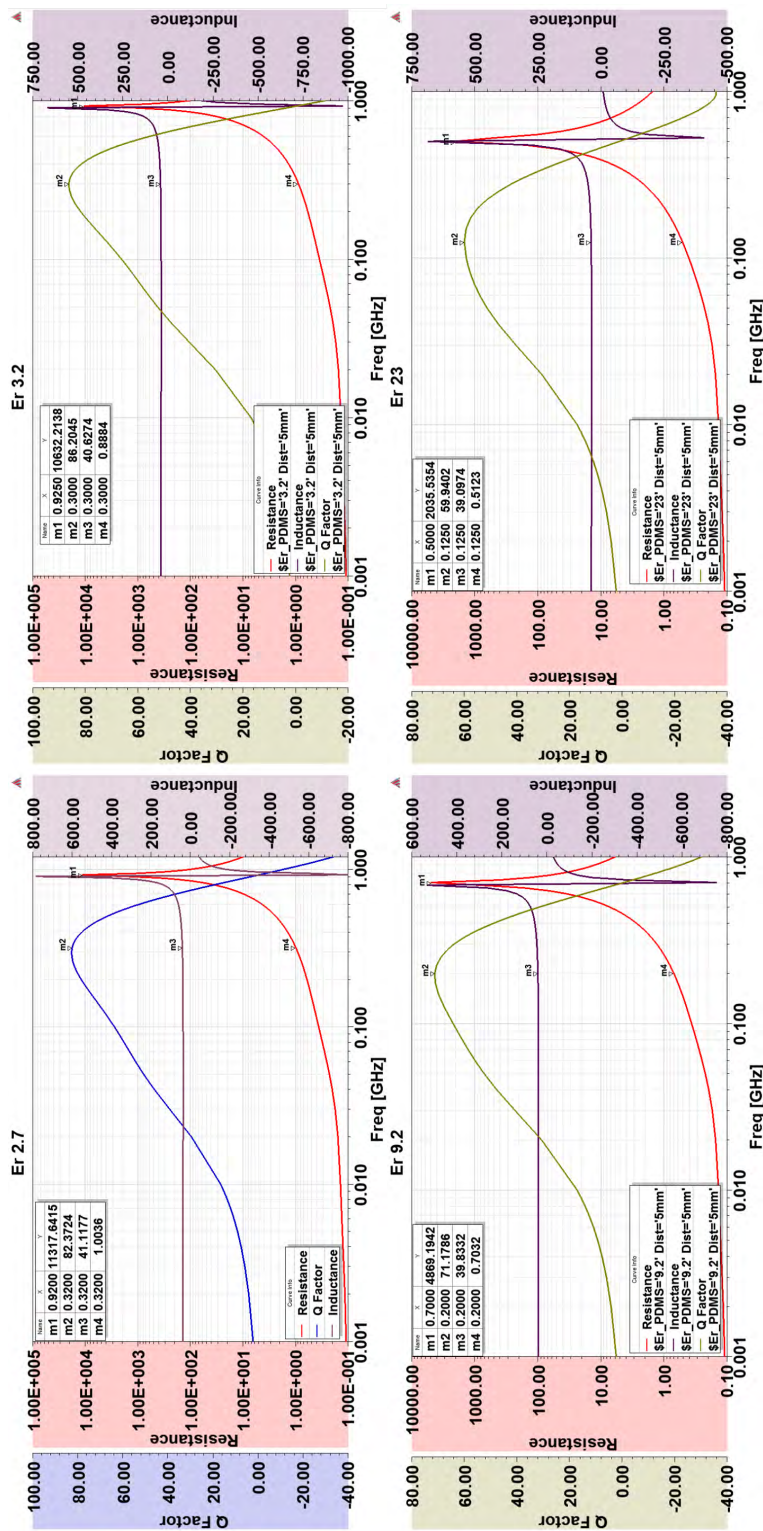


Figure 3.20: Comparison of impedance properties of a two turn eddy current sensor coated with different dielectric materials.

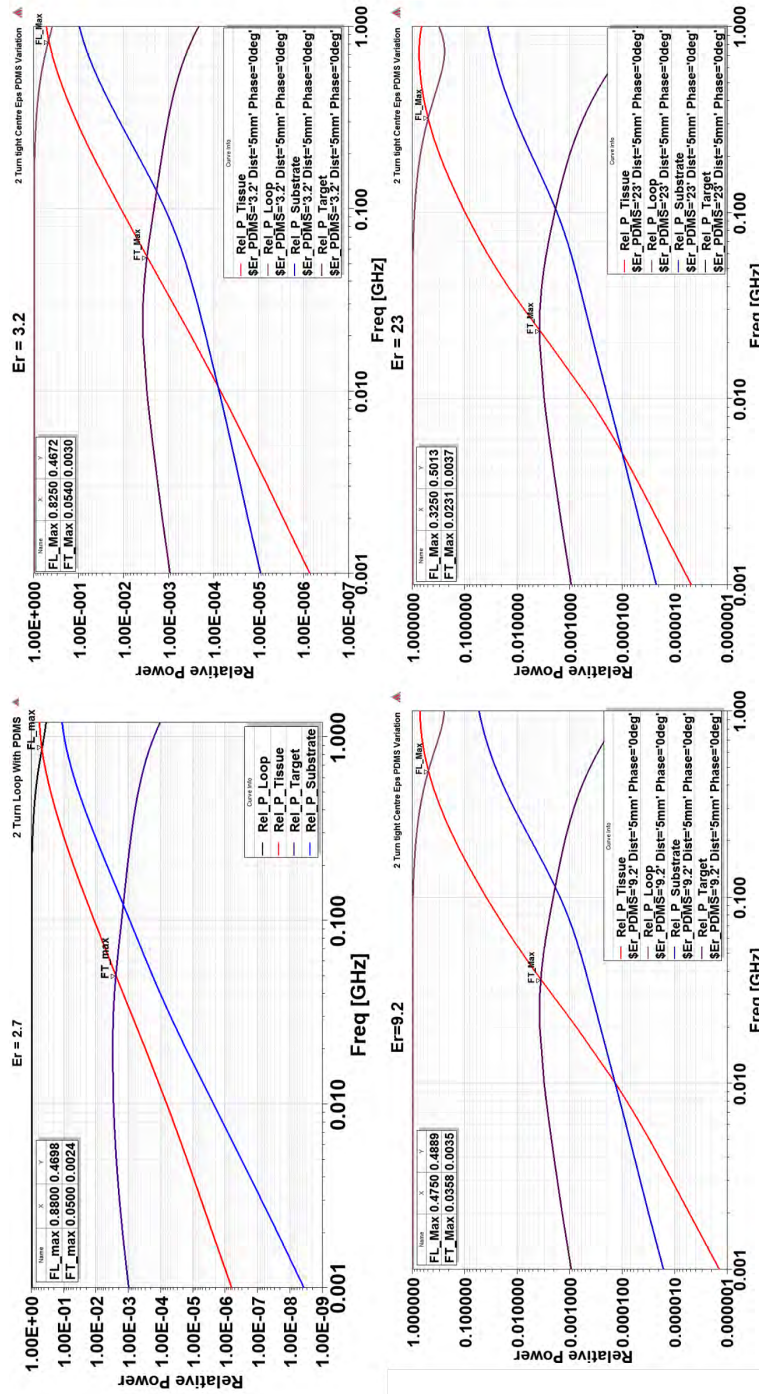


Figure 3.21: Comparison of relative power loss for a two turn eddy current sensor coated with different dielectric materials.

Table 3.5: Limiting frequencies for the different dielectric coatings.

Dielectric	F_{SRF}	F_{QPeak}	FL_{Max}	FT_{Max}
PDMS ($\epsilon_r = 2.7$)	920 MHz	320 MHz	860 MHz	60 MHz
PEEK ($\epsilon_r = 3.2$)	925 MHz	300 MHz	825 MHz	54 MHz
Alumina ($\epsilon_r = 9.2$)	700 MHz	200 MHz	475 MHz	36 MHz
Zirconia ($\epsilon_r = 23$)	500 MHz	125 MHz	325 MHz	23 MHz

There are two reasons for this behaviour. The E-fields are strongest near the loop and their intensity falls off rapidly with distance. Firstly, by coating the eddy current loop by a low loss dielectric, maximum near fields do not suffer any attenuation as in the case of direct the tissue contact. Secondly, lower the dielectric constant of the coating, higher is the dielectric contrast between tissue and coating. Due to this, lesser E-fields interact with the tissue. Consequently, the power absorbed by the tissue is also less. To verify this, the E-fields along the line placed the centre of the eddy current loop are plotted at the frequency (freq) 100 MHz in Fig. 3.22. It can be clearly seen that as the dielectric contrast increases, the E-fields are concentrated more inside the cover and their magnitude in tissue is lower. Also, there is no effect on the H-fields as expected (see Fig. 3.23). The curves are plotted for ϵ_r (Er_PDMS) of 3.2, 9.2, and 23 when the sensor is at the stand off distance of (Dist) 5mm.

FT_{max} as a Function of Stand-Off Distance

It can be noted that as the sensor is placed at a greater standoff distance, the amount of power coupled to the target reduces, and the amount of fields interacting

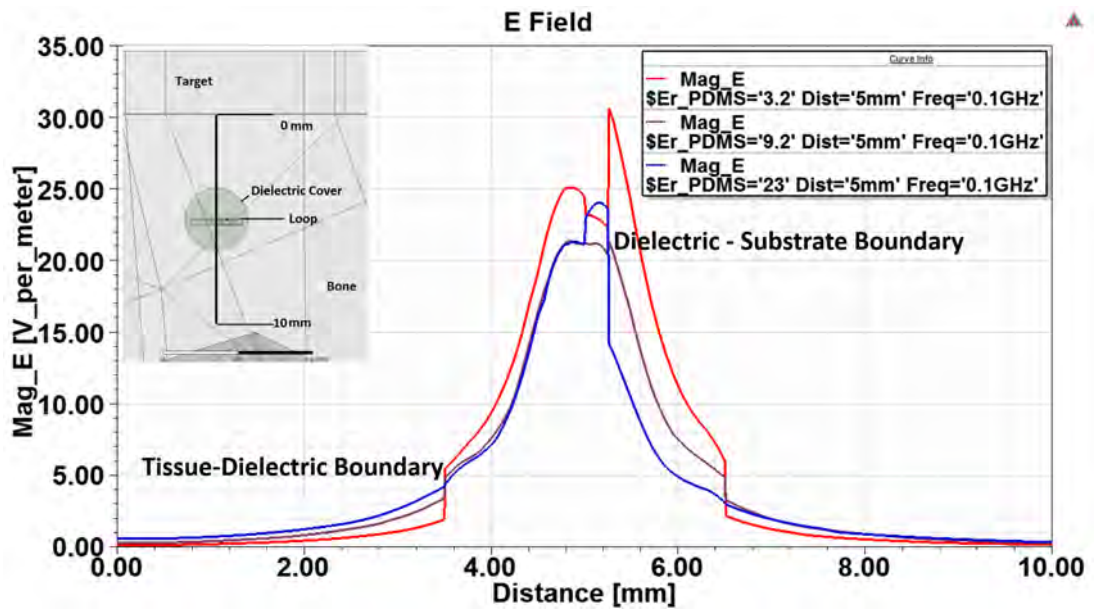


Figure 3.22: E-Field distribution along the line passing through the centre of EC loop.

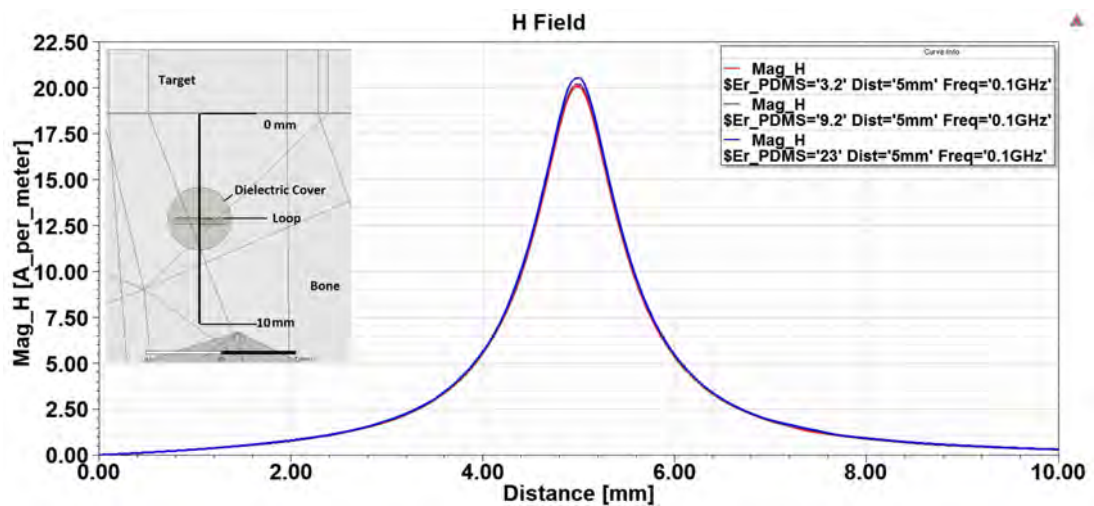


Figure 3.23: H-Field distribution along the line passing through the centre of EC loop.

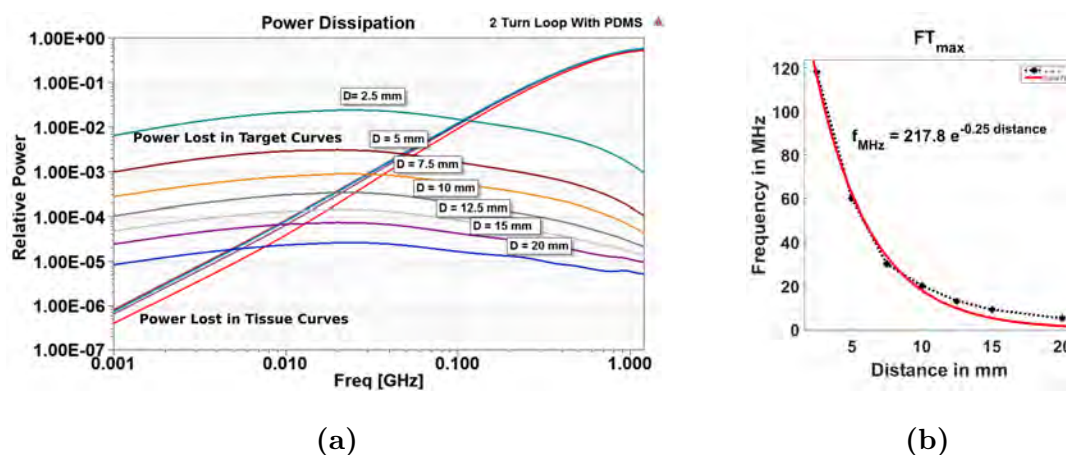


Figure 3.24: (a) Power dissipation in target and tissue as a function of frequency and standoff distance. (b) Curve fit for FT_{max} and standoff distance.

with tissue between the implant and sensor increases. Figure 3.24a shows the power dissipation as a function of frequency for various standoff distances. While the power lost in tissue does not change much, the power in titanium target drops logarithmically. Consequently the FT_{max} also decreases. The value of FT_{max} against the standoff distance is plotted in Fig. 3.24b. It drops exponentially. A curve fit expression is also developed (3.4) which can be used as a guideline to evaluate the maximum frequency of operation for a particular standoff distance d (in mm).

$$FT_{max} = 217.8e^{(-0.25d)} \quad (3.4)$$

3.5 Evaluation of the Sensitivity of EC sensor

The eddy current sensor output is nonlinear with respect to the distance of operation. The inductance (L), resistance (R), and the Q factor changes non-linearly with the standoff distance (see Fig. 3.7). Therefore to characterize the response of

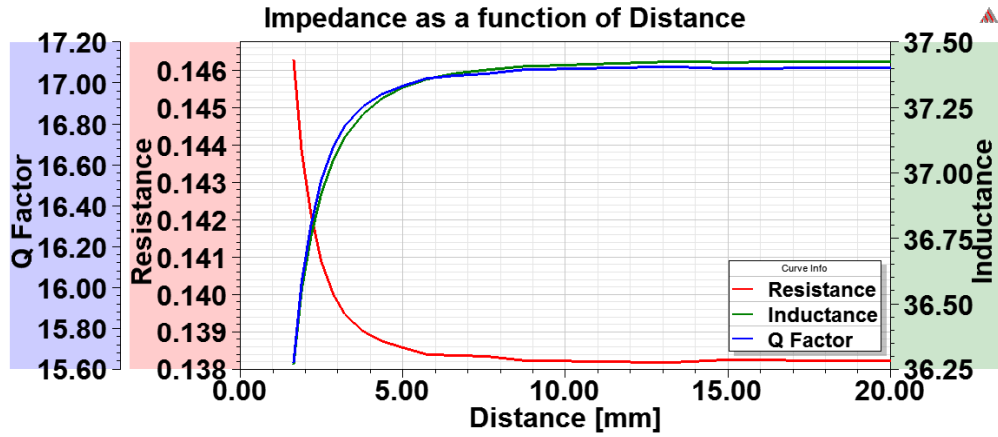


Figure 3.25: Variation of the impedance parameters as a function of the stand-off distance.

the sensor for motion sensing, the orthopaedic titanium plate is moved away from the loop from 1.25 mm to 20 mm in logarithmic steps of 5 samples per octave. This ensures that at smaller distances, where sensitivity is high, more measurements are captured. This allows for the reduction in the number of points (around 21) at which solution is generated compared to the linear distribution (around 74) without losing important information about the sensitivity and the range. The value of the resistance, inductance and Q factor of a two turn loop coated with a cylindrical PDMS layer with respect to the stand off distance is shown in Fig. 3.25.

The dependence of R,L And Q factor parameters on distance can be curve fitted using Eq. 3.5 where y can be the resistance, inductance or Q factor, x is the standoff distance and a , b , and c are the co-efficients of curve fit.

$$y = ax^b + c \quad (3.5)$$

The impedance parameters not only change with the standoff distance, but

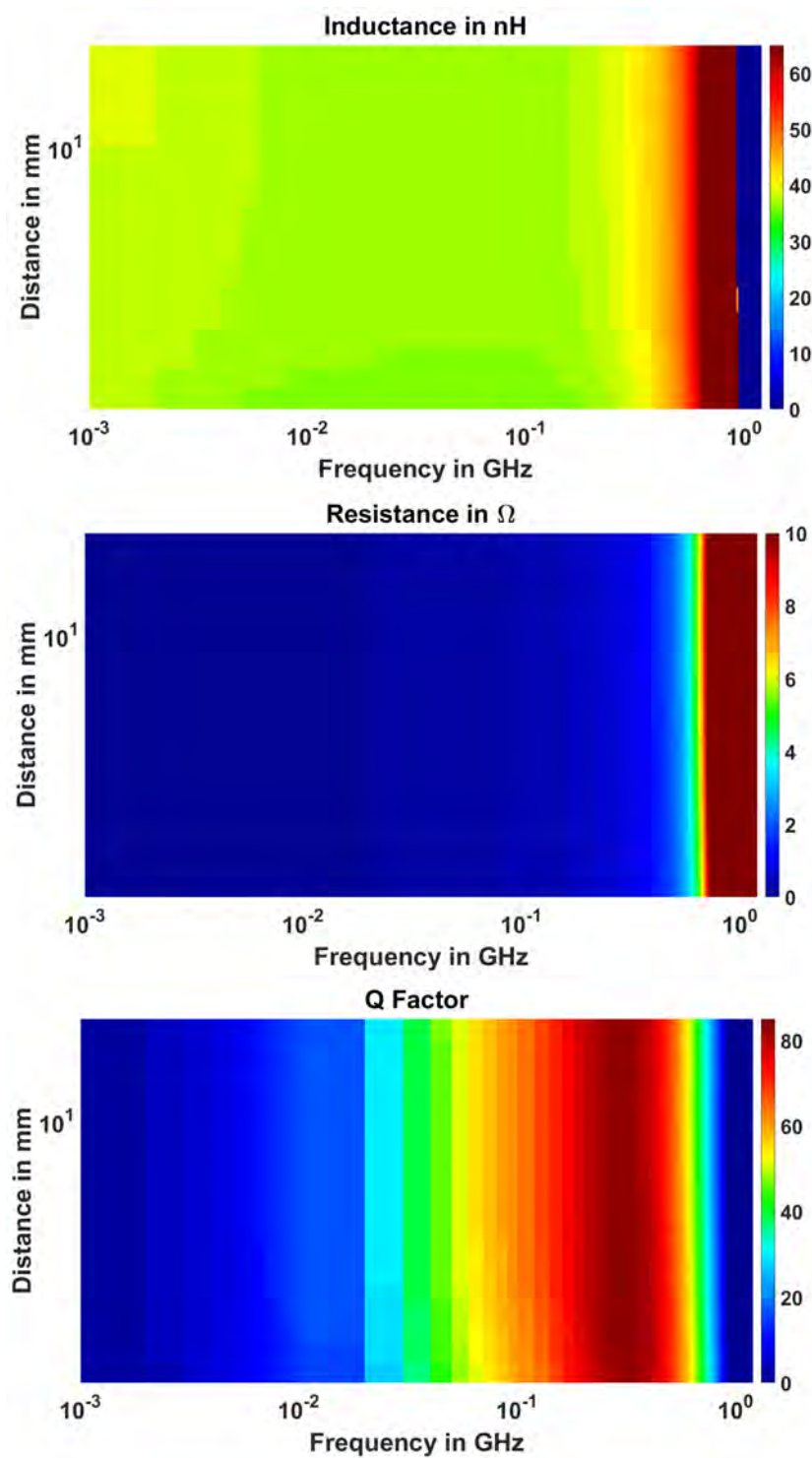


Figure 3.26: Variation of impedance parameters - L, R, and Q as a function of the stand-off distance and frequency.

also with the frequency as shown in Fig. 3.26. A MATLAB program is written to perform the curve fit on the distance data available for all the frequencies. This generates the a , b , and c coefficients for the entire frequency range. For inductance and Q factor, c will be a positive value whereas b and c will be negative. For resistance, a and c will be positive whereas b will be negative. This is taken into account while writing program for curve fit. Thus, for inductance the equation used is $y = c - ax^{-b}$ and for resistance the equation used is $y = ax^{-b} + c$. Consequently, all the coefficients are calculated positive by curve fit algorithm. This facilitates log-log plot of the values. The result of the curve fit are shown in Fig. 3.27 for inductance, resistance and Q factor. Following observations can be made from the curve fit analysis.

1. The curve fit at maximum frequency points is exceptionally good as seen from adjusted R^2 graph where its value is near to 1.
2. At F_{SRF} , the adjusted R^2 drops to low value for the three parameters. This indicates failed curve fit. Correspondingly, the curve fit coefficients have discontinuity or abrupt change at F_{SRF} and so are not reliable indicators of the actual behaviour. This behaviour is expected as the resistance becomes infinite and the reactance abruptly changes to negative value, therefore no current flows through the loop and so no eddy current effect.
3. The adjusted R^2 drops at a certain frequency before SRF for resistance (and so the Q factor). It is around 125 MHz. This also indicates that curve fit does not reproduce the data points well. Also it can be noted that at this frequency (F_{Worst}), co-efficient a becomes negative for resistance. Co-efficient c always remains positive which merely indicates that the resistance

is positive.

To investigate this issue of bad curve fit around 175 MHz, the resistance-distance curves are plotted for three different frequencies, at $f_1 < F_{Worst}$, F_{Worst} and $f_2 > F_{Worst}$ in Fig. 3.28. At lower frequency F_1 , the resistance decreases with increasing distance. At F_2 , the resistance increases with distance. At F_{Worst} is the transition frequency. Around this frequency, the resistance change is not well behaved. Therefore, the curve fit of the power law form fails at this frequency. Consequently, operating the sensor around this frequency is not recommended. At higher frequencies, the sensor may be operated and possibly with higher sensitivity but also with higher losses in body as well as loop.

3.6 Definition of The Sensor Parameters

The curve fit coefficients do not yield any substantial information by themselves. However, they can be used to calculate the output (R, L or Q factor) at any distance. This is used to define useful sensor parameters.

First, the sensitivity is defined as the change in the output quantity y (inductance, resistance, Q Factor) for the 10 μm displacement of the target expressed in logarithmic scale (to the base 10) by Eq. 3.6.

$$S_{10\mu\text{m}}(\text{dB}) = 10 \log \left(\frac{\Delta y}{y} \right) \quad (3.6)$$

The logarithmic scale is used to handle very small numbers and produce meaningful graphs. According to this definition, sensitivity of 10 dB means 1 part in 10 is changed for 10 μm motion, 20 dB corresponds to 1/100, 30 dB to 1/1000 and so on. Based on this definition, sensitivity range is defined at x dB. This is the range

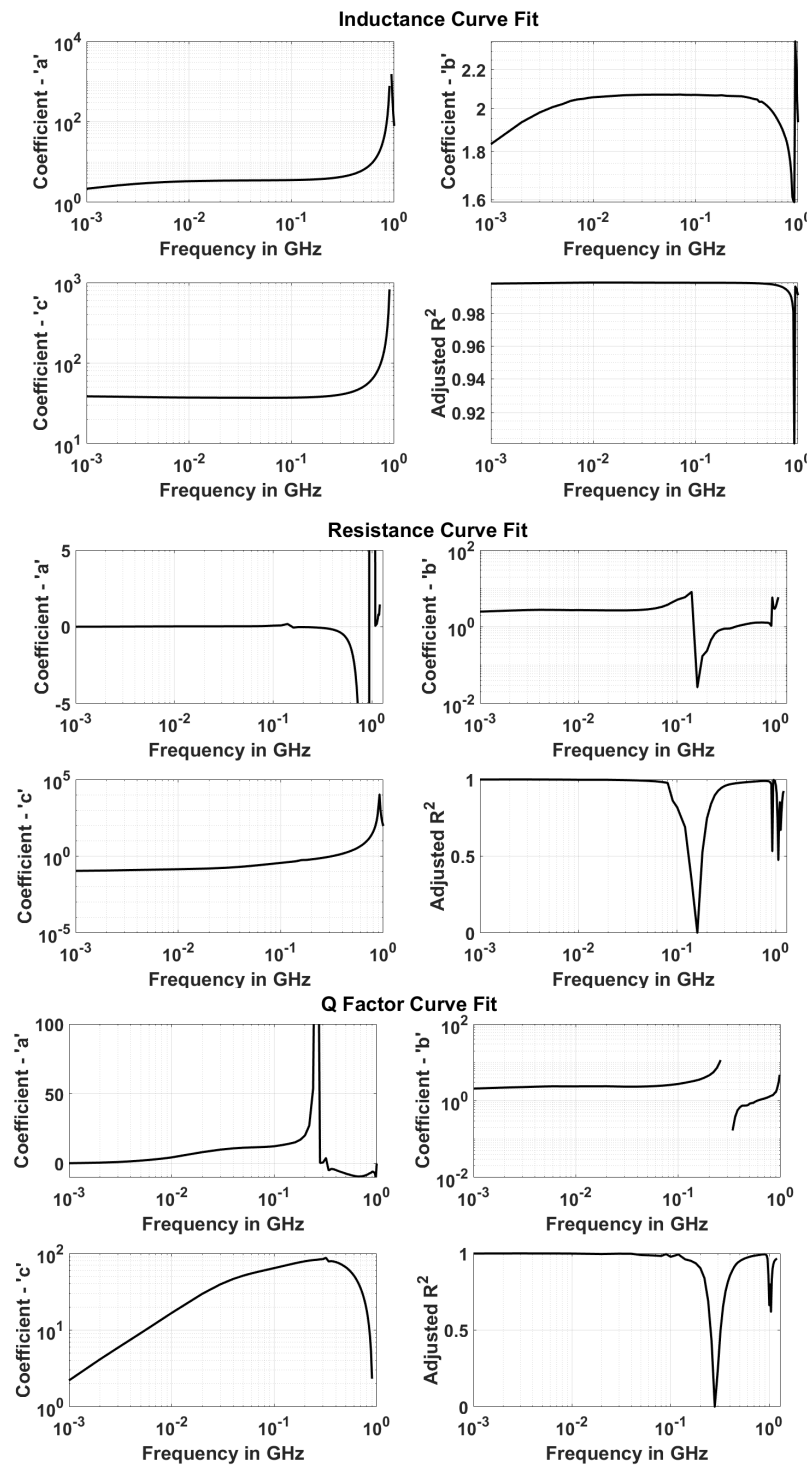


Figure 3.27: Curve fit analysis of the L, R and Q factor.

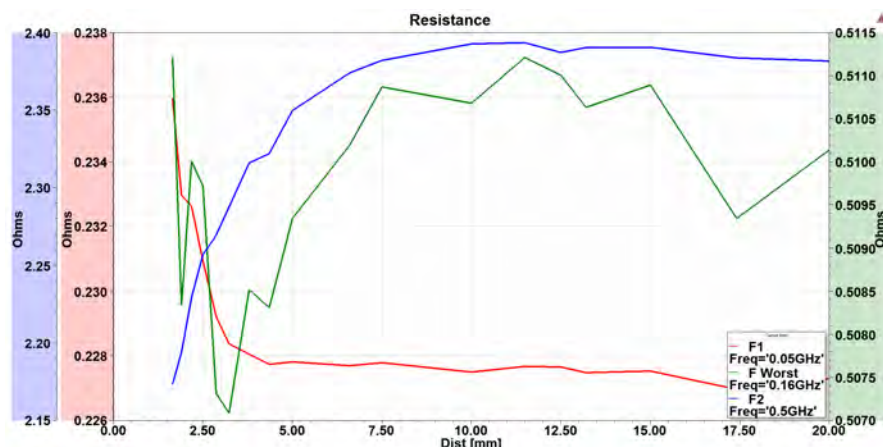


Figure 3.28: Resistance - distance curves at three frequencies $f_1 < F_{Worst}$, $f = F_{Worst}$ and $f_2 > F_{Worst}$.

at which the sensor can detect $10 \mu\text{m}$ displacement if the detection circuit can produce measurable output for x dB change. If the sensor is placed beyond this range, it cannot be used to detect the $10 \mu\text{m}$ motion.

Using Eq. 3.6, the sensitivity of the sensor with respect to inductance, resistance and Q factor is calculated at different frequencies between 1 MHz and F_{SRF} and stand-off distances between 1 mm to 20 mm. The results are plotted in Fig. 3.29. The colors represent the sensitivity in the dB value. The sensitivity decreases with the stand-off distance and increases with the frequency as is expected. Especially, inductance sensitivity shows this behaviour strikingly well. The resistance (and Q factor) sensitivity shows a drop at F_{Worst} frequency as explained above. However, due to this phenomenon, there, is an optimal frequency of operation between 1 MHz and F_{Worst} where sensitivity peaks (at 20 MHz).

While these figures give a rough estimate of what sensitivities could be expected at different frequencies and distance, the maximum range that a sensor can have

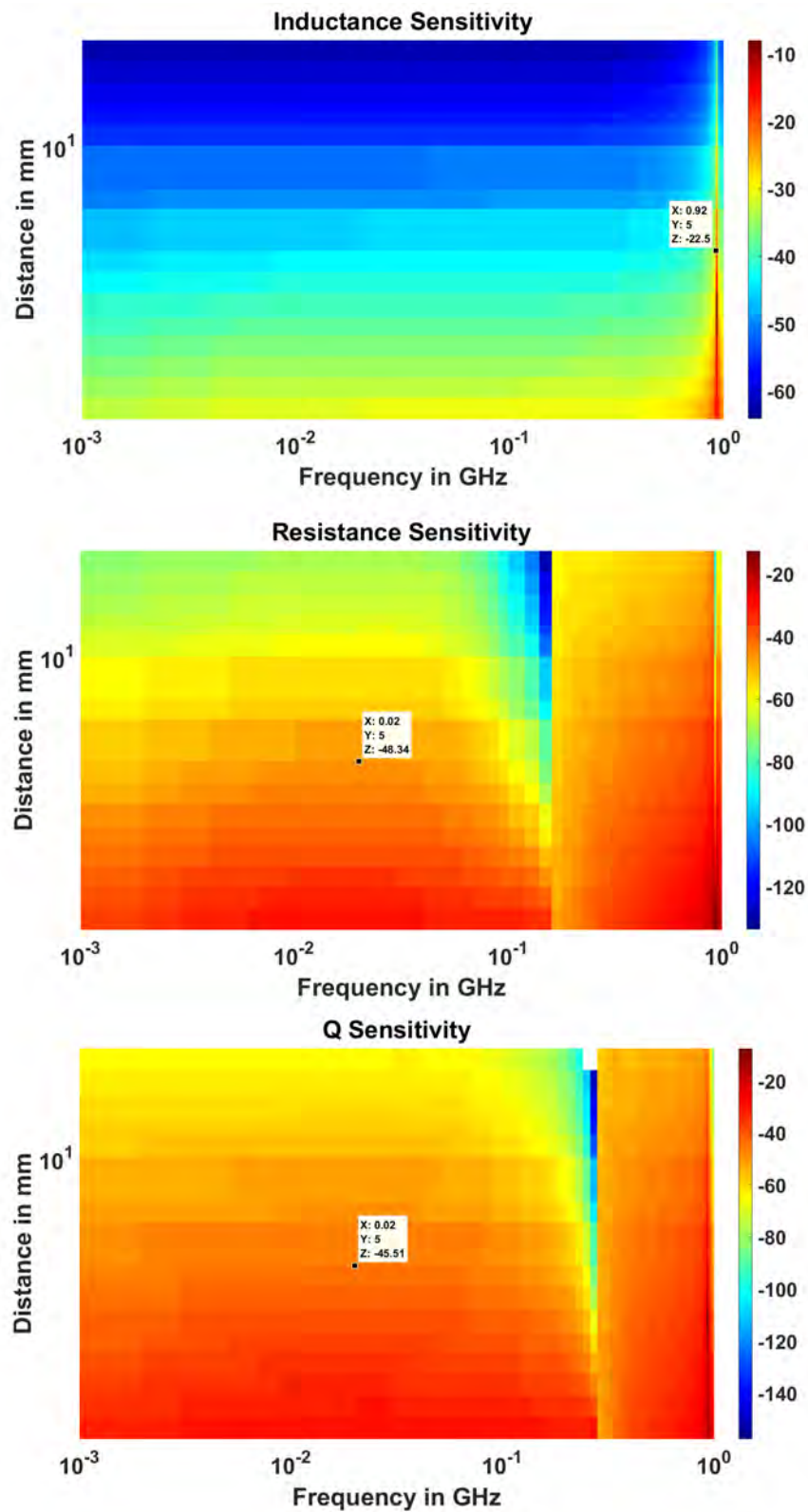


Figure 3.29: Sensitivity Analysis for Inductance, Resistance and Q factor.

for a given level of sensitivity, called as sensitivity range is plotted in Fig. 3.30.

It should be noted that Q factor is the quantity derived mathematically from resistance and inductance measurements. Therefore, if the inductance and resistance could not be measured at a given distance, the Q factor cannot be calculated as well. However, if they can be measured then Q factor can give higher resolution or sensitivity. The increased Q factor sensitivity range, therefore, is merely representative of the increased sensitivity and not the actual distance at which the device can work.

3.7 Summary

A numerical model of an eddy current sensor implanted in the tibial bone of the human knee is created. Then the reliable and correct simulation settings were determined and validated by experiment. It is seen that implanting the sensor inside the bone decreases the self resonant frequency of the sensor as well as sensitivity. To mitigate the effect of body, it is proposed to use a dielectric cover. It is established that higher the dielectric contrast between the bone and the dielectric cover, less power is absorbed in tissue. A new definition of sensitivity is proposed, based on the curve fit analysis, that measures the amount of impedance change with stand-off distance and frequency for 10 μm change in the position of the orthopaedic implant. The maximum possible range at a given sensitivity level is also calculated.

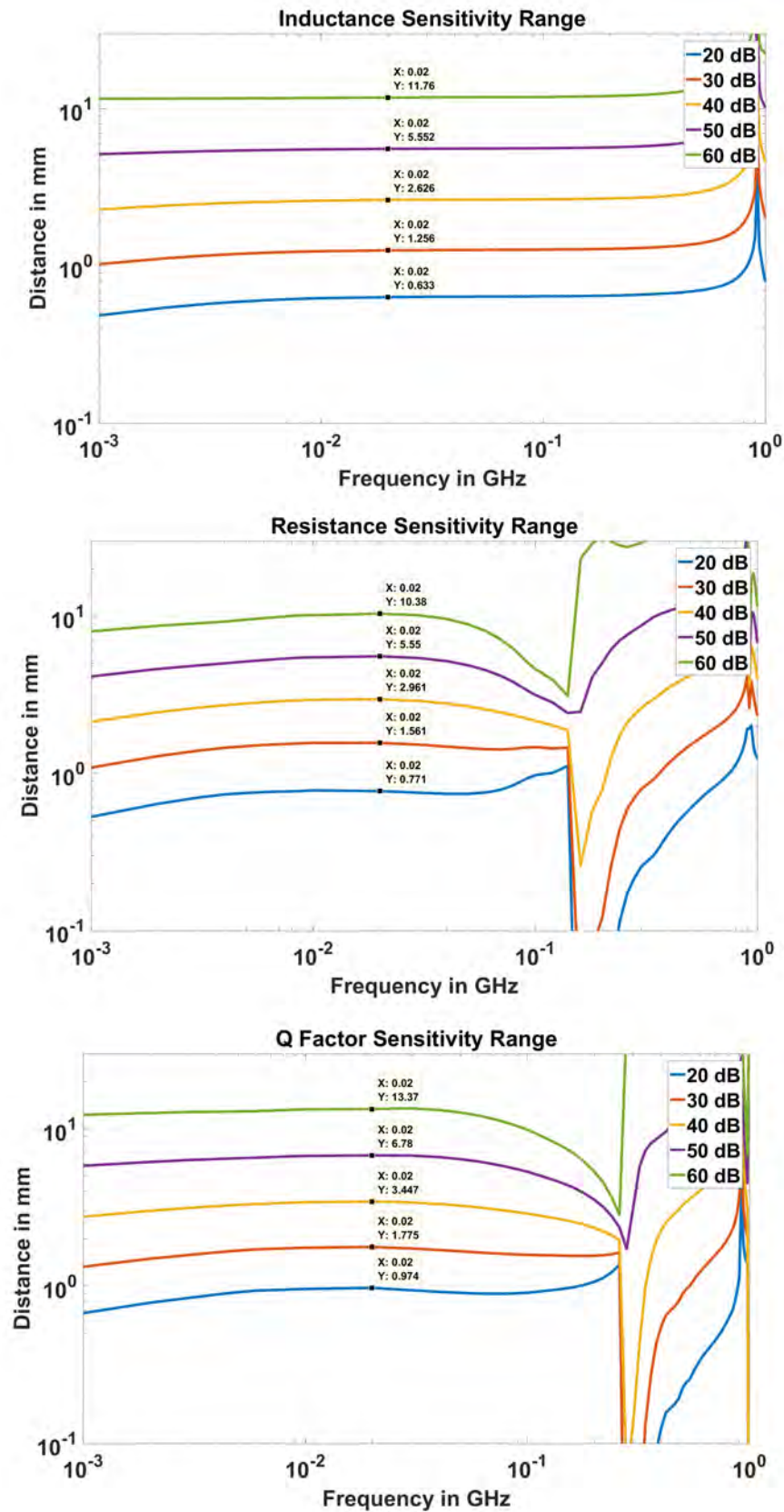


Figure 3.30: Sensitivity Range for Inductance, Resistance and Q factor.

Chapter 4

Eddy Current Sensors:

Experimental Setup

4.1 Introduction

The eddy current sensors are traditionally tested using the impedance analysers. However, since the present sensors are very small and need to be tested over a wide frequency range from tens of MHz to a few GHz, Vector Network Analyser is used. Also a micromotion stage is required to create a known amount of displacement of the orthopaedic implant target. In this chapter, the experimental setup and procedure to test the eddy current sensor is explained, followed by the discussion on the experimental results. Further, an eddy-current loop is integrated with Tunnelling Magneto Resistor and the heterodyne detection technique is employed to increase the sensitivity of the sensor.



Figure 4.1: Tibial implant cut from the titanium sheet of thickness of 4 mm.

4.2 Experimental Setup for EC Sensor Characterization

Orthopaedic Tibial plate

The process to generate a 3D model of the tibial implant in HFSS is explained in Chapter 3. From this model, a 2D (*.iges) file of the titanium implant is generated which is used for machining the implant from the titanium sheet. Using this file, the titanium implant (target) is fabricated. Since the titanium is a very reactive metal, its properties are changed when exposed to heat. Therefore a 4 mm thick titanium sheet is cut and machined using water jet cutting method to keep the temperature low. The titanium implant plates cut from the sheet are shown in Fig. 4.1.

Eddy current sensor

The eddy current sensor is fabricated on Rogers 6010 substrate using traditional PCB manufacturing setup by Lintek Pty.Ltd. at Quenbeyan in New South Wales,



Figure 4.2: SMA connectorized eddy current sensors.

Australia. Multiple sensors were arranged in a panel to maximize the yield. The individual sensors were laser tab routed for easy removal from the panel. The copper layers are silver-gold immersion coated for preventing the oxidation. The sensor pads were connected to the SMA connector using 0.1 mm diameter copper wires of length 10 mm. The connectorized sensors are shown in Fig. 4.2.

Micromotion Stage

To generate the motion of the order of tens of micrometers, a motorized stage is required. Such a micromotion stage is constructed using Newport M423 Linear translation stage and a Newport right angled bracket. The stage is driven by Newport TRB25CC actuator integrated with CONEX controller and Conex power supply. The controller is connected to the PC to enable the motion control programmatically. This micromotion stage with one degree of freedom (DOF) stage can be easily upgraded to a three DOF system with two rotational axes using Newport Tilt and Rotation platform, with ranges -4.3° to 7° for tilt and $\pm 2.5^\circ$ rotation as shown in the Fig. 4.3. To automate the entire measurement process,

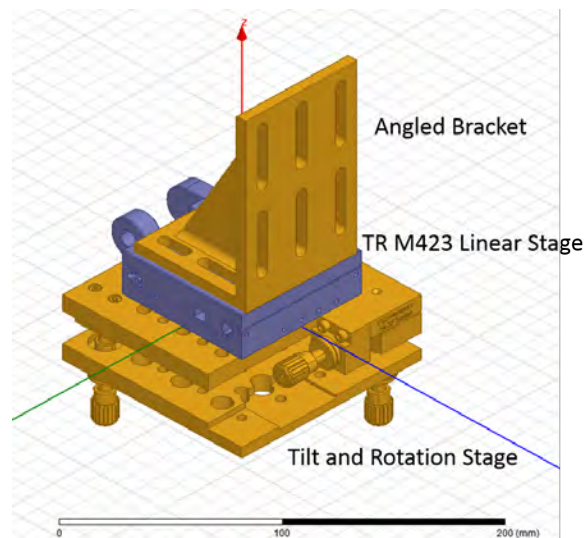


Figure 4.3: Micromotion stage with controller and 3 DOF assembly.

Agilent PNA-X is connected to the PC via LAN cable. Keysight IO libraries are installed to enable VISA connection. The schematic of the entire setup is shown in the Fig. 4.4.

Tibial Bone

Due to the ethical considerations, it is not possible to implant the sensor in an actual human being at this stage. Consequently, a femur bone from cow is used. One end of this bone is cleaved to get a flat surface. Then the tissue surrounding the bone are removed and the bone surface is revealed. Then three holes of diameter 3.5 mm are drilled at a distance of 5 mm, 10 mm and 15 mm from the edge of the flat end with a depth of about 20 mm by using a power drill. The holes are drilled in different lines to avoid the effect of bone-air discontinuity (Fig. 4.5a). The bone is aligned in such a way that the titanium implant mounted on the micro-motion stage can touch the flat surface of the bone (see Fig. 4.5b). The entire bone is

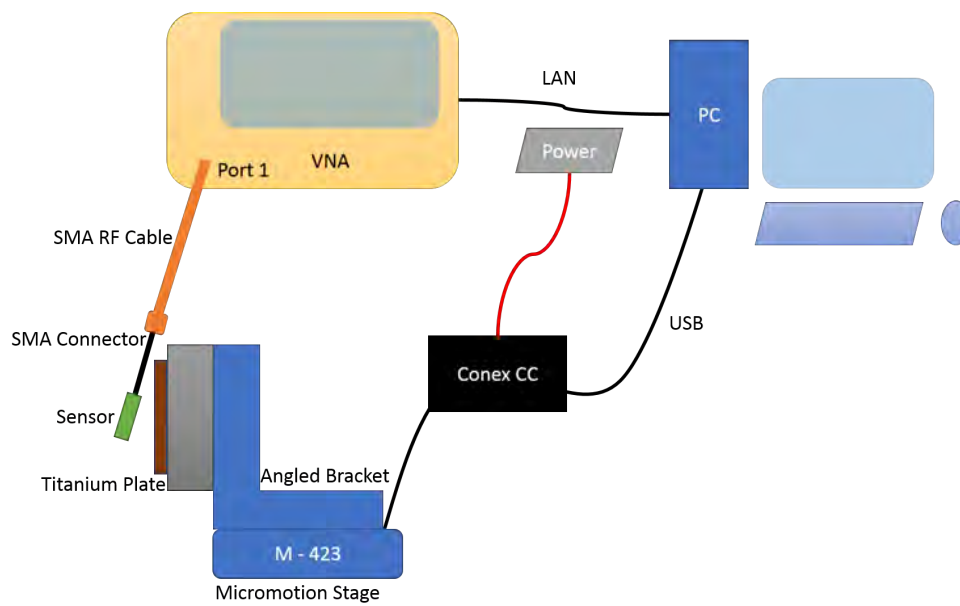


Figure 4.4: Schematics of the entire experimental setup showing micromotion stage, micromotion controller, VNA and PC.

covered with wet towel to avoid the dessication of the bone and the muscle tissues.

It is shown in Fig. 4.5c. The final measurement setup is shown in Fig. 4.6.



(a)



(b)



(c)

Figure 4.5: Cow bone preparation for experimental validation. (a) Bone cleaved to create a flat surface. (b) Hole drilled at three distances, 5 mm, 10 mm and 15 mm. (c) Placement of bone and titanium implant. (d) Bone covered with wet towel to avoid dessication.

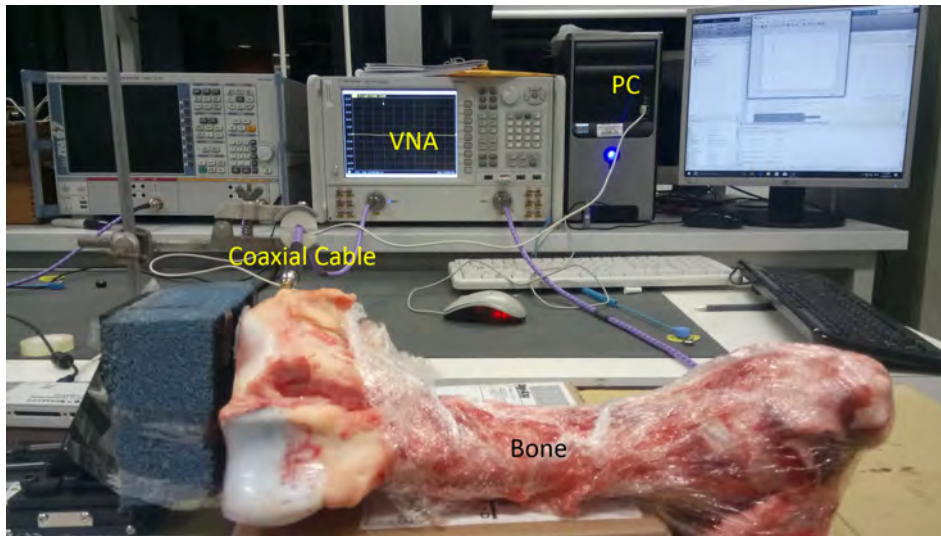


Figure 4.6: Experimental setup for moving the implant, capturing measurements from VNA and saving the results in a file for further analysis.

4.2.1 Experimental Procedure

The flowchart of the automated testing procedure is shown in the Fig. 4.7. First, the connection to the Conex CC controller via a COM port and VNA (Agilent PNA-X N5242A) via LAN port is initialized. Then, the controller state is checked and it is brought to zero position by issuing homing command. This is followed by the calibration of the VNA. The VNA is calibrated by using the open, short and broadband matched loads (Agilent 85052B 3.5 mm cal kit). The calibration is quite important in these experiments as the loop which has very low impedance, especially at lower frequency is directly connected to the 50Ω SMA connector of VNA. This introduces the mismatch of the order of tens of dBs. Hence, it is necessary to have a good calibration standard in place.

However, since the calibration is done till the co-axial cable end point and not the SMA connector with wires, their effect is de-embedded by using a 2 port fixture

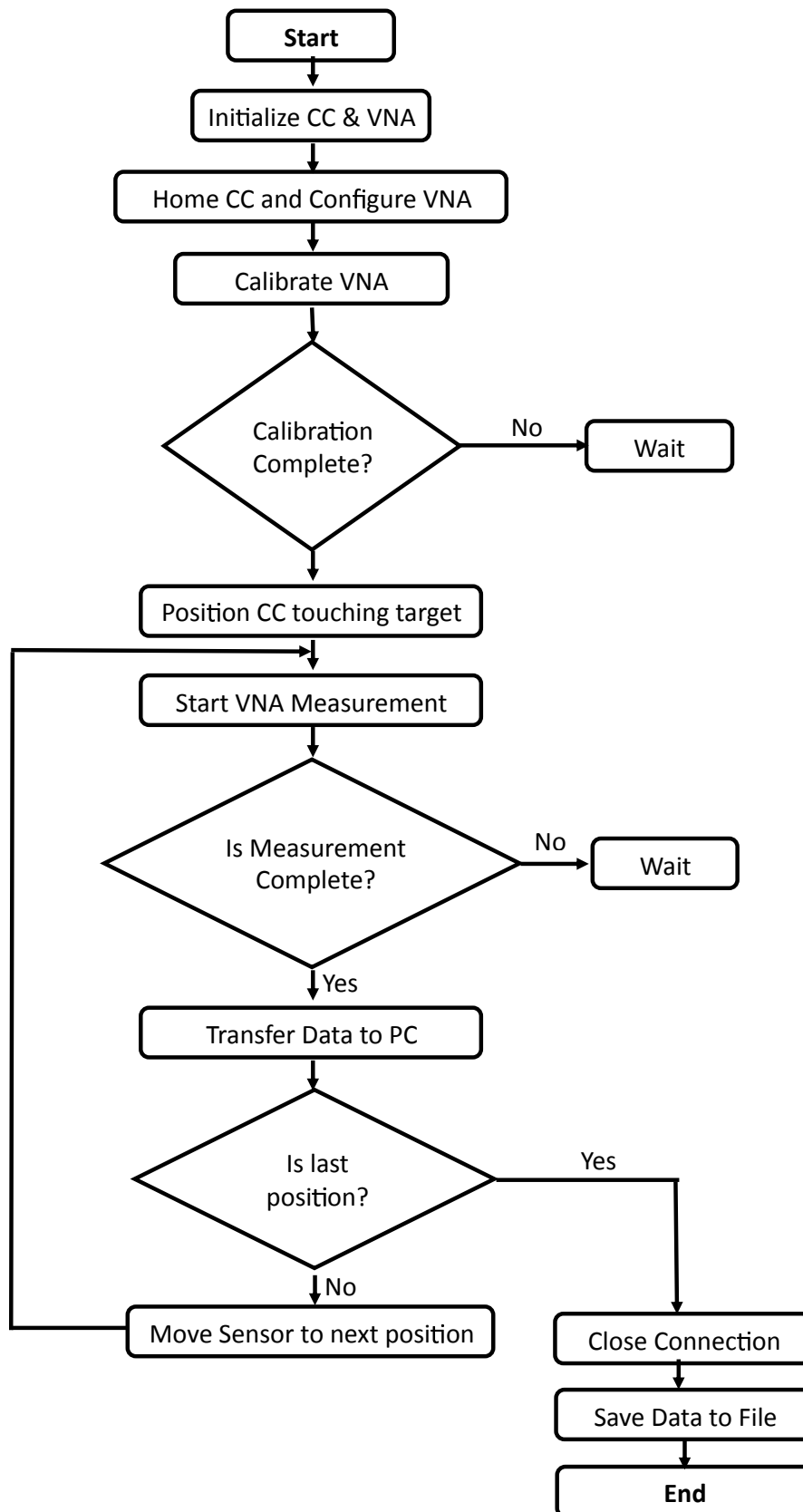


Figure 4.7: Flowchart for controlling the micromotion stage and acquiring measurements from VNA.

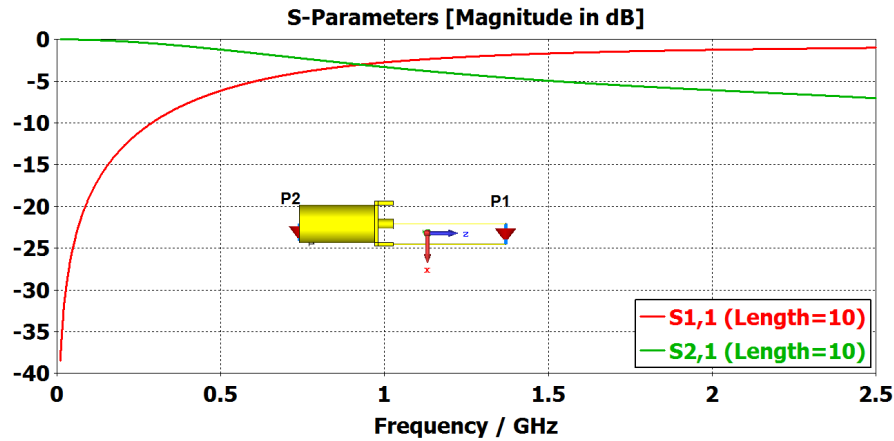


Figure 4.8: CST simulation of SMA connector with 10 mm wire.

removal tool. SMA connector and wires add extra impedance to the designed loop and it is necessary to remove their effect from the measurements. Therefore, the SMA connector with 10 mm long wire is simulated in CST as shown in Fig. 4.8. The two port results are exported in S2P format. This file is imported into VNA in fixture correction tool. This de-embeds the effect of the SMA connector and the 10 mm length wires.

Once the calibration is completed, the target is moved to the end position such that the sensor touches the target. This is taken as zero position. Then the motion stage is moved by the predetermined amount and its position is read back and verified. Then the VNA is triggered with proper settings for the frequency range, the number of frequency points, IF bandwidth (set to 100 Hz) and the number of averaging points (5 points per sample). The point to point averaging method is selected. Low IF bandwidth, high averaging and proper calibration and embedding ensures good quality of the measurements.

After the measurement is complete, the data is read in a binary block. The

results are S-parameters in dB magnitude and phase form, from which they are converted into impedance (Z) with real and imaginary parts using equation 4.1. The motion stage is again activated to go to the next position and the entire ‘move - measure - acquire’ loop is executed until the motion stage reaches the maximum displacement position.

$$Z_{11} = \left(\frac{S_{11} + 1}{S_{11} - 1} \right) 50 \quad (4.1)$$

4.2.2 Experimental Results

A MATLAB code is written that implements this algorithm. The VNA measurement parameters like IF bandwidth and number of averaging points are set to 100 Hz and 5 respectively to ensure that the output is stable. The results are captured at every 10 MHz increment from 10 MHz to 2.5 GHz. Initially, the sensor is tested in free space. The frequency response of the sensor is evaluated followed by the curve fit analysis for frequency-displacement-impedance data. This is followed by testing in the cow bone at three different distances 5 mm, 10 mm and 15 mm.

Frequency Response

The measured frequency response of the two turn loop before and after the de-embedding process is shown in Fig. 4.9. Following observations can be made from the results.

- With de-embedding, the F_{SRF} increases from 575 MHz to 1.15 GHz. This closely matches with the simulated F_{SRF} of 1.165 GHz.

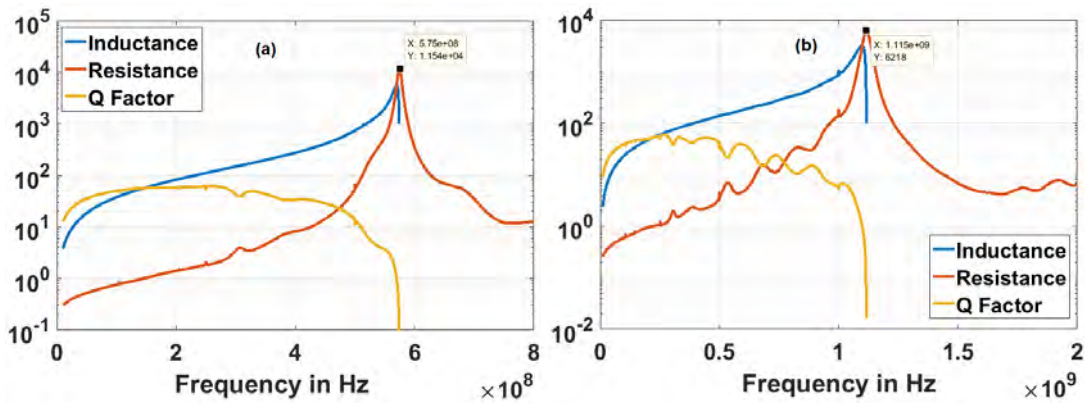


Figure 4.9: (a) Frequency response of the sensor before de-embedding. (b) Frequency response of the sensor after de-embedding.

- De-embedding introduces ripples in the resistance curve. This may be due to inaccurate EM modelling. In practice, the wires connecting the sensor and PCB sensor cannot stay very straight, as in simulations, but have some bends. Moreover, the solder joints are not considered in the simulations. Therefore, this may introduce minor errors, especially in the resistance part.
- To remove the ripples in the resistance, curve of the form $ae^{bx} + ce^{dx}$ is fitted to the de-embedded data till 950 MHz (as the ripples are present in the data below 950 MHz) as shown in Fig. 4.10. The original data from 950 MHz onwards is stitched to the curve data. It can be seen that the proposed curve fit smooths the data quite well.
- The measured and simulated R, L and Q-factors are compared in Fig. 4.11. The measured resistance is higher than the simulated resistance. This may be due to the wire resistance or SMA connector loss which is not accurately modelled by the simulation but dominates the small loop resistance which

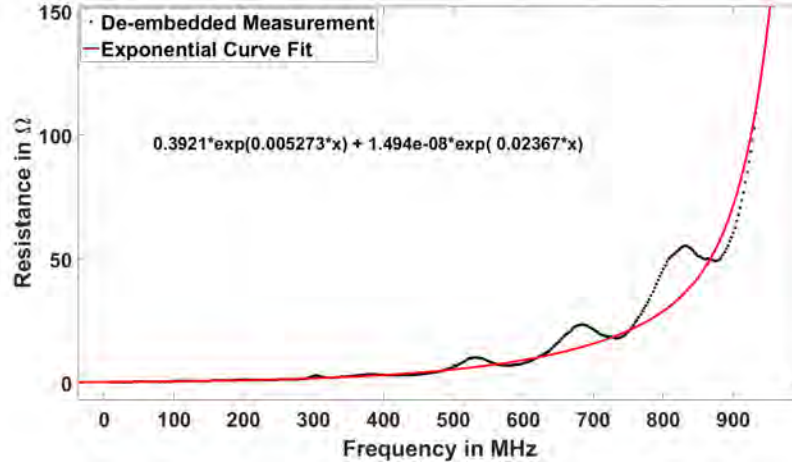


Figure 4.10: Exponential curve fit of the de-embedded resistance data.

is less than 0.5Ω . However, this leads to the decrease in the measured Q-factor. Overall, all of the experimental curves show behaviour similar to the that of simulations, especially inductance and the self resonant frequency.

Curve Fit Analysis

The normalized change in the resistance, inductance and Q-factor as a function of distance is already discussed in Section 3.2. The measured results show good agreement with the simulated results. However, in this section, the curve fit analysis is performed on the de-embedded and filtered (exponential curve fit for resistance) data for the distance-impedance curves as a function of frequency. To facilitate the comparison, the simulated and measured analysis is drawn side by side. First, the inductance, resistance and Q factor as a function of distance and frequency is plotted in Fig. 4.12. The adjusted R^2 is plotted in Fig. 4.13, the sensitivity analysis is plotted in Fig. 4.14 and ranges are plotted in Fig. 4.15.

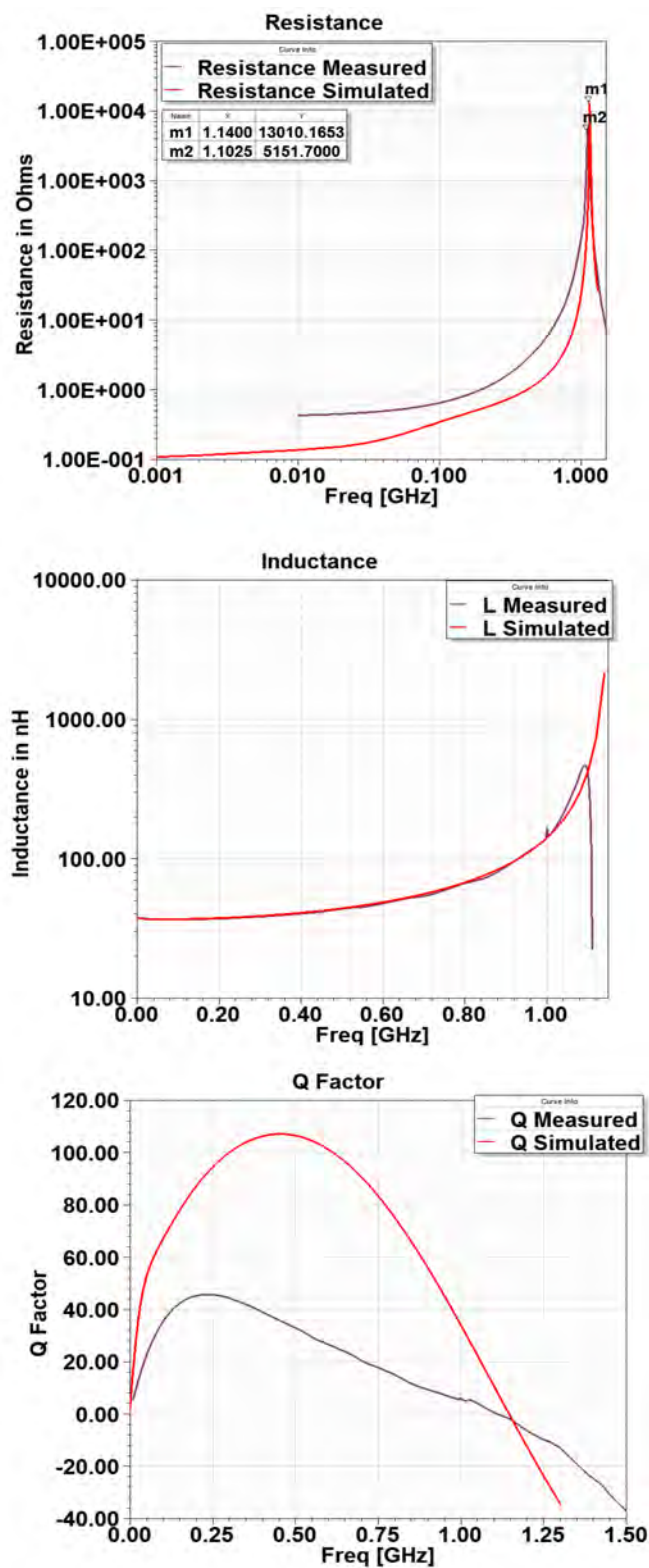


Figure 4.11: Comparison of simulated and measured R, L and Q parameters.

The simulated and measured results match very closely. However, the measured results show more sensitivity especially at higher distances than the simulated case. This may be due to the extra length of the rectangular loop created by the wires connecting SMA to the sensor head. Although de-embedding adjusts inductance and resistance and fixes the SRF of the sensor, it cannot prevent the EM fields generated by the extra wires. This issue can be rectified once the complete integrated circuit for measurement is developed. The agreement of the results especially, the F_{Best} and F_{Worst} frequencies validate the numerical simulations.

Experiments in a Cow Bone

The femur bone from cow is prepared as explained in the previous sections. Three holes at 5 mm, 10 mm and 15 mm are drilled using a power drill. The stand-off distance has a tolerance of ± 0.25 mm due to the human errors. The sensor is inserted in these holes and the motion in $10 \mu\text{m}$ steps is provided by the micromotion stage. The results at 100 MHz are plotted in Fig. 4.16. Following observations can be made:

- Resistance sensitivity is higher than the inductance sensitivity which confirms to the simulated results.
- At 15 mm stand-off distance, the VNA is unable to resolve $10 \mu\text{m}$ motion either for inductance or resistance.
- The sensitivities at 5 mm and 10 mm for resistance are about 270 ppm and 60 ppm respectively.
- The sensitivities at 5 mm and 10 mm for inductance are about 60 ppm and

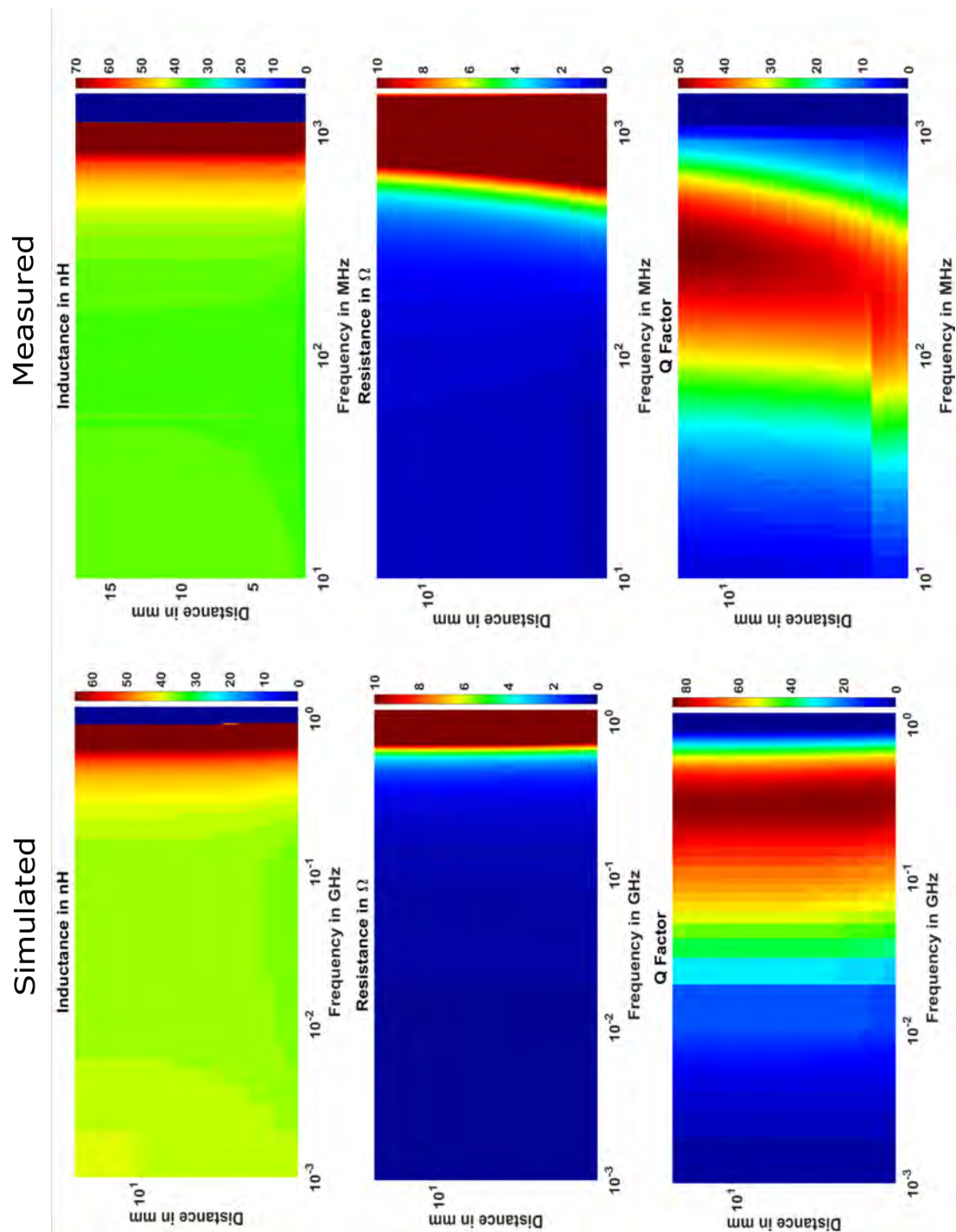


Figure 4.12: Comparison of simulated and measured inductance, resistance and Q factor.

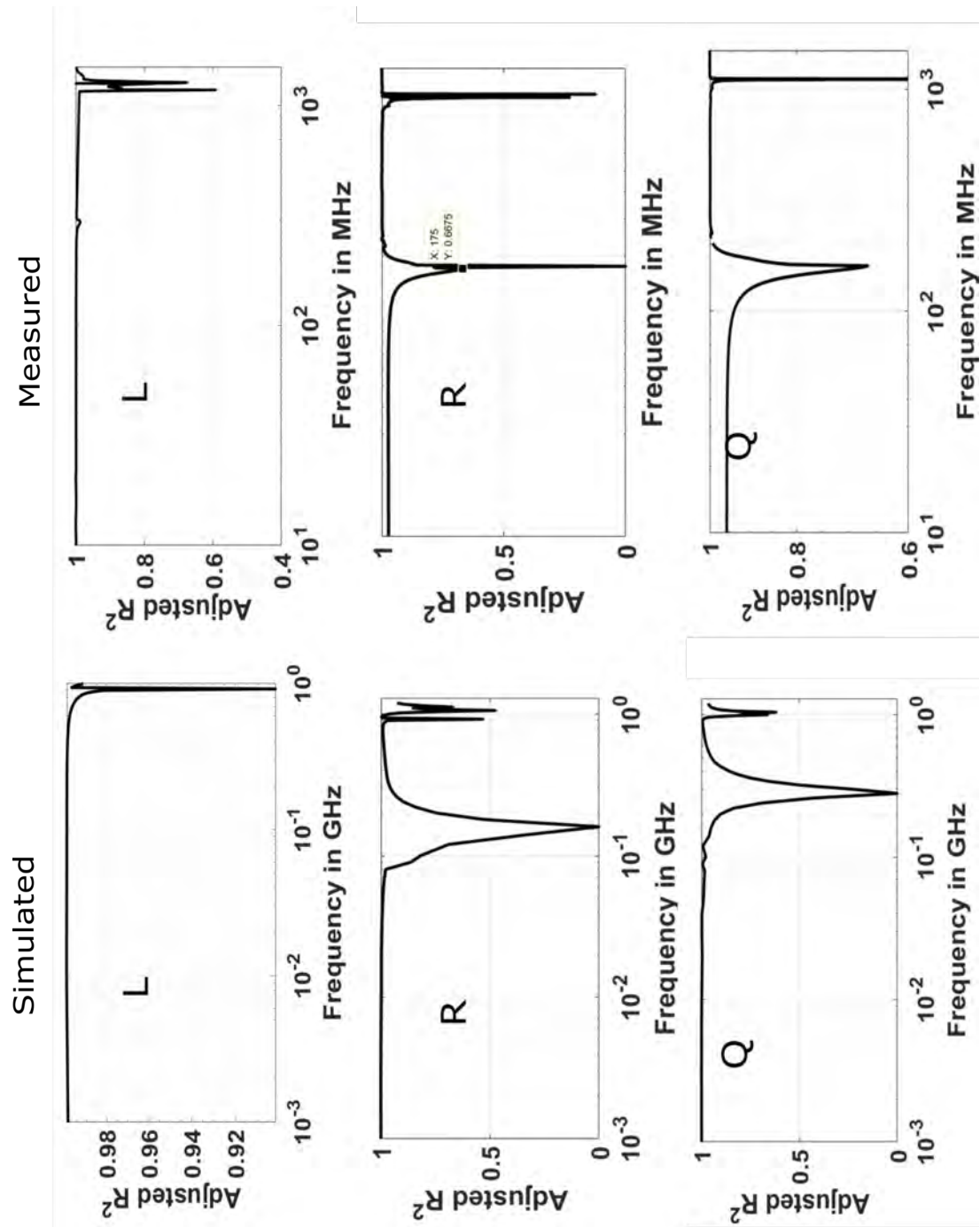


Figure 4.13: Comparison of simulated and measured adjusted R^2 inductance, resistance and Q factor.

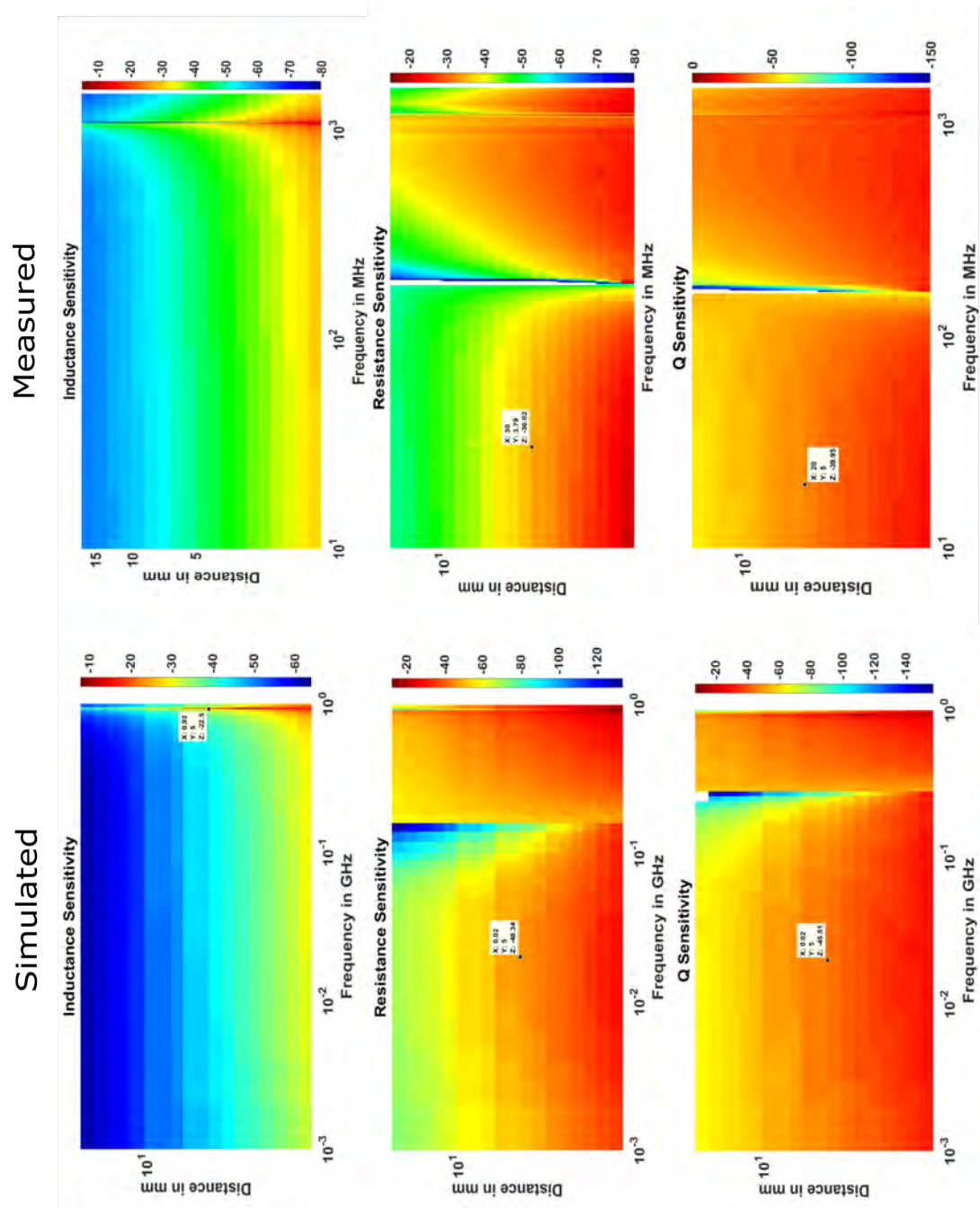


Figure 4.14: Comparison of simulated and measured sensitivities for inductance, resistance and Q factor.

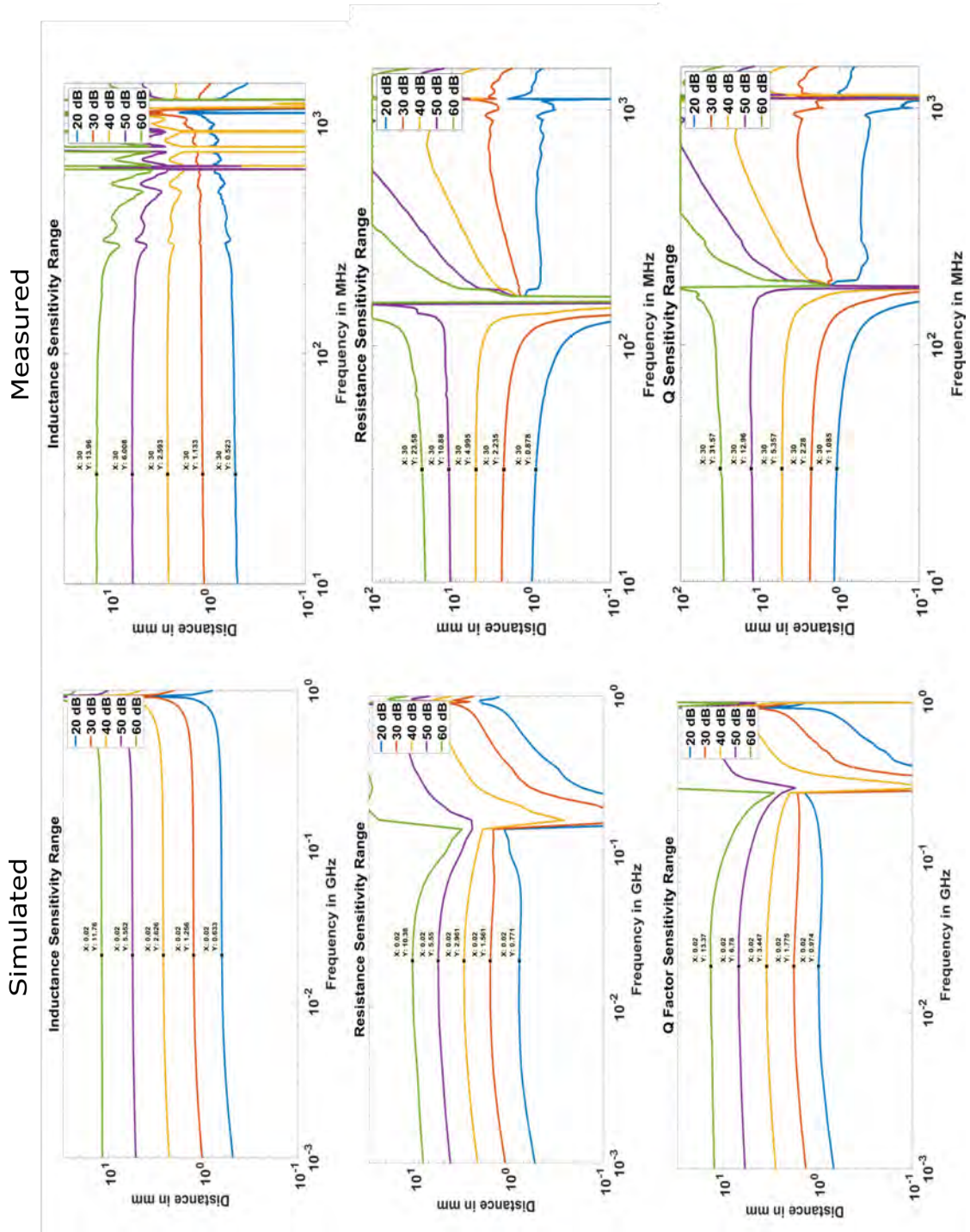


Figure 4.15: Comparison of simulated and measured ranges for inductance, resistance and Q factor.

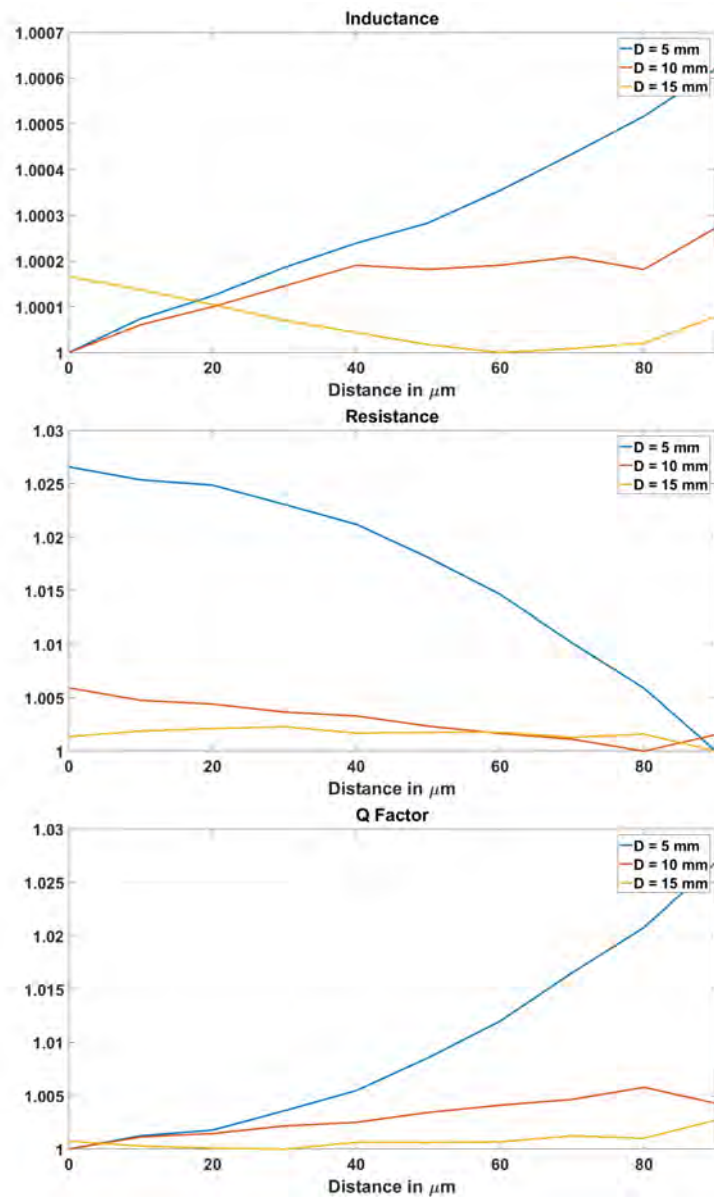


Figure 4.16: change in inductance, resistance and Q Factor with 10 μm motion of the implant at stand off distance of 5 mm, 10 mm and 15 mm.

30 ppm respectively.

- With an increase in the stand off distance, the sensitivities for both the resistance and inductance decrease. However, the decrease in the inductance sensitivity is less than the decrease in the resistance sensitivity.

4.3 Eddy Current-Tunnelling Magneto Resistive Sensor

4.4 Introduction

Eddy current sensor generates an alternating magnetic field which is maximum at the centre of the loop. This magnetic field can be detected by using an another class of magnetic sensors known as Magnetic Tunnel Junction (MTJ) devices that work on quantum tunnelling effect. Depending on the amplitude of the applied magnetic field, these devices change their resistance. Hence they are also known as Magneto-Resistive (MR) devices.

The magneto resistive sensors utilize the spin properties of electrons in nanoscale devices. In spintronics majority of the work focuses on the development of multilayer systems that consist of thin magnetic and non-magnetic layers. Usually, the magnetic layers are made from iron (Fe) or Cobalt (Co) whereas non magnetic metallic layers are made from copper (Cu) and/or Chromium (Cr). When a conducting non magnetic layer is placed between the magnetic layers, the MR effect greatly surpasses that of an individual layer. This effect is termed as Giant Magneto Resistance (or GMR) [130]. If the sandwiched layer is made up of insulating

dielectric instead of the metallic layer, then it is known as a Tunnelling Magneto Resistor (TMR).

In this section, a TMR sensor is used to detect the change in the magnetic field produced by the moving titanium implant. This section describes the fabricated TMR stack, its characterization and integration with the eddy current loop followed by the measurement procedure and results.

4.5 Magnetic Tunnel Junction Sensors

The magnetic tunnel junction sensors were fabricated at INESC Microsistemas e Nanotecnologias, Portugal. The magnetic tunnel junction sensors targeted to have a very high sensitivity and low Signal to noise ratio [131]. The MTJ stack is fabricated with a self-aligned process described in [132] by optical lithography and ion beam milling (Nordiko 3600 tool using a Ar+ beam with 105 mA ($390\mu A/cm^2$) with +735V and pressure of 0.2 mTorr)). The optimized stack is TJ937-940 – Si / 1000 SiO₂ / 5 Ta / 15 Ru / 5 Ta / 15 Ru / 5 Ta / 5 Ru / 20 IrMn / 2 CoFe₃₀ / 0.85 Ru / 2.6 CoFe₄₀B₂₀ / 1 MgO / 2 CoFe₄₀B₂₀ / 0.21 Ta / 4 NiFe / 0.20 Ru / 6 IrMn / 2 Ru / 5 Ta / 10 Ru / 15 TiWN₂ where thickness is in μm . The resistance area product $R \times A = 40K\Omega\mu m^2$. The linearity of the sensor is achieved by proper annealing steps that set the pinned layer perpendicular to the free layer [133]. The schematic pad layout of the fabricated TMR sensor is shown in Fig. 4.17.

An array of 4×8 sensors per chip is fabricated as shown in Fig. 4.18. The chips were diced and wire bonded to a polyimide flexible PCB. Then the sensor is characterized to measure the TMR. For this purpose, the sensor is placed between Helmholtz coils that generate uniform magnetic field. The magnetic field is varied

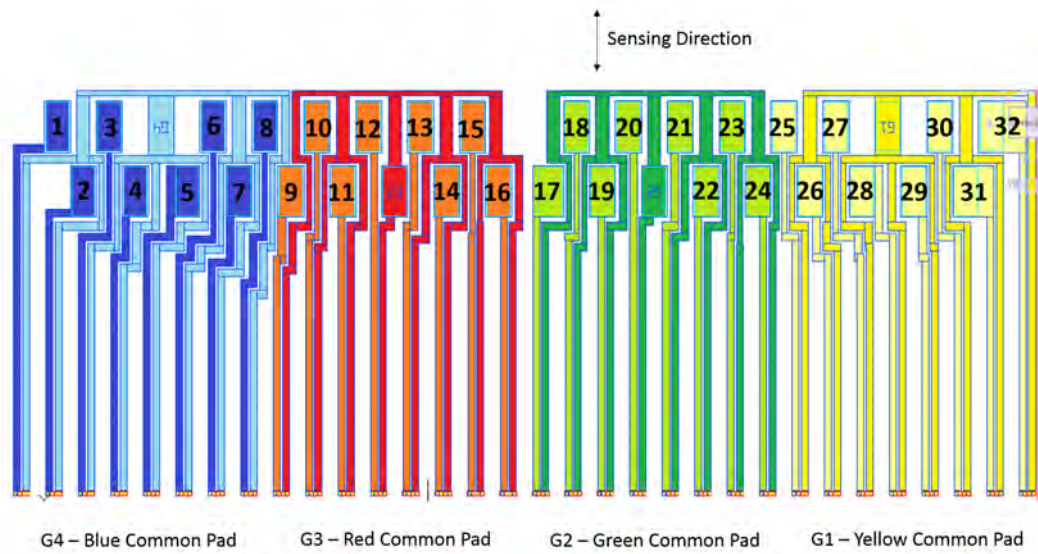


Figure 4.17: Pad schematic of the fabricated chip.

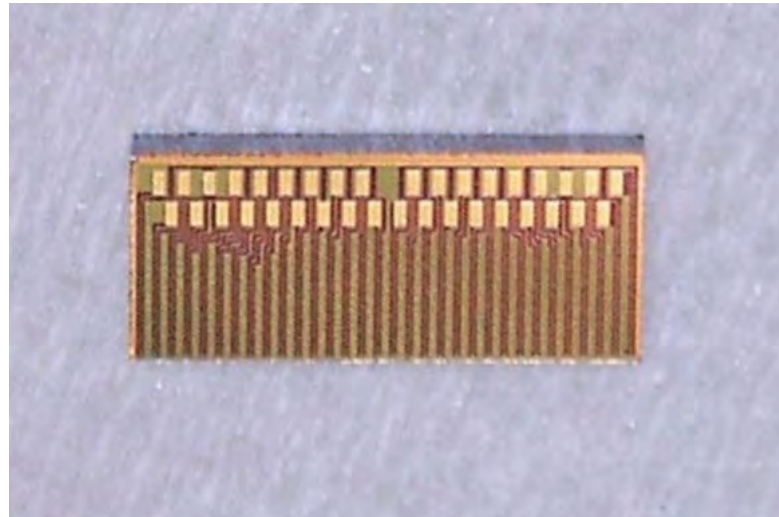


Figure 4.18: Fabricated TMR sensor chip.

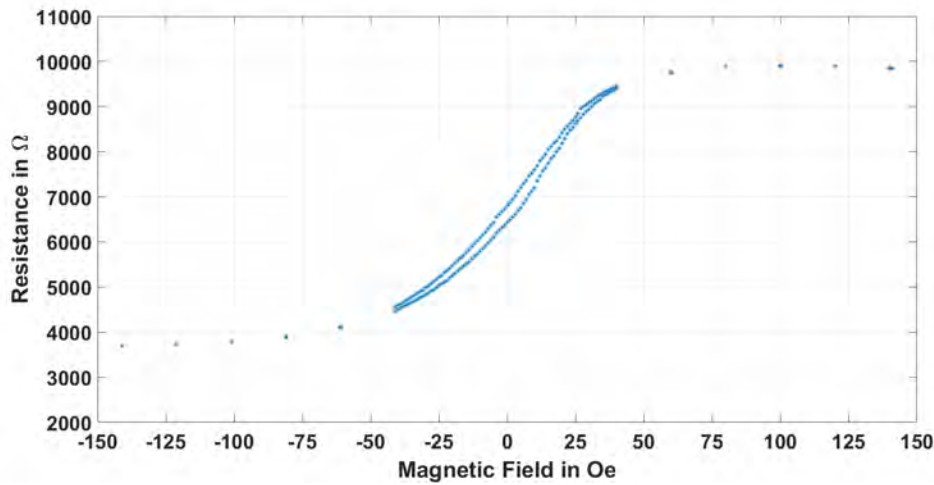


Figure 4.19: Resistance of the fabricated TMR sensor as a function of applied magnetic field.

by changing the current in the coil following the predetermined process. As the field is varied, the resistance of the sensor is measured when it is biased at a nominal current value of $10 \mu\text{A}$. The measured linear range of the sensor is ± 35 Oe as shown in Fig. 4.19. The TMR ratio, defined as $(R_{max} - R_{min})/R_{min}$ is 167%.

4.6 EC-TMR Sensor Integration

The TMR sensor IC is wire-bonded to the signal pads printed on a polyimide flexible substrate. Wire bonding is protected by a silicone-based glob top encapsulant. Since out of plane field detection is needed, the TMR sensor is mounted vertically on the horizontal EC loop using a superglue. The signal lines on PCB are soldered to SMA connectors which are further used for connections to the various measurement equipment. The width of this assembly is about 3 mm. When this assembly touches the plate, the loop is about 3 mm away. Since, it is required that



Figure 4.20: EC-TMR sensor integration.

the sensor should not touch the target we have given 0.15 mm extra space giving 3.15 mm distance between the target and the TMR sensor. The EC-TMR sensor integration with the silicon encapsulation is shown in the Fig. 4.20.

In the proposed range of frequency operation, the inductive coupling of the EC-TMR sensor assembly could produce higher voltage than the MR sensor response to the reflected eddy current field from the orthopaedic implant. Hence, to decouple this with the TMR response, heterodyne detection of the signal is proposed. The EC sensor is fed with a signal $f_E = 10$ MHz and TMR sensor is fed with a signal at $f_T = 9.99$ MHz using Agilent 33210 waveform generator. This produces the sum and difference signal at 19.99 MHz and 10 KHz respectively. The TMR sensor response can therefore be obtained at 10 KHz signal (obtained by low pass filtering) using DSP 7265 signal recovery Lock-in amplifier. To ensure the synchronization of signals, the internal clock reference was shared between the signal generators

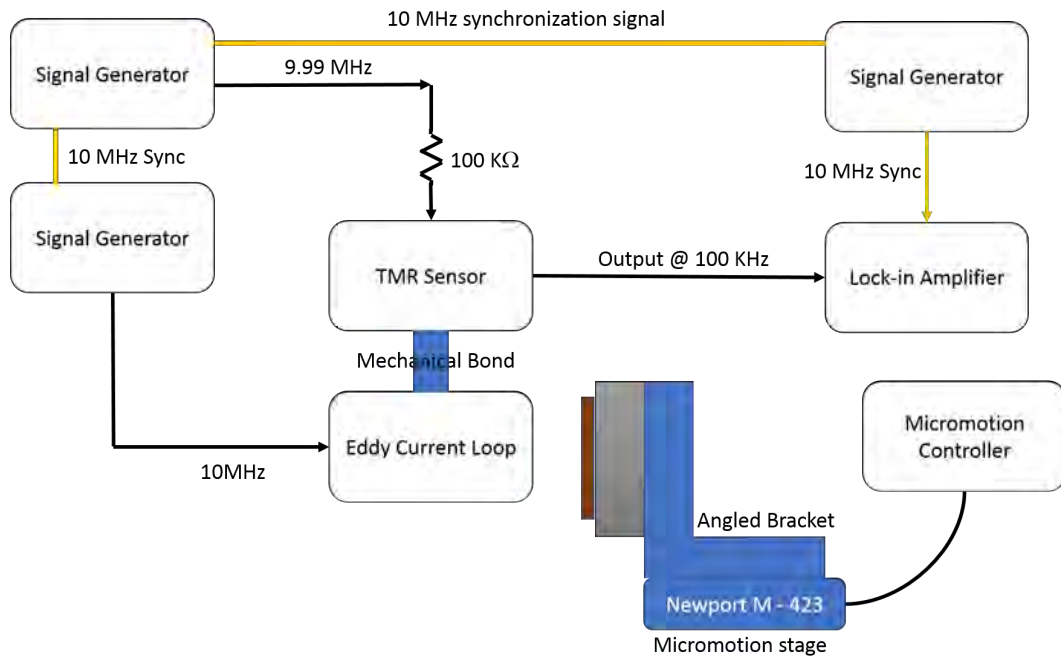


Figure 4.21: Schematic of the heterodyne detection technique for displacement measurement using EC-TMR sensor.

and a lock-in amplifier.

Three signal generators and lock-in amplifier are controlled using LabView. The micromotion stage from Newport Corp. is actuated using Conex CC controller. It is programmed for motion in $100 \mu\text{m}$ steps range using a MATLAB program. The circuit schematic of the setup is shown in Fig. 4.21. The entire measurement assembly is shown in Fig. 4.22.

4.7 Experimental Results

The TMR sensor is integrated with the EC loop and excited by a constant current source obtained by adding a $100\text{k}\Omega$ resistor in series with the sensor. The motion

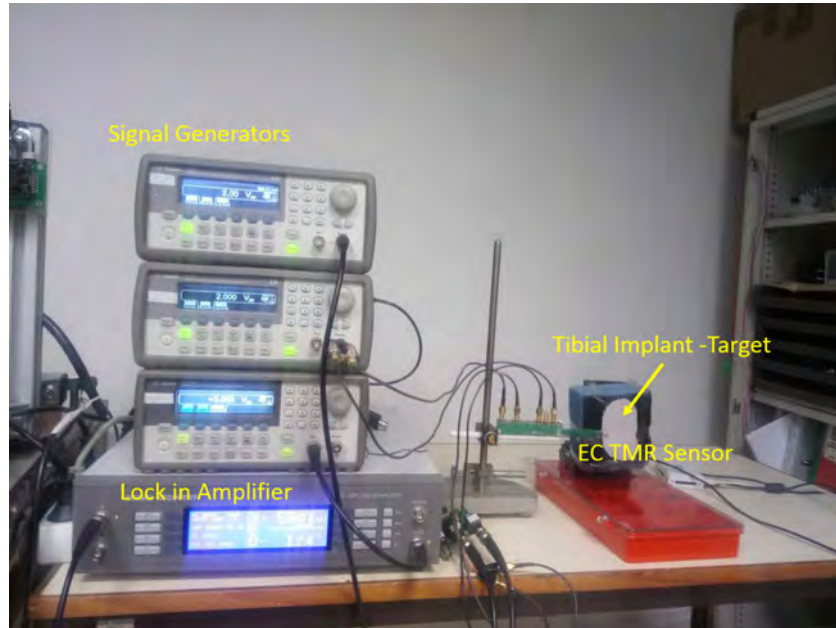


Figure 4.22: Experimental setup of EC-TMR sensor for heterodyne detection of micromotion sensor.

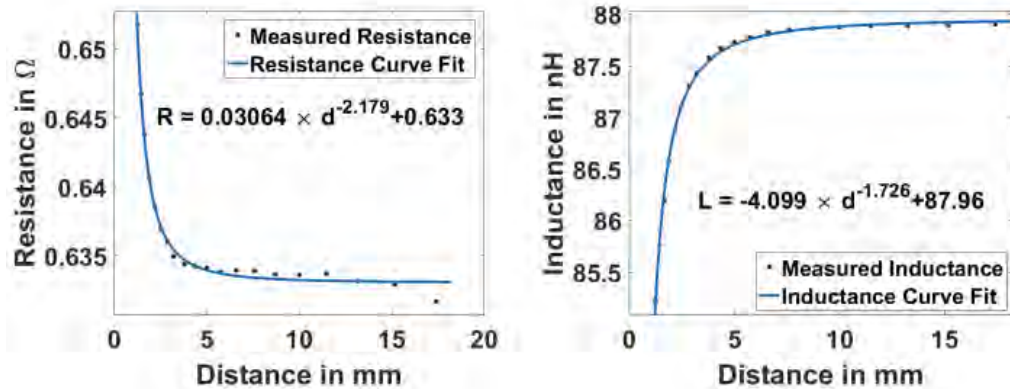


Figure 4.23: Exponential curve fit for the measured inductance and resistance of the eddy current loop.

stage is moved in steps of $100 \mu\text{m}$ and output of the lock-in amplifier is noted. The output of the sensor is normalized and expressed at percentage change with respect to the output at 3.15 mm stand-off distance according to the Eq. 4.2. The response of three turn loop eddy current sensor in free space is also measured using the VNA following the procedure explained previously. The resistance and inductance of the loop as a function of stand-off distance is measured and curve fitted as shown in Fig. 4.23. The curve fit parameters are noted and the values of resistance and inductance are interpolated using the fitted equations. These values are also normalised and expressed in percentage. All these results are compared in Fig. 4.24. It can be observed that the TMR sensor offers sensitivity which is almost a magnitude higher than the traditional eddy current probes.

$$\Delta Output = \left| \frac{V_{Current} - V_{initial}}{V_{initial}} \right| \times 100\% \quad (4.2)$$

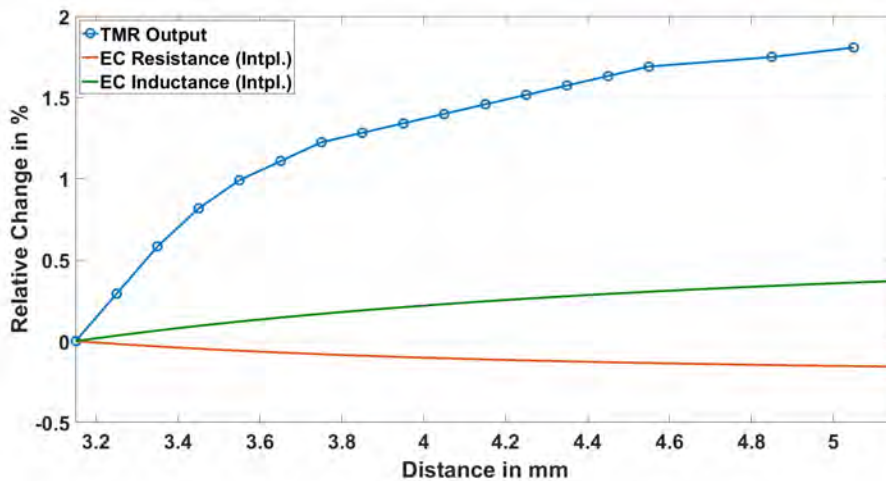


Figure 4.24: Output of TMR sensor and Eddy current sensor expressed as relative percentage change.

This way of representation is useful for a surgeon for interpretation of loosening of implant. For example, if the maximum change in output of the sensor during the complete motion of leg is 1% then corresponding micromotion would be about $450\ \mu\text{m}$ which would indicate substantial loosening of the implant.

4.8 Summary

First, the experimental setup for the characterization of the eddy current sensor is designed. The inductor loops are fabricated, titanium sheet is cut in shape, micro-motion stage is built, bovine femur is prepared and MATLAB codes for controlling VNA and motion stage are written. Then a process of calibration and de-embedding and proper configuration of VNA is established. Then the frequency-distance response of the EC sensor is measured and curve fit analysis is performed. Further, the experimental validation is done inside the cow bone.

A new integrated eddy current - TMR sensor head is fabricated, characterized and tested using heterodyne detection technique. This new approach shows an order of magnitude higher sensitivity than the traditional eddy current sensors at larger stand-off distance.

Chapter 5

Investigation of Changes in Sensor and Human Body

5.1 Introduction

In chapter 3, the effect of a human body on the eddy current sensor is analysed. To mitigate the adverse effects of the body, it is proposed to use the dielectric coating of low permittivity material. Electromagnetically, human body is a very non-homogeneous and dispersive medium. Moreover, the properties of the tissues change with age and gender. Further, the physical constitution of humans changes with ethnicity, race and nutrition [134]. This makes it necessary to analyse the eddy current sensor for various changes in the human tissue. Since it would be impractical to test various characteristics and performance of the sensor by implanting it in different human beings, simulations provide the only way of investigation.

This chapter presents the Monte Carlo analysis in which various parameters of

human body are varied and their effect on the sensor parameters like sensitivity and range are evaluated. Further, changes in the geometry of the sensors are also explored. Curve fit analysis and power dissipation analysis is extensively used to evaluate the performance in all the studies.

Since the curve fit analysis generates over eighteen figures for each parameter, they are not included in the body of this chapter but are given in Appendix A. The relevant values from these graphs are given in tables to facilitate further analysis, investigations and conclusions. Another deviation from curve fit analysis explained in the Chapter 3 is that the sensitivities are expressed in ppm (part per million) and not dB as the dB values though good for visualization in graph, are very compressed and not suitable for meaningful comparison.

5.2 Effect of Variation in Permittivity of Tibial Bone

After a Total Knee Replacement (TKR) surgery, many changes happen in the tibial bone. The bone regrows, its water content changes, and if the patient is suffering from bone loss (osteoporosis), then subsequently the bone density starts decreasing. It is shown in [135], that the density of the bone strongly correlates with its permittivity. Therefore, it is necessary to evaluate how this change affects the eddy current sensor. The permittivity and conductivity of the bone are simultaneously varied by $\pm 25\%$ to consider the case of maximum variation. The total variation is therefore 50% around the nominal values. It is sufficient to evaluate the extreme cases of variation as any intermediate values will have less impact on

Table 5.1: Effect of the variation of complex permittivity of the bone on the sensitivity of a two turn EC sensor directly implanted in bone without PDMS coating.

Design	Parameter	Standoff Distance			
		2.5 mm	5 mm	10 mm	15 mm
Bone High +25%	L	108.6824	13.6632	1.7284	0.516
	R	164.18	13.16	1.04	0.2361
	Q	267.2859	26.97	2.76	0.73
Bone Low -25%	L	109.1892	15.3024	2.1582	0.6868
	R	190.97	21.7	2.4308	0.674
	Q	295.8438	39.32	5.3289	1.6596
$\left(\frac{\Delta y}{y}\right) \times 100$ (in %)	L	0.464	10.712	19.914	24.868
	R	14.028	39.354	57.215	64.970
	Q	9.653	31.40	48.206	56.01

the performance of the sensor. First, the analysis is performed for the sensor without PDMS coating and then along with the PDMS coating. The F_{Best} for sensor encapsulated with PDMS is 20 MHz. For the sensor without encapsulation, F_{Best} is 10 MHz for lower complex permittivity of bone and 6 MHz for higher complex permittivity value.

The result plots of the curve fit analysis is given in appendix A. The sensitivities calculated from this analysis for the sensor without PDMS and with PDMS are tabulated in 5.1 and 5.2 respectively. The change in sensitivities between two extreme cases is also calculated as a relative percentage change in the measurement

Table 5.2: Effect of the variation of the complex permittivity of the bone on the sensitivity of a two turn EC sensor directly implanted in the bone with the PDMS coating.

Design	Parameter	Standoff Distance			
		2.5 mm	5 mm	10 mm	15 mm
Bone High +25%	L	115.53	13.74	1.64	0.475
	R	213.3	17.15	1.36	0.31
	Q	323.79	31.4	3.05	0.79
Bone Low -25%	L	115.28	13.8	1.67	0.48
	R	216.1	17.9	1.46	0.34
	Q	329.2	32.35	2.87	0.71
$\left(\frac{\Delta y}{y}\right) \times 100$ (in %)	L	0.216	0.434	1.796	1.941
	R	1.295	4.189	6.849	8.823
	Q	1.676	3.025	6.271	11.267

quantity y (L , R or Q factor). Following observations are made from this analysis.

1. As the complex permittivity reduces, the sensitivity increases. This may be because of the reduced losses in the tissue.
2. The F_{Best} for sensor without PDMS is about 4 times lower than the F_{Best} for the sensor with PDMS cover. It also changes with the permittivity of bone by about 40% for full ± 25 % deviation.
3. The sensitivity deviation (expressed in %) for the resistance is higher than that of the inductance in both the cases.
4. For an uncoated sensor implanted at the nominal stand-off distance of 5 mm, and for the 10 % allowable sensitivity change, the tolerable amount of permittivity deviation is $\pm 23.3\%$ for inductance, $\pm 6.35\%$ for resistance and $\pm 8\%$ for Q factor. A 10% sensitivity change corresponds to 10% error in the sensor output. This is considered as a maximum tolerable error.
5. For a sensor coated with PDMS and implanted at the nominal stand-off distance of 5 mm and 10 % allowable sensitivity change, the tolerable amount of permittivity deviation is $\pm 576\%$ for inductance, $\pm 59.7\%$ for resistance and $\pm 82\%$ for Q factor.
6. Therefore, the PDMS encapsulation enhances the immunity of the sensor to the changes in tissue permittivity by 24 times for inductance, 9.4 times for resistance and 10.25 times for Q factor.
7. The sensitivity of the sensor with PDMS is higher than that of the sensor without PDMS.

8. The sensitivity deviation of sensor without PDMS is higher than that of the sensor with PDMS. This is due to reduction in E-fields interacting with the bone tissue. Thus, PDMS encapsulation also prevents change in the sensitivity of the sensor with changes in the human body.
9. The change in sensitivity increases with the stand-off distance. This is due to more tissue presence between the loop and the target.

5.3 Effect of Rotation of The Sensor

The effect of positioning of the sensor inside the bone is discussed in this section. While implanting the sensor inside the bone, the sensor may get rotated and may not be exactly parallel to the target. The surgeon may not implant the device exactly parallel to the orthopaedic plate. In this case, it is necessary to know what could be the penalty on the sensitivity and range with rotation. Hence, the sensor is implanted at 0° , 45° , 60° and 90° and its effect is quantified by using the curve fit analysis.

Table 5.3 shows the sensitivity of the sensor parameters L , R , and Q factor at 4 different stand-off distances, 2.5 mm, 5 mm, 10 mm and 15 mm. The sensitivity increases with the rotation angle for resistance (and so Q factor) for the stand-off distance of 2.5 mm whereas it decreases for higher distance. To understand this, it is necessary to look into the mechanism of eddy currents developed on the target. When the rectangular loop is placed closer than its width, the coupling of the field with the target is very strong and the two parallel lines of the loop carrying opposite currents are distinctly mirrored on the target. When the loop is rotated, the projection of these lines on the target gets smaller. Therefore, the

Table 5.3: Sensitivity (in ppm) as a function of stand-off distance and rotation.

Angle	Parameter	Standoff distance			
		2.5 mm	5 mm	10 mm	15 mm
0°	L	112.1	14	1.76	0.52
	R	264.36	19.5	1.41	0.3
	Q	376.78	33.26	3	0.74
45°	L	107.37	11.28	1.19	0.32
	R	292.75	17.33	1	0.19
	Q	394.5	30	2.35	0.53
60°	L	105.83	9.89	0.93	0.23
	R	307.37	15.48	0.76	0.13
	Q	406.34	26.7	1.79	0.37
90°	L	102.5	8.77	0.75	0.18
	R	327.08	14.76	0.652	0.105
	Q	423.85	25.12	1.52	0.29

eddy current on target gets stronger leading to more dissipation on power in target and so higher resistance reflected back on the loop. This increases the sensitivity. On the contrary, when the loop is placed at a higher distance (like 10 mm), the projection of loop current on the target is bigger and so maximum current is accumulated on the edge. As the angle of rotation increases, this leads to lower currents at the edge which decreases the power lost in the implant (See Fig. 5.1) and so the reflected resistance on loop is lowered that decreases the sensitivity.

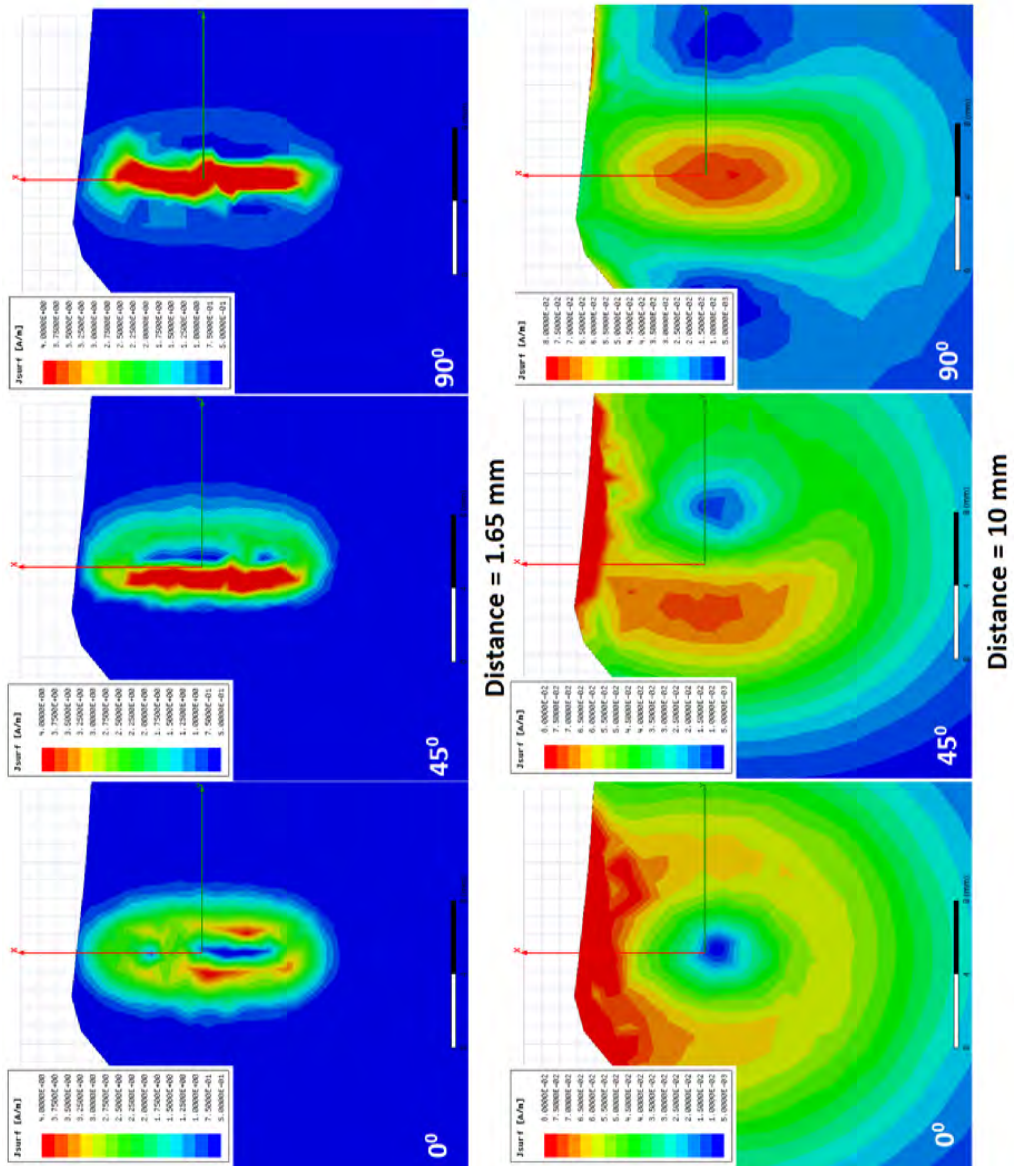


Figure 5.1: Current distribution on the target for different stand-off distances and rotation angles.

Table 5.4 lists the maximum ranges at different sensitivity levels and different angles. The range increases with the rotation angle for those levels of sensitivity for which initial range is less than 2.5 mm (like 20 dB and 30 dB). At higher level of sensitivity, the maximum range also decreases. This also corroborates the phenomenon described above.

In order to determine how much rotation can be tolerated at different stand off distances, the percentage error in sensitivity is calculated using equation 5.1 where y_0 is the sensitivity of L , R or Q at 0° and y_θ is sensitivity at angle θ .

$$Error = \left(\frac{y_\theta - y_0}{y_0} \right) \times 100\% \quad (5.1)$$

The error in the inductance, resistance and Q factor are plotted in Fig. 5.2. It should be noted that the effect of the sensitivity on the actual measurement is cumulative. For example, if the error in sensitivity is $\pm 50\%$, then for $10 \mu\text{m}$ of motion, the error will be $\pm 5 \mu\text{m}$, which seems negligible. However, if the implant shows $100 \mu\text{m}$ of motion, then 50% error would mean that the reading will show either $50 \mu\text{m}$ or $150 \mu\text{m}$ of motion.

In the first case, the patient and healthcare professional will wrongly assume that the implant is stable and will not take any action. On the contrary, for the later case, they may be unnecessarily alarmed and may go for resurgery even when it is not required. Therefore, a conservative error margin of 10% is assumed to be allowable. The maximum allowable limit on the angle rotation is therefore marked in the graphs by drawing 10% lines. The values are summarised in 5.5 can serve as a ready reference for healthcare professionals on the allowed rotational errors.

The graph visualizing the power dissipation in target and tissue as a function of rotation and frequency is shown in Fig. 5.3. The power dissipated in tissue

Table 5.4: Maximum range as a function of sensitivity level (in ppm) and angle of rotation in degrees.

Angle	Parameter	Range in mm				
		20	30	40	50	60
0°	L	0.6	1.22	2.6	5.6	12.1
	R	0.87	1.74	3.24	5.96	10.95
	Q	1.06	1.9	3.646	7.07	13.74
45°	L	0.66	1.27	2.5	5.2	10.56
	R	0.97	1.83	3.29	5.72	10.01
	Q	1.13	1.96	3.6	6.74	12.62
60°	L	0.706	1.309	2.542	4.9	9.78
	R	1.03	1.89	3.24	5.53	9.4
	Q	1.187	2	3.567	6.43	11.63
90°	L	0.73	1.33	2.5	4.82	9.24
	R	1.08	5.45	3.26	1.94	1.08
	Q	1.23	2.03	3.55	6.28	11.11

Table 5.5: Maximum angle of rotation allowed for $\pm 10\%$ error limit.

	2.5 mm	5 mm	10 mm	15 mm
L	90°	22°	15°	12.5°
R	42.5°	40°	15°	12.5°
Q	75°	45°	21°	17.5°

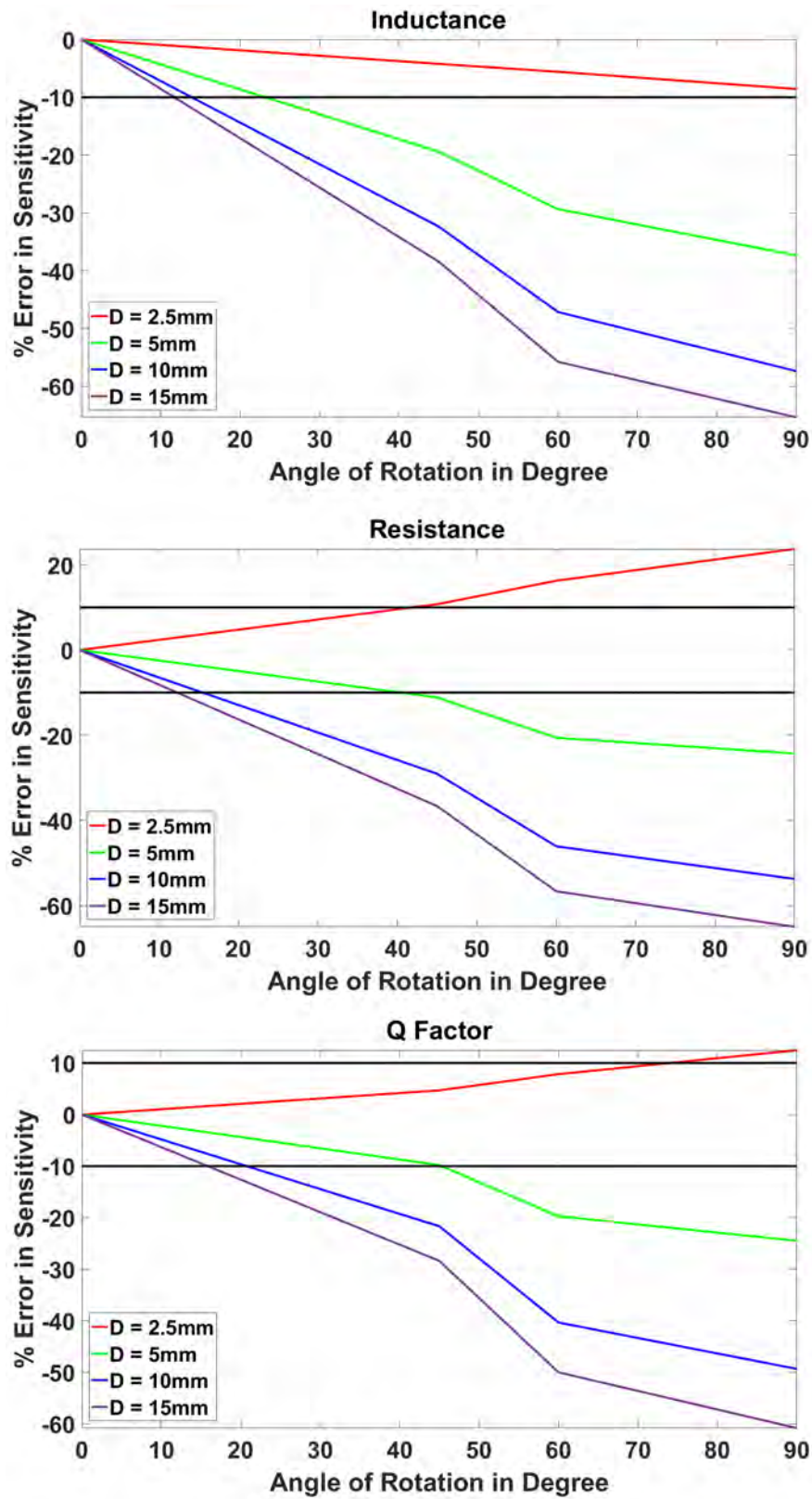


Figure 5.2: Percent error in inductance, resistance and Q Factor sensitivity as a function of rotation angle.

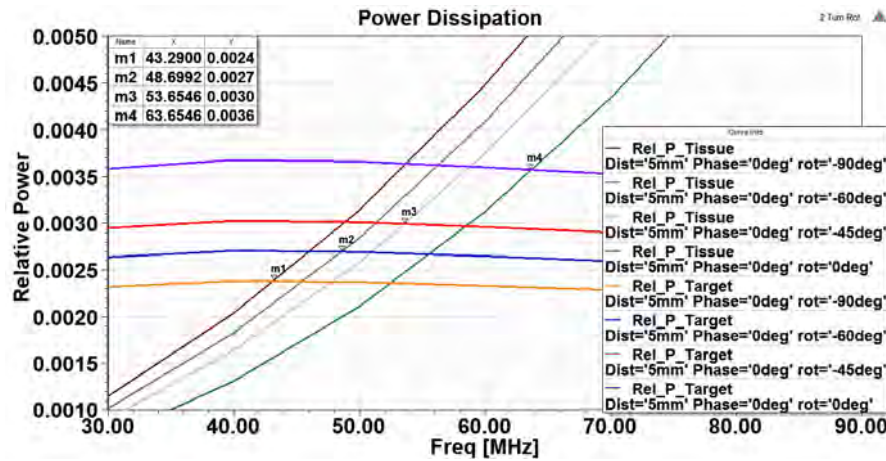


Figure 5.3: Relative power dissipation in the target and the tissue for different rotation angles.

increases and that in the target decreases, with the increasing the angle of rotation. This directly results in decrease in FT_{max} from 64 MHz to 43 MHz at the nominal distance of 5 mm.

5.4 Different Configuration of the Eddy Current Sensor

A two turn eddy current loop has been investigated in depth in this research. However, the other configurations of the loop are also possible. The other loop geometries that can fit on the rectangular PCB of dimensions 12 mm x 2.5 mm are shown in Fig. 5.4. They are one turn loop (1T), two turn loop (2T), three turn loop (3T), two turn wide trace loop (2W), three turn asymmetrically arranged loop (3A), and three turns printed on 2 layers (3T2L) loop. The effect of these geometry variations on sensor parameters is explored in this section.

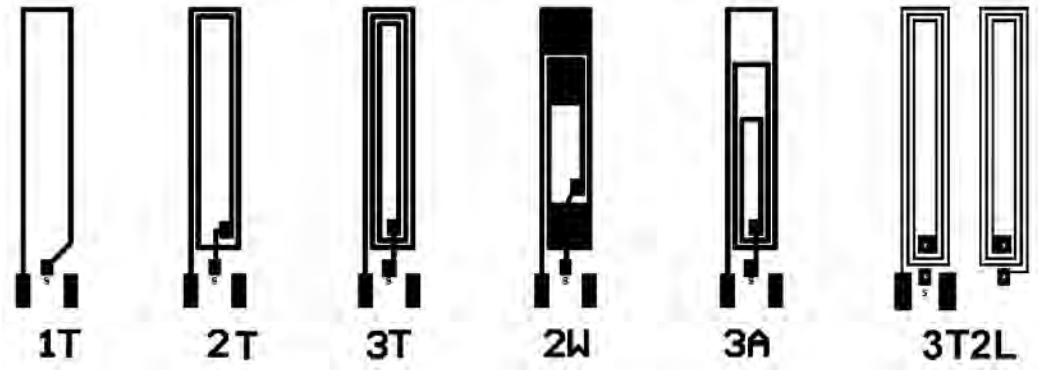


Figure 5.4: Different configurations for rectangular loops.

All these eddy current sensor geometries are printed on Rogers 6010 substrate with thickness 0.254 mm and laminated with 1 Oz./sq.foot copper (thickness = 35 microns). The nominal width of line is 0.2 mm. The length of the loop is 10 mm and the width is 2 mm.

Table 5.6: Electrical characteristics of different eddy current loop geometries in free space. Frequencies are in GHz, inductance is in nH and resistance is in Ω .

Design	f_{SRF}	Q_{peak}	$f_{QP_{peak}}$	$L_{QP_{peak}}$	$R_{QP_{peak}}$
1 Turn Loop	3.35	155.8	1.3	17.66	0.93
2 Turn Loop	1.172	90.87	0.36	38.12	0.95
3 Turn Loop	0.67	74.2	0.2	91.05	1.54
2 Turn Wide Trace Loop	1.57	92.81	0.649	24.70	1.27
3 Turn Asymmetric Loop	1.166	79.14	0.45	22.65	1.79
3 Turn 2 Layer	0.227	60.77	0.070	280	2

These are the possible configurations for a rectangular eddy current loop. These configurations are compared based on the impedance parameters (L, R, Q Factor),

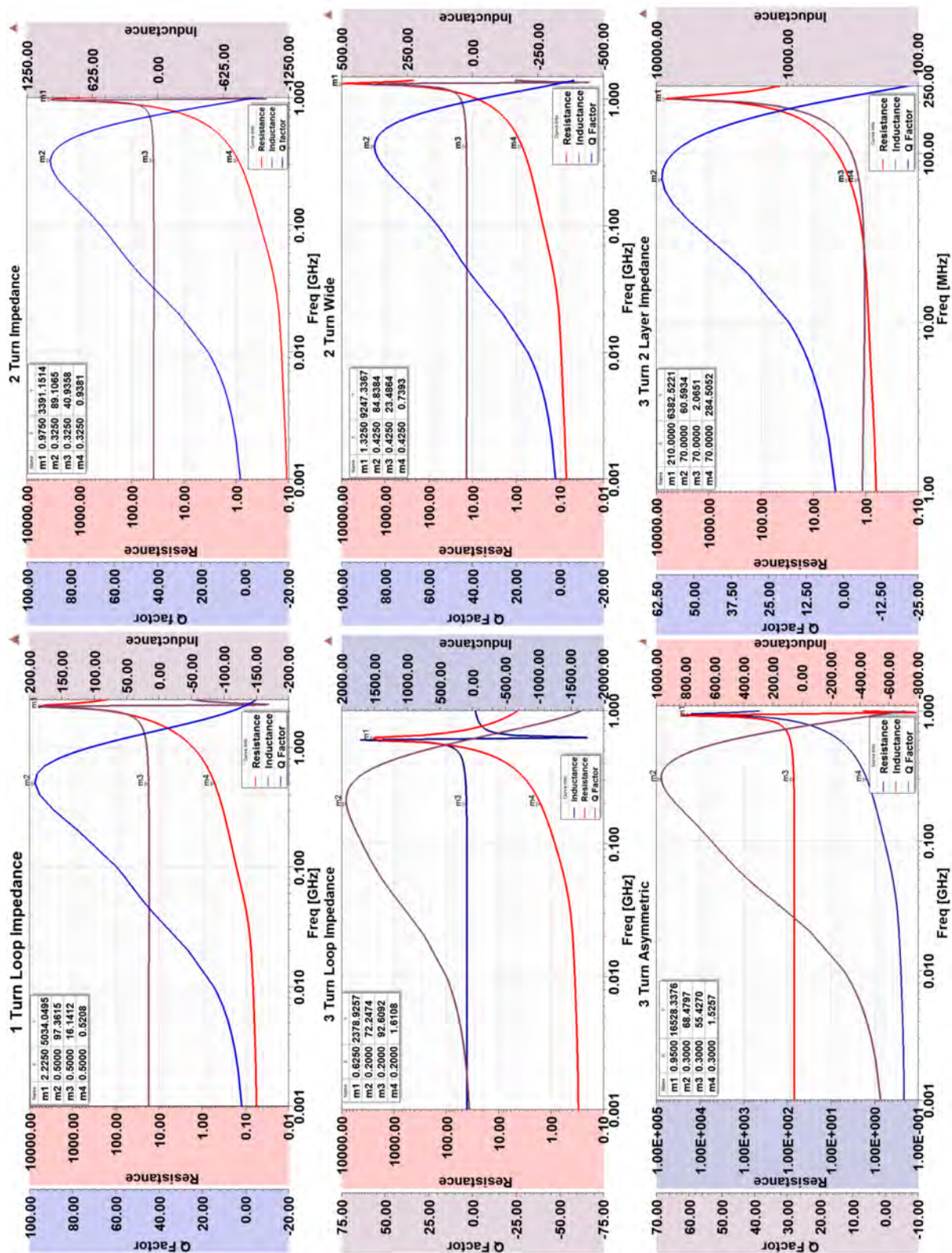


Figure 5.5: (a) Impedance parameters (L, R and Q-Factor) as a function of frequency for different loop configurations.

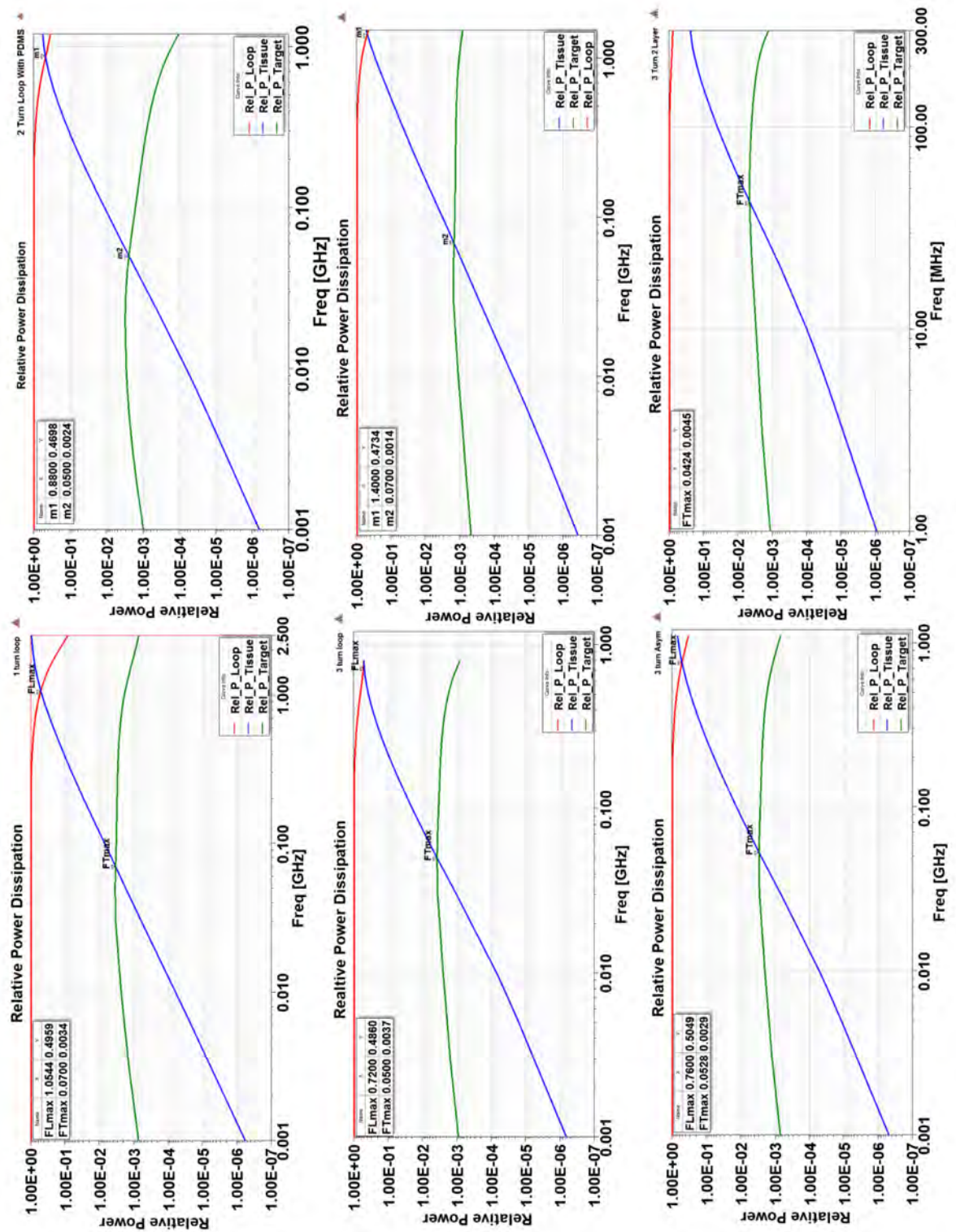


Figure 5.6: (b)Relative power dissipation in tissue, target and loop for different loop configurations.

Table 5.7: Electrical characteristics of different eddy current loop geometries inside human body. Frequencies are in GHz, Inductance is in nH and resistance is in Ω .

Design	f_{SRF}	Qmax	f_{QPeak}	L_{QPeak}	R_{QPeak}
1 Turn Loop	2.250	97.36	0.5	16.14	0.52
2 Turn Loop	0.925	86.2	0.3	40.62	0.88
3 Turn Loop	0.625	72.26	0.225	95.43	1.86
2 Turn Wide Trace Loop	1.07	87.76	0.325	32.33	0.75
3 Turn Asymmetric Loop	0.95	68.48	0.3	55.43	1.53
3 Turn 2 Layer	0.210	60.59	0.07	284.5	2.065

frequency parameters (F_{SRF} , F_{QPeak} , FT_{max} , FL_{max} and F_{Best}) and sensitivity parameters (sensitivity in ppm and range in mm). The frequency response and the power dissipation in tissue, target and loop for different configurations of the eddy current sensor are plotted in Fig. 5.5 and 5.6 to evaluate the frequency parameters.

The comparison of results of the impedance parameter analysis for different configurations in free space and human body is provided in Table 5.6 and Table 5.7. As expected, with the increasing number of turns, the F_{SRF} decreases. Similarly, the peak value of Q factor and F_{QPeak} also decreases. The two turn wide trace loop and three turn asymmetric loop has higher F_{SRF} , F_{QPeak} , and Q_{peak} values than the corresponding 2 turn loop and 3 turn loop respectively. The inductance and resistance for these geometries at F_{QPeak} is higher than the corresponding normal geometries. However, they provide higher frequency of operation and so a slightly higher Q factor.

Table 5.8: Comparison of the range of the sensor with different eddy current loop geometries.

Design	Parameter	Sensitivity level				
		20 dB	30 dB	40 dB	50dB	60 dB
1 T	L	0.6	1.238	2.674	5.848	12.82
	R	0.804	1.642	3.128	5.883	11.04
	Q	0.986	1.823	3.605	7.231	14.55
2 T	L	0.63	1.256	2.62	5.552	11.76
	R	0.77	1.56	2.96	5.55	10.38
	Q	0.98	1.775	3.447	6.78	13.37
3 T	L	0.612	1.228	2.599	5.561	11.91
	R	0.871	1.727	3.197	5.849	10.68
	Q	1.06	1.897	3.616	6.984	13.52
2W	L	0.609	1.206	2.512	5.288	11.15
	R	0.832	1.608	2.92	5.25	9.42
	Q	0.982	1.76	3.35	6.46	12.47
3A	L	0.623	1.229	2.551	5.352	11.25
	R	0.786	1.587	2.997	5.596	10.42
	Q	0.948	1.75	3.44	6.86	13.73
3T2L	L	0.6	1.237	2.68	5.87	12.91
	R	0.858	1.742	3.288	6.13	11.4
	Q	1.051	1.91	3.71	7.35	14.46

Table 5.9: Sensitivities of different configurations of eddy current loops at different stand-off distances.

Design	Parameter	Standoff Distance			
		2.5 mm	5 mm	10 mm	15 mm
1 T	L	119.53	15.8389	2.08	0.63
	R	228.28	18.1109	1.4361	0.3255
	Q	341.74	33.79	3.43	0.9036
2 T	L	116.3	13.78	1.64	0.47
	R	189.98	14.66	1.15	0.26
	Q	301.4	28.13	2.67	0.68
3 T	L	112.42	13.78	1.7	0.5
	R	253.171	18.2	1.29	0.272
	Q	368.6	32.1	2.86	0.69
2W	L	101.44	11.89	1.4	0.4
	R	183.18	12.11	0.79	0.16
	Q	281.86	24.47	2.16	0.53
3A	L	106.5	12.35	1.44	0.41
	R	194.13	15.16	1.16	0.26
	Q	293.75	28.75	2.86	0.75
3T2L	L	122.62	16.04	2.11	0.65
	R	272.72	21.27	1.63	0.36
	Q	387.98	36.26	3.47	0.88

Table 5.10: Different useful frequencies for the different loop configurations.

Design	F_{SRF} (GHz)	F_{QPeak} (GHz)	FL_{max} (GHz)	FT_{max} (MHz)	F_{Best} (MHz)	F_{Worst} (MHz)
1 T	2.250	0.5	1.05	70	30	300
2 T	0.925	0.3	0.86	60	30	275
3 T	0.625	0.225	0.72	50	40	250
2 W	1.07	0.325	1.4	70	40	325
3 A	0.95	0.3	0.76	53	40	275
3 T2L	0.210	0.07	-	42	30	150

The results of the curve fit analysis are summarized in Table 5.8 and Table 5.9. Finally, all the relevant frequencies for the different configurations are given in Table 5.10. The sensitivity is calculated at the F_{Best} frequency. It is seen that the range does not change appreciably with the number of loop turns at all the sensitivity levels. For the 2W and 3A geometries, which introduce smaller inner loops, the range is slightly lower than the rest of the configurations. For all the parameters like L, R and Q Factor, the range is highest for 3 turn 2 layer configuration. The sensitivity (expressed in ppm) is calculated at F_{Best} . It decreases with the increasing number of turns except for the 3T2L configuration, in which it is highest. This is also reflected in the increased range of operation. The sensitivity is also higher for a three turn loop, however, the best frequency for the three turn loop is also higher at 40 MHz and not at 30 MHz. However, the 3T2L configuration has best frequency at 30 MHz and yet has a better sensitivity.

For all the loop configurations, the F_{Best} in terms of highest sensitivity is in the

range of 20 MHz - 50 MHz. Moreover, FT_{max} (at stand off distance of 5 mm) is higher than the F_{Best} for all the variations. The loop geometry 3T2L is especially interesting. For all other geometries, the F_{Qpeak} and F_{worst} are very close and usually $F_{Worst} < F_{Qpeak}$. However, for 3T2L case, it is opposite, $F_{Worst} > F_{Qpeak}$. Also, F_{Qpeak} is close to the F_{Best} . This is the reason why this geometry shows highest sensitivity and operation range.

5.5 Summary

It is shown that the sensitivity of the sensor changes with the change in the complex permittivity of the tibial bone. The resistance of the sensor is affected most by the change in complex permittivity. The PDMS encapsulation enhances the immunity of sensor to permittivity changes by 24 times for inductance, 9.4 times for resistance and 10.25 times for Q factor as compared to non-encapsulated sensor. The rotation of the sensor with respect to the normal to the target surface decreases the sensitivity of the sensor. It is seen that the inductance is most severely affected by the rotation. The maximum allowable rotation angles corresponding to the 10 % error are found out for different stand-off distances. Different configurations of the eddy current loops are designed and investigated for sensitivity and range. While the best frequency of operation remains in the range of 20 -50 MHz, a three turn two layer loop provides the highest sensitivity and inductance value.

Part II

Data Telemetry Antenna

In the new era, thought itself will be transmitted by radio.

Guglielmo Marconi

Chapter 6

Miniaturized Implantable Antenna for Data Telemetry

6.1 Introduction

The space available on the PCB for the data telemetry antenna is about $2.5 \text{ mm} \times 2.5 \text{ mm}$. Since the available space is too small, 2.4 GHz ISM band can be targeted for the antenna design. As multiple sensors may be deployed, Frequency Division Multiplexing (FDM) may be required. IEEE 802.11 g/n provisions OFDM for communication. It allocates 20 MHz channels from 2.4 GHz to 2.485 GHz. So, the minimum bandwidth for such an antenna should be 20 MHz. Therefore, the aim is to design a miniaturized antenna operating at 2.4 GHz and having the -10 dB impedance bandwidth of 20 MHz.

6.2 Antenna Design

The antenna is designed using the circular archimedean spiral elements. The spirals are generated using parametric equation 6.1. The complementary spiral is generated when θ is advanced by 180° . Here 'R' is the maximum or outer radius of the spiral, 'N' is the number of turns and variable 't' is varied from 0 to $2\pi N$. Two such sets of complementary spirals are stacked one above the other separated by the substrate.

$$x(t) = \frac{R \times t \times \sin(t + \theta)}{2\pi N} \quad y(t) = \frac{R \times t \times \cos(t + \theta)}{2\pi N} \quad (6.1)$$

The antenna is fed from the spirals on layer 2 while the spirals on layer 1 are shorted at the centre. The two layers are connected using a shorting pin. The position of the shorting pin is varied along the length of the spiral to achieve the impedance matching and frequency tuning. The spiralling provides the larger current path thereby reducing the antenna dimensions. Further miniaturization is achieved by the use of shorting pin and high permittivity alumina substrate and superstrates. The antenna design is shown in Fig. 6.1.

The location of the shorting pin is varied by using equation $x = (Rad \times pt \times \sin(pt + pi))/(2\pi N)$ and $y = (Rad \times pt \times \cos(pt + pi))/(2 * pi * N)$ where Rad is outer radius of the spiral and pt gives the location of the short. pt is evaluated using expression $pt = para(2\pi N)/128$ where the variable $para$ can take any value between 1 to 128. The 128 in the denominator divides the entire spiral curve into 128 parts. For a finer control of position of shorting pin, this number can be increased. Thus, varying the single variable called $para$, the location of short on the spiral can be changed in the simulations.

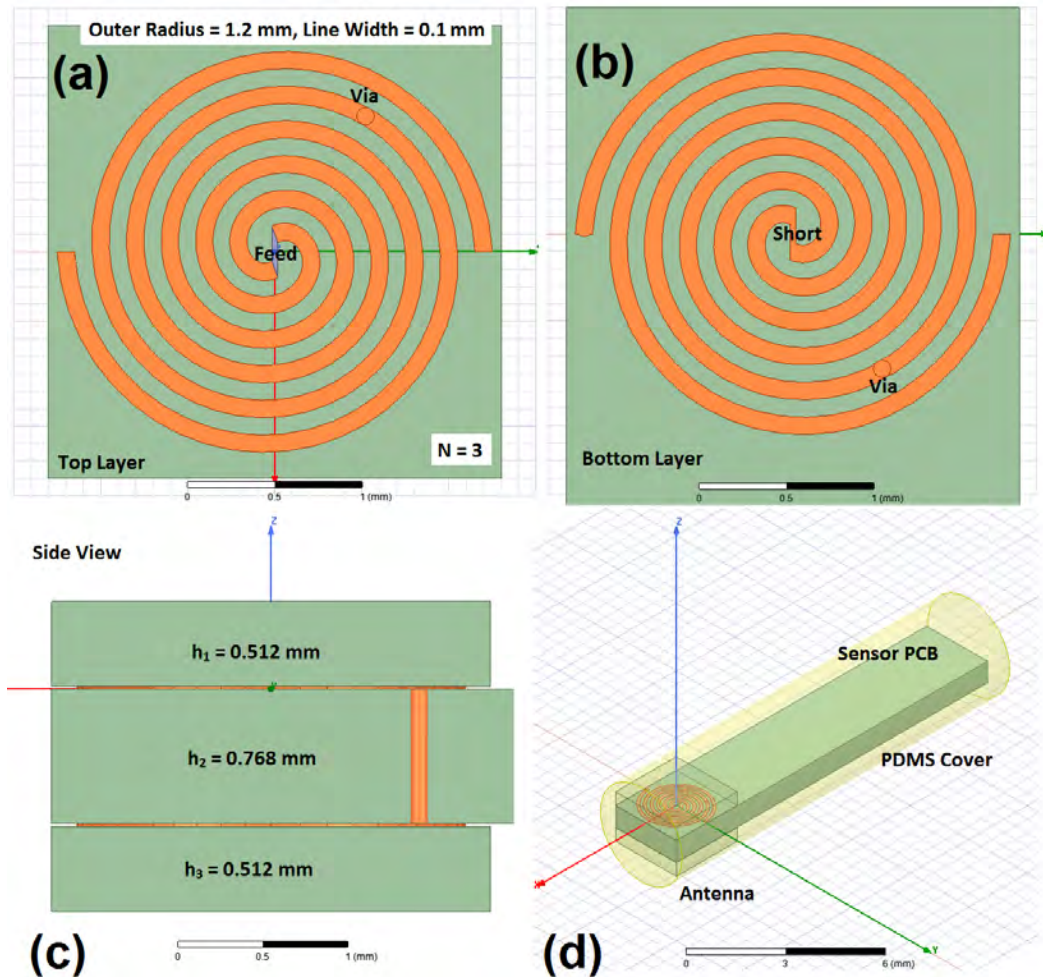


Figure 6.1: (a) Top layer of the complimentary spiral antenna showing the position of via, feed point, outer radius of spiral and line width of 0.1 mm. (b) Bottom layer of the antenna with the complimentary arms shorted at the centre. (c) Side view of the antenna showing the stacking of the alumina substrate and metal traces. (d) Antenna assembly enclosed in the PDMS cover.

The values of the geometrical parameters to achieve the resonance and impedance matching at 2.4 GHz are as follows. Number of turns ‘N’ = 3, outer radius of spiral ‘R’ = 1.2 mm, width of line = 0.1 mm, shorting pin position ‘para’ = 100, height of substrate = $h_2 = 0.768$ mm and height of superstrates = $h_1 = h_3 = 0.512$ mm.

Alumina is a biocompatible material which is chosen as a substrate. Due to such a miniaturized design with critical geometrical parameters, LTCC fabrication is preferred. Also, the alumina readily lends itself to the LTCC PCB manufacturing process. Further the traditional PCB manufacturing techniques like chemical etching or milling machine with woven glass substrates have trouble with spacings and linewidths less than 0.1 mm which is used in the current design of the antenna. Further, to have a via between the two layers of design, a hole of diameter as small as $75 \mu\text{m}$ must be drilled through the substrate of thickness 0.76 mm. Even with laser, such a small hole cannot be drilled through such a thick substrate. Hence, the traditional PCB techniques cannot be used for antenna fabrication. Conversely, LTCC can do all these operations easily as PCB is constructed layer by layer and the mass production is easier through the CAM techniques.

Therefore, a ceramic alumina substrate having $\epsilon_r = 7.3$ is chosen (Ferro Green L8 tapes with thickness $127 \mu\text{m}$) as a substrate. The conductor silver paste is FERRO CN33-498 having thickness of $10 \mu\text{m}$. Multiple layers can be stacked to get desired thickness of substrate and silver.

The entire sensor along with the antenna is encapsulated by the Polydimethylsiloxane (PDMS) material with $\epsilon_r = 2.7$. The antenna is simulated inside a detailed human leg provided by HFSS. The electromagnetic and other tissue properties for cortical bone, skin, fat and muscle are used from IT’IS database [124]. The tibial implant is modelled by Ti-6Al-4V, a titanium alloy, frequently used in implants,

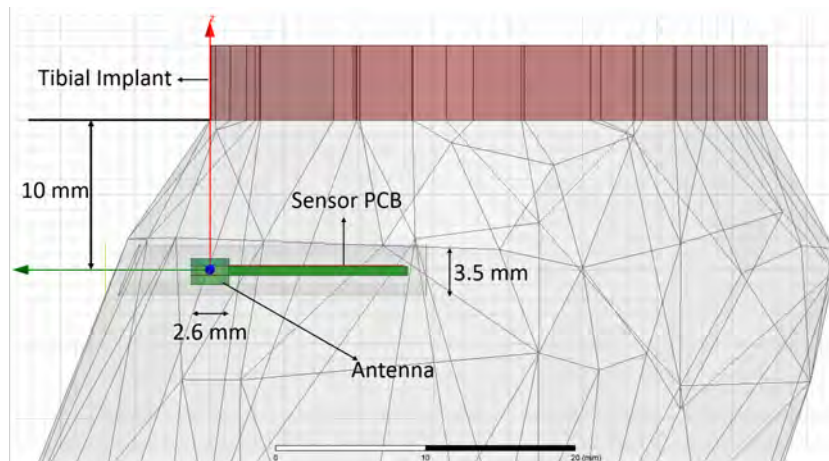


Figure 6.2: Placement of antenna inside the tibial bone near the titanium implant.

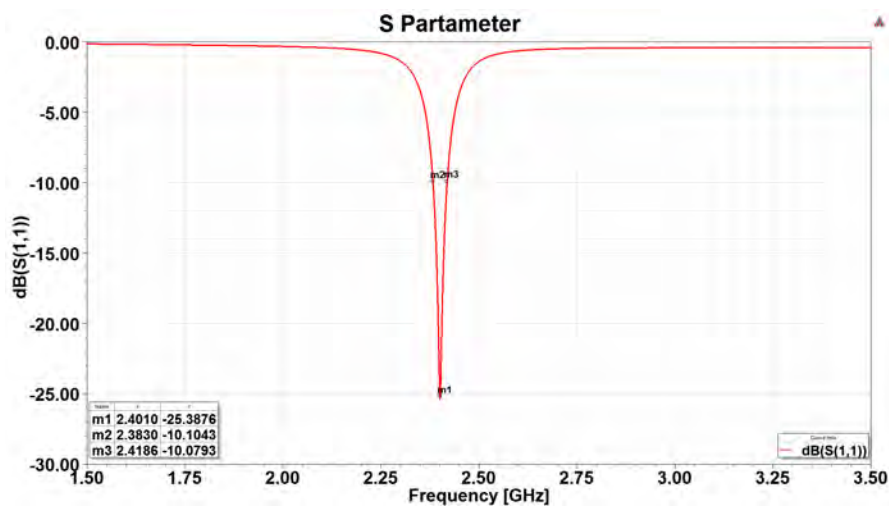


Figure 6.3: Frequency response of the optimized antenna.

having the conductivity $\sigma = 588235 \text{ S/m}$. The placement of the antenna embedded inside the tibial bone is shown in Fig. 6.2. The frequency response of the designed antenna is shown in Fig. 6.3. The antenna resonates at 2.4 GHz with a -10 dB bandwidth of 35 MHz from 2.383 GHz to 2.418 GHz. This covers the requirement of 20 MHz for OFDM communication. The antenna design could not be verified

experimentally due to the delays in setting up of LTCC fabrication facility.

Comparison of antenna with other antennas

Table 6.1 gives the comparison of the present design with the antennas already available in the literature [118, 120, 136–140]. The proposed antenna is smallest amongst the antennas reported in the recent literature. It achieves good impedance matching in the small form factor. However, the gain suffers due to the extreme miniaturization. It can also be noted that most of the antennas in literature are embedded beneath the skin (subcutaneously), whereas the proposed antenna is implanted deep inside the bone and reflections from tissue discontinuities (bone, muscle and skin) are also considered in the simulation. A similar analysis is done in [140] for a human arm and the gain is found to be comparable. Antennas in the proximity of knee is developed in [118, 120] but at 400 MHz MICS band.

6.3 Parametric Analysis

The parametric analysis of the antenna dimensions as well as the human body properties helps in identifying the dominant parameters that affect the performance of the antenna. It also helps in redesigning or retuning antenna for different frequency or for better radiation characteristics. In this section, therefore, the effect of different geometrical parameters like the radius of spiral, location of the shorting pin, and the linewidth of spiral are studied. Further, the effect of variation in the tissue properties of bone and muscle are also investigated.

Table 6.1: Comparison of the performance of present antenna with other published work.

Ref.	Tissue	Freq	Footprint in mm	Gain in dBi
[118]	3 Layer	MICS	r=5mm, h=40mm.	-27.2
[120]	3 Layer	MICS	r=5mm, h=40mm.	-21
[136]	Skin	ISM	9.48 X 7.8 X 0.76	-28.9
[137]	Skin	ISM	12 X12 X 1.27	-28
[138]	Skin	ISM	10 X 10 X 1.27	-22
[139]	Skin	ISM	13.2 X 15.8 X 0.635	-22.2
[140]	Arm	UHF	20.5 X 1 X 1	-35
This work	Leg	ISM	2.6 X 2.6 X 1.792	-36.2

Effect of the Outer Radius of Spiral

As the outer radius of the spiral is changed, the total length of the spiral also changes. Consequently the resonant frequency also changes substantially. The impedance matching also changes to some extent. However, since the spacing between the arms (slot dimension), thickness of the substrate and the trace width is kept constant, the effect on impedance matching is not significant. Fig. 6.4 shows the effect of variation in the outer radius of the spiral on the resonant frequency and the reflection coefficient. The radius is varied from 1 mm to 1.25 mm (as this is the maximum linear dimension available) and so the cross sectional area changes from $1\pi \text{ mm}^2$ to $1.5625\pi \text{ mm}^2$. Table 6.2 lists the radius, the cross section area and the resonant frequency for the parametric variation.

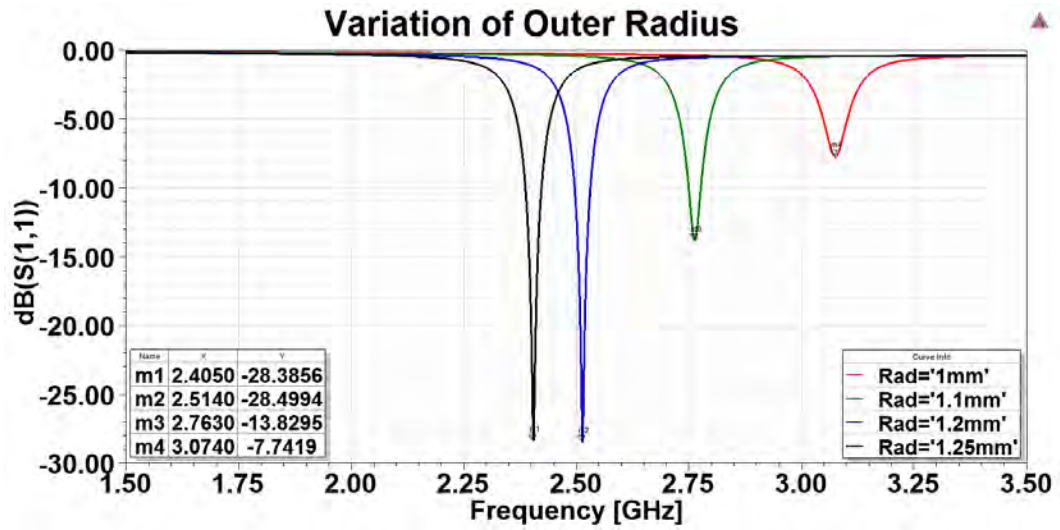


Figure 6.4: Effect of changing the outer radius of the spiral on the resonant frequency.

Table 6.2: Effect of changing the outer radius of spiral.

Radius	Cross Sectional Area	Resonant Frequency	S11 in dB
1 mm	$1\pi \text{ (mm}^2\text{)}$	3.07 GHz	-7.74
1.1 mm	$1.21\pi \text{ (mm}^2\text{)}$	2.76 GHz	-13.83
1.2 mm	$1.44\pi \text{ (mm}^2\text{)}$	2.51 GHz	-28.5
1.25 mm	$1.5625\pi \text{ (mm}^2\text{)}$	2.4 GHz	-28.4

Effect of the Trace width

The trace width is varied from 0.075 mm to 0.125 mm to investigate the sensitivity of the resonance frequency to the fabrication uncertainties. The results are shown in Fig. 6.5. The S parameter results are given in Table 6.3. Since the outer radius of the spiral is kept constant, changing the trace width also changes the gap between the adjacent traces (slot width).

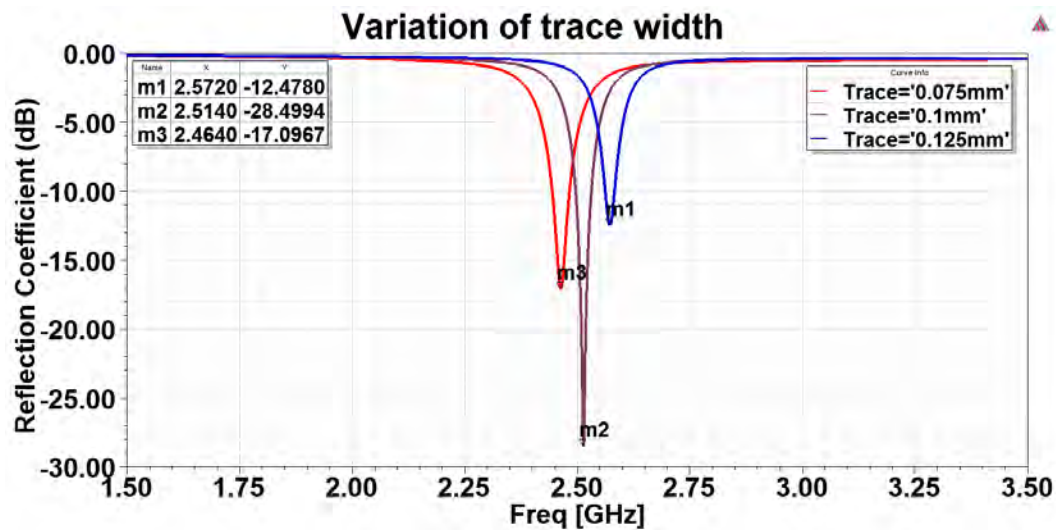


Figure 6.5: Effect of changing the width of the spiral trace on the resonant frequency.

Table 6.3: Antenna parameters for varying the trace width.

Trace Thickness	Resonant Frequency	S_{11}	-10 dB Bandwidth
0.075 mm	2.464 GHz	-17.1	38 MHz
0.1 mm	2.514 GHz	-28.5	40 MHz
0.125 mm	2.464 GHz	-12.48	21 MHz

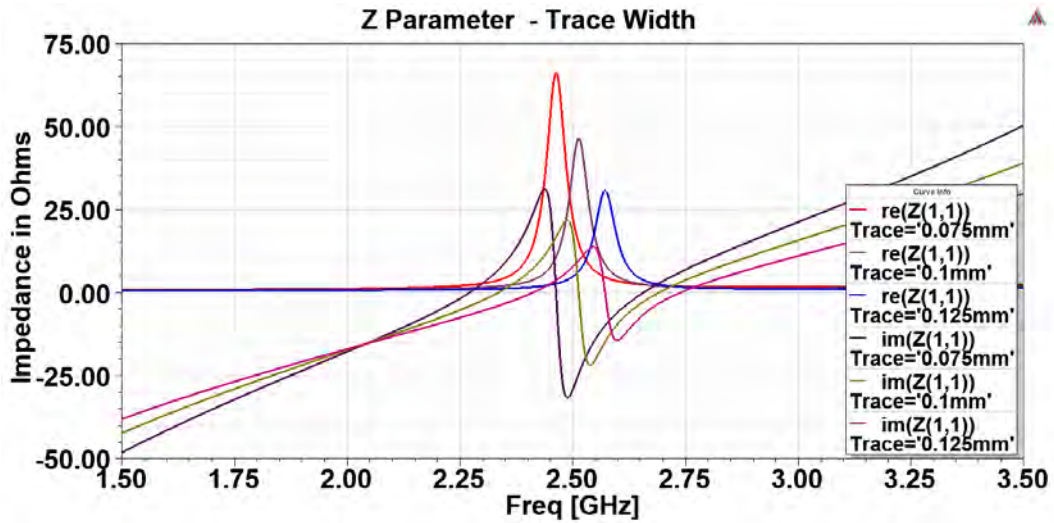


Figure 6.6: Effect of changing the width of the spiral trace on the impedance of the antenna.

The change of 0.05 mm in the process variations shifts the resonance by about 100 MHz which is more than the bandwidth offered by the antenna but falls inside the 100 MHz band offered by the 2.4 GHz - 2.5 GHz ISM band. Also, the impedance matching worsens for higher trace width, but still the antenna is matched within -10 dB limits. Also, the bandwidth increases with the trace width, however, since the antenna is not matched properly for thickness = 0.125 mm, the -10 dB bandwidth is low.

The real and imaginary part of the impedance is shown in the Fig. 6.6. It can be seen that the thicker trace offers a lower resistance and lower variation in the reactive impedance. Consequently, it offers better impedance matching and higher potential bandwidth. However, when trace thickness is increased the gap between adjacent traces decreases. Thus, it becomes difficult for fabrication and the probability for accidental shorting between the two traces increases. Therefore

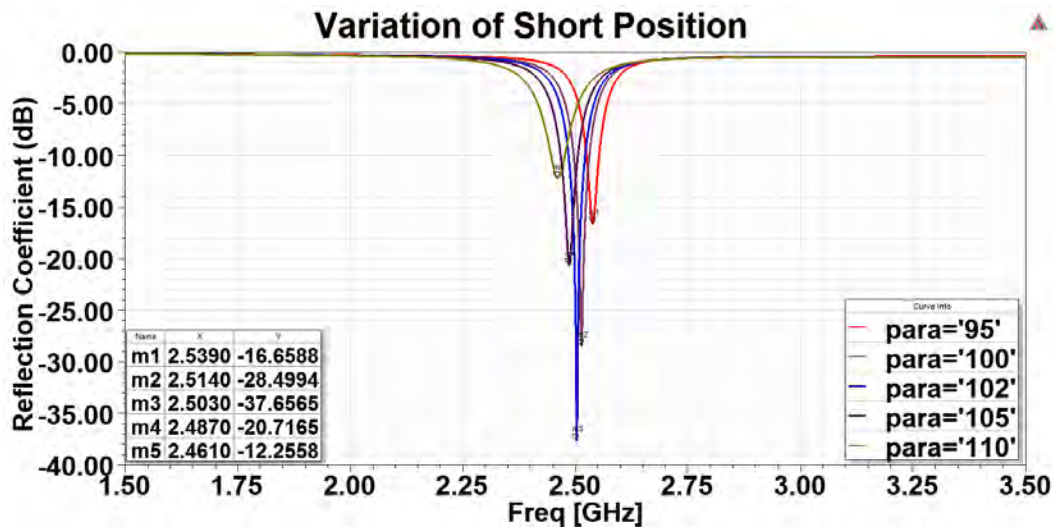


Figure 6.7: Effect of changing the position of the shorting pin on the resonant frequency.

trace thickness of 0.1 mm is judged to be quite suitable from fabrication point of view.

This implies that the process variation of ± 0.025 mm is tolerable to keep the antenna resonance in the 2.4 GHz ISM band, provided it is designed at the centre frequency of 2.45 GHz with the nominal trace thickness of 0.1 mm.

Effect of the Short Position

The position of the shorting pin is controlled by the variable 'para' defined in the antenna design section. Fig. 6.7 shows that the position of short can be varied between 95 to 110 to get resonant frequency variation within 80 MHz. The antenna matching is optimal at 2.5 GHz for the 'para' value of 100. Thus, a tolerable variation exists for the position of short such that the resonance stays in the ISM band.

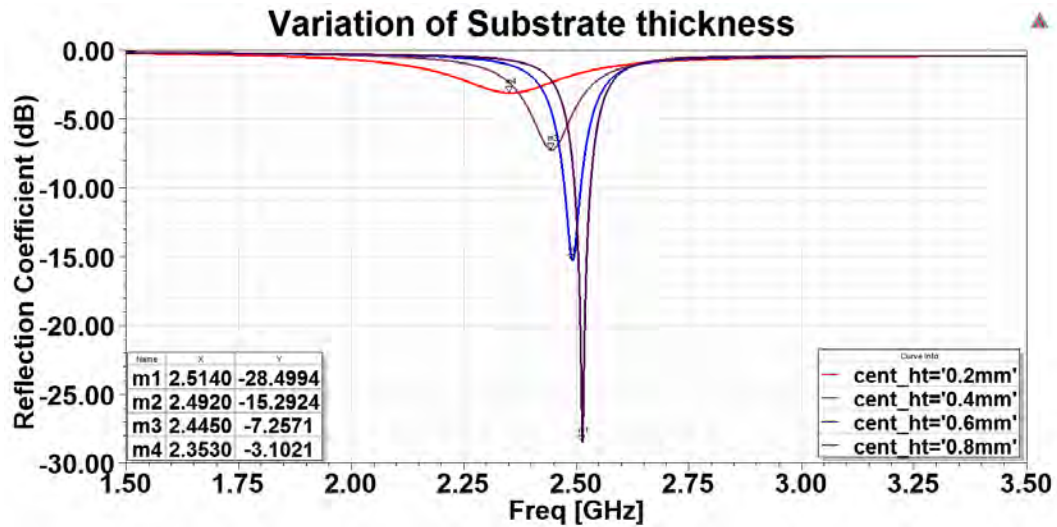


Figure 6.8: Effect of changing the thickness of the substrate on the resonant frequency.

Effect of Substrate Thickness

LTCC fabrication facility offers a possibility to change the thickness of the substrate. In this section, therefore, an investigation of the substrate thickness is carried out. The results are shown in Fig. 6.8. It can be seen that substrate thickness has great effect on the impedance matching of the antenna. With the thickness increasing from 0.2 mm to 0.8 mm the reflection coefficient becomes better. The resonant frequency also shifts from 2.35 GHz to 2.51 GHz. For any thickness between 0.3 mm to 0.8 mm the resonance is obtained within 2.4 GHz - 2.5 GHz range. In order to investigate the impedance mismatch, the real and imaginary part of the impedance is plotted in Fig. 6.9. It clearly shows that decreasing the substrate thickness increases the resistance which explains the worsening impedance mismatch. Also, the variation in reactive part increases which means lower potential bandwidth. To some extent this may be compensated by

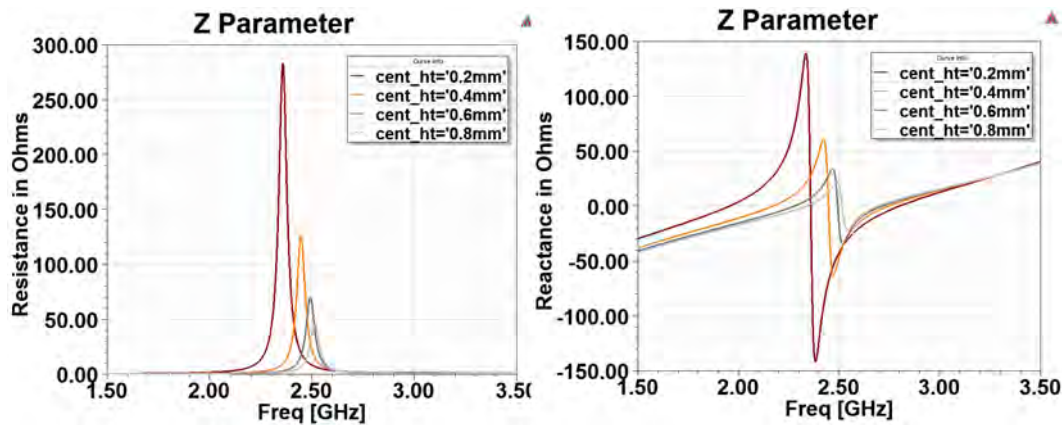


Figure 6.9: Effect of changing the thickness of the substrate on the impedance characteristics of the antenna.

increasing the trace width as seen from Fig. 6.6. Increasing the thickness beyond 0.8 mm is not suitable because of the limitation of the available space.

Effect of Inductive Sensor Loop

Antenna performance is usually affected by the presence of metallic objects or traces in their vicinity. Since the eddy current sensor loop is also printed on the same plane as the designed antenna, it is important to observe and quantify its effect. Fig. 6.10a shows the 3 different loop geometries simulated along with the designed antenna. From Fig. 6.10b, it can be seen that the presence of loop does not have any appreciable effect on the resonance frequency or the impedance matching of the antenna.

Fig. 6.11 shows the comparison of the cross coupling parameters (S_{21}). It is seen that the amount of power coupling between the antenna and the loop increases with the number of turn of the eddy current loop. While for one turn and two turn loop, the power coupling is below -45 dB, it rises to -35 dB for a three turn loop.

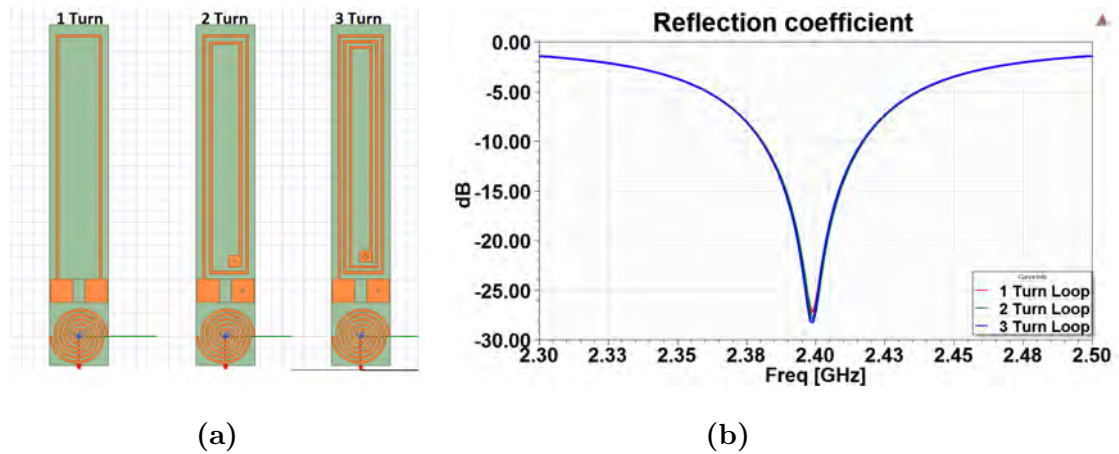


Figure 6.10: (a) Geometry of one turn, two turn and three turn loop geometries alongside the designed antenna.(b) Effect of the different loop geometries on the resonance of the antenna.

The radiation characteristics of the antenna for the three different designs of the loops are given in Table 6.4. Again, no appreciable change in the directivity or gain is seen. Thus, the presence of eddy current loops do not affect the performance of the antenna.

Since the eddy current loop works in the near field, the effect of the antenna on the impedance characteristics of loop is also examined. Fig. 6.12 compares

Table 6.4: Radiation performance of antenna in presence of the eddy current loop.

Loop Design	Radiation Efficiency	Directivity	Gain
1 Turn Loop	-36.4 dB	2.1 dB	-34.3 dB
2 Turn Loop	-37.32 dB	2.11 dB	-35.21 dB
3 Turn Loop	-36.08 dB	2.13 dB	-33.95 dB

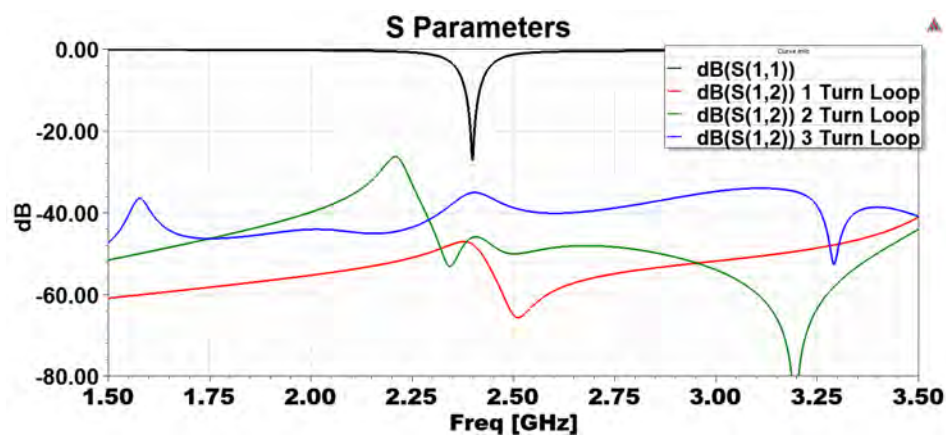


Figure 6.11: Effect of one turn, two turn and three turn loop geometries on the S parameters of the system.

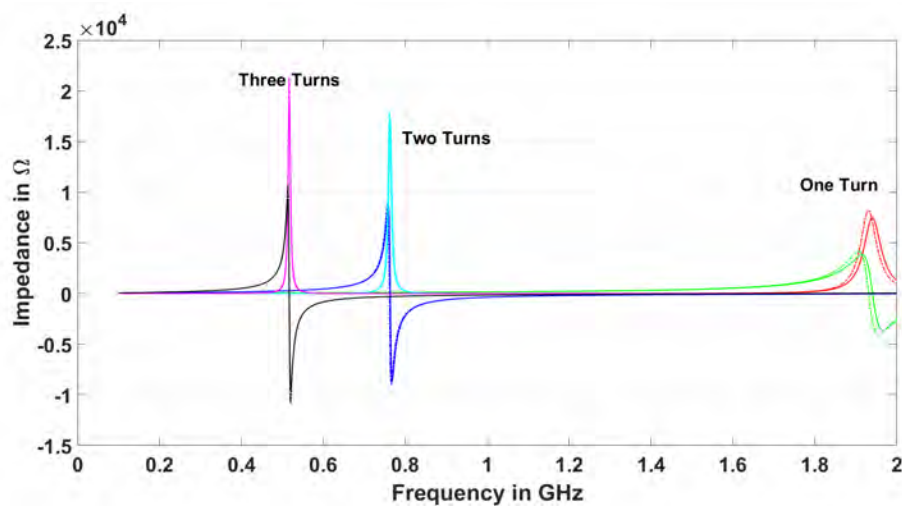


Figure 6.12: Effect of the antenna on the frequency response of the one turn, two turn and three turn loop geometries.

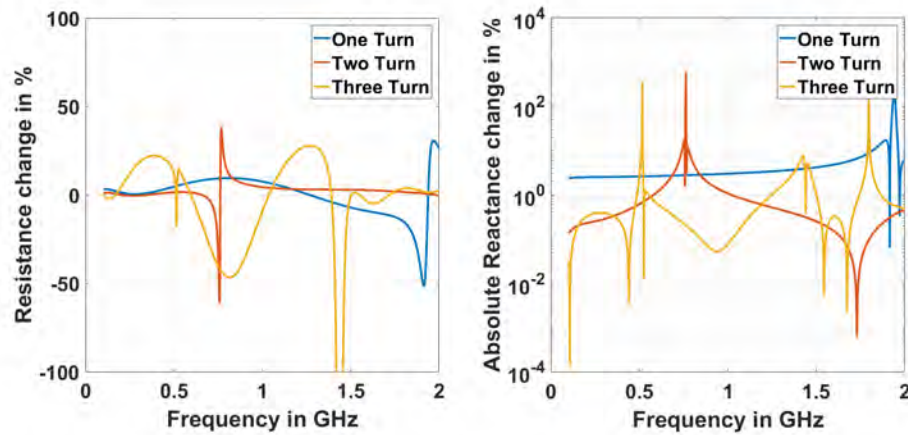


Figure 6.13: Relative change in the impedance of the eddy current loops due to the antenna.

the impedance characteristics of the eddy current loop in absence (solid line) and presence (dash-dot line) of the proposed antenna. It shows that the antenna does not disturb the self resonance frequency (SRF) of the eddy current loop by any appreciable amount. The change in SRF is highest for one turn loop and lowest for three turn loop. To quantify the effect, the relative change in the real and imaginary part of impedance expressed as % is plotted in Fig. 6.13. As expected, the effect increases with frequency with very high change in impedance ($> 50\%$) near the SRF. At very low frequencies (< 200 MHz), as the number of turns in loop increase the change in impedance decreases. It is about 2.5% for one turn loop and reduces to 0.1% for three turn loop. Also the effect on the reactive impedance is much more pronounced than on the resistance especially at higher frequencies. Therefore, operating the loop below 200 MHz is recommended to allow for minimal coupling between the antenna and the eddy current loop.

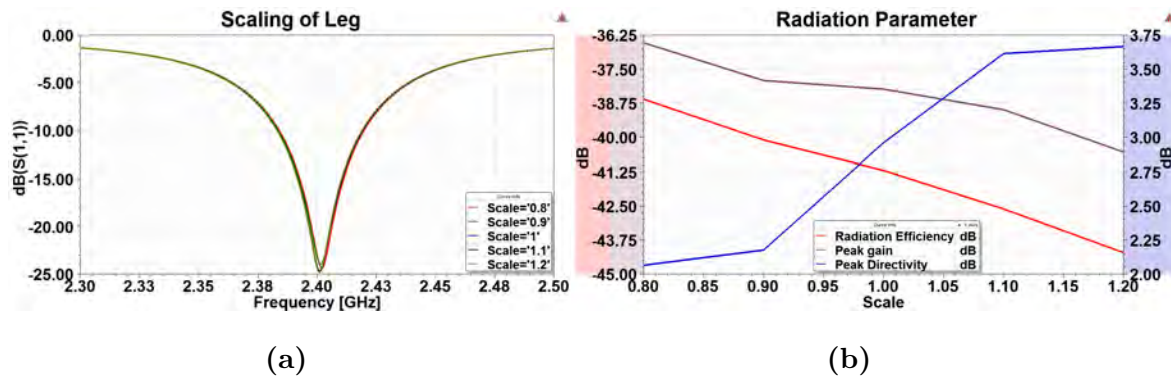


Figure 6.14: (a) Effect of the leg size variation on the frequency response. (b) Effect of leg size variation on the gain, radiation efficiency, and the directivity of antenna.

6.4 Tissue Parametric Analysis

People from various age groups having very different body constitutions undergo the orthopaedic surgeries. Therefore, it is necessary to evaluate the performance of antenna under different human tissue conditions. The parameters that can be varied are size of leg, amount of muscle tissue cover over the bone, and the complex permittivity of the tissue.

Effect of Size of the Leg

The size of leg is varied by $\pm 20\%$. The frequency response of the antenna with is shown in Fig. 6.14a. The frequency response is virtually unaltered. However since the size of the leg changes, the radiation characteristics also change. The peak gain, directivity and radiation efficiency is plotted in Fig. 6.14b. With the increase in the size of leg, the radiation efficiency decreases by 5.6 dB from -36.6 dB to -44.2 dB. However, since the peak directivity increases by 1.5 dB, the decrease

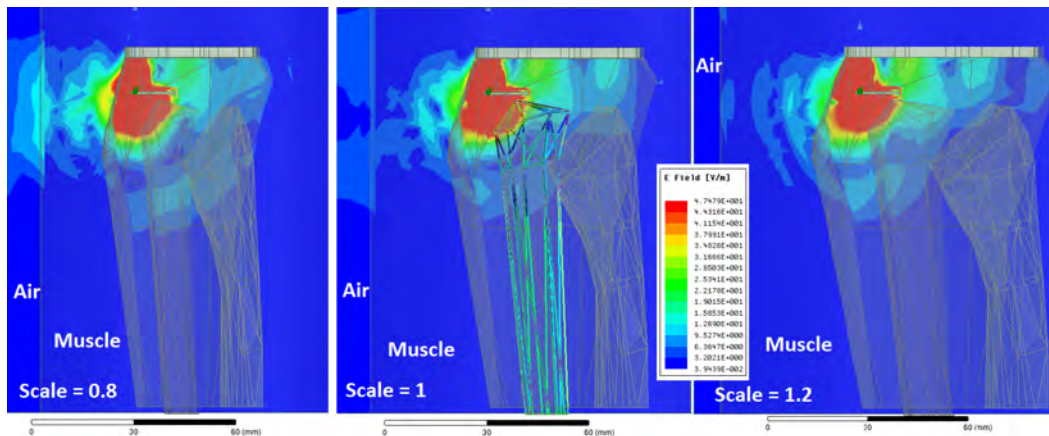


Figure 6.15: E-Field Distribution for different sizes of leg.

in peak gain is about 4 dB from -36.5 dB to -40.5 dB.

The E-field distribution is shown in Fig. 6.15. As the size of the leg is increased the amount of E-field extended in the air decreases. This causes the radiation efficiency to drop with the increasing size of the leg. Also, it can be seen that the maximum amount of E -field is concentrated inside the tibial bone. In other words, the deeper the antenna is implanted inside the body, worse is the radiation efficiency.

At this point, the effect of PDMS coating is also investigated. Besides providing bio-compatibility, it also provides better radiation efficiency and gain. The frequency response and the radiation characteristics of the antenna without PDMS cover are shown in Fig. 6.16a and Fig. 6.16b. While the resonant frequency shifts to the lower value, the radiation efficiency drops by about 6.5 dB. This phenomenon is also confirmed by the comparative E-field distribution shown in Fig. 6.17. This confirms that the PDMS coating protects antenna from detuning. It also prevents dropping of the radiation efficiency to some extent.

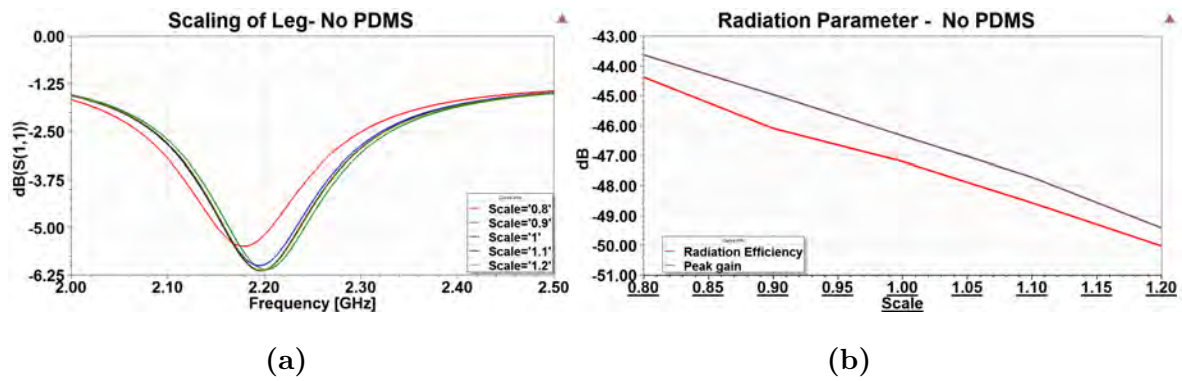


Figure 6.16: (a) Effect of the leg size variation on the frequency response of the antenna without PDMS coating. (b) Effect of the leg size variation on the gain, and radiation efficiency of the antenna without PDMS coating.

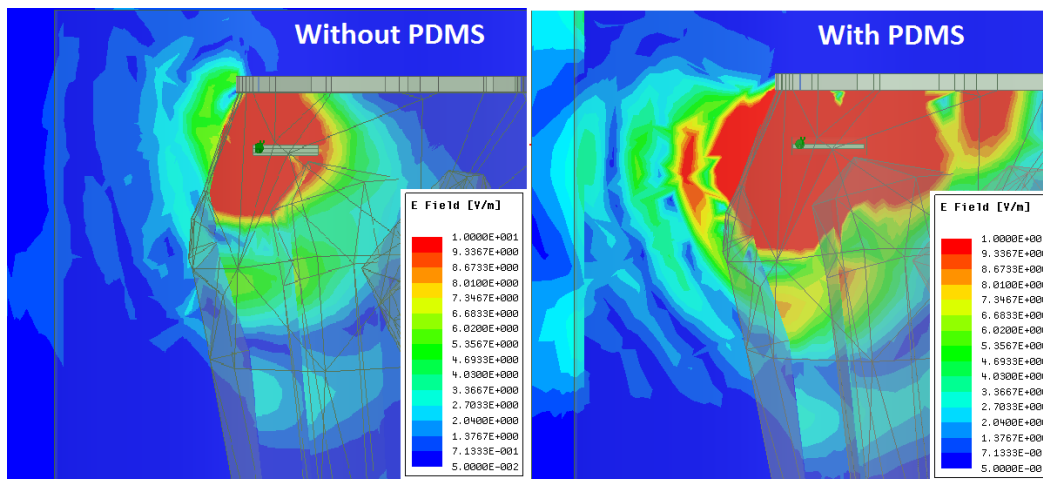


Figure 6.17: Comparison of the E-Field distribution with and without the PDMS Coating.

Effect of the Changing Permittivity of Bone

The antenna is embedded inside the tibial bone. This part of the bone is made up of cancellous tissue and undergoes repair and reformation during the healing phase. On the other hand, over the time, osteoporosis can cause the bone loss causing decrease in bone density (especially in the elderly population). This in turn affects the permittivity of the bone tissue. To study how this affects the electromagnetic properties of the antenna, the complex permittivity of the tibial bone is varied by $\pm 10\%$ and $\pm 25\%$. The value of ϵ' of bone is 11.41 at 2.4 GHz. Therefore, the simulations are done for 8.55, 10.27, 11.41, 12.55, and 14.26. Similarly, the conductivity is varied with values 0.288, 0.346, 0.384, 0.423, 0.48 S/m. These values correspond to -25%, -10%, 0%, 10%, 25% variation. When one of the parameters is varied, the other is kept at the nominal value. The resonant frequency does not change appreciably (not plotted) for either of the variation. This is predominantly because of the PDMS coating as explained in section above. The radiation efficiency is plotted in Fig. 6.18.

With the increasing permittivity of bone, the radiation efficiency increases but not significantly. The radiation efficiency at the lowest value of ϵ' may be a statistical outlier than an actual value. Therefore, it can be summarized that changing the permittivity of bone by about $\pm 25\%$ changes the radiation efficiency by about $\pm 0.1dB$. More variation is seen with respect to the conductivity of the bone tissue. The radiation efficiency varies by $\pm 0.75dB$ for $\pm 25\%$ variation. However, it is shown in [135], that the density of bone strongly correlates with the real part of permittivity and weakly coupled with the imaginary part. So while the conductivity affects the radiation efficiency greater than the permittivity, the

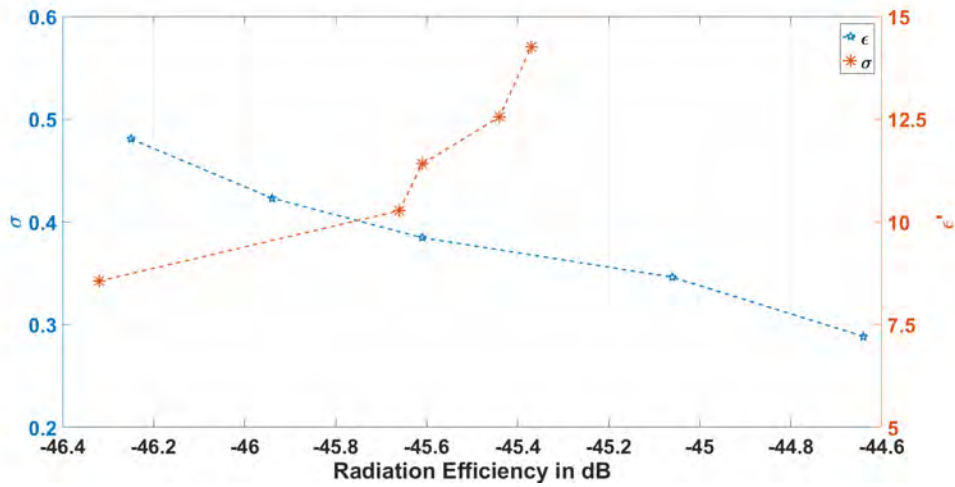


Figure 6.18: Effect of changing the permittivity of bone on radiation efficiency.

amount of variation in the conductivity due to the variation in the bone density is less than that of the permittivity.

Effect of the Muscle Thickness

In [141], the intra- and inter-muscular variation in human quadriceps of 16 females and 15 males of mean age 20 years has been carried out. It showed the maximum variation of ± 5 mm in the individual muscle tissues like *Vastus lateralis*, *Vastus medialis*, *Rectus Femoris* and *Vastus Intermedius*. Although, the sample size in the presented study was very less and for a single age group, it provides a starting point to determine the size variability that the big muscle have across gender and physical constitutions. Therefore, in the present investigation, for considering an extreme effect, the muscle tissue dimensions are varied by twice the amount (± 10 mm) reported in [141].

The radius of the cylinder representing the muscle tissue is varied between

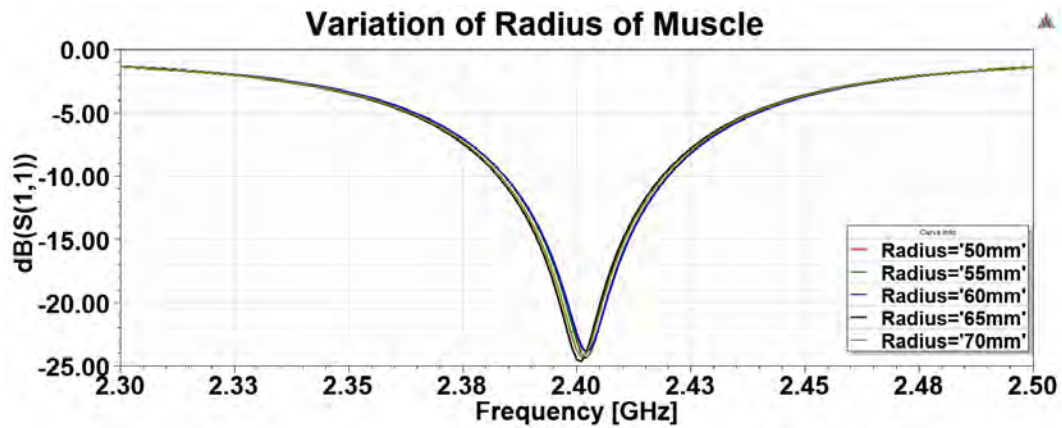


Figure 6.19: Effect of changing the muscle radius on the resonant frequency.

50 mm to 70 mm in 5 mm steps. The results are plotted in Fig. 6.19. It can be seen that this variation does not affect the resonant frequency of the antenna or its impedance matching appreciably. However, it affects the radiation properties. The peak gain and radiation efficiency variation is shown in Fig. 6.20. Both the peak gain and radiation efficiency decrease at the same rate with the increasing muscle thickness. The reduction in gain, therefore can be attributed to the reduction in radiation efficiency. The directivity and the radiation pattern does not change appreciably. The decrease in the radiation efficiency may be due to the increased losses in the muscle tissue. The total change in radiation efficiency is ± 3.5 dB as the muscle thickness changes by ± 10 mm.

Effect of the Complex Permittivity of Muscle

Similar to the bone, the muscle permittivity is also subject to change. Especially, since the muscle is a water rich tissue, both the epsilon and conductivity are more prone to changes than that of the bone. The nominal values of permittivity and conductivity of the muscle tissue at 2.4 GHz are 52.8 and 1.7 S/m respectively.

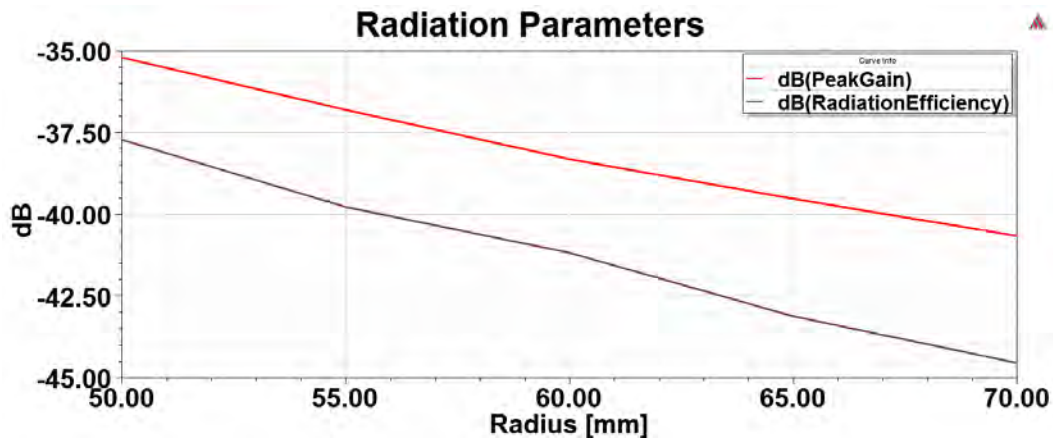


Figure 6.20: Effect of changing the muscle radius on the radiation parameters.

Therefore, the simulation variation values are [39.6 47.52 52.8 58.08 66] and [1.275 1.53 1.7 1.87 2.125] for the permittivity and conductivity respectively.

When the permittivity of the muscle is changed, the change in resonant frequency is less than 4 MHz. In this case also, the radiation efficiency increases with increase in the permittivity and decreases with the increase in conductivity. The results are plotted in Fig. 6.21. The maximum change in radiation efficiency is $\pm 0.5dB$ and $\pm 2.6dB$ for $\pm 25\%$ change in permittivity and conductivity respectively.

In summary, the order of parameters that affect radiation efficiency most is $size_{Muscle} > \sigma_{Muscle} > \sigma_{bone} > \epsilon_{Muscle} > \epsilon_{bone}$.

6.5 Summary

A highly miniaturized antenna working at 2.4 GHz is developed by employing spirals on both sides of a ceramic substrate. The spirals are connected using an appropriately positioned shorting pin. The position of the shorting pin controls

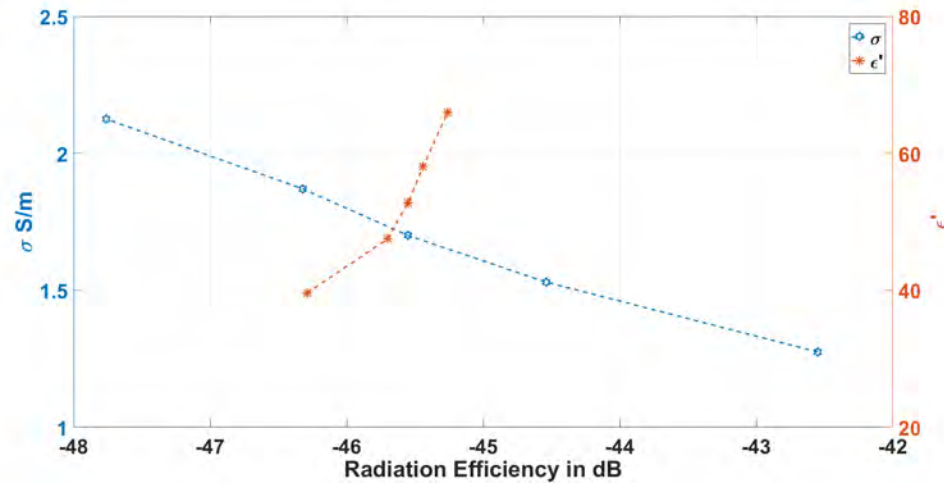


Figure 6.21: Effect of changing the muscle permittivity and conductivity on the antenna radiation parameters.

the resonant frequency as well as the impedance matching. The outer radius of the spiral and number of turns have the highest influence on the resonant frequency. The antenna offers bandwidth of 35 MHz which is sufficient for a single channel OFDM transmission having bandwidth of 20 MHz. A thorough parametric analysis is performed to evaluate the effect of geometry variation as well as tissue variation. The resonant frequency of antenna is found to depend highly on the geometrical parameters. The changes in tissue parameters do not affect the resonant frequency. However, it changes the radiation efficiency of the proposed antenna. Thus, an extremely miniaturized antenna for data telemetry is designed and examined closely in the human knee for detuning.

Chapter 7

Implantable M-Segment

Quadratic Fractal Slot Antenna

7.1 Introduction

In the last chapter, an ultra-miniaturized antenna working at 2.4 GHz (ISM) band is developed. The parametric and robustness analysis showed that the parameters like resonant frequency and impedance matching critically depend on fabrication process variations and slight errors can make the antenna go out of the desired band of operation. Further, the gain of antenna is low due to the highly miniaturized design and deep implant inside the bone. Consequently, the power requirements for data telemetry as well as circuit powering may not be met by the proposed miniaturized antenna.

Due to the limited space available inside the cylindrical hole drilled in the bone, it is proposed to place an antenna on the bone surface which is almost perpendicular to the drilled hole. This provides more area and this is supposed

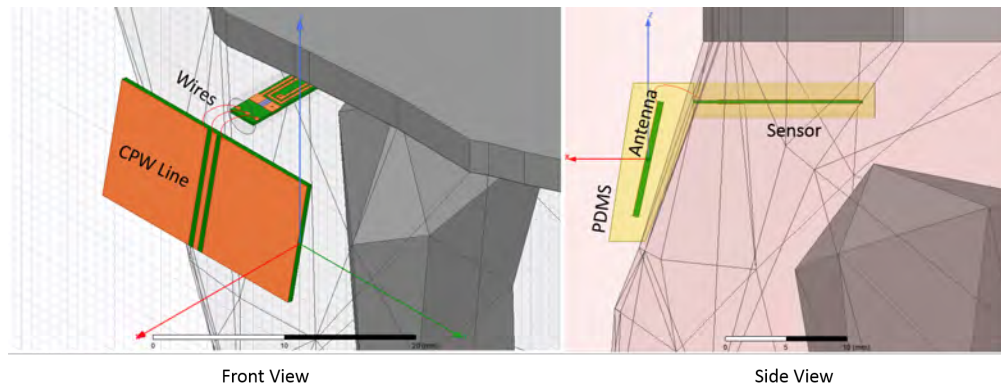


Figure 7.1: Placement of new antenna perpendicular to the sensor PCB showing wire bonds.

to increase the gain. The sensor and the antenna can be wire bonded and the whole assembly is encapsulated by the PDMS cover. This arrangement is shown in Fig. 7.1.

The antenna design should satisfy following criteria:

1. High gain - To support higher power transmission and long range for data telemetry.
2. Single layer simple design - To facilitate wire bonding between the sensor or transceiver chip and the antenna.
3. Stability of the response against the process and human body variations.

Highly miniaturized antennas suffer from low radiation efficiency and gain. Therefore availability of more space can increase the gain of the antenna. At the same time if the antenna design has a single layer, less energy is trapped inside the substrate and more is available for radiation. This should also increase the gain.

To ensure the ease of integration, a single layer CPW fed antenna is an ideal choice. A slot antenna can be easily fed by using a CPW line and it offers various design parameters like slot width, CPW line width and CPW gap for tuning and matching the antenna. Thus, a CPW fed slot antenna is chosen as a preferred starting point.

The PDMS cover shields the antenna from the tissue parameter changes. However, this means that the miniaturization offered by the high permittivity of the muscle tissue is also reduced. At 2.4 GHz, wavelength is 125 mm and a standard slot dipole will require 62.5 mm length. This large area is certainly not available for antenna placed on the surface of the bone as multiple sensors in the close vicinity may be required to be deployed. Therefore, a certain miniaturization is still required.

Also, since the sensor is not limited to be placed in the tibial region, but can be used in any joint like hip, ankle, shoulder or wrist, it may be required to tune the resonant frequency, matching condition as well as form factor. For example, the area available at wrist is considerably smaller than that available for hip. The higher area available in hip or shoulder region may be exploited to design an antenna with lower miniaturization but higher gain. Therefore, the aim of the research is to establish a detail and fairly accurate design procedure to miniaturize antenna without losing substantially on gain.

In [107, 142, 143], Asimina et. al. discussed the issue of miniaturization of an implantable antenna at length. They observed that dielectric materials with high permittivity and thin coating layers give better miniaturization. Apart from this, use of shorting pins [144] and patch stacking is also utilized for miniaturization. Other techniques include magnetic loading, metamaterial loading and the use of

lumped elements [145].

However, since the aim is to design a single layer antenna, neither the patch stacking nor the shorting pins are feasible. Metamaterial suffers from the problem of small bandwidth and metallic losses. In the literature, optimization algorithms are also utilized for antenna miniaturization. However, for implantable antenna design, since the problem domain is large due to the inclusion of human tissue material and its inhomogeneous nature, the time required for single simulation is of the order of few hours on a traditional high end computing resource. This severely limits the use of optimization algorithm even if only one goal of achieving desired resonant frequency is specified.

Another approach is to use the mathematical structures that systematically increase the current path. Using fractals is one such important tool in the hands of a microwave engineer. Fractals are the mathematical descriptions of fractured geometries which incorporate twists and bends according to some predefined rules and operations. One of the important properties of such curves is to have an infinite length curled up in a finite volume. This phenomenon is time and again exploited by the antenna and microwave community for miniaturization. While arbitrary bending and twisting may produce better compression in some cases, it is largely an optimization problem to be solved using simulation software, rather than a systematic approach that can be employed by the common antenna designer.

In the literature, several published papers have described the superior performance of the fractal antenna as compared to others [146–148]. They provide a definite and known miniaturization, better impedance matching over wide bandwidth. Especially in the case of implantable antennas, fractals can be useful as they can be readily designed with the given miniaturization factor, without the

need of trial and error or optimization approach both of which are quite time and resource consuming due to huge problem domain.

The electromagnetic properties of fractals are thoroughly discussed in [146, 149, 150] and it is well established that they are able to miniaturize the microwave components. When used for antennas, they provide frequency compression, multi resonant behaviour and the design approaches the small antenna limit. While the traditional fractals like Koch, Sierpinski, Minkowski and Hilbert were being investigated for their electromagnetic properties, some researchers randomized the geometry parameters of these fractal curves (like angles, lengths and line thickness) and then used the optimization algorithms like Particle Swarm optimization (PSO) and Genetic Algorithm (GA) to obtain the acceptable performance in various frequency bands like GPS and WiMax [151–153].

In all of the fractal geometries reported till date; it is the iteration number alone that decides the resonant frequency. Consequently, with the given initial length, the resonant frequencies and the form factors (length to width ratio) are fixed. Thus, the designer does not have any freedom or trade-off with the form factor and the frequency response of the device. Therefore, in the subsequent section a new fractal construct named *M-segment Quadratic Fractal* is introduced. With the proposed fractal curve, an antenna designer gets a flexibility of choosing between miniaturization achieved, resonant frequency and form factor.

7.2 M-Segment Quadratic Fractal Curve

A novel family of fractal curves is proposed which provides the designer a systematic way of miniaturizing the microwave components with the freedom of choosing

between form factor, design complexity and the achieved miniaturization. The proposed fractal curve is characterized by two integer values m and n . The m value determines the form factor of the fractal and its Hausdorff dimension while n value governs the iteration number. The equations governing the geometry of the fractals are also presented.

In the following sections, the modulus operandi to generate a new fractal geometry and the characteristic equations that describe the various parameters of the proposed curve are presented. It is followed by its application to the monopole antenna to characterize the resonance and so the miniaturization properties. The proposed fractal is then compared with the standard Von Koch curve to understand, quantify and compare its electromagnetic properties. The advantages of proposed fractal are also established. Then the results are discussed from the point of view of miniaturization and the expressions are developed to predict maximum miniaturization possible and the resonant frequency achieved with various iterations. The proposed fractals are also analysed by computing their lacunarity dimensions [154, 155]. This gives a comprehensive information about the proposed fractal geometry. This fractal is then used to design the implantable CPW fed fractal antenna.

7.2.1 Generation and Characterization of Fractals

Fig. 7.2 shows the geometry and the process of generation of different iterations of the proposed fractal curve. This fractal is generated and characterized by using two integer values $m \geq 2$ and $n \geq 0$ where m is the (seed) value corresponding to the number of segments a straight line of length 'L' will be divided whereas n cor-

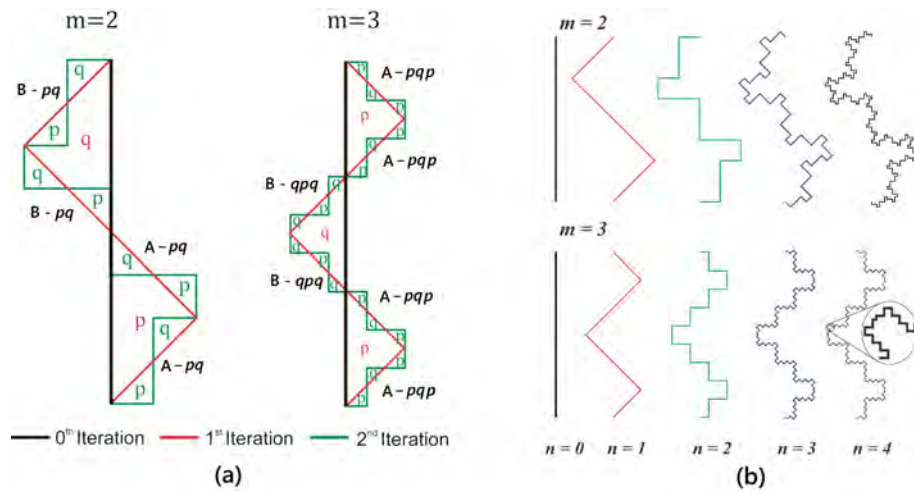


Figure 7.2: (a) Generating fractal iterations for even and odd value of m , using the operations ‘p’ and ‘q’. (b) First 4 fractal iteration stages for $m=2$ and $m=3$ family.

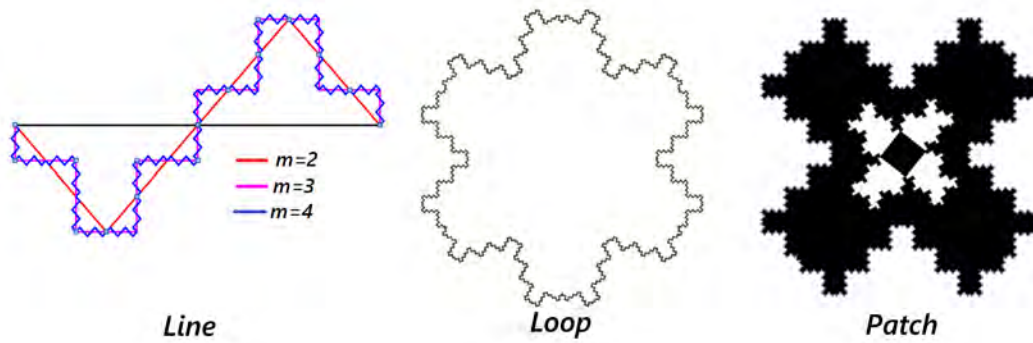


Figure 7.3: Example of different types of geometries possible with proposed fractal construct

responds to the iteration number. It can be noted that $n = 0$ always corresponds to a straight line irrespective of the value of m . The fractal can be generated by the use of 2 labels 'A' and 'B' and 2 operations 'p' and 'q'. The operations 'p' and 'q' are defined as follows:

p → Turn 45° clockwise, go forward till distance $L/(m\sqrt{2})$, then turn anticlockwise by 90° , go forward by distance $L/(m\sqrt{2})$.

q → Turn 45° anticlockwise, go forward till distance $L/(m\sqrt{2})$, then turn clockwise by 90° , go forward by distance $L/(m\sqrt{2})$.

If operation 'p' ('q') is performed on a line segment then every new line generated should be labelled 'A' ('B') respectively. Next iteration will be generated based upon this label. The straight line of 0^{th} iteration can be labelled 'A' or 'B' arbitrarily. It can be noted that each of these operations generate two line segments forming a right angle and hence the name quadratic fractal. In order to have a symmetry, the process of generating fractal for even and odd values of m , is slightly different. If m is an odd integer, then for a line segment having label 'A', the sequence of performing operations to obtain next iteration is $A \rightarrow (pqp\dots)_m$ while for a line segment having label 'B' the sequence of operations is $B \rightarrow (qpq\dots)_m$. If m is an even integer, irrespective of label, the operations have to be performed alternately, i.e. A or $B \rightarrow (pqpq\dots)_m$. In both the cases, the subscript m denotes the number of times of operations to be performed. For example for $m = 4$, the sequence of operation would be $A \rightarrow 'pqpq'$ while for $m = 5$, it would be $A \rightarrow 'pqpqp'$. This process of generating 1^{st} and 2^{nd} iteration from 0^{th} iteration (straight line) is shown in Fig. 7.2(a) for $m = 2$ and $m = 3$. The first five iterations from $n = 0$ to $n = 4$ for $m = 2$ and $m = 3$ are shown in Fig. 7.2(b).

It can be pointed out that, it is not necessary to use the same seed value m

for generating successive iterations. For example, as shown in Fig. 7.3(Line), $m = 2$, $m = 3$ and $m = 4$ are used to generate first, second and third iteration respectively. Thus, with the different permutations and combinations of m and n , one can get different linear geometries with the different form factors. The fractal can also be used to generate closed loops. Fig. 7.3 shows a loop generated by using $m = 3, n = 3$ fractal on the sides of a hexagon. Such closed structures can also be filled to create the patch resonators. In Fig. 7.3, the patch shows a outer square patch whose sides are modified by the $m = 3, n = 3$ curve. Inside this patch, another square modified by $m = 2, n = 3$ fractal is cut out as a slot. Inside this slot, a square patch which can be treated as scaled 0_{th} iteration, is introduced. These examples are provided to show the versatility of the proposed m -Segment Quadratic fractal curve. It is the imagination of designer that would limit the conception of novel and convoluted geometries possible with this fractal. All these geometries can be generated using computer by writing codes that implement the algorithm described above. In the present investigation, MATLAB is used for this purpose.

$$\text{Number of parts} = (2m)^n \quad (7.1)$$

$$\text{Length of each part} = L/(m\sqrt{2})^n \quad (7.2)$$

$$\therefore \text{Housdorff Dimension} = D = \frac{\log(2m)}{\log(m\sqrt{2})} \quad (7.3)$$

$$\text{Total Length of curve} = L(\sqrt{2})^n \quad (7.4)$$

The equations (7.1) to (7.4) characterize the proposed fractal geometry. Eq. (7.1) and (7.2) give the number and length of the line segments that would be generated for a given value of m and n from a single straight line. The number of line

segments grow with the n^{th} power of $2m$ while the length of each part reduces with the n^{th} power of $m\sqrt{2}$. Consequently, the Hausdorff dimension (Eq. (7.3)) changes with the value of m and hence the proposed structure is termed as a family of m segment fractal curves. Eq. (7.4) clearly shows that the total length of curve is independent of the seed value m . So, theoretically the resonance should occur at same wavelength irrespective of the m value. However, it is a well known fact that the perturbations smaller than the wavelength have lesser effect on an electromagnetic wave. As seen from the Eq. 7.2, higher the value of m , smaller is the length of segments. So even for the same iteration across the various values of m , the effectiveness of fractal curve would be different and so the structure is expected to resonate at different frequency. This is a remarkable property of the proposed construct. One can start with the same length and can get many different resonant values with the combinations of m and n .

A close inspection of the width of the proposed curve reveals that the width changes only with the odd number of iteration. The half width of the even iteration is same as that of its previous odd valued iteration. Since the structure is symmetrical in terms of width around the central axis (0th iteration line), calculating width for half of the structure (distance from tip to the center) suffices. The half width of the structure for odd value of n can be calculated by a series sum $\frac{L}{(2m)} + \frac{L}{(2m)^3} + \frac{L}{(2m)^5} + \dots + \frac{L}{(2m)^n}$. Using this expression, one can calculate the required form factor by doubling the half width. Usually, for all the practical applications in microwaves, considering the first two terms of the above series should be enough.

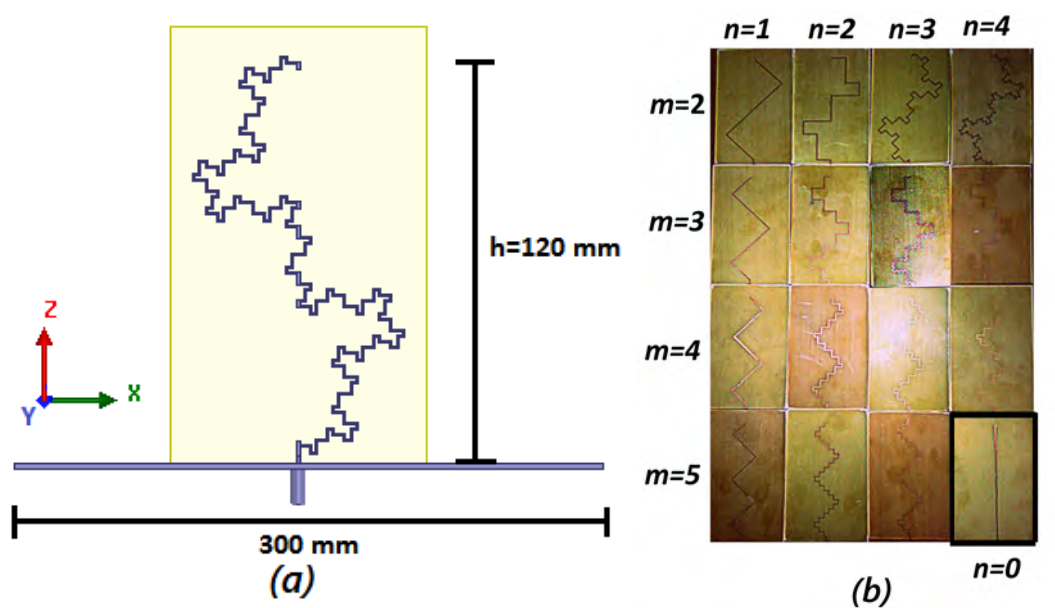


Figure 7.4: (a) Orientation of ($m=2,n=4$) antenna in Co-ordinate system. (b) Photograph of the fabricated fractal antennas.

7.2.2 Fractal Monopole Design

In order to evaluate the electromagnetic properties of the proposed fractal family, antennas with the values of $m = 2$ to 5 and $n = 1$ to 4 are designed and compared with the straight line monopole ($n = 0$). To generate the fractals for different values of m and n ; a MATLAB program is written according to the modulus operandi described above. The co-ordinates of the fractal so generated, are exported to HFSS to design a printed monopole antenna to perform full wave analysis. The fractal monopoles are designed on a metallic ground plane fed coaxially using an SMA connector. All the antennas are fabricated on commercially available FR-4 substrate with $\epsilon_r = 4.7$, $\tan\delta = 0.02$ and height 1.6 mm.

At this point, it is useful to evaluate the complexity of the fractals and effect of m and n from the fabrication point of view. For this purpose, we compare

two antennas, viz. $m = 4, n = 4$ and $m = 5, n = 3$. Using Eq. (7.1), the total number of parts are 4096 and 1000 respectively. From Eq. (7.2), the length of each part can be calculated as $L/1024$ and $L/353.55$. Thus, it can be seen that the antenna $m = 5, n = 3$ is easier to fabricate as the smallest length of part is more than that of $m = 4, n = 4$ antenna. Also, as the number of parts is smaller, so the time required for fabrication using standard milling machine setup is less for $m = 5, n = 3$ antenna. It can be noted that this parameter may not be an issue for photo etching fabrication process, as all the antennas will take same time. The antenna with $m = 5$ and $n = 4$ has the required line width of $15 \mu\text{m}$ with total number of parts = 10^4 , each having length $48 \mu\text{m}$. The available fabrication setup has the limitation of $100 \mu\text{m}$ dimension. So, $m = 5$ and $n = 4$ antenna is too complex and cannot be fabricated. The orientation of one of the antennas ($m = 2, n = 4$) in co-ordinate system is shown in Fig. 7.4 (a) . A photograph of all the fabricated antennas is shown in Fig. 7.4(b).

7.2.3 EM Analysis of The Fractal

The fabricated antennas are tested using Agilent N5242A Vector Network Analyser. The analysis of the proposed fractal is done by comparing the results of the proposed fractal with the standard Von Koch fractal reported in [149]. First, the measured results are discussed from their input impedance point of view. It is followed by the analysis of their resonant frequencies. An expression for determining resonant frequency from the geometry parameters m and n is developed. Finally, the proposed fractals are analysed in terms of their lacunarity dimension.

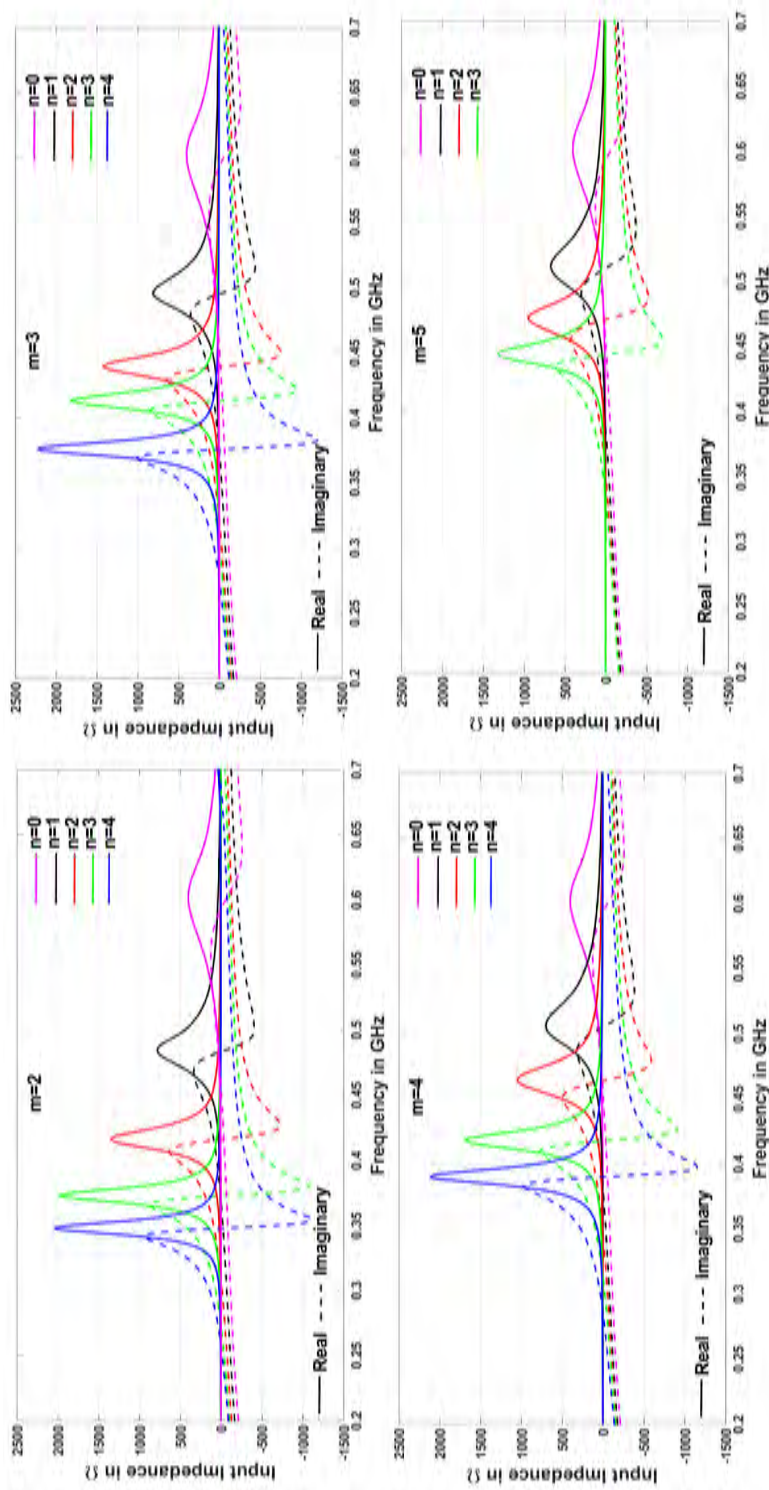


Figure 7.5: Measured Input impedance of the fabricated fractal antennas.

The measured input impedance of the antennas is plotted in Fig. 7.5. The figure is split into four graphs, each showing the comparison of members from a single family of the proposed curve. It can be seen that the 0^{th} iteration is same across all the families, from $m = 2$ to $m = 5$. This is obvious as it corresponds to a straight Euclidean line. The measurement of this 0^{th} iteration is used as reference in all the graphs. From the results, it can be noticed that the resonant frequency decreases with the increasing iteration number. Also, the real part of impedance increases with the increasing iteration number.

To further explore, analyse and quantify the proposed family of fractal curves, a comparison with the standard Koch curve is made. First five iterations ($n = 0$ to $n = 4$) of the Koch curve as reported in [149] are generated using MATLAB and exported to HFSS for full wave simulations. The starting length of the Euclidean line is taken same as that in our proposed curve (120 mm). The simulated input impedances of the various iterations of the Koch curve are plotted in Fig. 7.6 a. The similarity in the nature of the graphs of Fig. 7.5 and Fig. 7.6, shows that the proposed m -segment quadratic fractal shows the characteristic miniaturization behaviour of the fractal geometry.

For the quantitative analysis, the resonances of all the antennas are normalized with respect to the resonant frequency of the 0^{th} iteration. Fig. 7.6(b) shows the comparison of the measured normalized resonances for the different iterations of antennas ($n = 0$ to $n = 4$) of different families ($m = 2$ to $m = 5$) of proposed curve along with the Koch fractal. It can be seen that the families $m = 2$, $m = 3$ and $m = 4$ are better than Koch curve in terms of miniaturization. The response of Koch curve is in between that of $m = 4$ and $m = 5$ family. For the Koch curve, the total width can be calculated as 34.6 mm. For $m = 4$ family, the total width

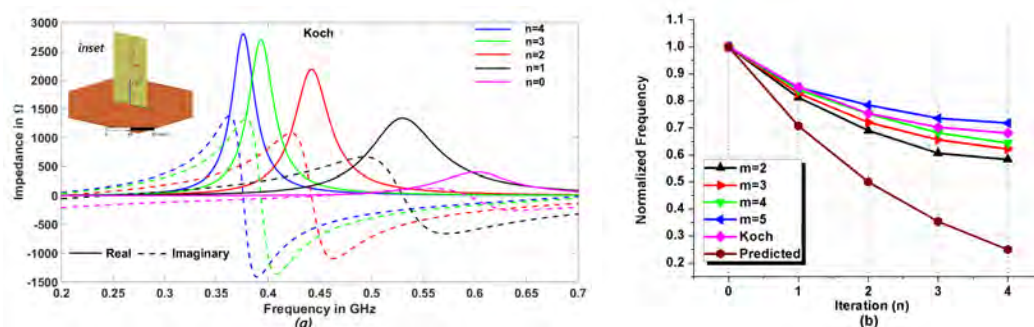


Figure 7.6: (a) Simulated input impedance of the first five iterations of the Koch fractal curve (inset: Orientation of Koch fractal antenna in HFSS). (b) Comparison of the measured normalized resonances for the different iterations of antennas ($n = 0$ to $n = 4$) of different families ($m = 2$ to $m = 5$) of proposed curve, with iterations of Koch fractal curve.

is nearly 30 mm while it is 24 mm for $m = 5$ family. Taking the average of two widths (i.e. 27 mm), there is a reduction of almost 22% in terms of width, by the use of proposed curve as opposed to Koch fractal. Thus, we can conclude that for similar resonance response, the proposed fractal saves about 22% of space than the Koch curve.

Next, it can be noted that as the value of m increases, the rate of decrease in resonant frequency with iteration number is reduced. Thus, even though the same iteration (i.e. same value of n) from different families of curves have same geometrical length, their resonant frequencies are different. As m increases, the resonant frequency for same value of n also increases. This behaviour proves that the smaller length of segments have smaller effect on miniaturization, irrespective of the total geometrical length. Also, in Fig. 7.6(b), the resonance predicted by equating geometrical length to electrical length ($\lambda_{eff}/4$) for the proposed geom-

entry is plotted. It also shows that, although the use of fractal geometry increases the geometrical length of the curve, it does not increase the electrical length of corresponding antenna at the same rate. From this plot of normalized resonances, it can be seen that electromagnetic miniaturizing ability of the fractal decreases with increasing fractal iteration. Such an exponential behaviour of the resonant frequencies can be captured by fitting the normalized experimental data in equation of the form

$$\frac{f_n}{f_0} = ae^{-bn} + c \quad (7.5)$$

where f_0 is the resonant frequency of 0^{th} iteration, n is the iteration number, f_n is the resonant frequency of n^{th} iteration and a and b are the coefficients of curve fit. Now as n goes to ∞ , we get the lowest possible resonant frequency or saturation frequency, i.e 'c' in above equation represents the saturation frequency and indicates maximum miniaturization possible for a given m^{th} member of the fractal family. For $n = 0$, $f_n/f_0 = 1$, which implies $c = 1 - a$.

With this understanding, the curve fitting is done using MATLAB. The corresponding expressions are given by Eq. 7.6. The fitness of the curve is usually evaluated using degree of freedom adjusted R^2 . It is the ratio of sum of square of regression and total sum of squares adjusted for degree of freedom. This parameter measures the correlation between the response values and predicted response values. The minimum adjusted R^2 for the proposed curve fit is 0.9983. It means the equation explains the 99.83% of the data. The maximum RMS error is 0.0078 for $m=2$ with maximum error of 0.01 at $m = 2$, $n = 3$. Thus the curve fit is excellent

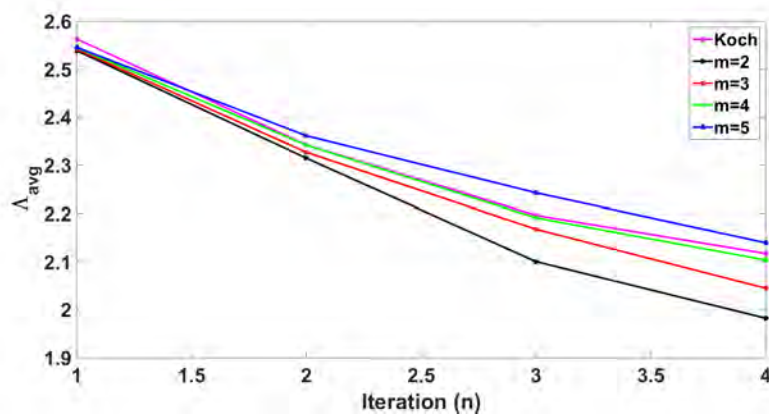


Figure 7.7: Average lacunarity as a function of the iteration number.

and the expressions closely represent the resonant frequencies of the antennas.

$$\frac{f_n}{f_0} = \begin{cases} 0.5289e^{-0.4681n} + 0.4711, & m=2 \\ 0.4854e^{-0.4519n} + 0.5146, & m=3 \\ 0.3998e^{-0.5135n} + 0.6002, & m=4 \\ 0.3194e^{-0.6207n} + 0.6806, & m=5 \end{cases} \quad (7.6)$$

These equations can be further condensed and generalized by expressing the coefficients in terms of m as given in Eq. 7.7. Substituting Eq. 7.7 into 7.5, one can predict the resonant frequency for any value of m and n . It should also be noted that the equation is valid for $m \geq 2$. Also as $m = (0, 1)$ would mean dividing a line in 0 or 1 parts, it doesn't make sense to input $m=0$ or 1 in the proposed expression.

$$a = -0.06841m + 0.6653; b = 0.04854m + 0.3522; c = 0.06841m + 0.3347 \quad (7.7)$$

Further, the average lacunarity dimension for all the fractal antennas Λ_{avg} is calculated by the methodology proposed in [154]. The process starts with a

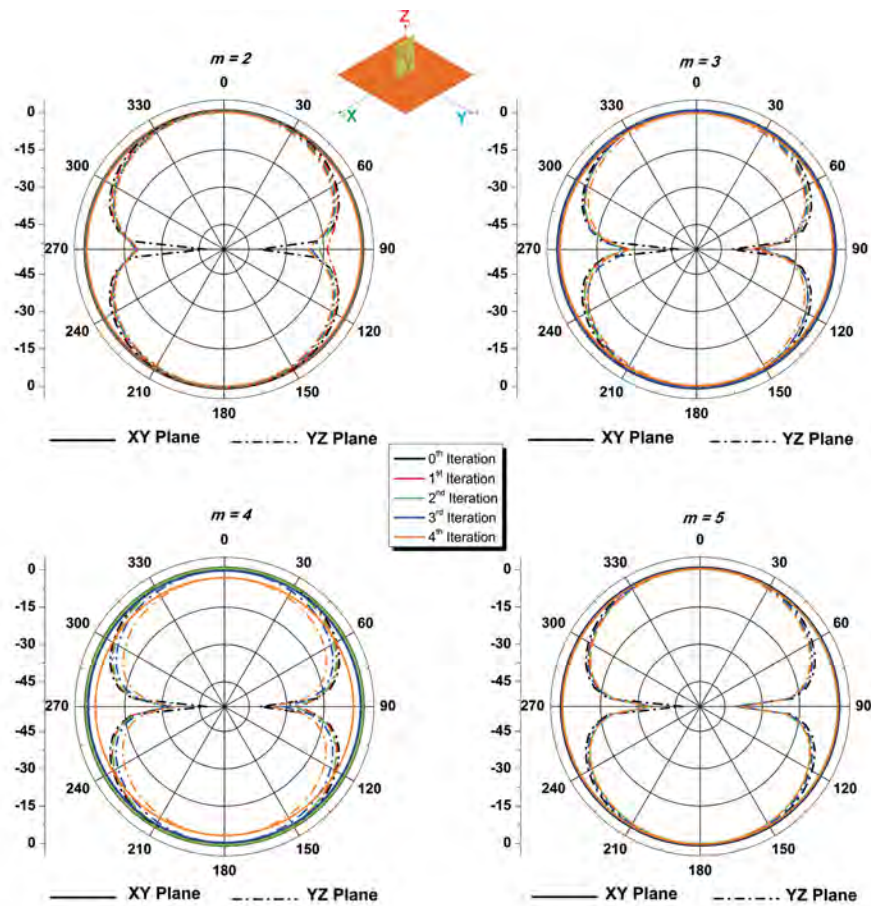


Figure 7.8: Radiation patterns of the four families ($m = 2$ to $m = 5$) of proposed fractal curves.

generation of 2D underlying matrix (all 1's) of size 2392×1417 for all the antennas except ($m = 4, n = 4$) and ($m = 5, n = 4$). For these two antennas, 3780×6378 matrix is used. The higher number ensures that the smallest feature of the antenna is atleast one pixel wide. The elements corresponding to the fractal geometry are then made zero. This is the digitization of the fractal antennas in a logical array. Then gliding box algorithm is used to calculate the lacunarity of each geometry, including Von Koch fractal. To obviate the effect of the box size, the box size

weighted average is calculated as suggested in [154, 155] and plotted in Fig. 7.7. Lacunarity gives information about the non-uniformity in the image. Higher the average lacunarity Λ_{avg} , more is the non-uniformity. This leads to higher resonant frequency as explained in [154].

From Fig. 7.7, $m = 2$ and $m = 3$ family has lower Λ_{avg} than the Koch curve. Lacunarity dimension of $m = 4$ family matches quite closely with the Koch curve, while that of $m = 5$ exceeds it. This behaviour also matches directly with the resonance characteristics explored above. A close observation of Fig. 7.7 shows that the even ($m = 2$ and $m = 4$) and the odd family ($m = 3$ and $m = 5$) family of fractals have different curve slopes. The slope of the odd family curve is almost linear while it decreases slowly for the even family. This can be explained by looking into the geometry of $m = 2$ and $m = 3$ family as shown in Fig. 7.2. Comparing iteration 2 of $m = 2$ and $m = 3$, it can be seen that the geometry maintains better uniformity for $m = 3$, whereas L-type sections are created for $m = 2$. This non-uniformity in even family leads to the increase in the lacunarity dimension which is cumulatively added with the increasing iteration number. Hence, the slope of Λ_{avg} decreases for even values of m , but stays the same for the odd values.

The radiation patterns for the different values of m , at their respective resonant frequencies, are plotted in Fig. 7.8. It can be clearly seen that there is virtually no degradation of radiation pattern as the fractal iteration progresses. It is omnidirectional in the XY plane and bidirectional in the YZ plane. The symmetry of the fractals around the initial generator (straight line monopole) ensures that the radiation pattern is not distorted. This is also a remarkable property of this fractal. Along with providing an extra degree of freedom in terms of form factor and resonant frequency, the proposed construct also maintain its symmetry which

leads to such good and clean radiation patterns.

From Fig. 7.8, it can be seen that the gain slightly decreases with the increasing iteration number. This may be because of the decreasing radiation efficiency iteration number increases. The nulls along the z direction are not so sharp for the lower values of m and n . The nulls start to become prominent as either iteration number n or seed value m increases. This is because, as the seed value m increases, the width of antenna decreases and it tends to be more like a linear monopole. Also, as the iteration number n increases, the resonant frequency of the antenna decreases. In other words, the antenna becomes electrically small and the radiation pattern approaches to that of a linear monopole. Thus, from radiation point of view, if deep nulls are required along the direction of antenna, higher values of m and n are suitable at the cost of increased complexity, whereas smaller values of m and n give more omnidirectional coverage, although radiation is still about 17 dB less than that at the broadside direction.

7.3 Design of the Implantable CPW fed M-Segment Quadratic Fractal Slot Antenna

Since a single layer design is required, CPW feeding mechanism is chosen. A slot dipole antenna can be easily fed using a CPW line. This choice offers atleast four parameters, viz. width of CPW line, CPW gap, length of CPW line and the width of the slot, for tuning the impedance matching of the antenna. Slot dipole is a dual of an electric dipole and has been extensively covered in the classic antenna theory textbooks [156]. Next section presents an empirical method of designing a

slot antenna on the dielectric substrate. Finally, the dimensions of the implantable fractal slot antenna are calculated using the effective permittivity calculations and the resonant frequency calculations of the fractal using Eq. 7.6.

7.3.1 Calculation of the Effective Permittivity for Slot Antenna

A dipole radiates efficiently at half wavelength. The length of such a dipole is given by $l = \lambda/2$. Since the practical antennas most of the time work at slightly smaller electrical length, the above expression can be modified as $l = \lambda/2.1$. The value is 2.1 is obtained by running a CST MWS simulation of an arbitrary length of the dipole and linewidth of 0.2 mm in air and observing its resonant frequency. For an antenna printed on a dielectric substrate the guided wavelength is determined by expression $\lambda_g = \lambda_0/\sqrt{\epsilon_{reff}}$. The length of the slot dipole printed on dielectric substrate in terms of frequency is therefore given by Eq. 7.8

$$L = \frac{c}{2.1f\sqrt{\epsilon_{reff}}} \quad (7.8)$$

In the literature, the effective permittivity for such an antenna is given by equation 7.9 [157, 158].

$$\epsilon_{reff} = (\epsilon_r + 1)/2 \quad (7.9)$$

This expression assumes that one half space of the antenna is covered by dielectric and other half is air. However, this is an inaccurate approximation. One half space of the antenna is filled with air. However, on the other side, there is a combination of thin dielectric substrate and air. This is shown in Fig. 7.9. Consequently, if the traditional value of ϵ_{reff} is used, one obtains higher value of effective permittivity.

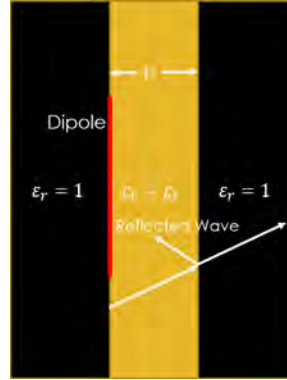


Figure 7.9: Dipole printed on a thin dielectric substrate.

Consequently, the antenna designed using above expression resonates at higher frequency and the error is as high as 20% [159].

The slotline on dielectric substrate is first analyzed by Cohn in 1969 [160]. Later, Janaswami et al have analyzed the characteristic impedance of a wide slot line on low permittivity substrate [161]. Based on their work, an iterative formula for the prediction of notch frequency of slot loaded printed UWB antenna was developed in [159]. This technique being based on the results by Janaswami, is limited to the low permittivity substrates. An alternative non iterative formulation/model for predicting the resonant frequency of the thin slots is developed in this section.

The model can be formulated by observing that, as the E-fields extend in air beyond the substrate, the effective dielectric constant should be lower than that predicted by Eq. 7.9. Therefore, the effective dielectric constant can be written as Eq. 7.10.

$$\epsilon_{reff} = \frac{\epsilon_r + 1}{2} - f(h) \quad (7.10)$$

where $f(h)$ is a term which is a function of the substrate height h . The expression

for $f(h)$ should be such that it gives correct result for ϵ_{reff} at the extreme values of height h . For $h = 0$, the expression should reduce to $\epsilon_{reff} = 1$ and for $h = \infty$, the expression should be $\epsilon_{reff} = (\epsilon_r + 1)/2$. This can be accomplished if $f(h)$ is defined as

$$f(h) = \frac{\epsilon_r - 1}{2} a^{-hb} \quad (7.11)$$

Furthermore, since the waves are reflected back from the boundary of air and dielectric substrate, the effective dielectric constant should increase. This can be handled by adding a term $(\sqrt{\epsilon_r} - 1)/(\sqrt{\epsilon_r} + 1)$. It should be noted that for the trivial values $h = 0$ or $h = \infty$ the term $(\sqrt{\epsilon_r} - 1)/(\sqrt{\epsilon_r} + 1)$ cannot be used as there is no dielectric air interface. Therefore the expression for the effective permittivity can be written as Eq. 7.12.

$$\epsilon_{reff} = \frac{\epsilon_r + 1}{2} - \frac{\epsilon_r - 1}{2} a^{-hb} + \frac{\sqrt{\epsilon_r} - 1}{\sqrt{\epsilon_r} + 1} \quad (7.12)$$

In this equation, a and b are the coefficients of curve fit. To determine their values, a slot dipole printed on a dielectric substrate is simulated. The length of the slot dipole is selected such that it resonates at 1 GHz in free space. The permittivity of substrate and its height are varied parametrically and the resonant frequencies are noted. The permittivity value are chosen as 2.2, 3.2, 4.4, 6, 7.2, 7.8, 9.6 and 10.2 whereas height is varied from 0.1 mm to 1 mm in steps of 0.1 mm and then from 1.25 mm to 10 mm in steps of 0.25 mm.

The effective permittivity can be calculated from the simulated resonant frequencies (f_{res}) using expression $\epsilon_{reff} = (1/f_{res})^2$. The value 1 in the numerator of this expression is a result of using a dipole of the length corresponding to the 1 GHz resonant frequency in free space. Since the parametric analysis is done for two parameters, ϵ_r and h , the 2D surface curve fit is done using curve fit toolbox

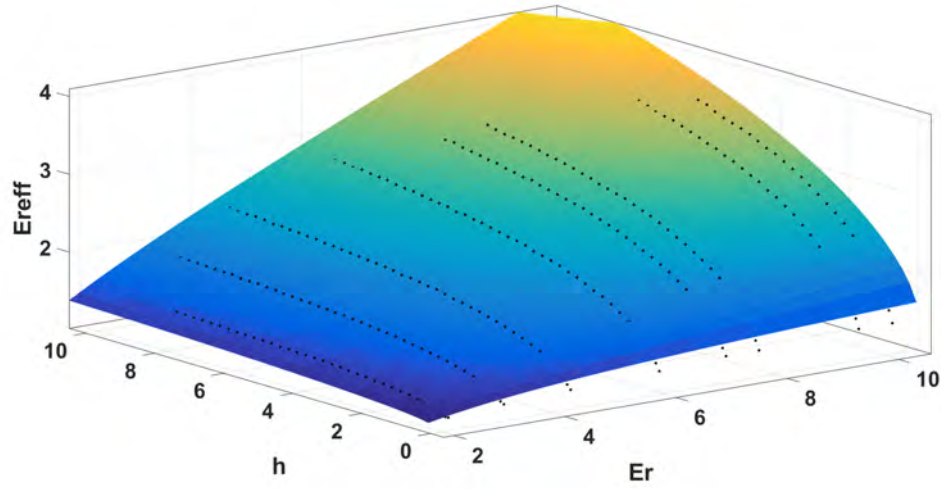


Figure 7.10: Effective Permittivity as a function of dielectric permittivity and height.

from MATLAB. The result is shown in Fig. 7.10. The calculated surface fits well with the data points with the adjusted R^2 of 0.987.

The coefficients of the curve fit are evaluated as $a = 2.217$ and $b = 0.68$. Therefore the final expression for the effective permittivity ¹ can be given as

$$\epsilon_{reff} = \frac{\epsilon_r + 1}{2} - \frac{\epsilon_r - 1}{2} 2.217^{(-h^{0.68})} + \frac{\sqrt{\epsilon_r} - 1}{\sqrt{\epsilon_r} + 1} \quad (7.13)$$

¹It should be noted that this effective permittivity should not be used for calculating Z of the slot antenna. It is an empirical result only valid for calculating the resonant frequency. Since current flows on the metallic surface, μ_{eff} should also be calculated, however, the entire effect is transferred to ϵ_{eff} . Hence any attempt to calculate the impedance using only the ϵ_{eff} will produce erroneous results.

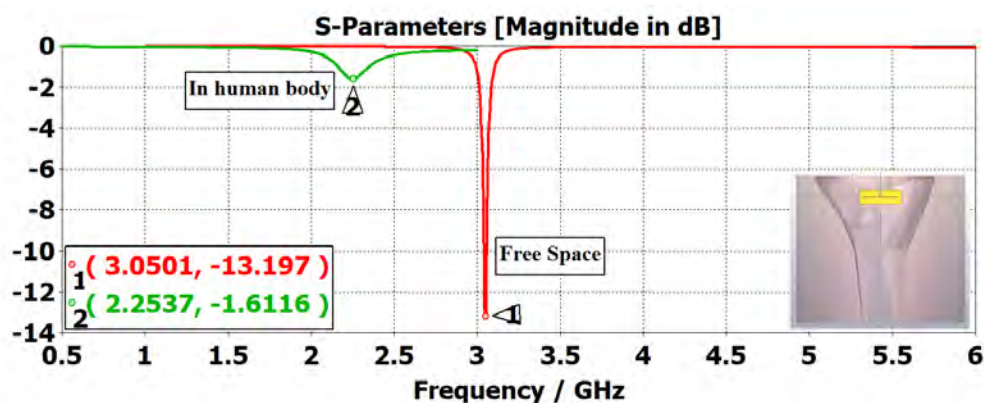


Figure 7.11: Resonant frequency shift for a slot antenna implanted inside human knee.

7.3.2 Design of the Slot Antenna

A slot antenna of length 25 mm is arbitrarily designed on Rogers 6010 substrate of $\epsilon_r = 10.2$ and height 0.508 mm. It is first simulated in free space followed by simulation in human body with PDMS encapsulation from all sides with thickness of 1 mm. The resonant frequency shifts from 3.05 GHz to 2.255 GHz. Therefore the ratio of miniaturization is given by Eq. 7.14. Fig. 7.11 shows the results with slot in body model in the inset.

$$\frac{f_b}{f_f} = 0.75 \quad (7.14)$$

All the techniques described in the sections above are now combined together to design the CPW fed M-segment quadratic fractal antenna implanted in the knee region of the human body. The antenna is expected to work at 2.4 GHz ISM band. Since the high dielectric substrates are preferable, Rogers 6010 laminate is used having thickness 0.254 mm. The design methodology is now described in detail.

1. Using Eq. 7.6, f_n is set at the desired frequency and f_0 is calculated. This

is the frequency corresponding to the straight slot dipole.

2. Since this should be the resonant frequency of the straight slot inside the body, the resonant frequency in free space f_f is calculated using Eq. 7.14.
3. From this frequency, the length of the antenna is calculated using Eq. 7.8 and Eq. 7.13. This length serves as zeroth iteration of the fractal design. Then using the MATLAB code, the required fractal is designed and exported to the numerical simulator for verification and tuning followed by the fabrication and experimental validation.

Since very high miniaturization is not targeted and the available space for implantable antenna is still small, it is decided to use the fractal with $m = 2$ and $n = 2$ to work at 2.4 GHz inside the body. Using the method described above, first f_2/f_0 is found to be 0.6785. Therefore, for $f_2 = 2.4$ GHz, f_0 is 3.537 GHz. Then using Eq. 7.14, $f_f = 4.72$ GHz is calculated. Finally, the length of the slot is calculated as 18.2 mm using the new expression for effective permittivity given by Eq. 7.13. The design was simulated using the frequency domain solver of CST Microwave Studio 2017. Fig. 7.12 shows the response of the designed antenna. It should be noted that using the old equation for effective permittivity, the calculated length would be 12.8 mm and the design method would fail.

This design resonates at 2.395 GHz which is very close to the design frequency but it is not impedance matched. For this purpose, the impedance of the antenna is observed Fig. 7.12b . Since the real part of the impedance is small, the CPW line required for matching would be prohibitively wide. To solve this issue, the current distribution on the antenna, plotted in Fig. 7.13 is observed.

It can be seen that the current at the end of the CPW line is minimum. This

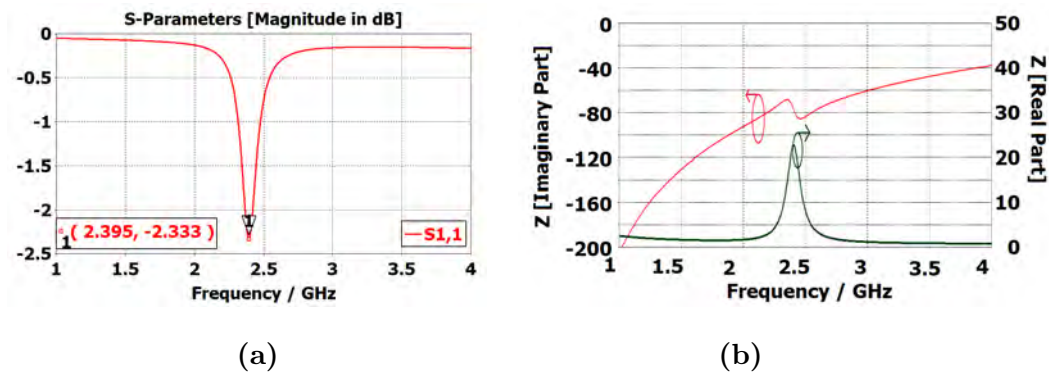


Figure 7.12: Response of the $m=2$, $n=2$ antenna designed for initial length of 18.2 mm.

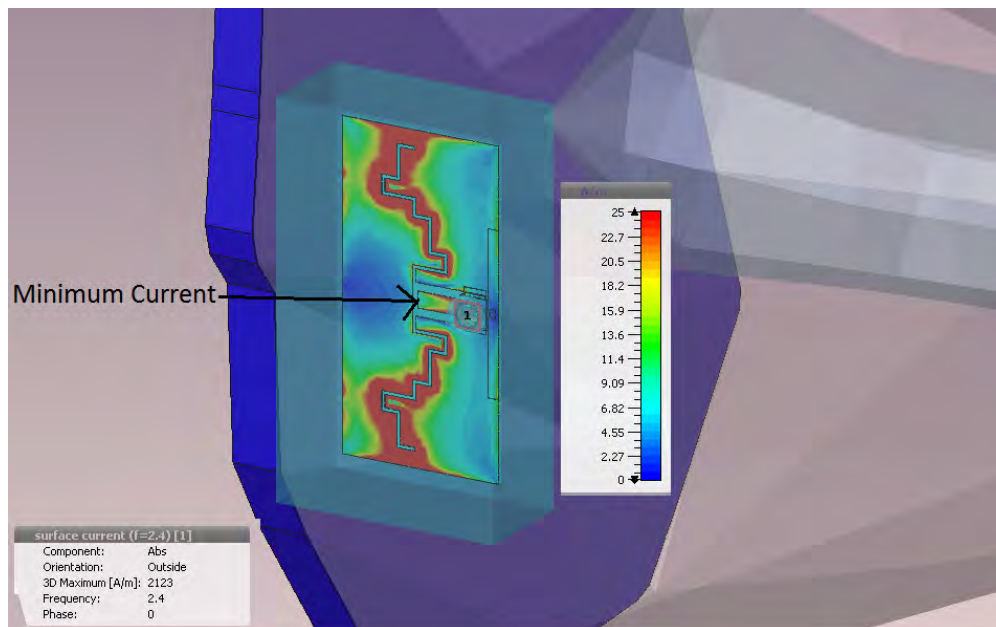


Figure 7.13: Current distribution on designed fractal antenna.

offers a high impedance to the slot antenna. In other words, the current does not flows efficiently around the slot. Therefore, to obtain impedance matching, the CPW line is extended beyond the slot. The effect of such variation on reflection coefficient is shown in the Fig. 7.15. The current distribution on the antenna with

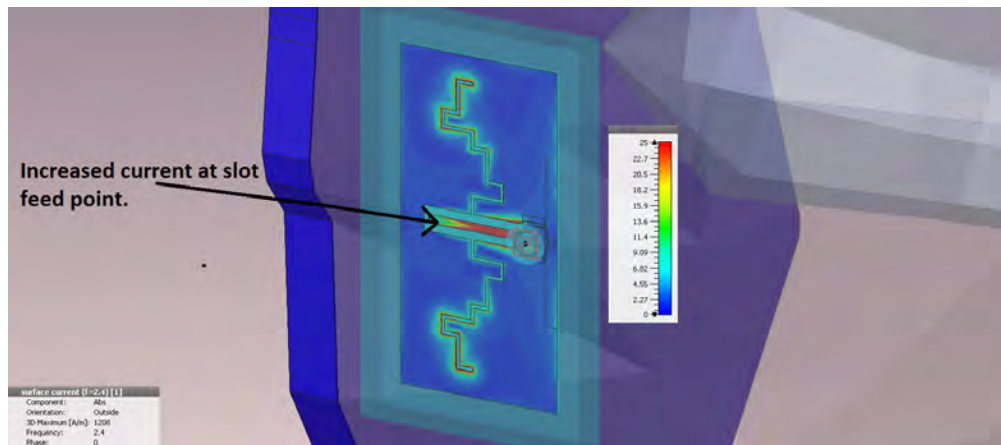


Figure 7.14: Effect of extending the CPW line beyond slot dipole on current distribution.

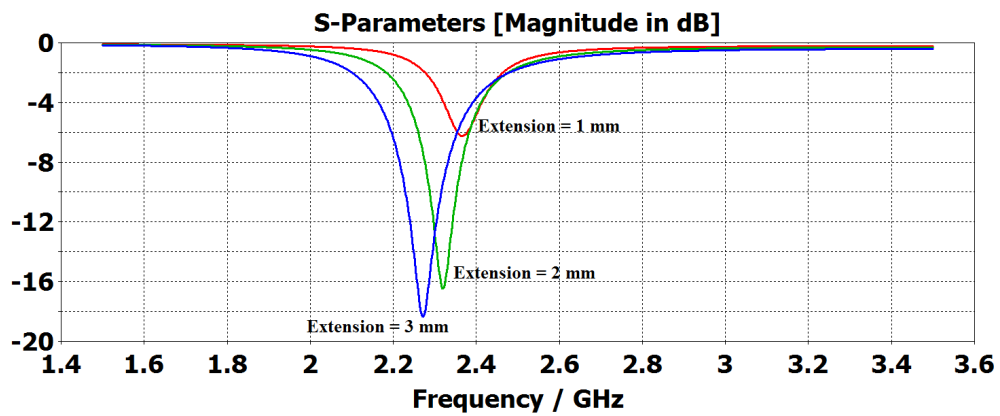


Figure 7.15: Effect of extending the CPW line beyond slot dipole on reflection coefficient.

extended CPW line is shown in Fig. 7.14. It can be seen that there is increased current at the slot feed location.

From Fig. 7.15 and 7.14, it can be seen that the impedance matching can be easily obtained by employing feed extension method. However, since this introduces longer current path, the antenna resonance shifts to a lower value of 2.27

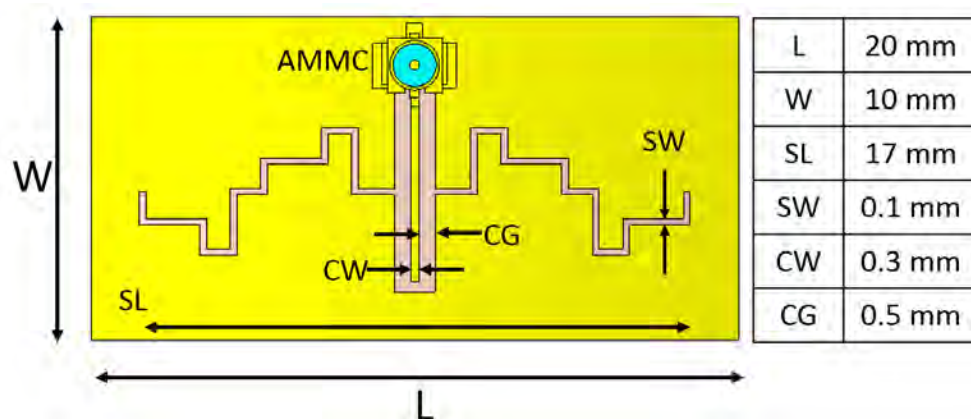


Figure 7.16: Final design of the fractal antenna with dimensions.

GHz. in order to retune it to 2.4 GHz, the fractal is regenerated by considering the zeroth iteration of length 17 mm. The final antenna design is shown in Fig. 7.16. The dimensions are given in the table alongside. The simulated frequency response is plotted in Fig. 7.17. It can be seen that the antenna is matched with resonance at 2.43 GHz and -10 dB bandwidth is 100 MHz from 2.39 GHz to 2.49 GHz.

7.4 Experimental Setup and Results

The antenna is fabricated by standard PCB process at Lintek Pty. Ltd. Since the antenna is very small, the standard SMA connector cannot be used. Therefore, a 50 Ω Micro Miniaturized Connector from Amphenol (AMMC) is soldered to the antenna using SMT soldering. One end of a female to female AMMC coaxial cable is snap connected to the soldered AMMC jack connector. A male to male AMMC to SMA adapter from amphenol is used to connect the AMMC cable to the SMA coaxial cable of the VNA. A PDMS sheet is made by mixing 10 part of PDMS from Sigma-Aldrich and 1 Part of Sylgard curing agent from Dow Corning and curing it

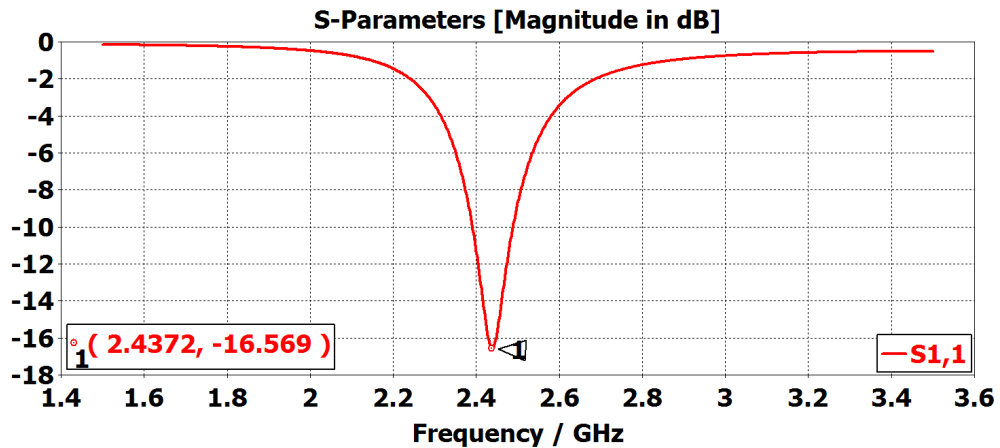


Figure 7.17: Frequency response of impedance matched antenna.

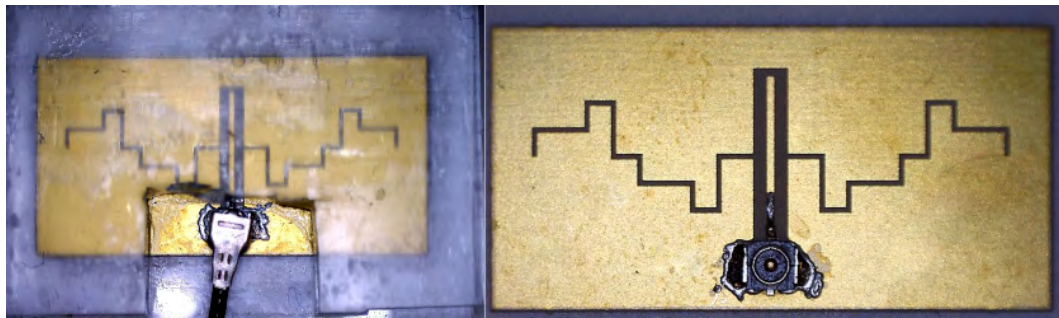


Figure 7.18: Fabricated Single band fractal antenna with and without PDMS.

in the oven at 65° C for 2 hours. The antenna is glued to the base sheet by using a few drops of Loctite superglue. A rectangular slot is cut from another sheet to accommodate the AMMC coaxial cable. It is then glued to the antenna from top. The photograph of the fabricated antenna with and without PDMS cover, taken using a MicroPro digital microscope is shown in the Fig. 7.18.

The experimental validation of the the antenna is done using a femur bone from cow. The cow bone with the antenna connected to the Agilent PNA-X 5242a is shown in Fig. 7.19. The Antenna is then covered with the muscle tissue as shown

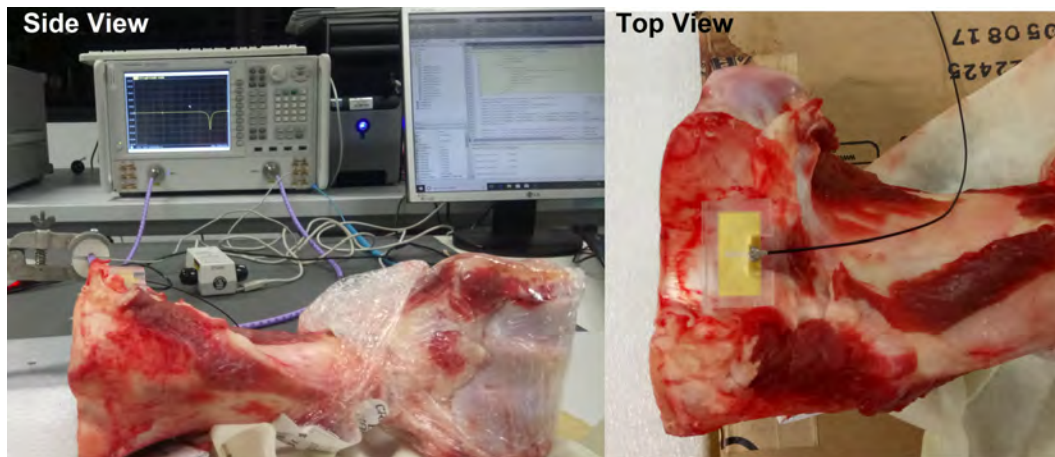


Figure 7.19: Antenna connected with the VNA, top and side view.



Figure 7.20: Antenna covered with the muscle tissue.

in Fig. 7.20. The measured S parameter from VNA is also shown. The simulated and measured results are compared in Fig. 7.21. It can be seen that the resonant frequency shifts slightly to the lower value of 2.37 GHz than the simulated case of 2.43 GHz. This may be due to the effect of the rectangular hole cut in the top layer for accommodating the AMMC cable due to which high permittivity muscle came in close contact with the antenna lowering the resonant frequency. The measured -10 bandwidth of the antenna is 85 MHz from 2.33 GHz to 2.415 GHz which is close to the simulated 100 MHz bandwidth.

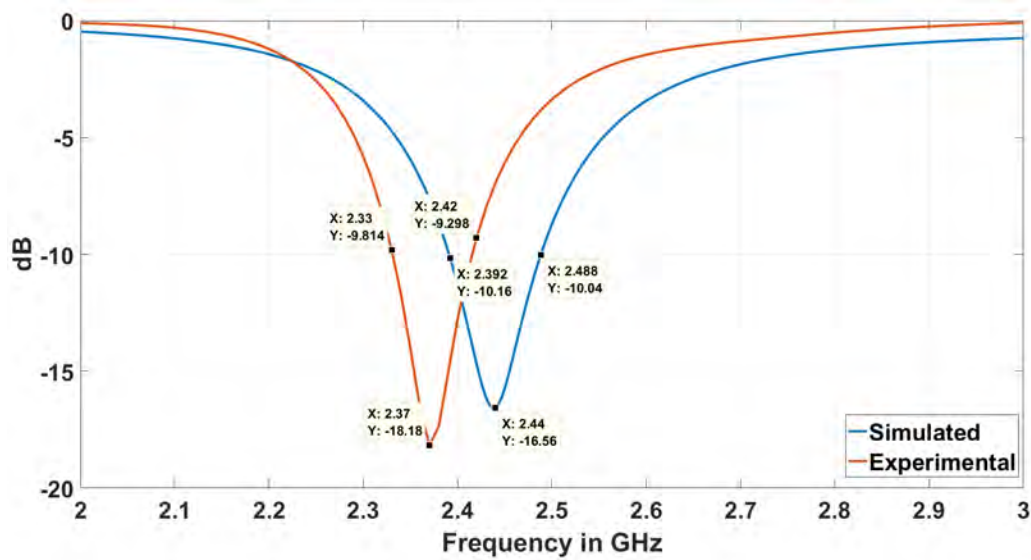


Figure 7.21: Comparison of the frequency response of the simulated and measured antenna.

7.5 Parametric Analysis

The parametric analysis of the proposed antenna is performed to get an insight on impedance matching, frequency (de)tuning and the effect of changing the tissue properties.

7.5.1 Effect of Slot and CPW Line Parameters

Impedance matching and resonance are affected by changing the width and gap of the CPW line as well as the width of the slotline. Due to the fractal geometry, if the width of the slot is made too wide, the subsequent section may get merged. In the following sections, the effect of slot width, width of CPW line and gap width on antenna parameters like reflection coefficient, resonant frequency and bandwidth is discussed.

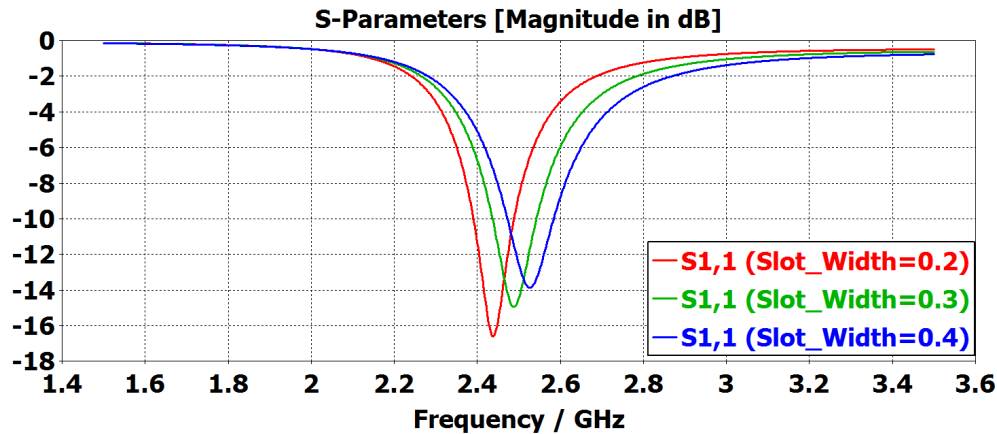


Figure 7.22: Effect of changing the width of the slot on the impedance matching and the resonant frequency of the antenna.

Effect of Slot Width

As the slot width increases from 0.2 mm to 0.4 mm, the impedance matching decreases slightly from -16 dB to -14 dB while resonance frequency shift to higher value from 2.44 GHz to 2.52 GHz. The -10 dB bandwidth of 100 MHz remains almost constant. Thus, the slot width parameter can be used to fine tune the resonant frequency. The results are shown in Fig. 7.22.

Effect of width of CPW line

The width of the CPW controls the impedance matching. The effect of changing the width of the central conductor of the CPW line from 0.25 mm to 1 mm is shown in the Fig. 7.23. The gap between the line and ground is kept constant at 0.5 mm. The change in resonant frequency is less than 10 MHz and the antenna operation stays within the ISM band. However, the best impedance matching is observed for 0.5 mm of width of the CPW line.

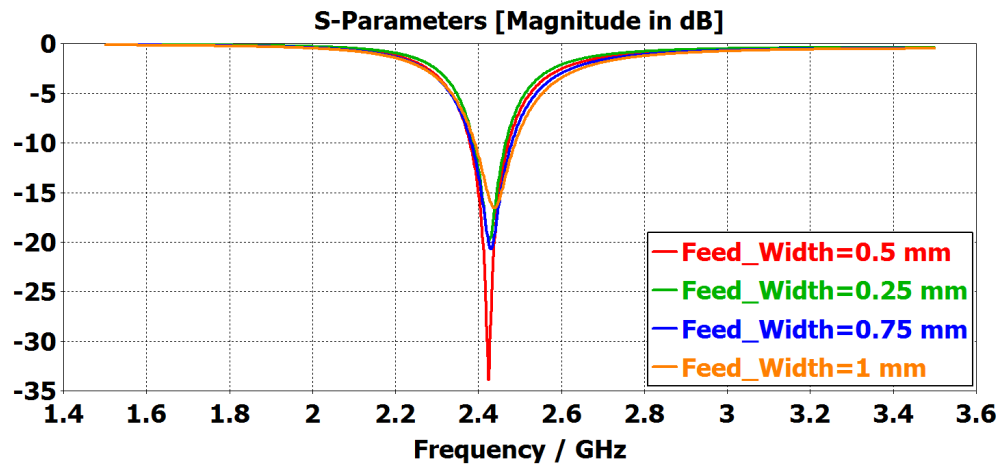


Figure 7.23: Effect of changing the width of the CPW line on the reflection coefficient of the slot fractal antenna.

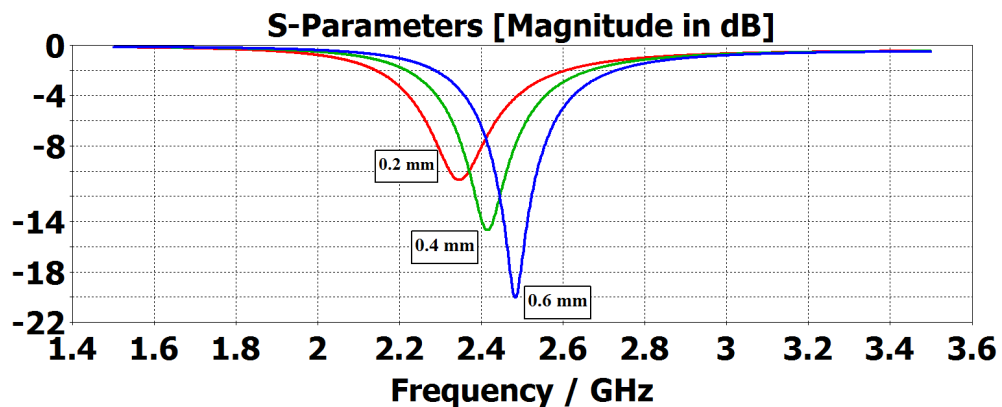


Figure 7.24: Effect of changing the gap between the CPW line and ground on the impedance matching and the resonant frequency of the slot fractal antenna.

Effect of Gap between CPW Line and Ground

Another parameter that controls the impedance of the CPW line is the gap between the CPW line and the ground. Therefore, the gap is changed from 0.2 mm to 0.6 mm in steps of 0.2 mm keeping the line width constant at 1 mm. The results are

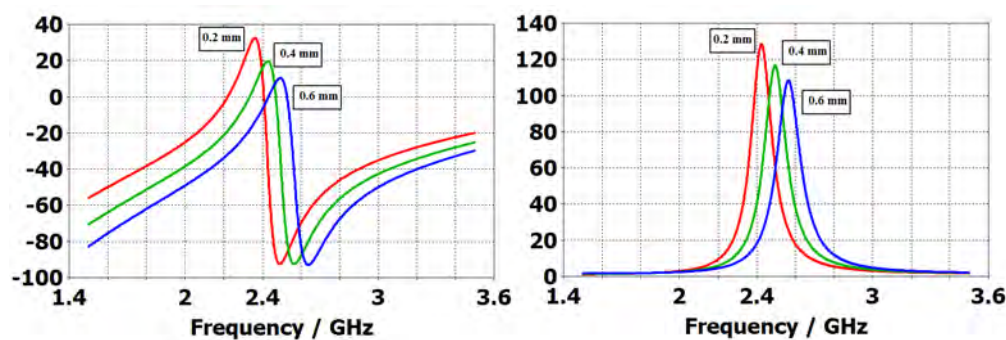


Figure 7.25: Effect of changing the Gap between the CPW line and ground on the impedance of the slot fractal antenna.

plotted in Fig. 7.24 It can be seen that gap controls the impedance matching as well as the resonant frequency. The resonance changes from 2.34 GHz to 2.48 GHz with the increasing gap. This change of 140 MHz is more than the -10 dB bandwidth of 100 MHz of the fractal slot antenna. The peak resistance changes from 128Ω to 108Ω while the peak reactance changes from 32.5Ω to 10Ω (Fig. 7.25). Clearly the gap heavily influences the reactive component of the impedance.

From this parametric analysis of the antenna geometric parameters, it can be recommended that gap of CPW line can be first used to tune the impedance such that it is around -10 dB. Then the slot width can be used to tune the resonant frequency to exact design frequency. Finally, the width of CPW line can be used for good antenna matching upto -20 dB or -30 dB level.

7.5.2 Effect of Biocompatible PDMS Coating

In [162], the effect of the coating cover on the hertzian dipole is treated analytically using Green's function. As an example, it is demonstrated that for a thin substrate (like $h = 0.1\lambda_g$), there is an optimum thickness of coating that maximizes the

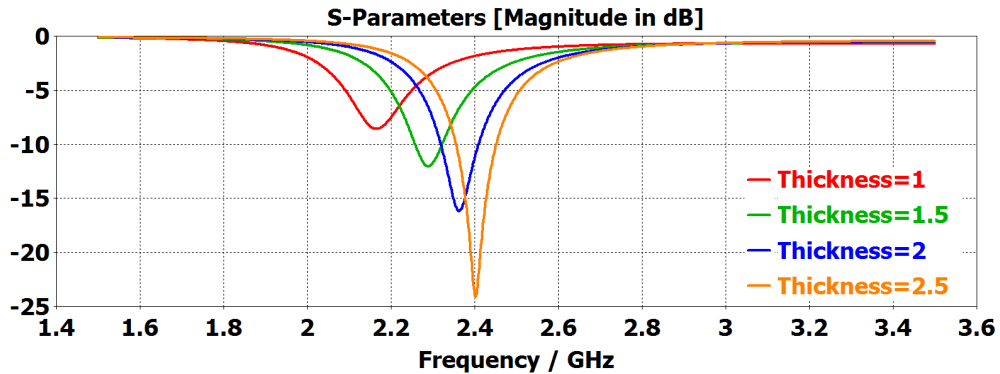


Figure 7.26: Effect of changing the thickness of the coating on the impedance matching and resonant frequency of the fractal slot antenna.

radiation efficiency. This value is a function of both the substrate thickness and the relative permittivity and permeability of the two materials. In [163], the parametric analysis of the permittivity of the biocompatible coating on a PIFA like antenna was performed. It showed that as the permittivity of coating increases, the resonant frequency decreases, which is expected. However, no study was done with respect to the radiation characteristics. In this section, a detail parametric study is performed by varying the permittivity as well as the thickness of the biocompatible cover.

Effect of Thickness of Coating

The thickness of the coating was varied from 1 mm to 2.5 mm in steps of 0.5 mm. The effect on frequency response of the antenna is shown in Fig. 7.26. As the thickness of coating is increased, the resonant frequency also increases from 2.16 GHz to 2.4 GHz. This is due to the fact that lesser and lesser amount of fields interact with the muscle tissue and therefore the miniaturization effect of muscle

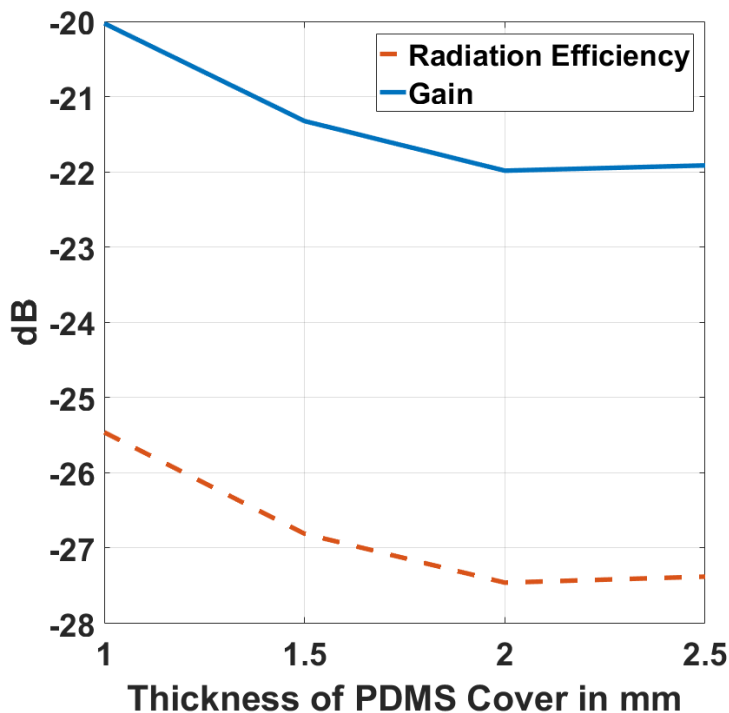


Figure 7.27: Effect of changing the thickness of the coating on the gain and radiation efficiency of the antenna.

due to the high dielectric constant is diminished. Also, the impedance matching is affected drastically by the thickness of PDMS cover. Consequently, the thickness control of the PDMS layer is crucial to maintain the resonant frequency as well as impedance matching.

The effect of PDMS thickness on the radiation characteristics is shown in the Fig. 7.27. With increase in the thickness of coating, the gain decreases monotonically. This is due to the corresponding decrease in the radiation efficiency. There is no effect on the radiation pattern or the directivity of the antenna as seen from Fig. 7.28.

Farfield Directivity Abs ($\Phi=0$) Farfield Directivity Abs ($\Phi=90$)

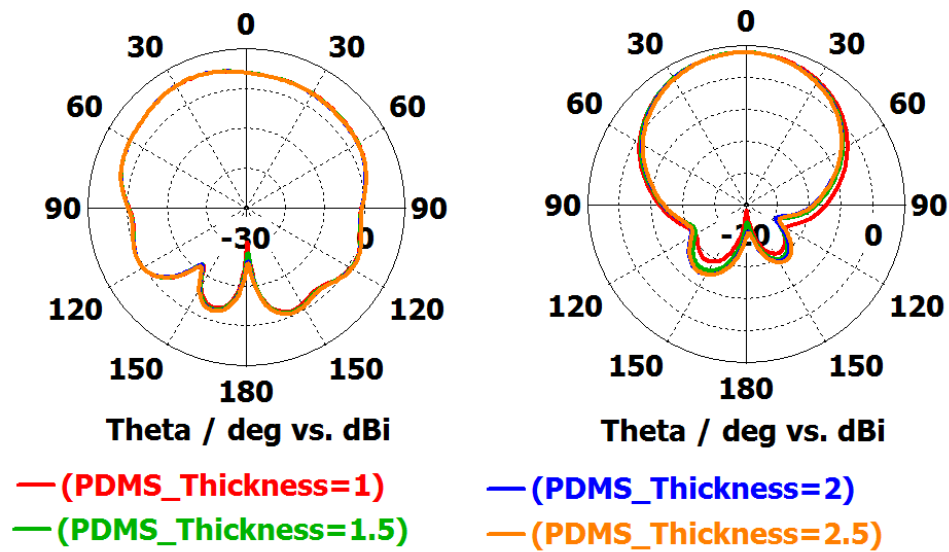


Figure 7.28: Effect of changing the thickness of the coating on the radiation pattern of the antenna in $\Phi = 0^\circ$ and $\Phi = 90^\circ$ planes at 2.4 GHz.

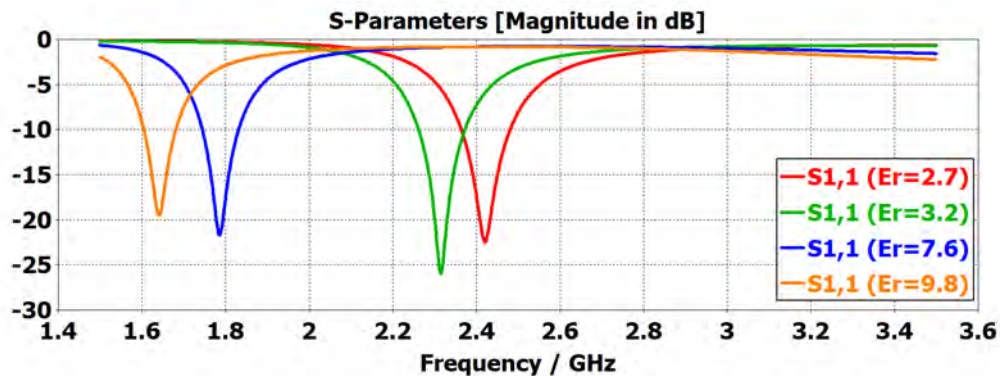


Figure 7.29: Effect of changing the permittivity of the coating on the impedance matching and the resonant frequency of the fractal slot antenna.

Effect of the Permittivity of Coating

Increasing the permittivity of coating is expected to decrease the resonant frequency of the antenna. However, estimating the radiation characteristics is non-

Table 7.1: Effect of changing the permittivity of the coating on the antenna performance.

ϵ_r	f_r	S_{11}	-10 dB BW	Rad. Efficiency	Directivity	Gain
2.7	2.42 GHz	-22 dB	120 MHz	-27.84 dB	5.46 dB	-22.38 dB
3.2	2.31 GHz	-26 dB	110 MHz	-26.28 dB	5.412 dB	-20.87 dB
7.6	1.78 GHz	-21.6 dB	90 MHz	-22.97 dB	5.56 dB	-17.4 dB
9.8	1.64 GHz	-19.4 dB	75 MHz	-22.96 dB	4.67 dB	-18.3 dB

trivial as the fields are concentrated in the biocompatible coating but since the dielectric contrast between coating and muscle is reduced, the fields also extend more into the muscle tissue. For this purpose, the parametric analysis of the dielectric permittivity of coating is done.

Usually, the biocompatible material that are used as coating are PDMS ($\epsilon_r = 2.7$), PEEK ($\epsilon_r = 3.2$) and variants of alumina ($\epsilon_r = 7.6$ and $\epsilon_r = 9.2$). Therefore, the simulations are carried out by choosing these permittivity values for the coating. The frequency response is shown in Fig. 7.29. The values of resonant frequency, -10 dB bandwidth, gain, directivity and radiation efficiency are given in Table 7.1. The radiation characteristics are evaluated at their respective resonant frequencies.

It can be seen that the antenna is matched for all the cases although the resonant frequency has shifted from 2.42 GHz to 1.64 GHz with ϵ_r increasing from 2.7 to 9.8. Also, the -10 dB bandwidth reduces from 120 MHz to 75 MHz as expected from miniaturized antennas. However, the radiation efficiency improves from -28 dB to -23 dB. This is because of the reduction in the dielectric contrast

of the encapsulation and the muscle tissue.

7.5.3 Effect of the Muscle Tissue Parameters

Sensitivity of an antenna to the variation in dielectric constant of the human body and their shape and size is a critical issue. Especially, if the antenna is detuned by a large value due to changes in human body, its response may go out of the designated ISM band. In this section, the proposed CPW fed fractal slot antenna is subjected to the variation in the permittivity of muscle tissue as well as their thickness. The effect on resonant frequency, bandwidth, radiation efficiency, and gain is discussed.

Effect of Changing the Muscle Size

The amount of muscles around the leg changes from person to person and from time to time. Hence, it is necessary to evaluate the performance of antenna, under different muscle cover thickness. Following the $\pm 20mm$ rule described in 6, in this section, the designed fractal antenna is evaluated for changes in the muscle tissue size. Fig. 7.30 shows the effect of changing the muscle radius on the frequency response of the proposed antenna. It can be seen that as the muscle radius increases, the impedance matching changes very slightly and there is almost no change in the resonant frequency. This robustness is due to the biocompatible PDMS cover. While this reduces the effect of miniaturization by increased permittivity of muscle tissue, the antenna's frequency performance remains unchanged.

However, the muscle cover does influence the radiation performance of the antenna. As the muscle thickness increases, the radiation efficiency decreases.

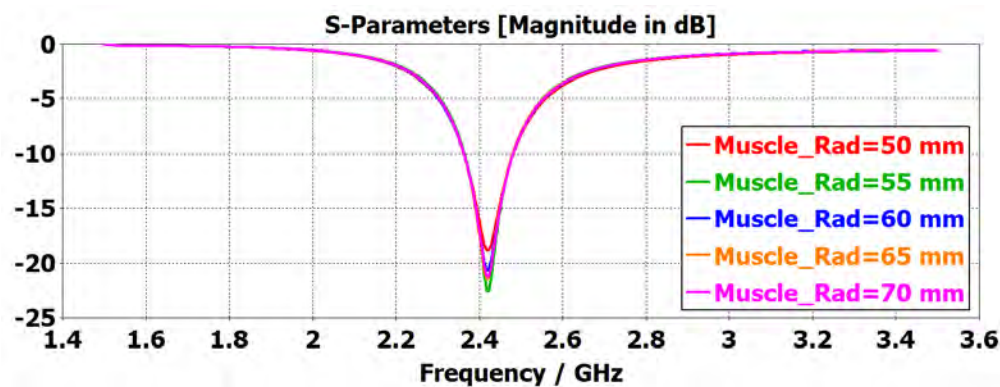


Figure 7.30: Effect of changing the muscle radius on the frequency response of fractal antenna.

For 50 mm muscle radius the radiation efficiency is -26.7 dB which reduces -32.3 dB for 65 mm of muscle radius. Correspondingly the gain of the antenna also changes from -22 dB to -26.8 dB. Fig. 7.31 shows the radiation pattern variation for changing muscle radius in three principle planes - $\phi = 0^\circ$, $\phi = 90^\circ$, and $\theta = 90^\circ$. The directivity and shape of the radiation pattern is almost unchanged although the gain reduces steadily with increasing muscle thickness. The reduction in gain is due to the reduction in radiation efficiency as more power is absorbed in the muscle tissue (Fig. 7.32). The total variation in gain or radiation efficiency for ± 20 mm of muscle thickness is about ± 3.3 dB.

Effect of Changing Muscle Permittivity

The muscle permittivity can also change based on the water content of the muscle. Therefore, the permittivity of the muscle is changed by 10% around the nominal values. Both the real and imaginary part of the complex permittivity are changed simultaneously at all frequencies.

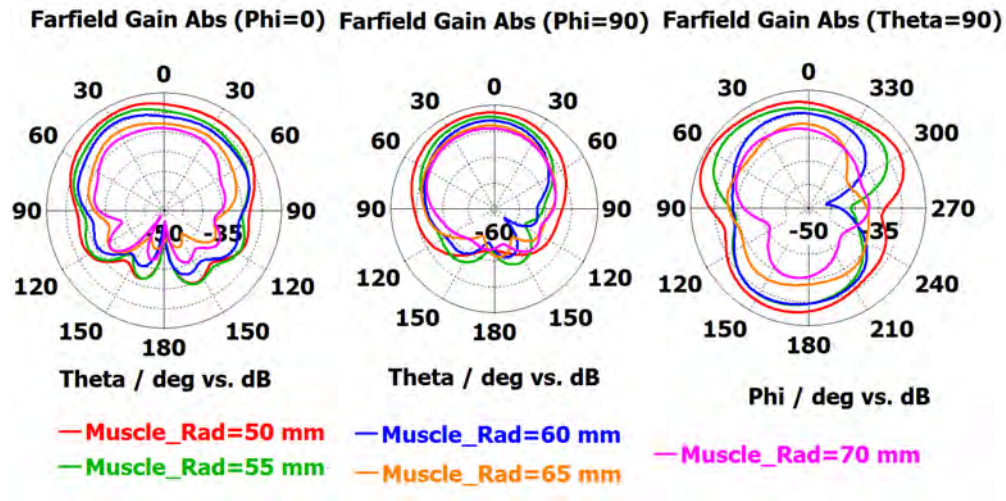


Figure 7.31: Effect of changing the muscle radius on the gain of the fractal slot antenna in three principle planes.

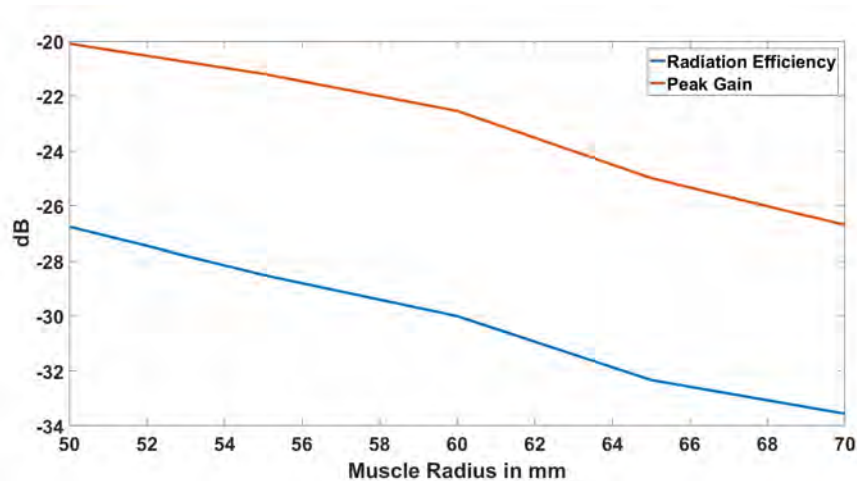


Figure 7.32: Gain and radiation efficiency as a function of muscle radius at the resonant frequency of the antenna.

The permittivity data so obtained is then fitted in Cole-Cole model by CST to enforce causality. The effect on frequency response is shown in Fig. 7.33. The result is for the muscle radius of 65 mm. It can be seen that the resonant frequency

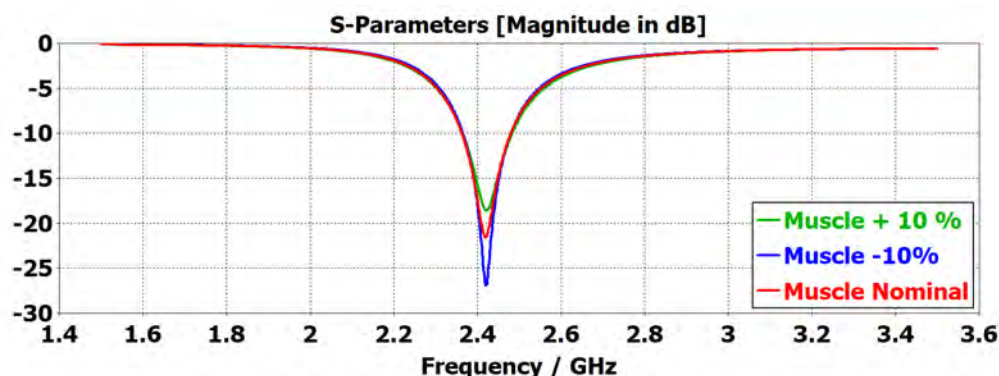


Figure 7.33: Effect of changing the muscle permittivity on the frequency response of the fractal slot antenna.

does not change but the impedance matching is affected.

The radiation efficiency changes from -29.91 to -34.6 dB as the permittivity (ϵ_r' and ϵ_r'') changes from $\pm 10\%$ of the nominal value. since the directivity is almost constant around 5.7 dBi, the gain changes from -24.4 dB to -28.8 dB. This is expected as the conductivity of the muscle increases, the losses also increase and so the radiation efficiency decreases. Thus a change of 20% causes about 4.5 dB of change in the gain of the antenna.

7.6 Summary

A new fractal geometry termed as *M Segment Quadratic Fractal* that provides the freedom of choosing between form factor, miniaturization achieved and resonant frequency is proposed. The equations providing the resonant frequency from the fractal structure are derived. An empirical equation to predict the resonant frequency of the slot is presented. A method to design a simple single layer miniaturized slot antenna implanted inside the human body on tibial bone is proposed.

A CPW fractal slot antenna working at 2.4 GHz is designed, simulated and verified experimentally. The parametric analysis of antenna geometry parameters is conducted and recommendations on tuning and impedance matching of antenna are made. The robustness of antenna to the changes in the human body are also evaluated. The resonant frequency of antenna is kept constant by utilizing the cover made up of biocompatible PDMS material. The change in radiation characteristics due to the changes in human body are also investigated in detail.

Chapter 8

Design of Wideband Fractal Slot Antenna

8.1 Introduction

In the previous chapter, the design methodology for a CPW fed implantable antenna was presented. Using the design procedure, an antenna designer can design the implantable antenna at any given frequency of operation which has the desired miniaturization and form factor without heavily compromising on the radiation characteristics. In most of the cases, the design can be perfected within couple of iterations for impedance matching and slight frequency tuning. However, as demonstrated in the parametric and robustness analysis of the proposed fractal antenna, it is possible that antenna might get detuned from the designed frequency due to the process variations in the biocompatible coating, PCB manufacturing tolerances and shape, size and dielectric variations of the human tissues. This would result in the impedance mismatch and reduced signal strength.

In order that the antenna works well even with large variations within the human body as well as process tolerances, it is necessary to design wideband antenna. Due to the wideband nature of the antenna, despite the frequency shifts, it will be able to function in the desired 2.4 GHz ISM band. In this chapter, design of such wideband antennas is presented. The design procedure, impedance matching and parametric analysis is presented followed by the experimental verification. The -10 impedance bandwidth of about 320 MHz, centred at 2.4 GHz is obtained.

In order to increase the impedance bandwidth of narrow band antennas, usually techniques like thick substrates and wide slots are employed [158, 164–168]. Many of these designs are based on the trial and error obtained by the parametric analysis and by observing the current distribution. The main aim of these techniques is to obtain either multi-mode excitation or multiple resonances. However, as explained in the previous chapter, trial and error and other optimization techniques take a relatively large amount of computational resources and time. Therefore, this approach is avoided in the present research.

The technique of coupling two closely spaced resonances to obtain a wideband response is employed. The M-segment Quadratic Fractal presented in Chapter 7 is quite a versatile geometry. Many different resonances can be created by using the same zeroth iteration. Therefore, many antennae with varying bandwidth and impedance matching characteristics can be designed by choosing different resonant elements and by controlling the coupling between them. Also, the capacitively coupled CPW feed offers many parameters for getting good impedance match across the entire band.

8.2 Design of Wideband Antenna

When the two resonators resonating at close frequencies interact with each other, they can merge to form a wideband antenna. For demonstrating this, two fractal dipole resonators are designed on the Rogers 6010 substrate with thickness 0.254 mm using following procedure.

1. Since, the target frequency is 2.4 GHz, the two resonances are chosen to be at 2.3 GHz and 2.5 GHz respectively. The ratio of the two frequencies is 0.92.
2. From equation 7.6, it can be seen that for variation $m=2$ and $n=2$, the amount of miniaturization is 0.67 while that for $m=2$ and $n=3$ is 0.6. The ratio of these two numbers is 0.89 which is quite close to the target ratio of 0.92. Therefore, these two fractal geometries are selected for the design procedure.
3. Following the procedure described in the previous chapter, the length of the zeroth iteration line is calculated as 16 mm.
4. Fractals are generated in MATLAB and imported in CST to be cut as slots from the ground plane of the CPW antenna.

There are 3 possible configurations in which the two resonators could be arranged. They are shown in the Fig. 8.1. In the first configuration (left), the two fractal dipoles are arranged one above the other. In second configuration (centre), one arm of a dipole belongs to one fractal ($m = 2, n = 2$) while other arm belongs to other fractal ($m = 2, n = 3$) such that arms of one fractal dipole are on same

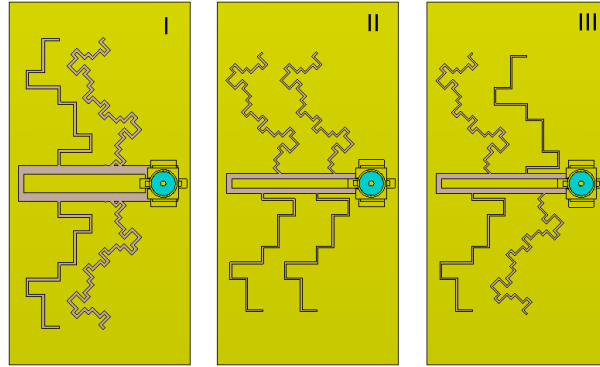


Figure 8.1: Three different configurations of the wideband antenna design.

side of the CPW line. The third configuration is similar to the second one except that the arms of same fractal dipole are on opposite side of the CPW line. The third configuration(right) is termed as the criss-cross geometry.

The frequency response of the three configurations is compared in Fig. 8.2. It can be seen that, configuration three (criss-cross) gives the best result in terms of the antenna matching. Because of the criss cross pattern the current has more uniform distribution along the entire patch in the entire band, due to the mirror symmetry along both the axes. The $m = 2$, $n=3$ geometry resonates at the lower frequency while the $m=2$, $n=2$ geometry resonates at higher frequency as shown in Fig. 8.9. Also, due to the larger paths required for the current in criss cross configuration, the resonant frequency shifts to the lower value. The resonances also come close creating a wideband response.

The dimensions of the final wideband antenna design are given in the Table 8.1. The entire antenna has dimension $20 \text{ mm} \times 10 \text{ mm} \times 0.254 \text{ mm}$ and is encapsulated inside the 2 mm thick PDMS coating from all the sides. The variations of these different parameters is considered in the parametric analysis section.

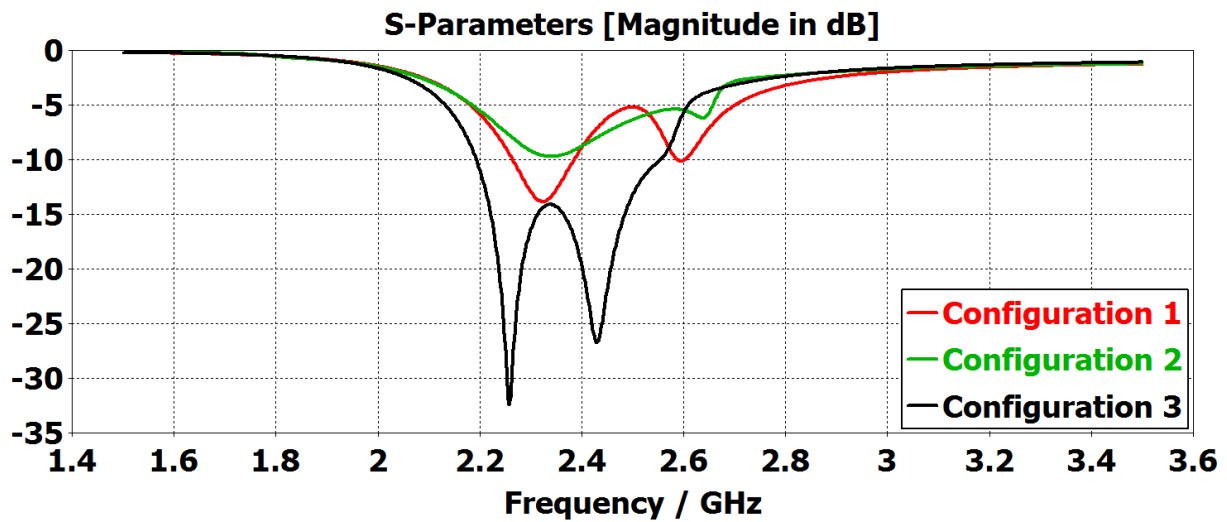


Figure 8.2: Frequency response of the three different configurations of the wideband antenna design.

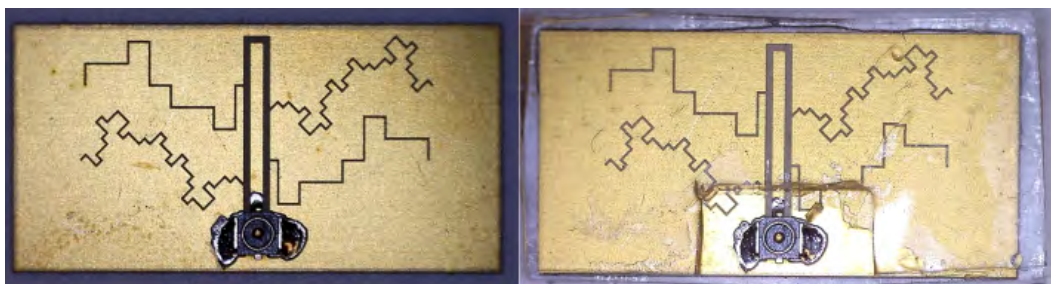
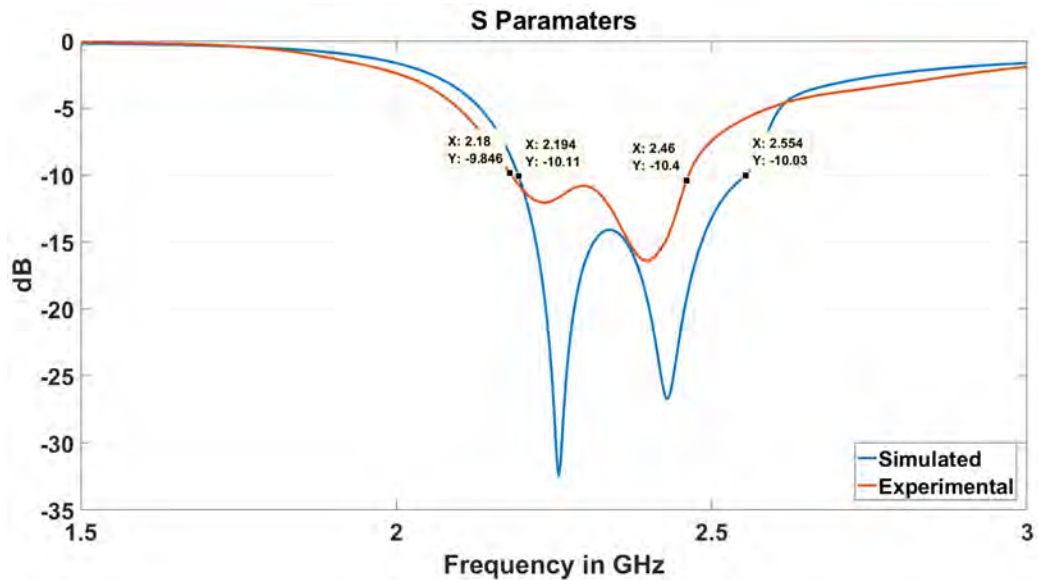


Figure 8.3: Fabricated wideband antennas with and without PDMS coating.

Table 8.1: Final dimensions of the wideband fractal antenna.

Slot Width	CPW Width	CPW Gap	CPW Length	Coupling Distance
0.1 mm	0.5 mm	0.3 mm	6.5 mm	3.5 mm

**Figure 8.4:** Comparison of the simulated and fabricated wideband fractal antenna.

The measurements are done inside the cow bone covered with the muscle tissue as explained in section 7.4. The fabricated wideband antenna with the AMMC connector- with and without PDMS coating is shown in Fig. 8.3. The comparison of the simulated and the measured antenna is shown in Fig. 8.4. The measured results agree well with the simulations. The measured -10 dB impedance bandwidth of the antenna is from 2.18 GHz to 2.46 GHz ($BW = 280$ MHz).

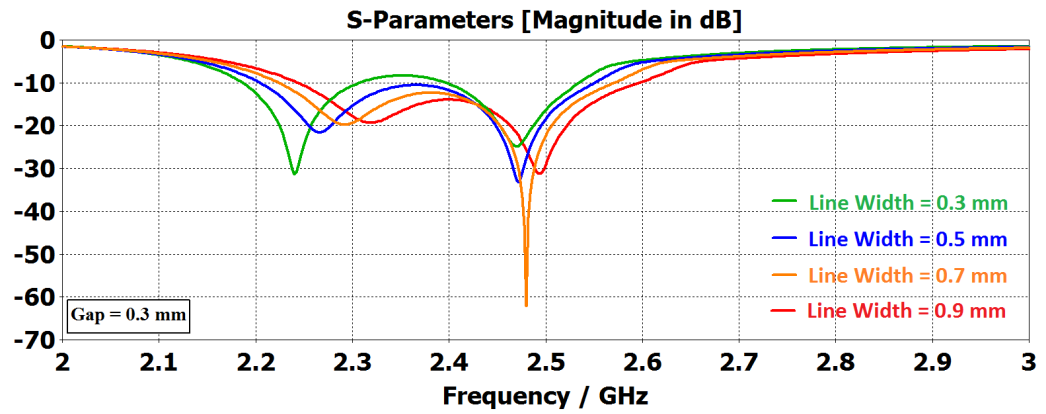
8.3 Parametric Analysis

8.3.1 Effect of CPW Line Parameters

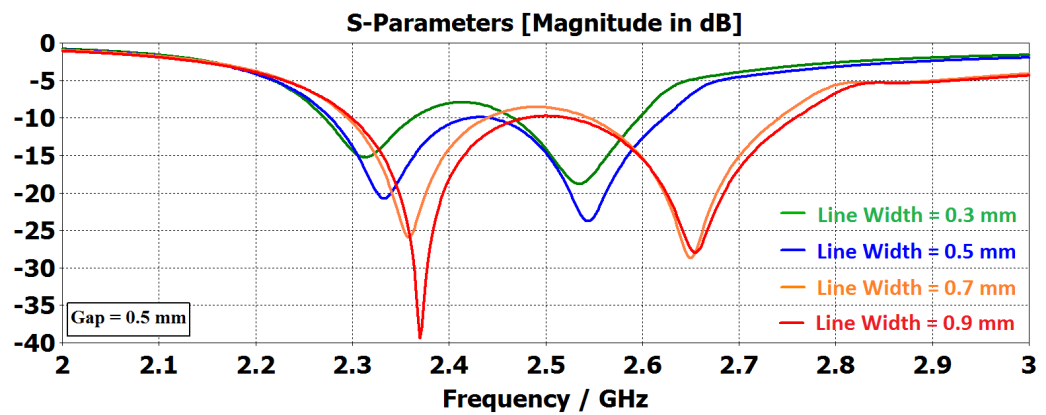
CPW structure has two parameters, line width and the gap between the ground plane and the line. These two parameters control the characteristic impedance of the transmission line. This in turn decides the impedance matching and the resonant frequency of the antenna. To evaluate their effect, both these parameters are varied. The line length is varied from 0.3 mm to 0.9 mm in steps of 0.2 mm whereas the gap is varied from 0.3 mm to 0.7 mm in steps of 0.2 mm. The length of the CPW line is kept at 6.5 mm. Therefore, total 12 combinations were evaluated. The results are shown in Fig. 8.5.

Changing the width of the CPW line has a pronounced effect on the lower band while the upper band is relatively unchanged. Increasing the width of the line shifts the resonant frequency to a higher value. This is due to the inductive reactance offered by the CPW line at the feed point. Wider the line, lower is the inductive reactance and higher the operating frequency. Since the lower resonance is affected more than the upper, the two frequencies come closer as the line width increases. Due to this, the reflection coefficient is improved over the entire band.

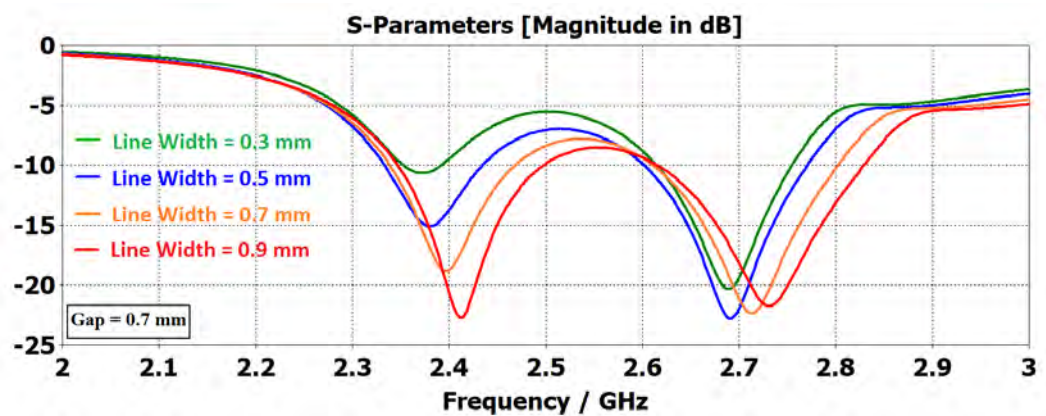
Gap between the CPW line and the ground plane has more effect on the impedance of the line. As the gap increases from 0.3 mm to 0.7 mm the impedance matching gradually worsens. Keeping in view the ease of fabrication, the gap of 0.3 mm seems to be a suitable choice. Also, increasing the gap pushes the band towards higher frequencies. This is due to the fact that it covers the fractal path of the slot dipole. More the gap width, more portion of the fractal is lost. An alternative to this would be shifting the fractal to the edge of the CPW line. How-



(a)



(b)



(c)

Figure 8.5: Effect of changing the width of the CPW line for different values of gap between line and ground plane (a)Gap = 0.3 mm (b)Gap = 0.5 mm (c)Gap = 0.7 mm

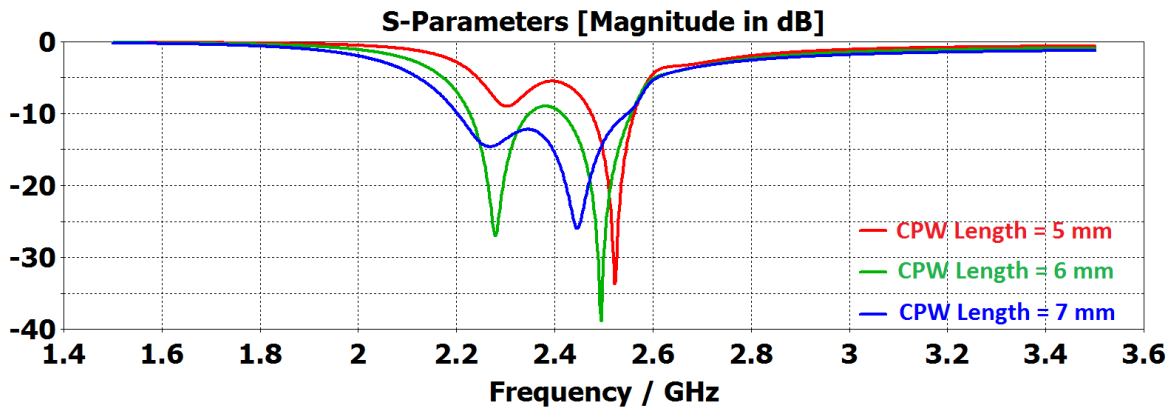


Figure 8.6: Effect of changing the length of the CPW line on the frequency response of the wideband fractal slot antenna.

ever, this would require redesign of the fractal with new lengths followed by further tuning of CPW parameters for impedance matching which would then become an iterative process of tuning CPW line parameters and recalculating the fractal.

From this investigation, it can be concluded that a CPW line of width greater than 0.5 mm and gap less than 0.3 mm is suitable for obtaining a wideband response with reflection coefficient better than -10 dB in the entire band.

The CPW line extends beyond the slot and this creates an additional variable for impedance tuning. Therefore, the length of the CPW line is varied from 5 mm to 7 mm. The S_{11} response of this parametric analysis is plotted in 8.6. Increasing the length of the CPW line lowers the higher resonant frequency while improving the impedance matching at lower resonant frequency. The length greater than 6 mm can give a clean -10 dB band of operation from 2.2 GHz to 2.54 GHz with the bandwidth of 340 MHz. Radiation properties like directivity, radiation efficiency and gain are not affected significantly with variation of only 0.03 dB, 0.2 dB, 0.18 dB respectively.

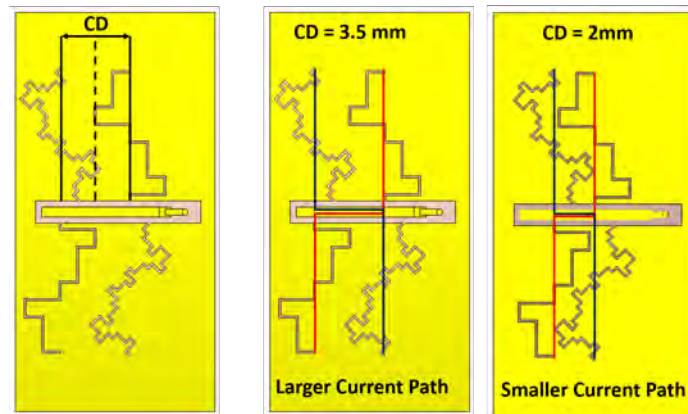


Figure 8.7: Design of criss cross antenna showing different coupling distances.

8.3.2 Effect of Coupling Distance

Coupling between two elements of comparable size can shift their resonant frequency. In order to investigate the effect of this phenomenon, the distance between the two fractal elements of the designed antenna is changed. Since the geometry is convoluted, the distance between the initial generator (straight line) is considered as coupling distance ' CD '. This is shown in Fig. 8.7. The coupling distance is varied symmetrically around the centre line between the two resonators from 2 mm to 3.5 mm. Coupling distance smaller than 2 mm is not possible because of the geometry overlap. Coupling distance more than 3.5 mm is not possible as the fractal curves go out of the antenna dimensions.

The frequency response of this parametric analysis is shown in Fig. 8.8. As the coupling distance increases, the resonances shifts towards the lower value. Further, the impedance matching across the entire band improves. For coupling distance less than 2.5 mm, the response in the entire band is not below -10 dB. Also the ratio between two frequencies is fairly constant.

Such a response is observed due to the criss-cross arrangement of the resonators.

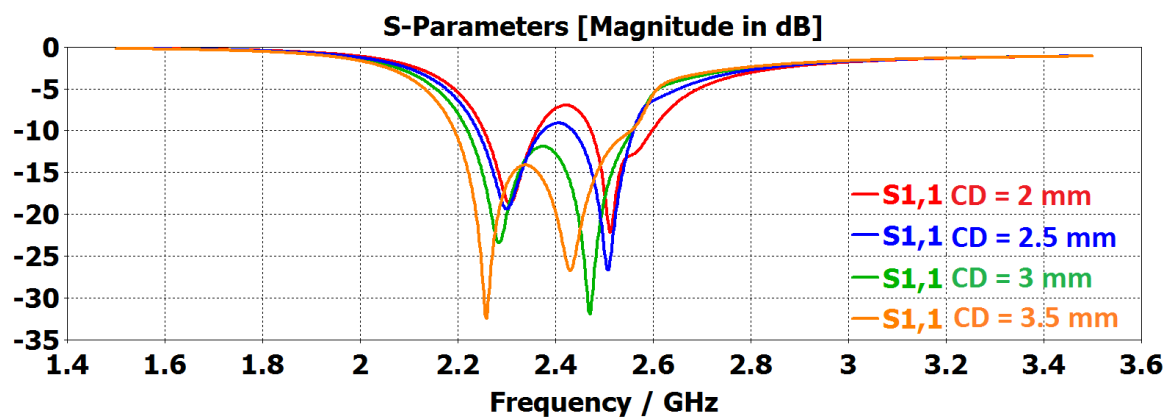


Figure 8.8: Effect of changing the coupling distance between two resonators on the frequency response of the wideband fractal slot antenna.

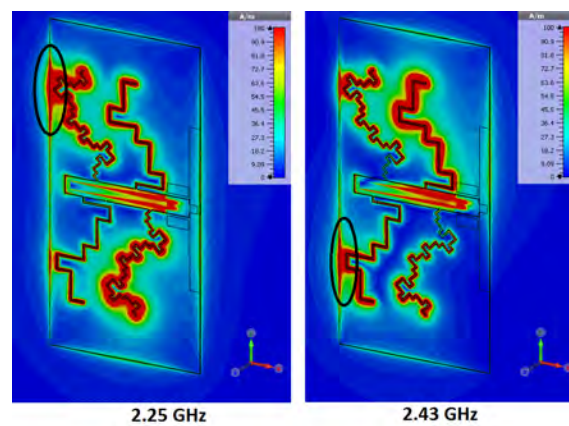


Figure 8.9: Current distribution on the wideband fractal slot antenna at 2.25 GHz and 2.43 GHz for $CD = 3.5$ mm shows the spreading of current at the edge of antenna.

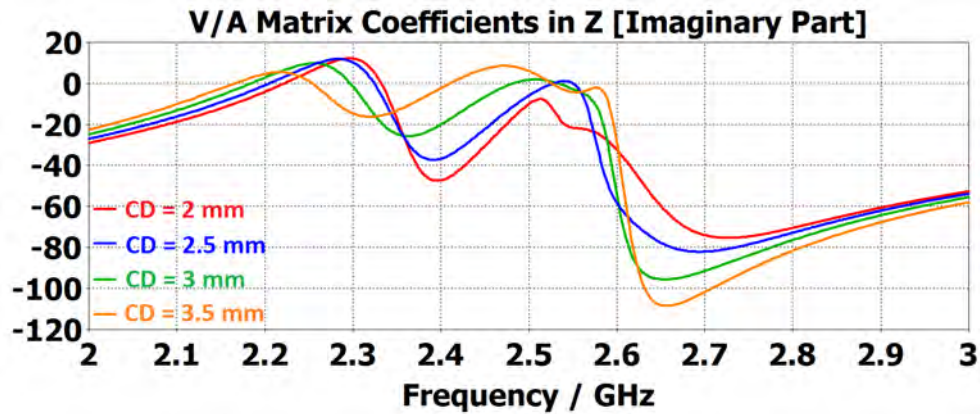


Figure 8.10: Effect of changing the coupling distance between two resonators on the imaginary part of the impedance of the wideband fractal slot antenna.

As the coupling distance increases, the current path for each dipole also increases (8.8). Further, as one of the arms of each dipole shifts closer to edge of the ground, the current also spreads more, as seen in Fig. 8.9. Hence both the resonances shift towards lower value with the increasing coupling distance. Further, as the distance increases, the variation of reactive component of the impedance around zero ohms is minimized as shown in Fig. 8.10. This translates into better reflection coefficient in the entire band.

8.3.3 Effect of Ground Plane

In the proposed design of the wideband antenna, the ground plane dimensions were kept identical to that of a single band antenna (length = 20 mm and width = 10 mm) presented in 7. In this section, the effect of reducing the length of the ground plane is investigated.

Figure 8.11 shows that as the ground length is reduced, the impedance matching at the lower resonance worsens. As the ground length is reduced, the resistance

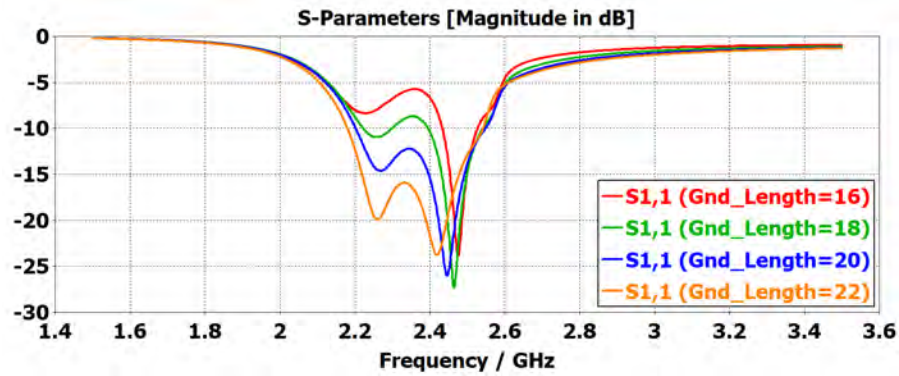


Figure 8.11: Effect of changing the length of the ground plane on the frequency response of antenna.

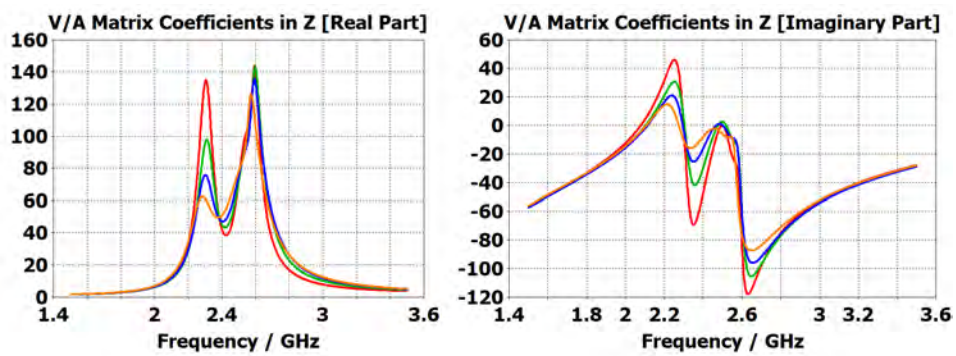


Figure 8.12: Effect of changing the length of the ground plane on the resistance of the antenna.

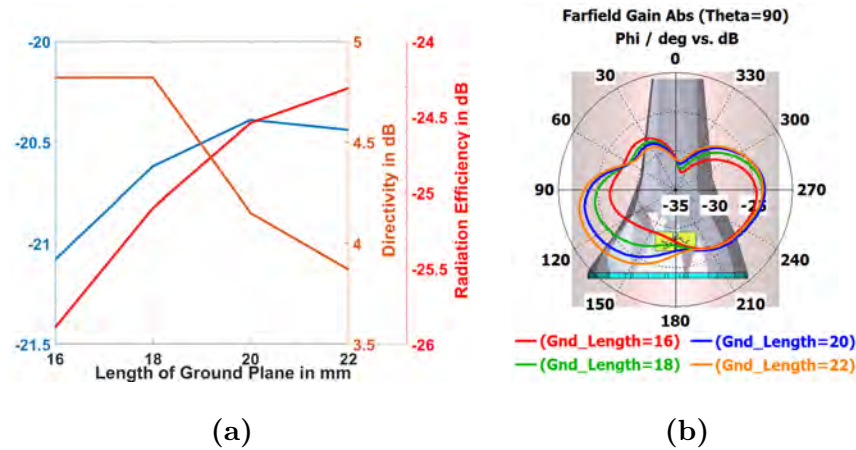


Figure 8.13: (a) Effect of the ground length variation on the peak gain and the radiation efficiency. (b) Effect of the ground length variation on the radiation pattern in $\Theta = 90$ plane

to the current increases. Also, as the current spreads along the edges of ground, the inductance also increases. This effect is especially dominant at the lower frequency as seen from Fig. 8.12. Due to this effect, the impedance match is disturbed and the reflection co-efficient worsens at the lower band.

The radiation characteristics are plotted in Fig. 8.13. For a smaller length of ground plane, the directivity of antenna is more but the radiation efficiency is low and vice-versa. Therefore gain has a peak value of -20.5 dB for the optimal antenna length of 20 mm. Figure 8.13b clearly shows the increased radiation along the length of the ground plane with the increase in its dimension. The radiation patterns in other planes (not shown) remain undisturbed.

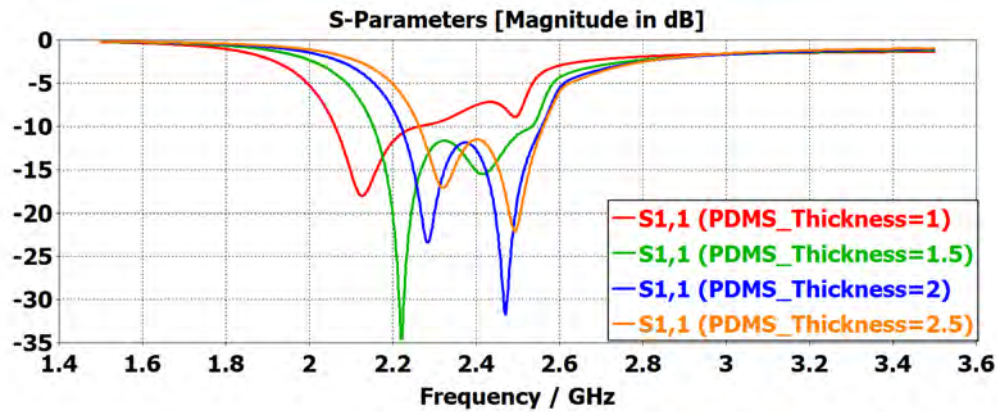


Figure 8.14: Effect of changing the thickness of the PDMS cover on the reflection co-efficient of the wideband fractal slot antenna.

8.3.4 Effect of PDMS Thickness

PDMS coating on antenna provides biocompatibility as well as insulates antenna from muscle tissue parameter changes. However, as it is in the near field, the thickness of the PDMS plays an important role in the resonant frequency and the impedance matching of the antenna. In the single element fractal slot antenna designed in chapter 7, it was observed that the change in the thickness of this encapsulation (Fig. 7.26), changes the resonant frequency as well as impedance matching and antenna may detune out of the desired ISM band. Therefore, it is crucial to investigate the effect of the PDMS variation on the response of the designed wideband antenna.

Fig. 8.14 shows the effect of varying the thickness of the PDMS cover on the frequency response of the designed wideband antenna. As the PDMS thickness decreases, the resonances shift to the lower frequency. This is because thinner the PDMS cover, more is the dielectric loading due to the high permittivity muscle tissue. However, for the thickness less than 1.5 mm, S_{11} is not below -10 dB across

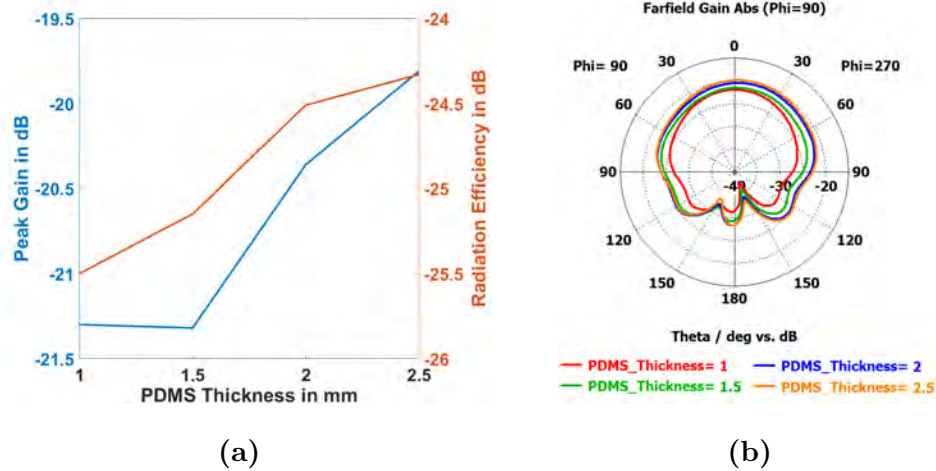


Figure 8.15: (a) Effect of PDMS cover thickness variation on peak gain and radiation efficiency. (b) Effect of PDMS cover thickness variation on radiation pattern in $\Phi = 90$ plane.

the entire band. For higher thickness values, the antenna covers the entire 2.4 GHz ISM band. Thus, unlike the single band fractal antenna proposed in 7, the variation in the PDMS thickness does not render antenna useless in the ISM band due to the wide bandwidth of operation.

The radiation performance of the antenna with respect to the thickness of PDMS layer is plotted in Fig. 8.15a. It can be seen that, as the thickness increases, the gain of the antenna also increases. This is due to the increase in the radiation efficiency. As the thickness of the PDMS layer increases the near field power absorbed by the muscle tissue decreases from 70 % to 52 % . This in turn increases the radiation efficiency by almost 1.5 dB as thickness is increased from 1.5 mm to 2.5 mm. Increasing the PDMS thickness has no effect on the shape of the radiation pattern as seen from Fig. 8.15b.

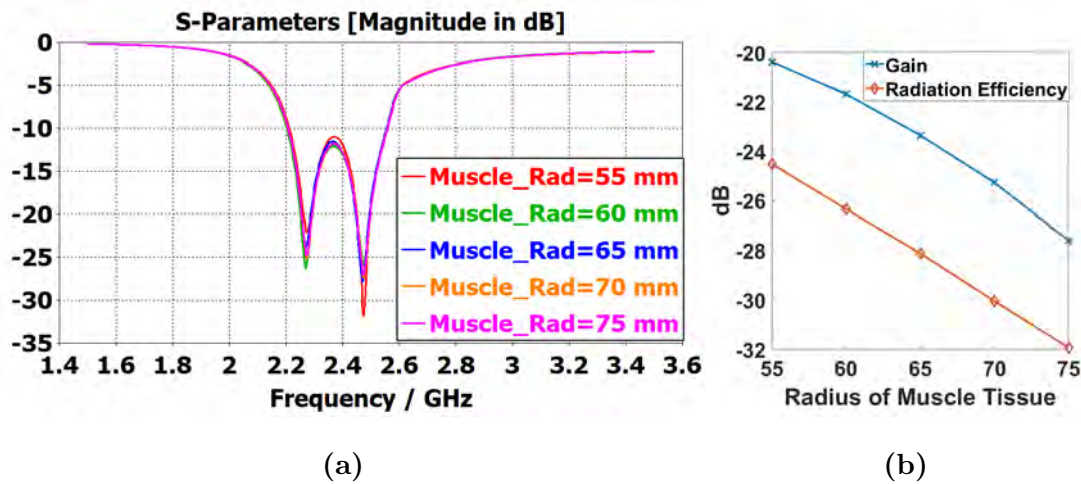


Figure 8.16: (a) Effect of changing the radius of the muscle on the reflection co-efficient of the wideband fractal slot antenna. (b) Effect of changing the radius of the muscle on the peak gain and radiation efficiency of the wideband fractal antenna.

8.3.5 Effect of Muscle Dimensions

The muscle radius was varied from 55 mm to 75 mm in steps of 5 mm. The resonant frequency of the single band antenna presented in last chapter doesn't change, so it was expected that it doesn't change for the wideband antenna as well. The frequency response plotted in Fig. 8.16a confirms this expectation. The simulated radiation characteristics like peak gain and radiation efficiency is plotted in Fig. 8.16b.

Since the lossy muscle tissue increases with the radius, the radiation efficiency invariably decreases, which is also seen for a single band antenna. The peak gain changes from -20.3 dB to -27.8 dB. Also, the slope of the peak gain and the radiation efficiency is same because there is no change in the peak directivity. The

radiation pattern also does not change (not plotted) with the change in muscle dimension.

8.4 Summary

A wideband antenna is designed by coupling two fractal slot resonators. The effect of coupling distance is examined through the current distribution and S parameter analysis and optimized values are found. The antenna is fabricated and tested in the femur bone of cow. The simulated and experimental results show good agreement. Wideband antenna allows for variation in bone and muscle properties and dimensions and so maintains the data connectivity. Parametric analysis for all the geometric and tissue parameters is also done to validate that the antenna works well in the 2.4 GHz ISM band.

Chapter 9

Conclusion and Future Work

9.1 Summary of the Research Work

A rectangular mm sized eddy current sensor head is designed, simulated, fabricated and tested for the detection of micromotion of an orthopaedic implant. New sensor parameters: sensitivity and range are defined in dB values to facilitate the circuit design. It is proved that encapsulating the sensor with low dielectric constant material can help in increasing the the frequency of operation and so the sensitivity. Also, it allows for variation in the dielectric characteristics of the human tissues and yet maintains the sensitivity with $\pm 10\%$ of the sensitivity change. A new EC-TMR sensor integration is explored. A heterodyne detection technique is used to increase the sensitivity of the micromotion sensor head.

An extremely miniaturized antenna is designed for data telemetry using complementary Archimedian spirals printed on two sides of the substrate and connected by using a via. The frequency and impedance matching of this antenna can be tuned by the position of the via and the number of turns of the Archime-

dian spiral. The antenna is covered with a high dielectric material to achieve good impedance matching and miniaturization.

A new geometrical construct named M Segment Quadratic Fractal Curve is proposed. This fractal provides two tuning parameters, iteration number 'n' and the Housdorff fractal dimension number 'm' that can be used to control the resonant frequency and the miniaturization achieved. Two different implantable slot antennas were designed using these fractals. The antennas have bone on one side and muscle tissue on other side. An empirical expression to design the slot antenna on a dielectric slab is derived. Using the expressions for fractals and the slot antenna a complete design procedure is presented. A technique of impedance matching of these antenna by extending the CPW line is explained. Two fractal resonators fed from the same CPW line are exploited for creating a wideband antenna by merger of two closely spaced (in frequency) resonances. The variation of the frequency response of antenna to the tissue geometry and electromagnetic characteristics is explored in depth.

9.2 Future Work

The research started with the open questions like which sensor can be used to detect the micromotion of the orthopaedic implant? What could be the effect of human body on its performance and so on as explained in Chapter 2. The work done in this thesis addressed all those questions. However, it raises further questions that can lead to the complete development of the wireless implant micromotion sensing device. The questions that a future research should answer are listed as follows:

1. What should be the integrated circuit design that can detect the resistance or inductance of an eddy current sensor within 1 ppm accuracy?
2. Conversely, what accuracy in ppm, can a 'normal' eddy current detection circuit achieve? Depending on this value, the maximum stand-off distance can be evaluated.
3. What could be the total power requirement of the implanted system? Can the required power be supplied with the designed antennas?
4. What should be the external antenna design? Is it possible to use the mobile phone antenna directly? If not, then can some wearable antenna be designed that can be wrapped around the joint for data and power transmission?
5. If the required power could not be supplied by external antenna, then can a super capacitor be used to store energy? Is time division of operation - (i.e. alternate powering and measurement cycle) a solution?
6. Multiple EC-TMR Sensors can be implanted inside the bone to capture motion along different axes and degree of freedom. This can provide valuable information about how the gait of the person affects the micromotion and hence the stability of the orthopaedic implant. While multiple sensors can be embedded, the cross talk between the two sensors should be avoided. For this purpose, they can be used at different frequencies. Alternatively, a time sharing principle may be used for operation. In other words, the research problem is - how to ensure multiple sensors do not corrupt each other's data? Will the OFDM technique be sufficient? or should the TDM be used so that each sensor responds only in its own time slot?

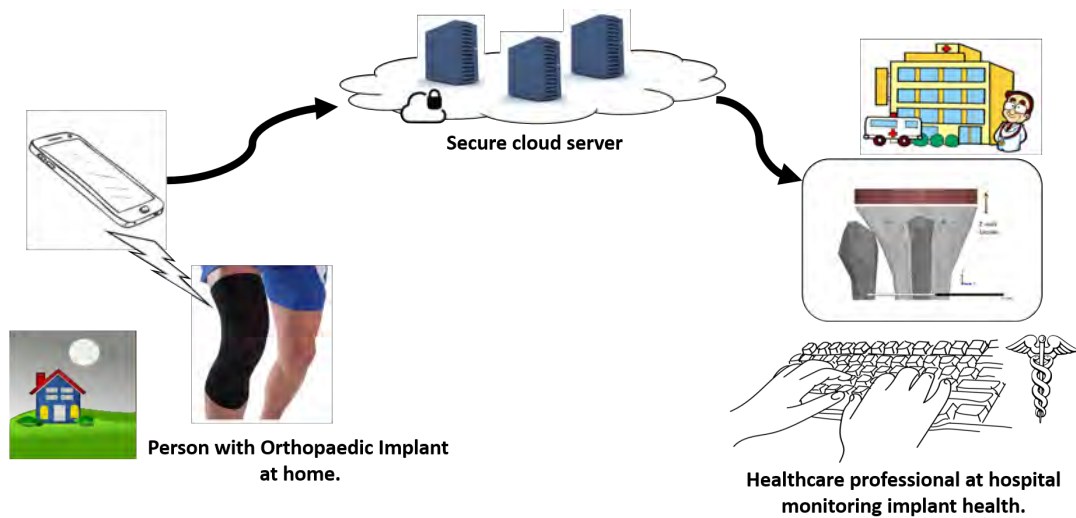


Figure 9.1: High level system architecture of the wireless orthopaedic implant micro-motion device.

7. Which modulation scheme to be used for data telemetry, OOK or FSK or PSK? Which modulation scheme can provide with the least amount of power consumption?
8. If EC-TMR integrated sensor is used, then is it possible to design and fabricate an out of plane field detection MTJ device? A TMR sensor with sensing direction out of plane of fabrication will alleviate the need of perpendicular positioning of sensor on the eddy current loop. However, it requires specialized materials or flux guides to convert the out of plane H - fields to the in-plane H-fields.

Finally, a high level system architecture is shown in Fig. 9.1. A patient who has undergone joint replacement located in a remote area can wear the external wearable sleeve with embedded electronics. This can interrogate the implanted sensor as the person continue to perform their daily tasks. The wearable sleeve

communicates to the external internet enabled device. This can be a smart phone, tablet, laptop or PC. A microservice or app running on these device will upload the data to the secure central or cloud server with additional data that identifies the person. This data is then made available to the healthcare provider who can analyse it and provide the necessary advice if needed.

Further, the datasets from multiple patients can be analysed to correlate micro-motion of the implant with stresses and strains developed during physical activity. Correlations with weight, age and implant structure and material can also be researched. This will lead to significant well being of the people suffering from orthopaedic disorders or injuries.

Appendix A

Curve Fit Analysis

A.1 Effect of Changing Permittivity of Bone

The density, shape and size of the tibial bone can change from person to person as well as within same person due to recuperation and/or osteoporosis. This will result is change in complex permittivity of the bone. In this section, the complex permittivity is changed by $\pm 25\%$ and the curve fit analysis is done on the frequency-standoff distance data. Based on this data, further analysis is performed and results are given in chapter 5.

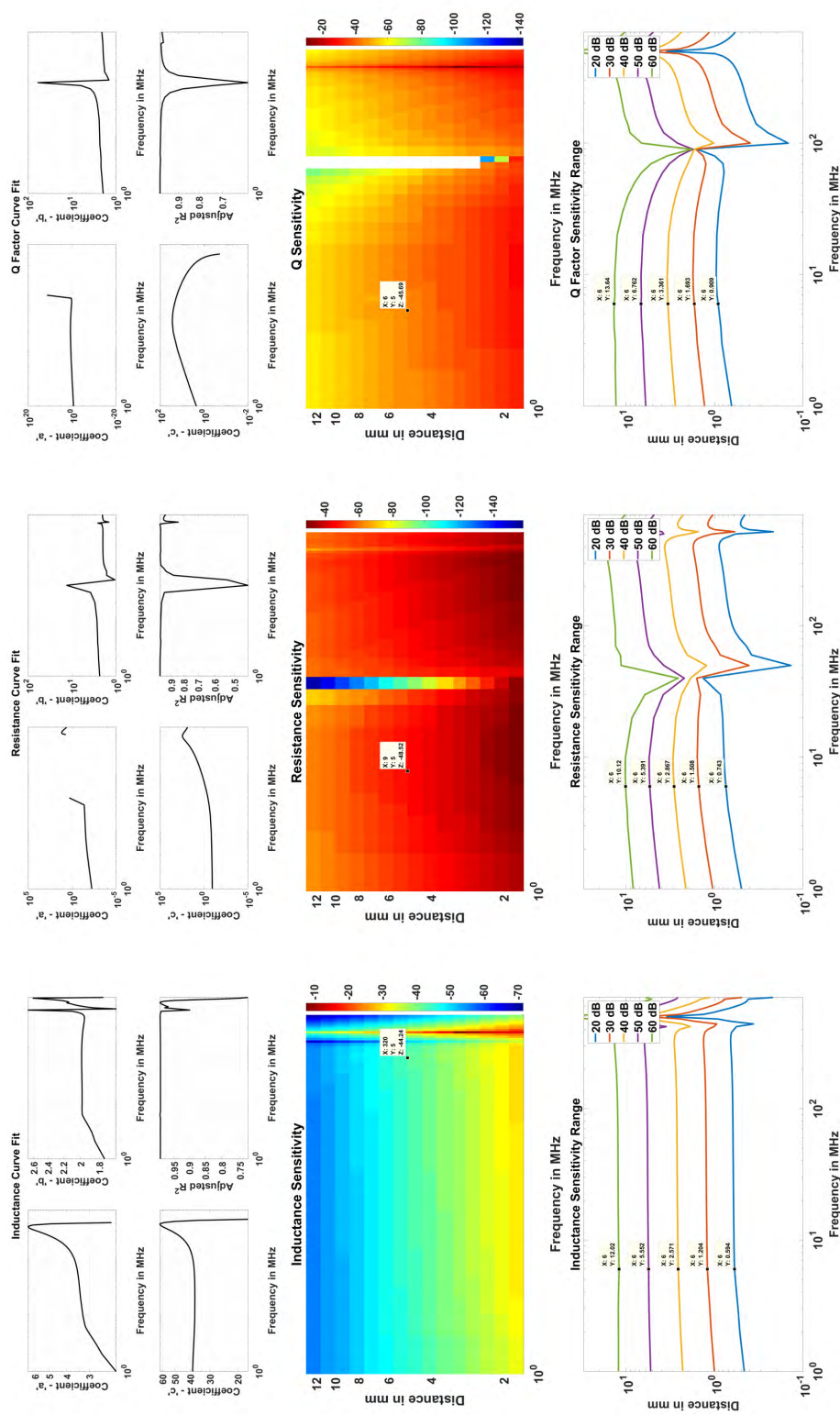


Figure A.1: Curve fit analysis for a two turn loop without PDMS coating with +25 % change in bone complex permittivity.

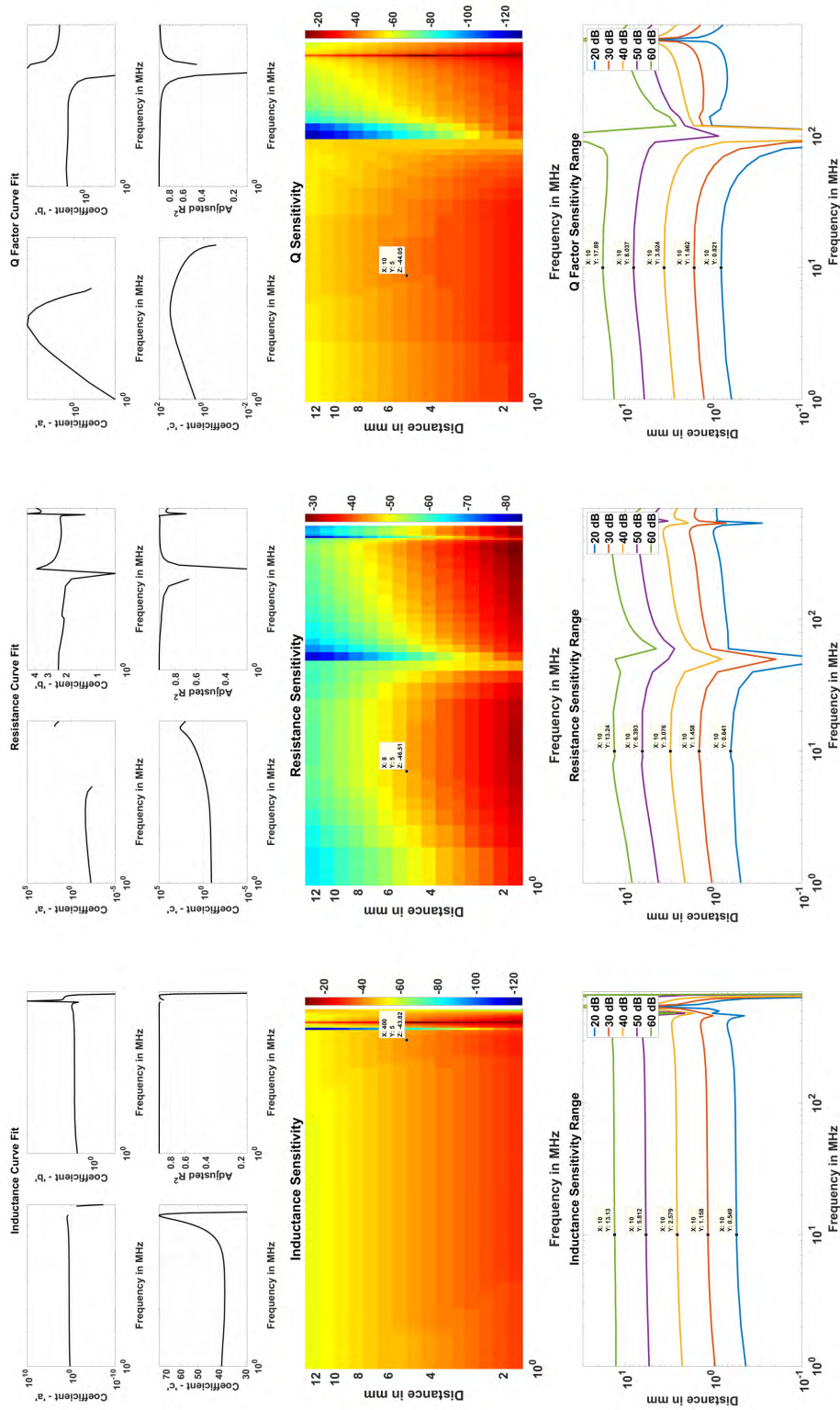


Figure A.2: Curve fit analysis for a two turn loop without PDMS coating with -25 % change in bone complex permittivity.

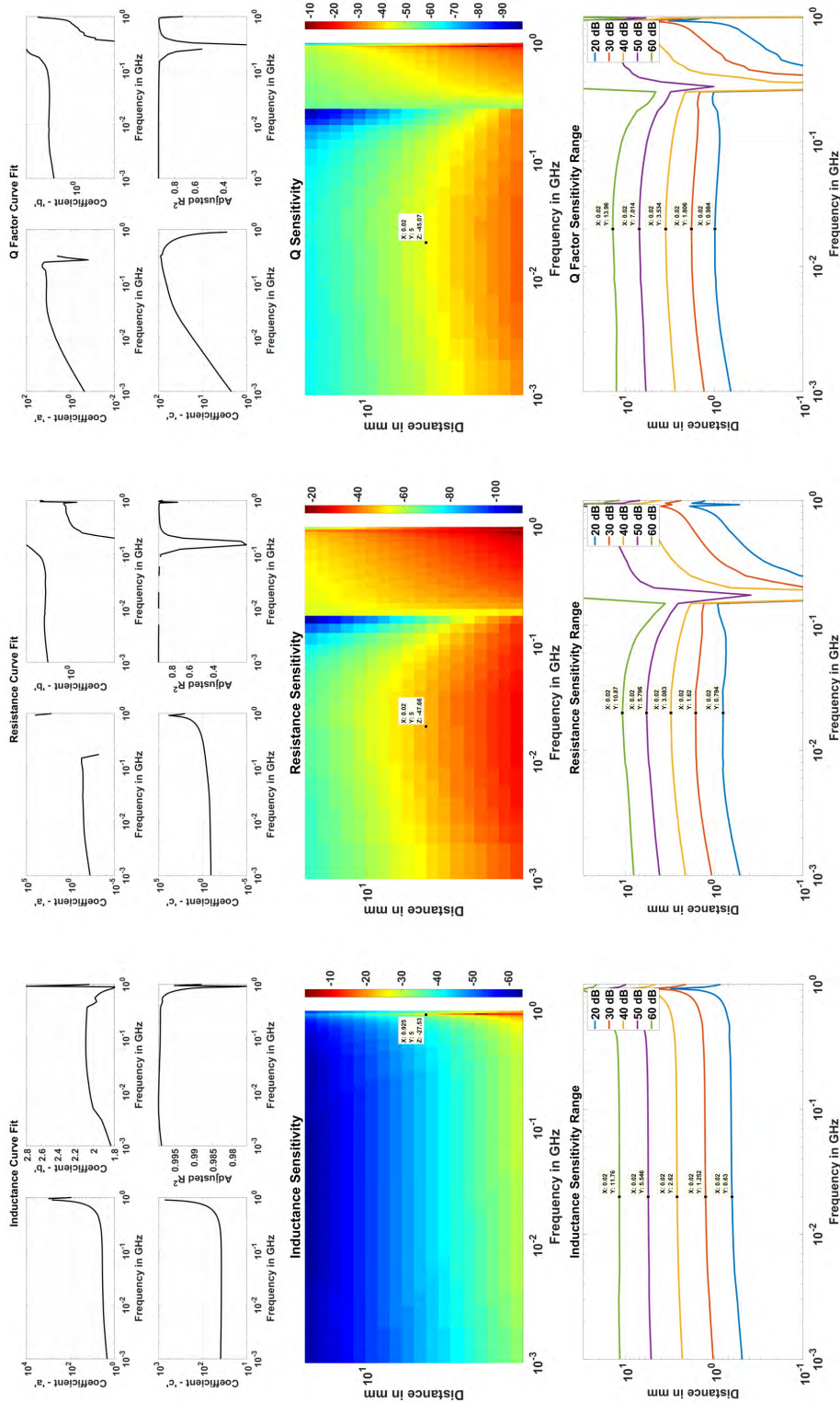


Figure A.3: Curve fit analysis for a two turn loop with PDMS coating with +25 % change in bone complex permittivity.

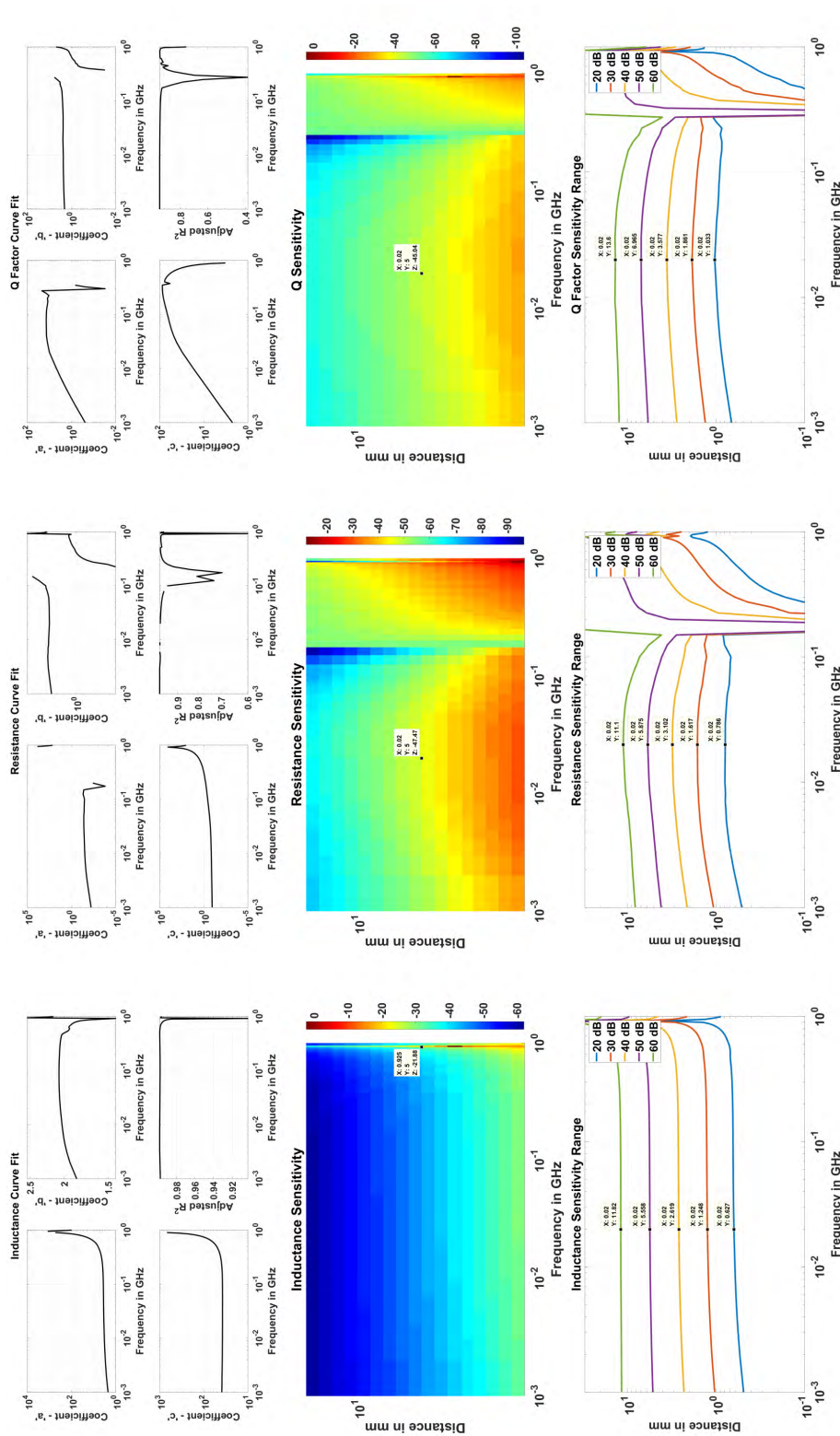


Figure A.4: Curve fit analysis for a two turn loop with PDMS coating with -25 % change in bone complex permittivity.

A.2 Effect of Rotation of the Sensor

The sensor is implanted inside bone by the surgeon. Therefore, it is possible that the loop is not exactly parallel to the implanted plate. In this case, there may be drop in output and sensitivity. If sensitivity changes, the displacement will be reported with some error. In this section , the curve fit analysis of the rotated sensor is provided for reference, based on which further analysis is presented in chapter 5.

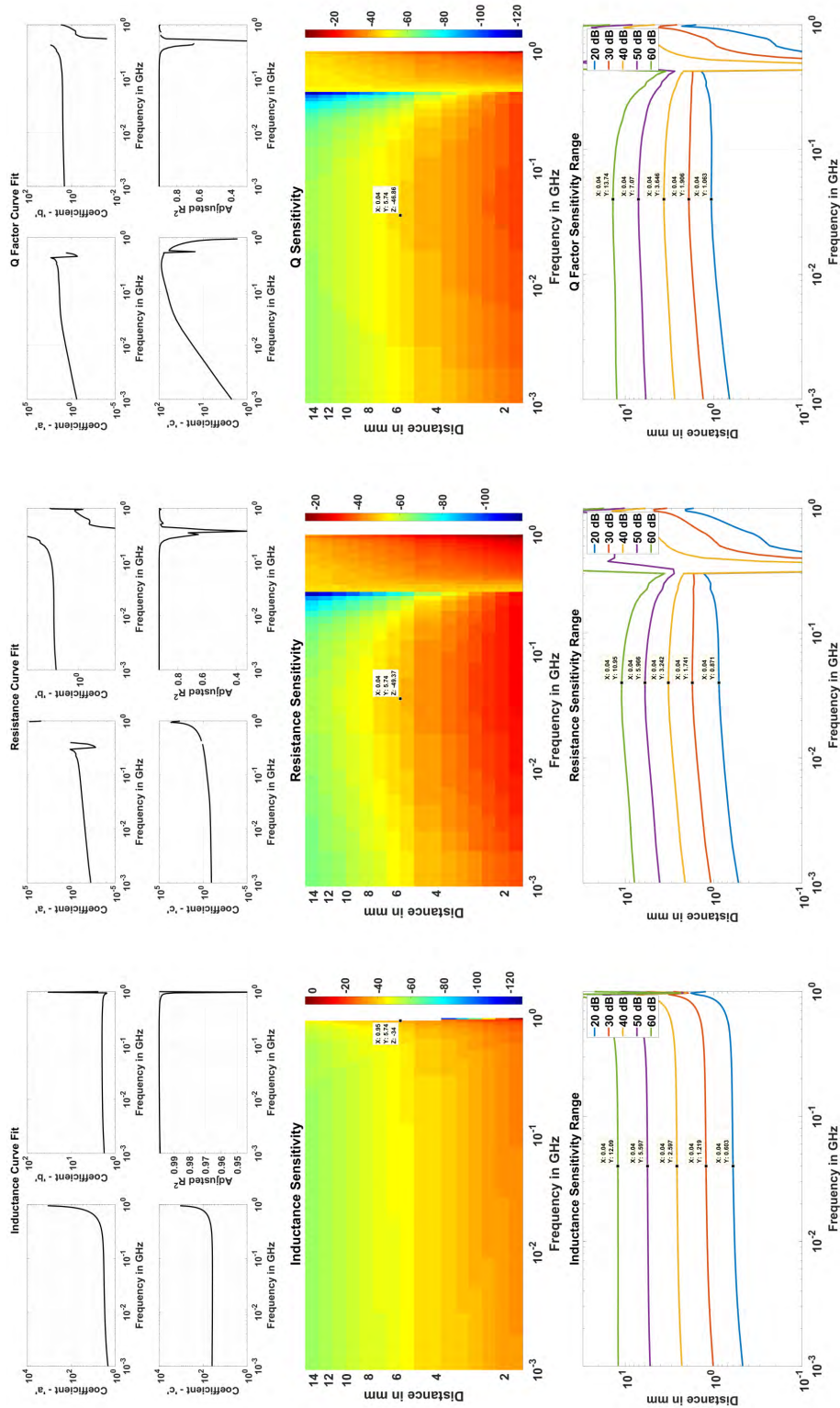


Figure A.5: rotation Angle = 0°

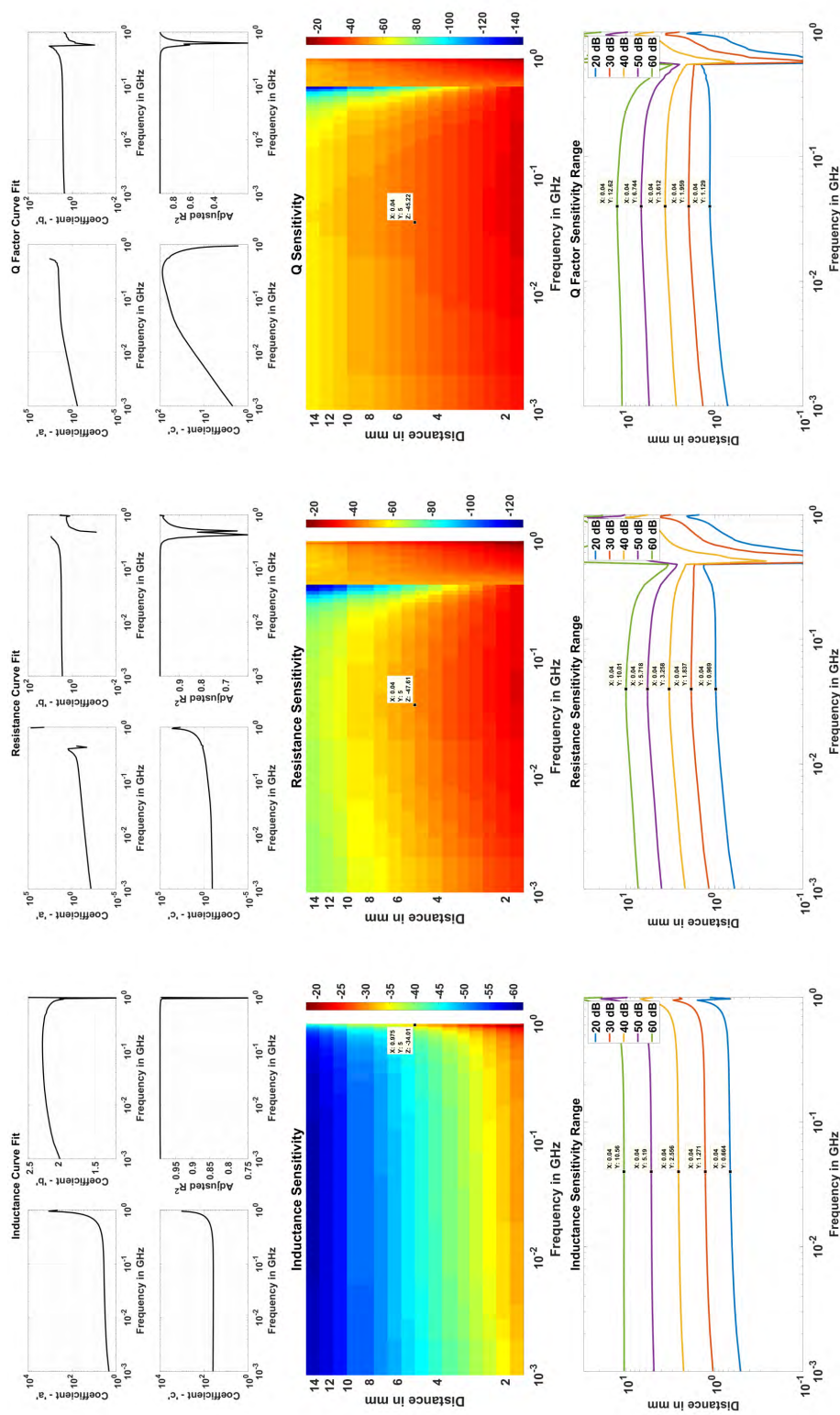


Figure A.6: rotation Angle = 45°

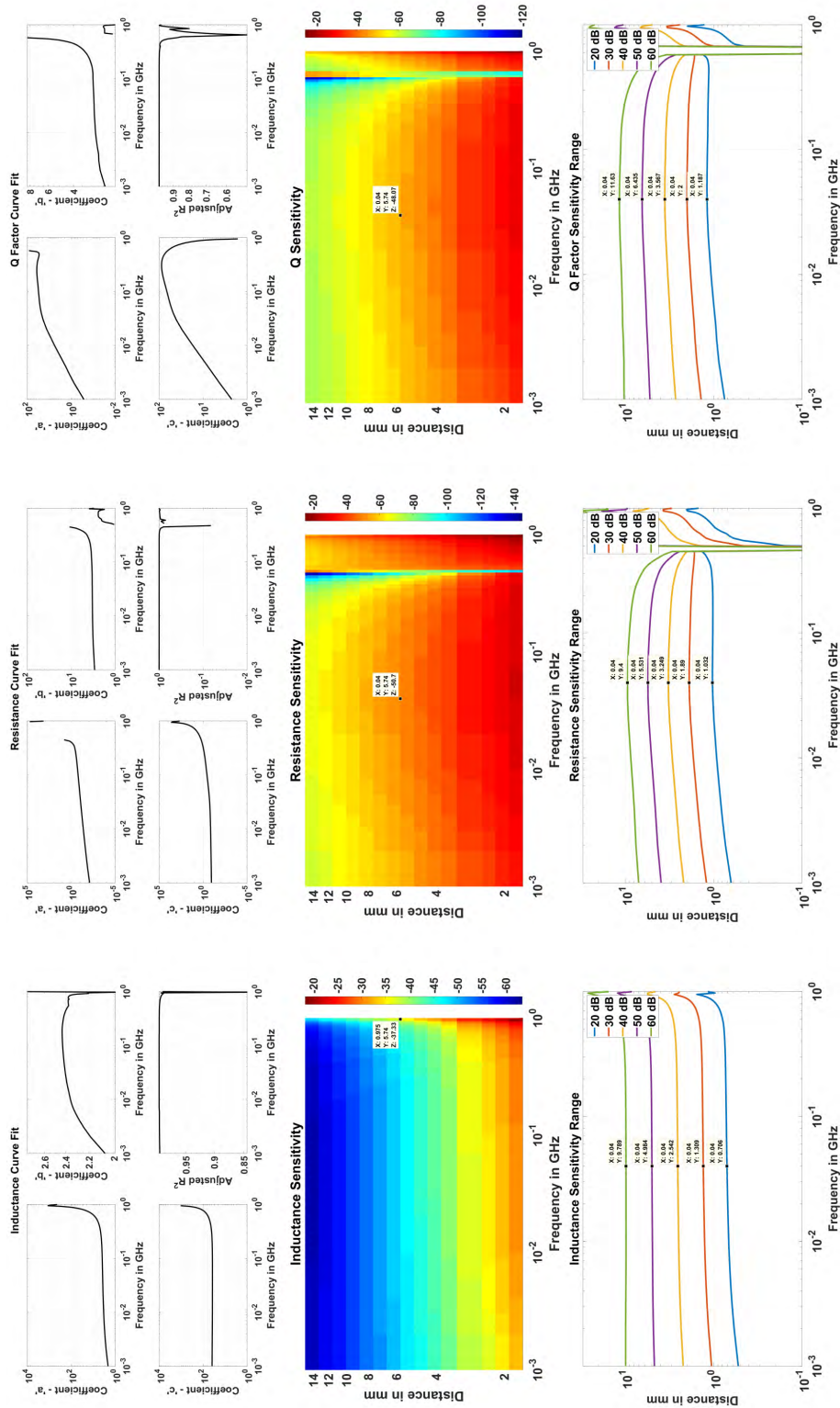


Figure A.7: rotation Angle = 60°

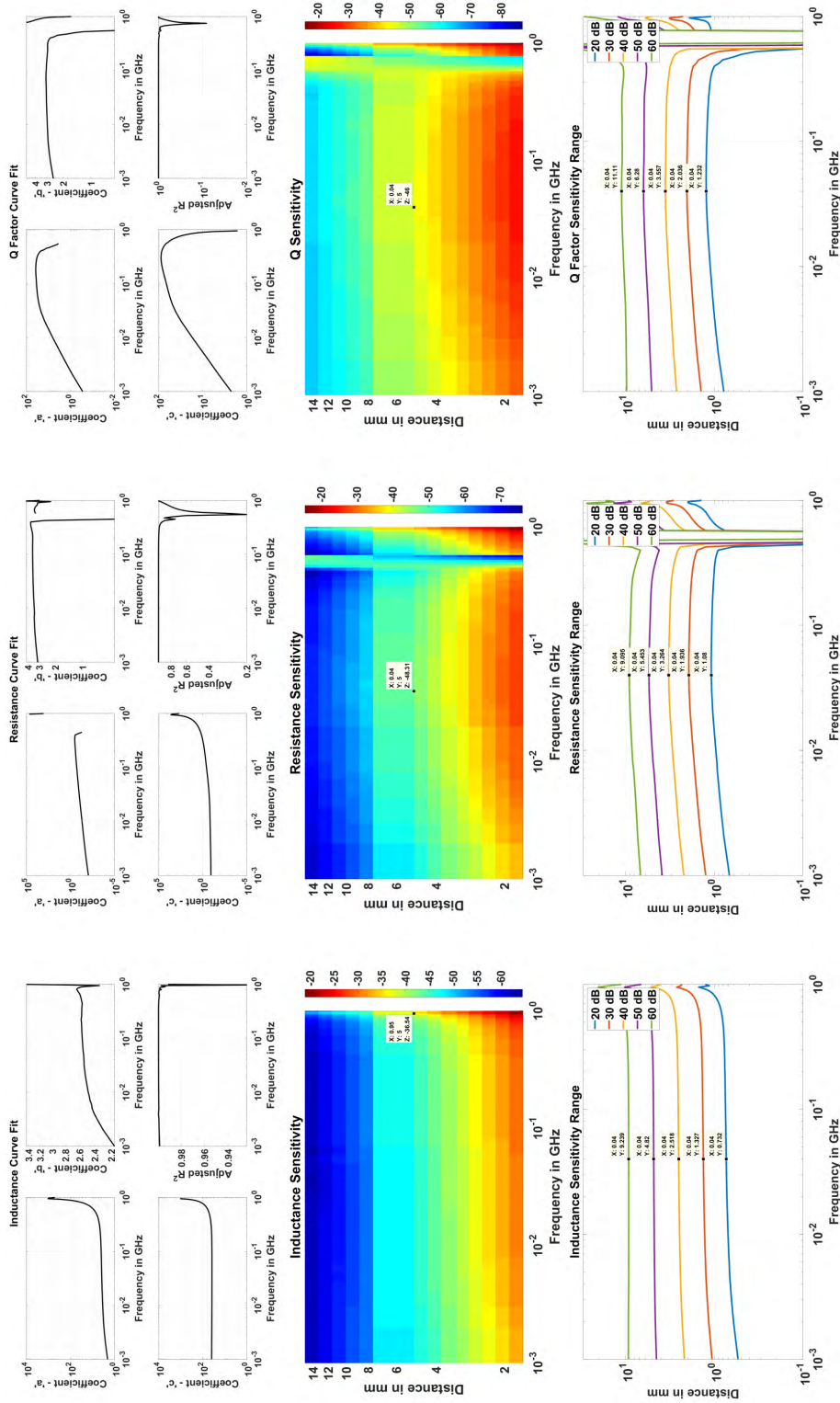


Figure A.8: rotation Angle = 90°

A.3 Different Eddy Current Loops

The number of turns of the eddy current have major effect on the inductance and resistance of the loop. With increasing number of turns N , the resistance increases linearly but inductance increases in proportion to N^2 . Also, due to capacitance between the two adjacent lines, the self resonant frequency drops to lower value. On one end, it is good to have higher inductance as it provides higher magnetic field. On the other hand lowering of self resonant frequency can decrease the stability. In chapter 5, the different aspects of changing the loop geometry are analyzed. Here, the curve fit analysis of the frequency-standoff data of inductance, resistance and Q factor is provided for reference.

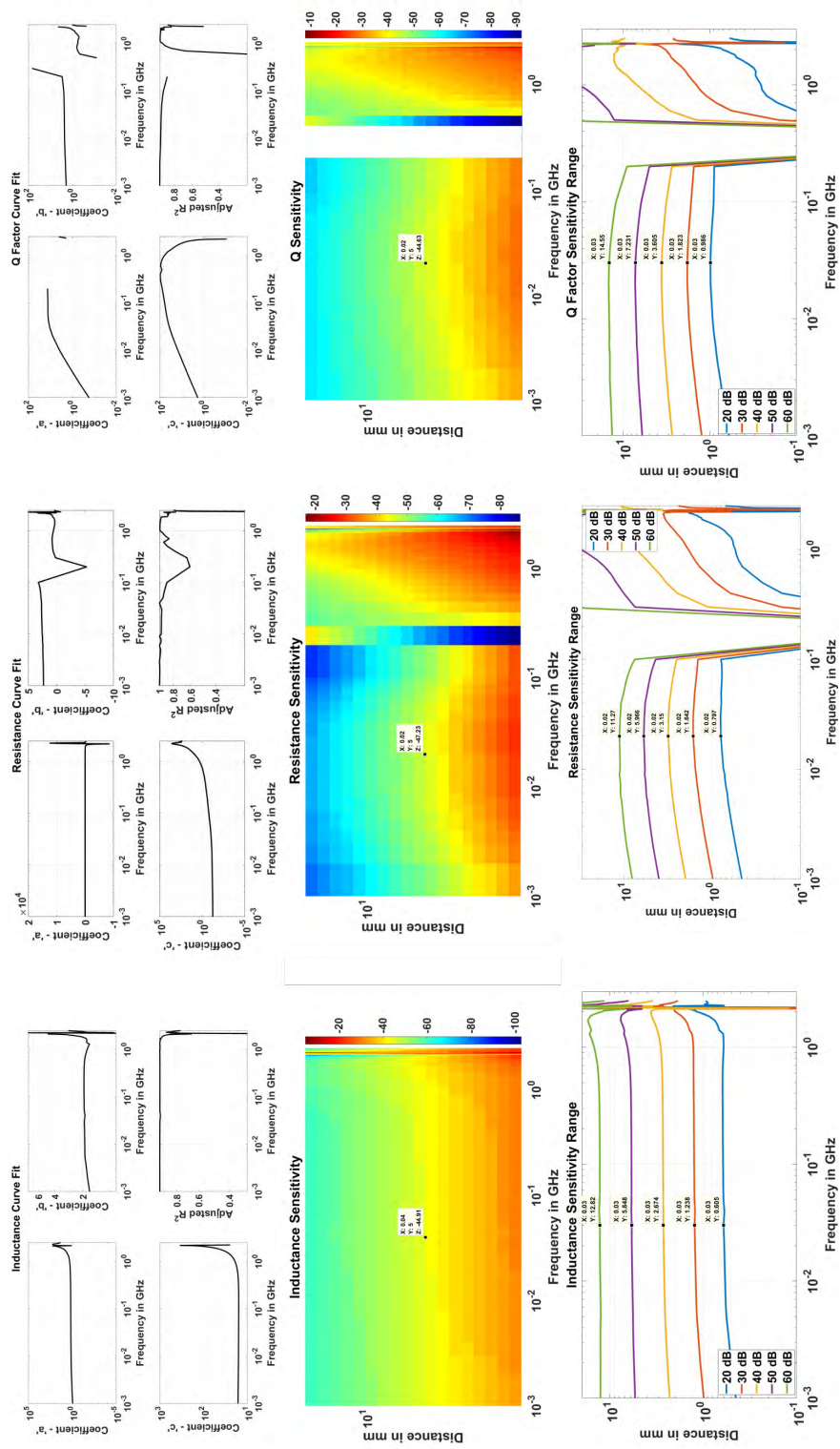


Figure A.9: Curve fit analysis for a one turn loop.

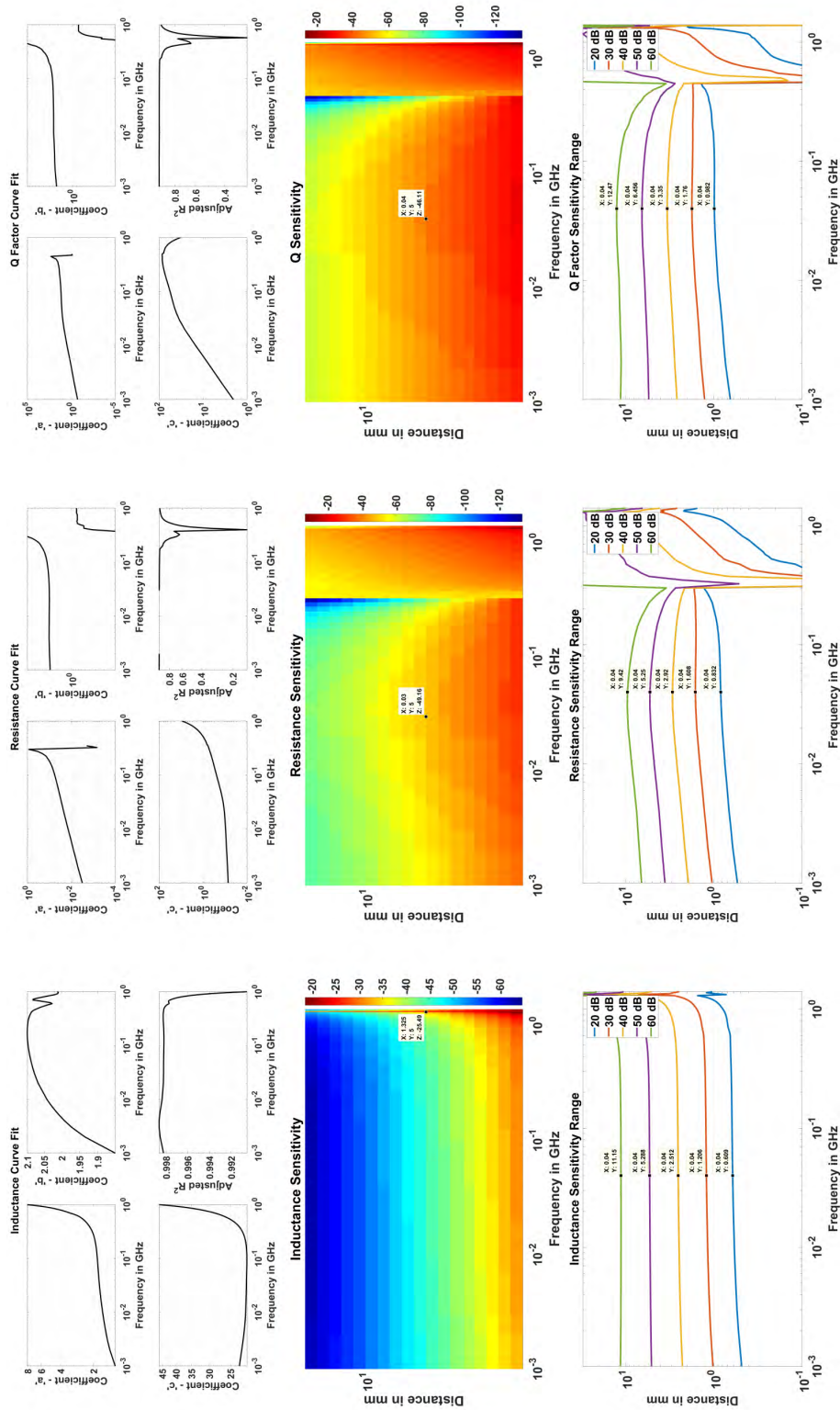


Figure A.10: Curve fit analysis for a two turn wide trace loop.

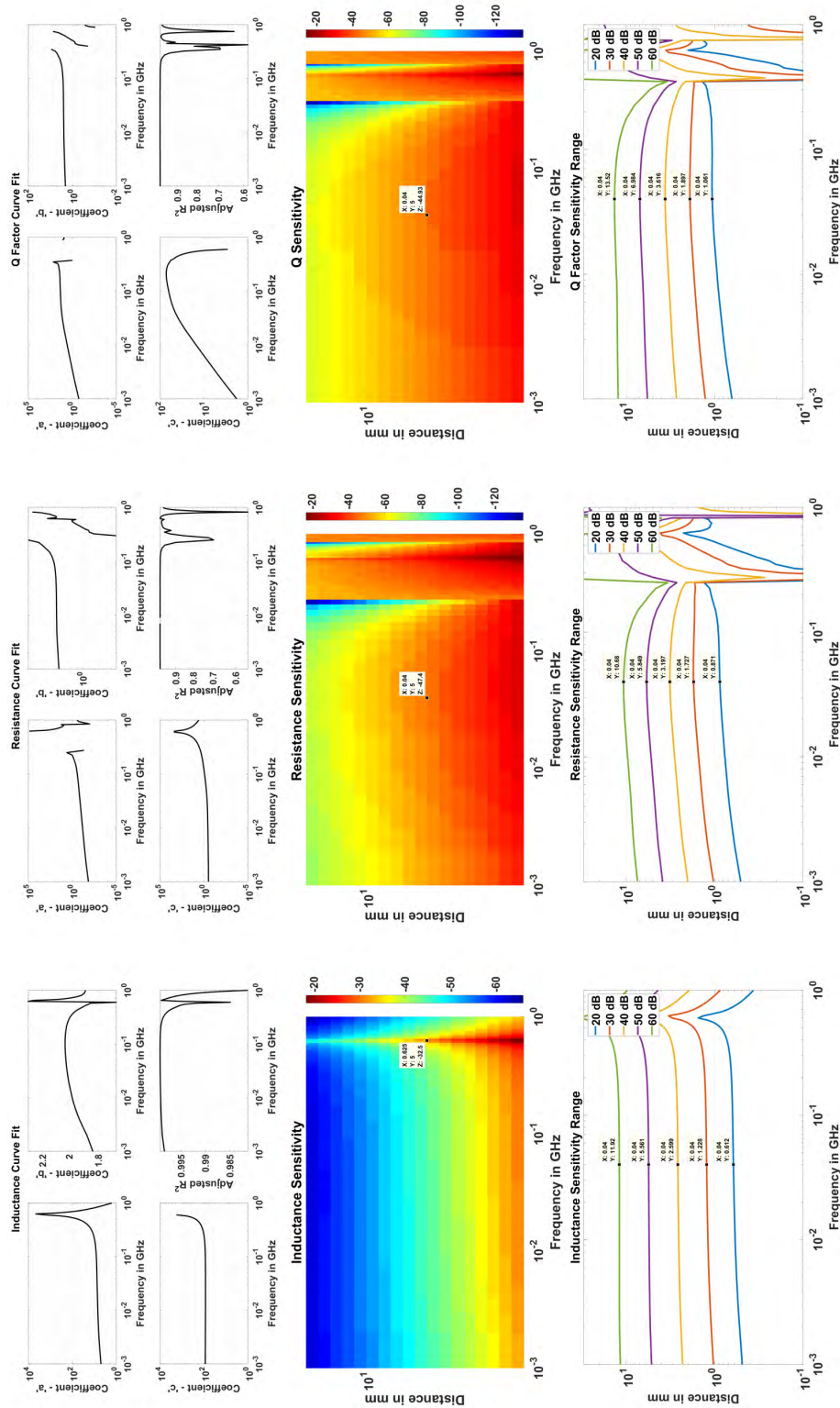


Figure A.11: Curve fit analysis for a three turn loop.

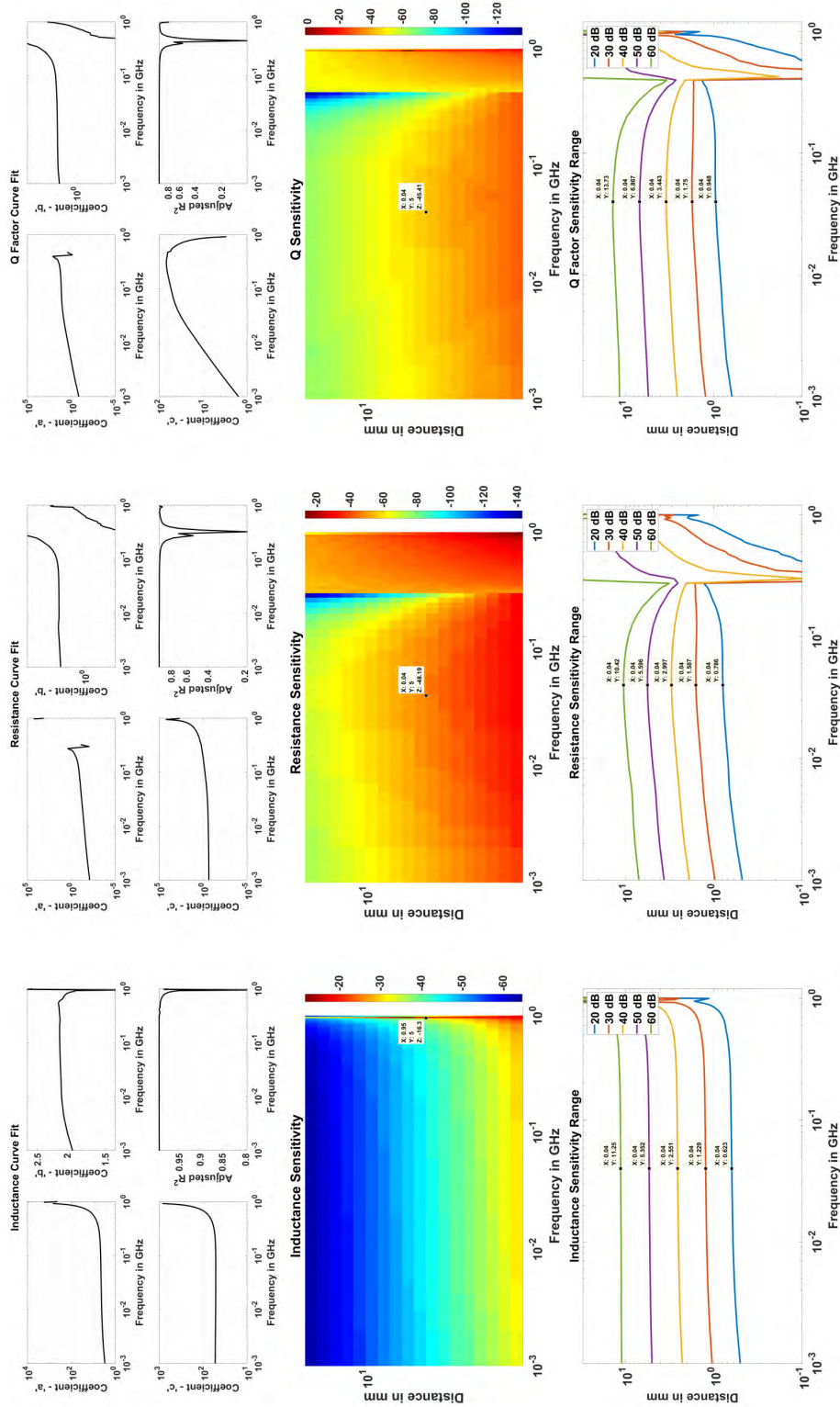


Figure A.12: Curve fit analysis for a three turn asymmetric loop.

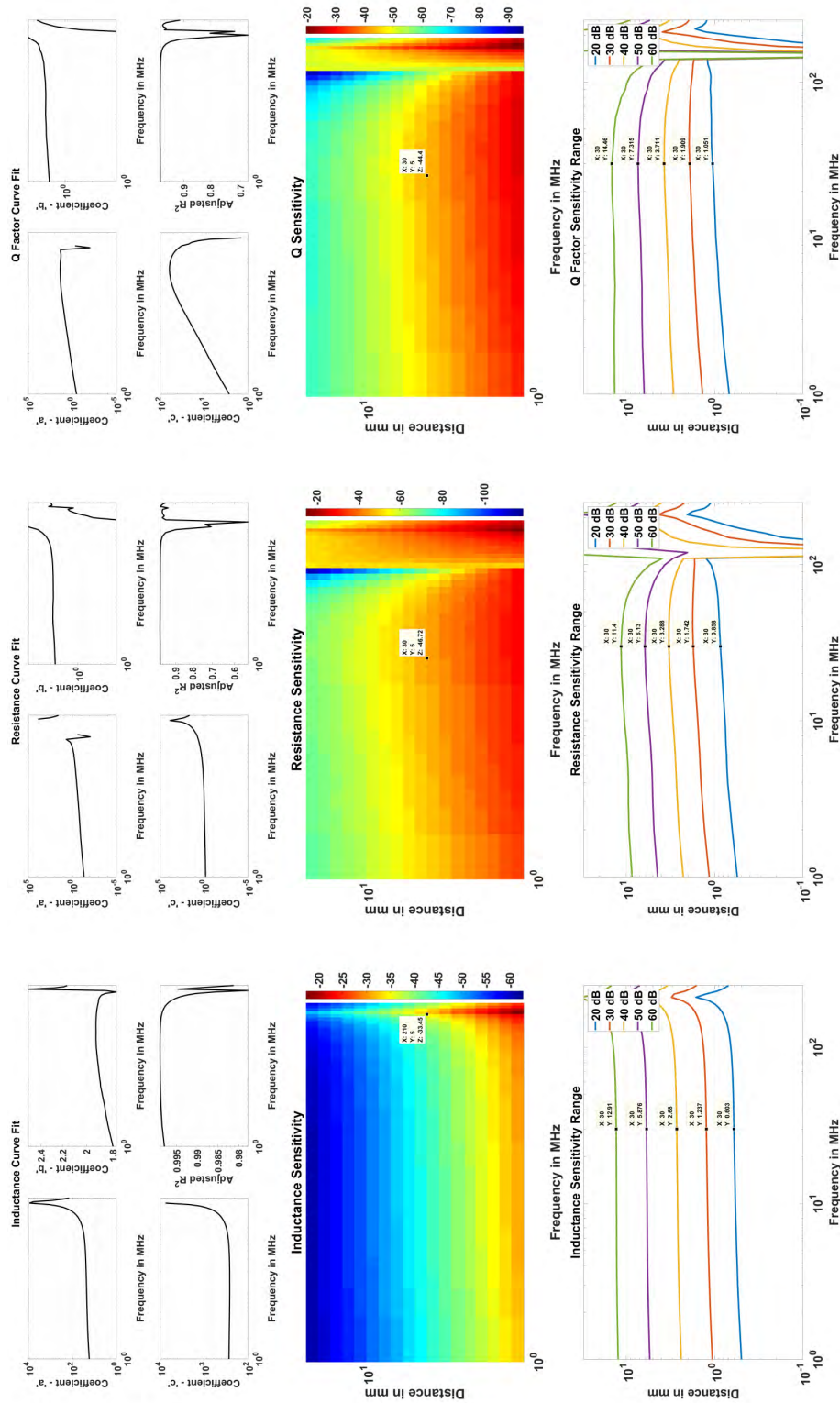


Figure A.13: Curve fit analysis for a three turn two layer loop.

Appendix B

MATLAB Codes

```
1 % HFSS Impedance Analysis
2 % Date Created 27 /05 /2017
3 % Author: Rajas Khokle
4
5 %% Get Frequency Points, Target Steps and Data from CSV Files
6 clear all;
7 close all;
8 % Frequency
9 [filename,pathname]=uigetfile('*.csv'); % Locate the file
10 fullfile=strcat(pathname,filename); % Create filename
11 Frequency=csvread(fullfile,1,1); % Frequency Vector
12 N=length(Frequency); % Length of Frequency Vector
13 % Distance
14 [filename,pathname]=uigetfile('*.csv'); % Locate the file
15 fullfile=strcat(pathname,filename); % Create filename
16 Distance=csvread(fullfile,1,1); % Distance Vector
```

```

17 M=length(Distance); % Length of Distance Vector
18 % Inductance
19 [filename,pathname]=uigetfile('*.csv'); % Locate the file
20 fullfile=strcat(pathname,filename); % Create filename
21 L=csvread(fullfile,1,1); % Inductance Data Matrix
22 % Resistance
23 [filename,pathname]=uigetfile('*.csv'); % Locate the file
24 fullfile=strcat(pathname,filename); % Create filename
25 R=csvread(fullfile,1,1); % Resistance Data Matrix
26 % Q Factor
27 [filename,pathname]=uigetfile('*.csv'); % Locate the file
28 fullfile=strcat(pathname,filename); % Create filename
29 Q=csvread(fullfile,1,1); % Q Data Matrix
30 %% Plot the 2D Data
31 figure();surf(Frequency,Distance,L);view(2);colormap('hot');
32 xlabel('Frequency in GHz');ylabel('Distance in mm');
33 title('Inductance in nH');ylim([Distance(1) Distance(end)]);
34 shading 'flat';set(gca, ...
    'FontWeight','Bold','FontSize',32);colormap;
35 figure();surf(Frequency,Distance,R);view(2);colormap('hot');
36 xlabel('Frequency in GHz');ylabel('Distance in mm');
37 title('Resistance in \Omega');ylim([Distance(1) Distance(end)]);
38 shading 'flat';set(gca, ...
    'FontWeight','Bold','FontSize',32);colormap;
39 figure();surf(Frequency,Distance,Q);view(2);colormap('hot');
40 xlabel('Frequency in GHz');ylabel('Distance in mm');
41 title('Q Factor');ylim([Distance(1) Distance(end)]);
42 shading 'flat';set(gca, ...
    'FontWeight','Bold','FontSize',32);colormap;

```

```
43 %% Statistical Analysis of the Data
44
45 %% Fit Inductance
46 % Preallocate the Memory for Curve Fit
47 La=zeros(N,1);
48 Lb=zeros(N,1);
49 Lc=zeros(N,1);
50 LR2=zeros(N,1);
51 S_L_Range=zeros(N,1);
52 A_L_Range=zeros(N,1);
53 % Curve Fit Inductance Data for Various Frequencies
54 for i=1:N
55     [fit,gof]=createFit_LAR_LM(Distance,L(:,i));
56     La(i)=fit.a;
57     Lb(i)=fit.b;
58     Lc(i)=fit.c;
59     LR2(i)=gof.adjrsquare;
60 % Sensitivity Range is the distance at which the sensitivity ...
    drops to 10%
61 % with respect to the sensitvity at Gap=1mm
62     S_L_Range(i)=nthroot(0.1,(Lb(i)-1));
63 % Amplitude Range is defined as the distance at which the ...
    Quantity reaches
64 % to 99% of its Final Value
65     A_L_Range(i)=10.^(-(1/abs(Lb(i))).*log10(0.01.*abs(Lc(i))./abs(La(i))));
66 end
67 % Plot the results
68 % figure();loglog(Frequency,-La,'Linewidth',3,'color',[0 0 0]);
69     % title('Curve Fit Co-efficient For Inductance');
```

```

70     % xlabel('Frequency in GHz'); ylabel('Coefficient - ...
        'a');grid on;
71     % set(gca,'fontsize',32,'fontweight','bold');
72 % figure();loglog(Frequency,-Lb,'Linewidth',3,'color',[0 0 0]);
73     %title('Curve Fit Co-efficient For Inductance');
74     %xlabel('Frequency in GHz');ylabel('Coefficient - ...
        'b');grid on;
75     %set(gca,'fontsize',32,'fontweight','bold');
76 % figure();loglog(Frequency,Lc,'Linewidth',3,'color',[0 0 0]);
77     %title('Curve Fit Co-efficient For Inductance');
78     %xlabel('Frequency in GHz');ylabel('Coefficient - ...
        'c');grid on;
79     %set(gca,'fontsize',32,'fontweight','bold');
80 % figure();plot(Frequency,LR2,'Linewidth',3,'color',[0 0 0]);
81     %title('Goodness of Curve Fit For Inductance');
82     %xlabel('Frequency in GHz');ylabel('Adjusted R^2');grid on;
83     %set(gca,'fontsize',32,'fontweight','bold');
84
85 figure();
86 subplot(2,2,1);loglog(Frequency,-La,'Linewidth',3,'color',[0 0 0]);
87     xlabel('Frequency in GHz');ylabel('Coefficient - 'a');grid on;
88     set(gca,'fontsize',24,'fontweight','bold');xlim([1e-3 1e0]);
89     xticks([0.001 0.01 0.1 1]);
90 subplot(2,2,2);loglog(Frequency,-Lb,'Linewidth',3,'color',[0 0 0]);
91     xlabel('Frequency in GHz');ylabel('Coefficient - 'b');grid on;
92     set(gca,'fontsize',24,'fontweight','bold');xlim([1e-3 1e0]);
93     xticks([0.001 0.01 0.1 1]);
94 subplot(2,2,3);loglog(Frequency,Lc,'Linewidth',3,'color',[0 0 0]);
95     xlabel('Frequency in GHz');ylabel('Coefficient - 'c');grid on;

```

```
96     set(gca,'fontsize',24,'fontweight','bold');xlim([1e-3 1e0]);
97     xticks([0.001 0.01 0.1 1]);
98 subplot(2,2,4);plot(Frequency,LR2,'Linewidth',3,'color',[0 0 0]);
99     xlabel('Frequency in GHz');ylabel('Adjusted R^2');grid on;
100    set(gca,'fontsize',24,'fontweight','bold');xlim([1e-3 1e0]);
101    xticks([0.001 0.01 0.1 1]);
102
103 % figure();loglog(Frequency,S_L.Range,'Linewidth',3,'color',[0 0 0]);
104     %title('Nominal Sensitivity Range For Inductance');
105     %xlabel('Frequency in GHz');ylabel('Range in mm');grid on;
106     %set(gca,'fontsize',32,'fontweight','bold');
107 % figure();loglog(Frequency,A_L.Range,'Linewidth',3,'color',[0 0 0]);
108     %title('Nominal Amplitude Range For Inductance');
109     %xlabel('Frequency in GHz');ylabel('Range in mm');grid on;
110     %set(gca,'fontsize',32,'fontweight','bold');
111
112 figure();
113 subplot(1,2,1);loglog(Frequency,S_L.Range,'Linewidth',3,'color',[0 ...
114     0 0]);
115     title('For Inductance');xlabel('Frequency in GHz');
116     ylabel('Sensitivity Range in mm');grid on;
117     set(gca,'fontsize',32,'fontweight','bold');xlim([1e-3 1e0]);
118     xticks([0.001 0.01 0.1 1]);
119 subplot(1,2,2);loglog(Frequency,A_L.Range,'Linewidth',3,'color',[0 ...
120     0 0]);
121     title('For Inductance');xlabel('Frequency in GHz');
122     ylabel('Amplitude Range in mm');grid on;
123     set(gca,'fontsize',32,'fontweight','bold');xlim([1e-3 1e0]);
124     xticks([0.001 0.01 0.1 1]);
```

```
123 %% Fit Resistance
124 % Preallocate the Memory for Curve Fit
125 Ra=zeros(N,1);
126 Rb=zeros(N,1);
127 Rc=zeros(N,1);
128 RR2=zeros(N,1);
129 S_R.Range=zeros(N,1);
130 A_R.Range=zeros(N,1);
131 % Curve Fit Resistance Data for Various Frequencies
132 for i=1:N
133     [fit,gof]=createFit_LAR_LM(Distance,R(:,i));
134     Ra(i)=fit.a;
135     Rb(i)=fit.b;
136     Rc(i)=fit.c;
137     RR2(i)=gof.adjrsquare;
138 % Sensitivity_Range the distance at which the sensitivity drops ...
    to 10%
139 % with respect to the sensitivy at Gap=1mm
140     S_R.Range(i)=nthroot(0.1,(Rb(i)-1));
141 % Amplitude Range is defined as the distance at which the ...
    Quantity reaches
142 % to 90% of its Final Value
143     A_R.Range(i)=10.^((1/abs(Rb(i))).*log10(0.01.*abs(Rc(i))./abs(Ra(i))));
144
145 end
146
147 % figure();loglog(Frequency,Ra,'Linewidth',3,'color',[0 0 0]);
148     %title('Curve Fit Co-efficient For Resistance');
```

```
149     xlabel('Frequency in GHz');ylabel('Coefficient - ...
        'a');grid on;
150     %set(gca,'fontsize',32,'fontweight','bold');
151 % figure();plot(Frequency,Rb,'Linewidth',3,'color',[0 0 0]);
152     %title('Curve Fit Co-efficient For Resistance');
153     xlabel('Frequency in GHz');ylabel('Coefficient - ...
        'b');grid on;
154     %set(gca,'fontsize',32,'fontweight','bold');
155 % figure();loglog(Frequency,Rc,'Linewidth',3,'color',[0 0 0]);
156     %title('Curve Fit Co-efficient For Resistance');
157     xlabel('Frequency in GHz');ylabel('Coefficient - ...
        'c');grid on;
158     %set(gca,'fontsize',32,'fontweight','bold');
159 % figure();plot(Frequency,RR2,'Linewidth',3,'color',[0 0 0]);
160     %title('Goodness of Curve Fit For Resistance');
161     xlabel('Frequency in GHz');ylabel('Adjusted R^2');grid on;
162     %set(gca,'fontsize',32,'fontweight','bold');
163
164 figure();
165 subplot(2,2,1);loglog(Frequency,Ra,'Linewidth',3,'color',[0 0 0]);
166     xlabel('Frequency in GHz');ylabel('Coefficient - 'a');grid on;
167     set(gca,'fontsize',24,'fontweight','bold');xlim([1e-3 1e0]);
168     xticks([0.001 0.01 0.1 1]);
169 subplot(2,2,2);loglog(Frequency,-Rb,'Linewidth',3,'color',[0 0 0]);
170     xlabel('Frequency in GHz');ylabel('Coefficient - 'b');grid on;
171     set(gca,'fontsize',24,'fontweight','bold');xlim([1e-3 1e0]);
172     xticks([0.001 0.01 0.1 1]);
173 subplot(2,2,3);loglog(Frequency,Rc,'Linewidth',3,'color',[0 0 0]);
174     xlabel('Frequency in GHz');ylabel('Coefficient - 'c');grid on;
```

```

175     set(gca,'fontsize',24,'fontweight','bold');xlim([1e-3 1e0]);
176     xticks([0.001 0.01 0.1 1]);
177 subplot(2,2,4);plot(Frequency,RR2,'Linewidth',3,'color',[0 0 0]);
178     xlabel('Frequency in GHz');ylabel('Adjusted R^2');grid on;
179     set(gca,'fontsize',24,'fontweight','bold');xlim([1e-3 1e0]);
180     xticks([0.001 0.01 0.1 1]);
181
182
183 % figure();loglog(Frequency,S_R.Range,'Linewidth',3,'color',[0 0 0]);
184     %title('For Resistance');xlabel('Frequency in ...
        GHz');ylabel('Range in mm');
185     %grid ...
        on;set(gca,'fontsize',32,'fontweight','bold');xlim([1e-3 ...
        1e0]);
186     %xticks([0.001 0.01 0.1 1]);
187 % figure();loglog(Frequency,A_R.Range,'Linewidth',3,'color',[0 0 0]);
188     %title('For Resistance');xlabel('Frequency in ...
        GHz');ylabel('Range in mm');
189     %grid ...
        on;set(gca,'fontsize',32,'fontweight','bold');xlim([1e-3 ...
        1e0]);
190     %xticks([0.001 0.01 0.1 1]);
191
192 figure();
193 subplot(1,2,1);loglog(Frequency,S_R.Range,'Linewidth',3,'color',[0 ...
        0 0]);
194     title('For Resistance');xlabel('Frequency in GHz');
195     ylabel('Sensitivity Range in mm');grid on;
196     set(gca,'fontsize',32,'fontweight','bold');xlim([1e-3 1e0]);

```

```

197     xticks([0.001 0.01 0.1 1]);
198 subplot(1,2,2);loglog(Frequency,A-R-Range,'Linewidth',3,'color',[0 ...
    0 0]);
199     title('For Resistance');xlabel('Frequency in GHz');
200     ylabel('Amplitude Range in mm');grid on;
201     set(gca,'fontsize',32,'fontweight','bold');xlim([1e-3 1e0]);
202     xticks([0.001 0.01 0.1 1]);
203 %% Fit Q Factor
204 % Preallocate the Memory for Curve Fit
205 Qa=zeros(N,1);
206 Qb=zeros(N,1);
207 Qc=zeros(N,1);
208 QR2=zeros(N,1);
209 S_Q_Range=zeros(N,1);
210 A_Q_Range=zeros(N,1);
211 % Curve Fit Inductance Data for Various Frequencies
212 for i=1:N
213     [fit,gof]=createFit_IAR_LM(Distance,Q(:,i));
214     Qa(i)=fit.a;
215     Qb(i)=fit.b;
216     Qc(i)=fit.c;
217     QR2(i)=gof.adjrsquare;
218 % Sensitivity Range is distance at which the sensitivity drops to 10%
219 % with respect to the sensitivty at Gap=1mm
220     S_Q_Range(i)=nthroot(0.1,(Qb(i)-1));
221 % Amplitude Range is defined as the distance at which the ...
    Quantity reaches
222 % to 90% of its Final Value
223     A_Q_Range(i)=10.^((-1/abs(Rb(i))).*log10(0.01.*abs(Rc(i))./abs(Ra(i))));

```

```

224 end
225 % Plot the results
226 % figure();loglog(Frequency,Qa,'Linewidth',3,'color',[0 0 0]);
227     %title('Curve Fit Co-efficient For Q ...
           Factor');xlabel('Frequency in GHz');
228     %ylabel('Coefficient - ''a'');grid on;
229     %set(gca,'fontsize',32,'fontweight','bold');
230 % figure();plot(Frequency,Qb,'Linewidth',3,'color',[0 0 0]);
231     %title('Curve Fit Co-efficient For Q ...
           Factor');xlabel('Frequency in GHz');
232     %ylabel('Coefficient - ''b'');grid on;
233     %set(gca,'fontsize',32,'fontweight','bold');
234 % figure();loglog(Frequency,Qc,'Linewidth',3,'color',[0 0 0]);
235     %title('Curve Fit Co-efficient For Q Factor');
236     %xlabel('Frequency in GHz');ylabel('Coefficient - ...
           ''c'');grid on;
237     %set(gca,'fontsize',32,'fontweight','bold');
238 % figure();plot(Frequency,QR2,'Linewidth',3,'color',[0 0 0]);
239     %title('Goodness of Curve Fit For Q ...
           Factor');xlabel('Frequency in GHz');
240     %ylabel('Adjusted R^2');grid on;
241     %set(gca,'fontsize',32,'fontweight','bold');
242
243 figure();
244 subplot(2,2,1);loglog(Frequency,-Qa,'Linewidth',3,'color',[0 0 0]);
245     xlabel('Frequency in GHz');ylabel('Coefficient - ''a'');grid on;
246     set(gca,'fontsize',24,'fontweight','bold');xlim([1e-3 1e0]);
247     xticks([0.001 0.01 0.1 1]);
248 subplot(2,2,2);loglog(Frequency,-Qb,'Linewidth',3,'color',[0 0 0]);

```

```
249     xlabel('Frequency in GHz');ylabel('Coefficient - 'b'');grid on;
250     set(gca,'fontsize',24,'fontweight','bold');xlim([1e-3 1e0]);
251     xticks([0.001 0.01 0.1 1]);
252 subplot(2,2,3);loglog(Frequency,Qc,'Linewidth',3,'color',[0 0 0]);
253     xlabel('Frequency in GHz');ylabel('Coefficient - 'c'');grid on;
254     set(gca,'fontsize',24,'fontweight','bold');xlim([1e-3 1e0]);
255     xticks([0.001 0.01 0.1 1]);
256 subplot(2,2,4);plot(Frequency,QR2,'Linewidth',3,'color',[0 0 0]);
257     xlabel('Frequency in GHz');ylabel('Adjusted R^2');grid on;
258     set(gca,'fontsize',24,'fontweight','bold');xlim([1e-3 1e0]);
259     xticks([0.001 0.01 0.1 1]);
260
261 % figure();loglog(Frequency,S-Q_Range,'Linewidth',3,'color',[0 0 0]);
262     %title('Sensitivity Range For Q Factor');xlabel('Frequency in ...
263         GHz');
264     %ylabel('Sensitivity Range');grid on;
265     %set(gca,'fontsize',32,'fontweight','bold');
266 % figure();loglog(Frequency,A-Q_Range,'Linewidth',3,'color',[0 0 0]);
267     %title('Amplitude Range For Q Factor');xlabel('Frequency in ...
268         GHz');
269     %ylabel('Amplitude Range');grid on;
270     %set(gca,'fontsize',32,'fontweight','bold');
269 figure();
270 subplot(1,2,1);loglog(Frequency,S-Q_Range,'Linewidth',3,'color',[0 ...
271         0 0]);
272     title('For Q Factor');xlabel('Frequency in GHz');
273     ylabel('Sensitivity Range in mm');grid on;
274     set(gca,'fontsize',32,'fontweight','bold');xlim([1e-3 1e0]);
275     xticks([0.001 0.01 0.1 1]);
```

```
275 subplot(1,2,2);loglog(Frequency,A-Q-Range,'Linewidth',3,'color',[0 ...
    0 0]);
276     title('For Q Factor');xlabel('Frequency in GHz');
277     ylabel('Amplitude Range in mm');grid on;
278     set(gca,'fontsize',32,'fontweight','bold');xlim([1e-3 1e0]);
279     xticks([0.001 0.01 0.1 1]);
280
281
282 %% Plotting Sensitivity as a function of Frequency and Distance
283
284 %% Preallocation of Variables
285 L_Sen=ones(size(L));
286 Out_LC=ones(size(L));
287 Out_LC1=ones(size(L));
288 DelOut_LC=ones(size(L));
289
290 R_Sen=ones(size(R));
291 Out_RC=ones(size(R));
292 Out_RC1=ones(size(R));
293 DelOut_RC=ones(size(R));
294
295 Q_Sen=ones(size(Q));
296 Out_QC=ones(size(Q));
297 Out_QC1=ones(size(Q));
298 DelOut_QC=ones(size(Q));
299 %% Inductance Sensitivity
300 for j=1:N
301     for i=1:M
302         L_Sen(i,j)=Distance(i);
```

```

303     Out_LC(i,j)=La(j).*L_Sen(i,j).^ (Lb(j))+Lc(j);
304     Out_LC1(i,j)=La(j).*(L_Sen(i,j)+0.02).^ (Lb(j))+Lc(j);
305     DelOut_LC(i,j)=(Out_LC1(i,j)-Out_LC(i,j))./Out_LC(i,j));
306
307     end
308
309 end
310 % ...
        figure();surf(Frequency,Distance,(abs(DelOut_LC)));view(2);colormap('jet');
311     %ylim([Distance(1) Distance(end)]);shading ...
        'flat';xlabel('Frequency in GHz');
312     %ylabel('Distance in mm');title('Inductance ...
        Sensitivity');colorbar;
313     %set(gca, 'FontWeight','Bold','FontSize',32);
314 % ...
        figure();surf(Frequency,Distance,log2(1/abs(DelOut_LC)));view(2);colormap('jet');
315     %ylim([Distance(1) Distance(end)]);shading ...
        'flat';xlabel('Frequency in GHz');
316     %ylabel('Distance in mm');title('Inductance ...
        Sensitivity');colorbar;
317     %set(gca, 'FontWeight','Bold','FontSize',32);
318 figure();surf(Frequency,Distance,1e6*(abs(DelOut_LC)));view(2);colormap('jet');
319     ylim([Distance(1) Distance(end)]);shading ...
        'flat';xlabel('Frequency in GHz');
320     ylabel('Distance in mm');title('Inductance ...
        Sensitivity');colorbar;
321     set(gca, 'FontWeight','Bold','FontSize',32);
322

```

```

323 % ...
      figure();surf(Frequency,Distance,10.*log10(abs(DelOut_LC)));view(2);
324 %colormap('jet');ylim([Distance(1) Distance(end)]);shading ...
      'flat';
325 %xlabel('Frequency in GHz'),ylabel('Distance in mm');
326 %title('Inductance Sensitivity');colorbar;
327 %set(gca, 'FontWeight','Bold','FontSize',32);
328 %% Resistance Sensitivity
329 for j=1:N
330     for i=1:M
331         R_Sen(i,j)=Distance(i);
332         Out_RC(i,j)=Ra(j).*R_Sen(i,j).^(Rb(j))+Rc(j);
333         Out_RC1(i,j)=Ra(j).*(R_Sen(i,j)+0.01).^(Rb(j))+Rc(j);
334         DelOut_RC(i,j)=(Out_RC1(i,j)-Out_RC(i,j))./Out_RC(i,j));
335
336     end
337
338 end
339 figure();surf(Frequency,Distance,10.*log10(abs(DelOut_RC)));view(2);
340     colormap('jet');ylim([Distance(1) Distance(end)]);shading 'flat';
341     xlabel('Frequency in GHz');ylabel('Distance in mm');
342     title('Resistance Sensitivity');set(gca, ...
          'FontWeight','Bold','FontSize',32);
343 %% Q Sensitivity
344 for j=1:N
345     for i=1:M
346         Q_Sen(i,j)=Distance(i);
347         Out_QC(i,j)=Qa(j).*Q_Sen(i,j).^(Qb(j))+Qc(j);
348         Out_QC1(i,j)=Qa(j).*(Q_Sen(i,j)+0.01).^(Qb(j))+Qc(j);

```

```
349         DelOut_QC(i,j)=(Out_QC1(i,j)-Out_QC(i,j))./Out_QC(i,j));
350     end
351
352 end
353 figure();surf(Frequency,Distance,10.*log10(abs(DelOut_QC)));view(2);colormap('jet');
354     ylim([Distance(1) Distance(end)]);shading ...
355         'flat';xlabel('Frequency in GHz'),
356         ylabel('Distance in mm');title('Q Sensitivity');
357     set(gca, 'FontWeight','Bold','FontSize',32);colormap;
358 %% Sensitivity Range Calculation
359 %% Define sensitivity level in dB and convert to linear; Preallocate
360 db=-[20 30 40 50 60];
361 lin=10.^(db./10);
362 %% Pre-allocation for speed
363 L_S=ones(N,1);
364 Out_L=L_S;
365 Out_L1=L_S;
366 DelOut_L=L_S;
367 L_S_Range=ones(N,length(db));
368
369 R_S=ones(N,1);
370 Out_R=L_S;
371 Out_R1=L_S;
372 DelOut_R=L_S;
373 R_S_Range=ones(N,length(db));
374
375 Q_S=ones(N,1);
376 Out_Q=L_S;
```

```

377 Out_Q1=L-S;
378 DelOut_Q=L-S;
379 Q-S_Range=ones(N,length(db));
380 %% Inductance Sensitivity Range
381 for k=1:length(db)
382     for j=1:N
383         for i=1:100000
384             L_S(j)=i./1000;
385             Out_L(j)=La(j).*L_S(j).^(Lb(j))+Lc(j);
386             Out_L1(j)=La(j).*(L_S(j)+0.01).^(Lb(j))+Lc(j);
387             DelOut_L(j)=(Out_L1(j)-Out_L(j))./Out_L(j);
388             if abs(DelOut_L(j))<lin(k)
389                 break;
390             end
391         end
392     end
393 L_S_Range(:,k)=L_S;
394 end
395 %%
396 figure();
397 for k=1:length(db)
398     loglog(Frequency,L_S_Range(:,k),'LineWidth',4);
399     hold on;
400 end
401 grid on; set(gca,'fontsize',32,'fontweight','bold','XScale','log');
402 xlabel('Frequency in GHz','fontsize',32,'fontweight','bold');
403 ylabel('Distance in mm','fontsize',32,'fontweight','bold');
404 title('Inductance Sensitivity ...
         Range','fontsize',32,'fontweight','bold');

```

```
405 legend('20 dB','30 dB','40 dB','50 dB','60 dB');
406 %% Resistance Sensitivity Range
407 for k=1:length(db)
408     for j=1:N
409         for i=1:100000
410             R_S(j)=i/1000;
411             Out_R(j)=Ra(j).*R_S(j).^(Rb(j))+Rc(j);
412             Out_R1(j)=Ra(j).*(R_S(j)+0.01).^(Rb(j))+Rc(j);
413             DelOut_R(j)=(Out_R1(j)-Out_R(j))./Out_R(j));
414             if abs(DelOut_R(j))<lin(k)
415                 break;
416             end
417         end
418     end
419     R_S_Range(:,k)=R_S;
420 end
421 figure();
422 for k=1:length(db)
423     loglog(Frequency,R_S_Range(:,k),'LineWidth',4);
424     hold on;
425 end
426 grid on; set(gca,'fontsize',32,'fontweight','bold','XScale','log');
427 xlabel('Frequency in GHz','fontsize',32,'fontweight','bold');
428 ylabel('Distance in mm','fontsize',32,'fontweight','bold');
429 title('Resistance Sensitivity ...
         Range','fontsize',32,'fontweight','bold');
430 legend('20 dB','30 dB','40 dB','50 dB','60 dB');
431 %% Q Sensitivity Range
432 for k=1:length(db)
```

```

433 for j=1:N
434     for i=1:100000
435         Q-S(j)=i/1000;
436         Out_Q(j)=Qa(j).*Q-S(j).^ (Qb(j))+Qc(j);
437         Out_Q1(j)=Qa(j).*(Q-S(j)+0.01).^ (Qb(j))+Qc(j);
438         DelOut_Q(j)=(Out_Q1(j)-Out_Q(j))./Out_Q(j));
439         if abs(DelOut_Q(j))<lin(k)
440             break;
441         end
442     end
443 end
444 Q-S.Range(:,k)=Q-S;
445 end
446 figure();
447 for k=1:length(db)
448     loglog(Frequency,Q-S.Range(:,k),'LineWidth',4);
449     hold on;
450     end
451     grid on; set(gca,'fontsize',32,'fontweight','bold','XScale','log');
452     xlabel('Frequency in GHz','fontsize',32,'fontweight','bold');
453     ylabel('Distance in mm','fontsize',32,'fontweight','bold');
454     title('Q Factor Sensitivity ...
           Range','fontsize',32,'fontweight','bold');
455     legend('20 dB','30 dB','40 dB','50 dB','60 dB');

1 % Experiment Setup - Refer to flowchart --
2 % Author : Rajas Khokle
3 % Date : 12/ 06 /2017

```

```
4 % IMPORTANT: Need to run MATLAB in Administrator mode to get ...
    access to controller
5 % Update: Added code to interface Agilent PNA-x 1 Port Measurement
6
7 %% Append the necessary path
8 close all;
9 clear variables;
10 A=NET.addAssembly('C:\Program Files ...
    (x86)\Newport\MotionControl\CONEX-CC\...Bin\Newport.CONEXCC.CommandInterface.dll');
11 delete(instrfind);          % Delete any previously opened ...
    ports/instances
12 %% Initialize the Controller
13 CC=CommandInterfaceConexCC.ConexCC(); % set CC equal to the ...
    library.class
14 R=CC.OpenInstrument('COM3'); % Open the ...
    instrument
15 %% Connect VNA
16 oldObjects=instrfind;      % For VNA ...
    Old Objects
17 if ~isempty(oldObjects)
18     delete(oldObjects);
19     clear oldObjects;
20 end
21
22 VNAVISAAAddress='TCPIP0::169.254.60.85::inst0::INSTR'; % ...
    Address for VNA
23 % Define frequency range of 2.3GHz to 2.6GHz
24 frequencyRange = [10e6 1e9]; % 10 ...
    MHZ to 1GHZ
```

```

25 % Number of points in measurement
26 numPoints = 100;
27 % Create a VISA connection to interface with instrument
28 instrObj = visa('agilent',VNAVISAAddress);
29 % Set up connection parameters for transfer of measurement data ...
    from the
30 % instrument
31 instrObj.InputBufferSize = 10e6;
32 instrObj.ByteOrder = 'littleEndian';
33 % Open connection to the instrument and clear hardware buffer of ...
    instrument
34 fopen(instrObj);
35 clrdevice(instrObj);
36 % Display information about instrument
37 IDNString = query(instrObj, '*IDN?');
38 fprintf('Connected to: %s\n', IDNString);
39 %% Initialize VNA
40 %%%%%%%%%%%%%%%%%%%%%%%%%%%%%%%%%%%%%%%%%%%%%%%%%%%%%%%%%%%%%%%%%%%%%%%%%
41 %%%%%%%%%%%%%%%%%%%%%%%%%%%%%%%%%%%%%%%%%%%%%%%%%%%%%%%%%%%%%%%%%%%%%%%%% Measurement Setup %%%%%%%%%%%%%%%%%%%%%%%%%%%%%%%%%%%%%%%%%%%%%%%%%%%%%%%%%%%%%%%%%%%%%%%%%
42 %%%%%%%%%%%%%%%%%%%%%%%%%%%%%%%%%%%%%%%%%%%%%%%%%%%%%%%%%%%%%%%%%%%%%%%%%
43
44 % Prompt user to ask if they want to calibrate the instrument
45 doCalibration = questdlg('Do you want to calibrate your PNA?', ...
46     'ExampleMeasureSparameter', 'yes', 'no', 'no');
47 if strcmpi(doCalibration, 'yes')
48     %Launch wizard-guided calibration and prompt user to confirm ...
        completion
49     fprintf(instrObj, 'SYSTEM:CORR:WIZ MAIN');
50     hMsgBox = msgbox('Press OK when calibration is complete', ...

```

```
51         'ExampleMeasureSparameter', 'help', 'modal');
52     % Wait till user has confirmed that the calibration is complete
53     uiwait(hMsgBox);
54 end
55
56 % Perform a System Preset
57 fprintf(instrObj, 'SYSTEM:FPRreset');
58 fprintf(instrObj, '*CLS');
59
60 % Wait till system is ready as Preset could take time
61 opcStatus = 0;
62 while(~opcStatus)
63     opcStatus = str2double(query(instrObj, '*OPC?'));
64 end
65
66 % Start S11 Trace on PNA
67 fprintf(instrObj, 'CALCulate:PARAMeter:DEFine:EXT ...
        'SParamMeasurementS11', S11'); % Define a measurement name ...
        and parameter
68 fprintf(instrObj, 'DISPlay:WINDow1:STATE ON'); ...
        % Create a new display window ...
        and turn it on
69 fprintf(instrObj, 'DISPlay:WINDow1:TRACe1:FEED ...
        'SParamMeasurementS11'); % Associate the measurements to ...
        WINDow1
70 fprintf(instrObj, 'DISPlay:WINDow1:TITLe:STATE ON'); ...
        % Turn ON the Title
71 fprintf(instrObj, 'DISPlay:ANNotation:FREQuency ON'); ...
        % Turn ON Frequency Annotation
```

```
72 fprintf(instrObj, 'DISPlay:WINDow1:TRACel:STATe ON'); ...
    % Turn ON Trace Annotation
73
74 % Set the frequency ranges
75 fprintf(instrObj, sprintf('SENSe:FREQuency:START %sHz', ...
76     num2str(frequencyRange(1))));
77 fprintf(instrObj, sprintf('SENSe:FREQuency:STOP %sHz', ...
78     num2str(frequencyRange(2))));
79 %% Get Some information about the controller
80 [result1, response1, errString1] = CC.VE(1); %Controller Version ...
    Information
81     if result1==0
82         fprintf('Controller Version is : ');
83         disp(response1);
84     else
85         disp(errString1);
86     end
87 [result2, response2, errString2]=CC.SL_Get(1); %Get Negative ...
    Software Limit
88     if result2==0
89         fprintf('Negative Limit : ');
90         disp(response2);
91     else
92         disp(errString2);
93     end
94 [result3, response3, errString3]=CC.SR_Get(1); %Get Positive ...
    Software Limit
95     if result3==0
96         fprintf('Positive Limit : ');
```

```
97         disp(response3)
98     else
99         disp(errString3);
100    end
101 [result4, response4, errString4] = CC.TP(1);           % Get ...
        Current Position
102     if result4==0
103         fprintf('Current Position : ');
104         disp(response4)
105     else
106         disp(errString4);
107     end
108 %% Initialize by Homing
109 [Home,ErrHome]=CC.OR(1);                             % Home ...
        the device
110 % Wait till homing ends
111 % Check Controller state. Statuscode=32- Ready from Homing,
112 % 33- Ready from Moving.1E-Homing LED should Turn Green
113 [result5,errorCode,statusCode,errString]=CC.TS(1);
114 if result5≠0
115     fprintf('Controller Error :');
116     disp(errString);
117     disp(errorCode);
118 else
119     while statusCode=='1E'
120         [result5,errorCode,statusCode,errString]=CC.TS(1);
121         if result5≠0
122             fprintf('Controller Error : ');
123             disp(errString);
```

```

124         disp(errorCode);
125     end
126 end
127 end
128 % Print Position after Homing
129     [result4, response4, errString4] = CC.TP(1);    % Get ...
           Current Position
130     if result4==0
131         fprintf('Current Position : ');
132         disp(response4)
133     else
134         disp(errString4);
135     end
136 %% Define motion sequence here
137     stepSize=0.05;                                % 50 ...
           um motion
138     totalRange=1;                                % ...
           Range of 1 mm
139     numSteps=floor(totalRange./stepSize);        % Total number of ...
           step required
140     positionArray=zeros(1,numSteps);            % array to get array of ...
           positions
141     rawDataRI=zeros(numPoints,numSteps)        % Raw S11 Data in Real & ...
           Imag Part
142
143 %% Define Psotion Array Here
144     PosArray = [1.25 1.44 1.65 1.9 2.18 2.5 2.87 3.23 3.79 4.35 5 ...
           5.74 ...
145         6.6 7.58 8.7 10 11.49 13.23 15.16 17.41 20];

```

```
146
147
148 %% Start the Motion & Record the measurement
149     for seq=1:length(PosArray)
150         % Get Controller state
151         [result5,errorCode,statusCode,errString]=CC.TS(1);
152         % Check if Controller is ready to Move
153         if (statusCode=='32' || statusCode=='33' || statusCode=='34')
154             % If Yes, then Get Current Position
155             [result4, responsePos, errString4] = CC.TP(1);
156             if result4==0
157                 fprintf('Current Position : ');
158                 disp(responsePos)
159             else
160                 disp(errString4);
161             end
162             Position1 = responsePos;
163             % Position2 =responsePos+stepSize;
164             Position2 =PosArray(seq);
165             % Advance to next Position
166             [resultPosition, errStringMove] = CC.PA-Set(1, Position2);
167             % Wait till end of Motion
168             [result5,errorCode,statusCode,errString]=CC.TS(1);%Check ...
169             Controller
170             if result5≠0
171                 fprintf('Controller Error :');
172                 disp(errString);
173                 disp(errorCode);
174             else
```

```
174         while statusCode=='28'
175             [result5,errorCode,statusCode,errString]=CC.TS(1);
176             if result5≠0
177                 fprintf('Controller Error : ');
178                 disp(errString);
179                 disp(errorCode);
180             end
181         end
182     end
183     % Query for new position
184     [result4, responsePos, errString4] = CC.TP(1);
185     % If Yes, then Get Current Position
186     if result4==0
187         fprintf('Current Position : ');
188         disp(responsePos)
189     else
190         disp(errString4);
191     end
192 else
193     fprintf('Controller is Not Reay to Move!');
194 end
195
196 % Save the position in this block
197 positionArray(seq)=responsePos;           % All the positions in ...
198     the array
199 %%
200
201 % Start Sweep and Averaging
```

```
202 % Set the number of sweep points
203 fprintf(instrObj, sprintf('SENSE:SWEep:POINTs ...
    %s', num2str(numPoints)));
204 fprintf(instrObj, 'SENSE1:AVERAge:STATE OFF');           % Turn ON ...
    averaging
205 % fprintf(instrObj, 'SENSE1:AVERAge:COUNT 20'); %Set number of Avg ...
    count
206
207 %
208 % % Select measurements and set measurement trigger to immediate
209 fprintf(instrObj, 'CALCulate:PARAMeter:SElect ...
    'SParamMeasurementS11');
210 % fprintf(instrObj, 'TRIG:SOURce IMMEDIATE');
211 fprintf(instrObj, ':SENSE:SWEep:MODE CONTinuous');
212 fprintf(instrObj, 'DISPlay:WIND:Y:AUTO');           % ...
    Autoscale display
213 % Since the instrument may take time to make the measurement, ...
    wait until it
214 % is done before requesting measurement data
215 opcStatus = 0;
216 while(~opcStatus)
217     opcStatus = str2double(query(instrObj, '*OPC?'));
218 end
219 % Set instrument to return the data back using binblock format
220 fprintf(instrObj, 'FORMat REAL,64');
221
222 % Set byte order to swapped (little-endian) format. SWAPped is ...
    required
223 % when using IBM compatible computers
```

```

224 fprintf(instrObj, 'FORMat:BORDER SWAP');
225
226 % Request 1-port measurement data from instrument
227 fprintf(instrObj, 'CALC:DATA:SNP:PORTs? '1'');
228
229 % Read the measured data
230 rawDataDB = binblockread(instrObj, 'double');
231 fread(instrObj,1);
232
233 % Read back the number of points in the measurement and reshape the
234 % measurement data
235 numPoints = str2double(query(instrObj, ' SENSE:SWEep:POINTs?'));
236 % Reshape measurement data to [frequency, real, imag] array
237 rawDataDB = reshape(rawDataDB, numPoints, 3);
238 freqRange = rawDataDB(:,1);
239
240 % Convert retrieved magnitude info from dB
241
242 sparamMag = 10.^((1/20).*rawDataDB(:,2)); % For 1 ...
    Port Only
243 % Convert retrieved phase info from degrees to radians
244
245 sparamPhase = rawDataDB(:,3).*(pi/180); % For 1 ...
    Port Only
246 % Convert to Complex form
247 rawDataRI(:,seq) = sparamMag.*(cos(sparamPhase)+1i*sin(sparamPhase));
248
249 % S11=reshape(rawDataRI,1,1,numPoints); % ...
    For 1 Port

```


Bibliography

- [1] J. R. H. Foran. Total knee replacement. [Online]. Available: <https://orthoinfo.aaos.org/en/treatment/total-knee-replacement/>
- [2] *Australian Orthopaedic Association Hip and Knee Arthroplasty Annual Report*, 2015.
- [3] *Australian Orthopaedic Association Shoulder Arthroplasty Annual Report*, 2015.
- [4] *National Joint Registry for England, Wales, Northern Ireland and the Isle of Man*, 2015.
- [5] *American Joint Replacement Registry Annual Report*, 2014.
- [6] *The New Zealand Joint Registry Annual Report*, 2015.
- [7] *Portugese Arthroplasty Register Annual Report*, 2015.
- [8] *Online LROI annual report Dutch Arthroplasty Register*, 2015. [Online]. Available: <https://www.lroi.nl>
- [9] *SIRIS - hip and knee implant register*, 2014.

- [10] *Belgian National Arthroplasty Register*, 2015.
- [11] G. Garellick, J. Kärrholm, H. Lindahl, H. Malchau, C. Rogmark, and O. Rolfson, *Swedish Hip Arthroplasty Register Annual Report*. Swedish Hip Arthroplasty Register, 2013.
- [12] *Hip and Knee Replacements in Canada: Canadian Joint Replacement Registry 2015 Annual Report*, 2015.
- [13] *South African National Joint Registry*, 2015.
- [14] P. Sadoghi, M. Liebensteiner, M. Agreiter, A. Leithner, N. Böhler, and G. Labek, “Revision surgery after total joint arthroplasty: A complication-based analysis using worldwide arthroplasty registers,” *The Journal of Arthroplasty*, vol. 28, pp. 1329–1332, 2013.
- [15] M. Motifard, M. Pesteh, M. R. Etemadifar, and S. Shirazinejad, “Causes and rates of revision total knee arthroplasty: Local results from isfahan, iran,” *Advanced Biomedical Research*, 2015.
- [16] H. Kienapfel, S. S. S, and P. Meudt, Eds., *Reconstruction of the knee joint*. Springer-Verlag, Springer-Verlag; 1996.
- [17] B. Per-Ingvar, Z. G. A., and A. Tomas, *Tissue-Integrated Prostheses: Osseointegration in Clinical Dentistry*. Quintessence: Quintessence, 1985.
- [18] S. Patil, C. Luis, and H. Finn, “Porous femoral fixation in total hip arthroplasty with short anatomical stem: Radiographic evaluation.” *Clin Orthop Surg*, vol. 9, no. 3, pp. 255–262, 2017.

- [19] R. S. Laskin, Ed., *Total Knee Replacement*. Springer-Verlag, 1991.
- [20] H. Kienapfel, C. Sprey, A. Wilke, and R. Griss, "Implant fixation by bone ingrowth," *The Journal of Arthroplasty*, vol. 14, no. 3, pp. 355–368, 1999.
- [21] S. Goodman and P. Aspenberg, "Effect of amplitude of micromotion on bone ingrowth into titanium chambers implanted in the rabbit tibia," *Biomaterials*, vol. 13, no. 13, 1992.
- [22] S. Szmukler–Moncler, H. Salama, Y. Reingewirtz, and J. H. Dubruille, "Timing of loading and effect of micromotion on bone–dental implant interface: Review of experimental literature," *Journal of Biomedical Materials Research: Applied Biomaterials*, 1997.
- [23] X. Liu and G. L. Niebur, "Bone ingrowth into a porous coated implant predicted by a mechano-regulatory tissue differentiation algorithm," *Biomechanics and Modeling in Mechanobiology*, 2008.
- [24] M. Jasty, R. Krushell, E. Zalenski, D. O'Connor, R. Sedlacek, and W. Harris, "The contribution of the nonporous distal stem to the stability of proximally porous-coated canine femoral components." *Journal of Arthroplasty*, vol. 8, no. 1, pp. 33–41, 1993.
- [25] N. Conlisk, C. Howie, and P. Pankaj, "Computational modelling of motion at the bone–implant interface after total knee arthroplasty: The role of implant design and surgical fit," *The Knee*, vol. 24, no. 5, pp. 994–1005, 2017.

- [26] I. Udofia, F. Liu, Z. Jin, P. Roberts, and P. Grigoris, "The initial stability and contact mechanics of a press-fit resurfacing arthroplasty of the hip." *Journal of Bone and Joint Surgery (Br)*, 2007.
- [27] P. Aspenberg, S. Goodman, S. Toksvig-Larsen, L. Ryd, and T. Albrektsson, "Intermittent micromotion inhibits bone ingrowth," *Acta Orthopaedica Scandinavica*, 1992.
- [28] H. Kawahara, D. Kawahara, M. Hayakawa, Y. Tamai, T. Kuremoto, and S. Matsuda, "Osseointegration under immediate loading: biomechanical stress-strain and bone formation–resorption," *Implant Dentistry*, 2003.
- [29] M. Gortchacow, M. Wettstein, D. P. Pioletti, M. Muller-Gerbl, and A. Terrier, "Simultaneous and multisite measure of micromotion, subsidence and gap to evaluate femoral stem stability," *Journal of Biomechanics*, 2012.
- [30] R. Pilliar, J. Lee, and C. Maniopoulos, "Observations on the effect of movement on bone ingrowth into porous-surfaced implants," *Clinical Orthopaedics and Related Research*, vol. 208, pp. 108–113, 1986.
- [31] J. M. Bragdon, C. Burke, D. O'Connor, D. Lowenstein, and J. Harris, "In vivo skeletal responses to porous-surfaced implants subjected to small induced motions," *Journal of Bone and Joint Surgery - American*, vol. 79, no. 5, pp. 1232–1238, 1997.
- [32] M. Karl, F. Graef, and W. Winter, "Determination of micromotion at the implant bone interface - an in-vitro methodologic study," *Dentistry*, 2015.

- [33] L. Ryd, "Micromotion in knee arthroplasty," *Acta Orthopaedica Scandinavica*, pp. 3–80, 1986.
- [34] V. M. Camine, H. Rüdiger, D. Pioletti, and A. Terrier, "Full-field measurement of micromotion around a cementless femoral stem using micro-ct imaging and radiopaque markers," *Journal of Biomechanics*, vol. 49, pp. 400–4008, 2016.
- [35] M. DiSilvestro, S. Swope, T. Dietz, and D. McNulty, "The design and development of a measurement system for the investigation of dynamic micromotion in total knee joint replacements," *IEEE Transactions on Instrumentation and Measurement*, vol. 54, no. 3, pp. 1126–1132, 2005.
- [36] M. Varga and K.-J. Wolter, "Sensors and imaging methods for detecting loosening of orthopedic implants - a review," *IEEE 20th International Symposium for Design and Technology in Electronic Packaging*, 2014.
- [37] W. . Dihlmann, S. W. Dihlmann, and L. Hering, "Alloarthroplasty of the hip joint. radiologic diagnosis of loosening and infection in cemented total endoprostheses." *Radiologe*, vol. 31, pp. 496–505, 1991.
- [38] J. Cahir, A. Toms, T. Marshall, J. Wimhurst, and J. Nolan, "Ct and mri of hip arthroplasty," *Clinical Radiology*, vol. 62, pp. 1163–1172, 2007.
- [39] H. J. Cooper, A. S. Ranawat, H. G. Potter, L. F. Foo, S. T. Jawetz, and C. S. Ranawat, "Magnetic resonance imaging in the diagnosis and management of hip pain after total hip arthroplasty," *The Journal of Arthroplasty*, vol. 24, pp. 661–667, 2009.

- [40] S. Mayer-Wagner, W. Mayer, S. Maegerlein, R. Linke, V. Jansson, and P. E. Müller, “Use of 18f-fdg-pet in the diagnosis of endoprosthetic loosening of knee and hip implants,” *Arch Orthop Trauma Surg*, vol. 130, pp. 1231–1238, 2010.
- [41] B. Huang, M. W.-M. Law, and P.-L. Khong, “Whole-body pet/ct scanning: Estimation of radiation dose and cancer risk,” *Radiology*, vol. 251, no. 1, pp. 166–174, 2009.
- [42] A. P. Georgiou and J. L. Cunningham, “Accurate diagnosis of hip prostehsis loosening using a vibrational techniques,” *Clinical Biomechanics*, vol. 16, pp. 315–323, 2001.
- [43] S. Bhunia, S. J. Majerus, and M. Sawan, *Implantable Biomedical Microsystems Design Principles and Applications*. Elsevier, 2015.
- [44] A. Inmann and D. Hodgins, Eds., *Implanatable Sensor Systems for Medical Applications*. Woodhead Publishing, 2013.
- [45] C. E. P., *Biosensors and invasive monitoring in clinical applications*. SpringerLink, 2013.
- [46] K. S. Nikita, Ed., *Handbook of Biomedical Telemetry*, ser. Biomedical Engineering. IEEE Press, 2014.
- [47] V. K. Khanna, *Implantable Medical Electronics : Prosthetics, Drug Delivery, and Health Monitoring*. Springer International Publishing, 2016.
- [48] I. V. Antoniac, Ed., *Handbook of Bioceramics and Biocomposites*. Springer International Publishing, 2016.

- [49] L. A. Díaz, *Handbook on Advanced Design and Manufacturing Technologies for Biomedical Devices*. Boston MA: Springer, 2015.
- [50] K. E. Gurhan, D. Catherine, and M. Franco, *Remote Powering and Data Communication for Implanted Biomedical Systems*. Springer International Publishing, 2015.
- [51] W. Burtleson and S. Carrara, Eds., *Security and privacy for implantable medical devices*. Springer New York, 2014.
- [52] H. Xiali and D. Xiaojiang, *Security for Wireless Implantable Medical Devices*. Springer New York, 2013.
- [53] S. Pal, *Design of Artificial Human Joints & Organs*. Springer, 2013.
- [54] M. Heimlich, D. Bokor, R. Khokle, and K. Esselle, “Implanted sensing system for joint replacement,” Australia Patent WO 2017 /143 400A1, 2017.
- [55] C. F. Njeh, T. Fuerst, E. Diessel, and H. K. Genant, “Is quantitative ultrasound dependent on bone structure? a reflection,” *Osteoporosis International*, 2001.
- [56] T. B. M. Lescure, *Selected papers on laser distance measurements*, T. B. M. Lescure, Ed. SPIE PRESS BOOK, 1995.
- [57] X. Li, C. Chudoba, T. Ko, C. Pitris, and J. G. Fujimoto, “Imaging needle for optical coherence tomography,” *OPTICS LETTERS*, vol. 25, no. 20, pp. 1520–1522, 2000.

- [58] W. G. et al, “Optical needle endoscope for safe and precise stereotactically guided biopsy sampling in neurosurgery,” *Optics Express*, pp. 26 117–26 126, 2012.
- [59] D. Preethichandra and K. Shida, “A simple interface circuit to measure very small capacitance changes in capacitive sensors,” *IEEE Transactions on Instrumentation and Measurement*, vol. 50, no. 6, pp. 1583–1586, 2001.
- [60] A. J.Fleming, “A review of nanometer resolution position sensors: Operation and performance,” *Sensors and Actuators A: Physical*, vol. 190, pp. 106–126, 2013.
- [61] W. Y. Du and S. W. Yelich, *Resistive, Capacitive, Inductive, and Magnetic Sensor Technologies*. CRC Press, 2014.
- [62] P. May and E. Zhou, *Numerical Modelling*. InTech Open, 2012, ch. Numerical Modelling and Design of an Eddy Current Sensor, pp. 159–183.
- [63] J. S. Wilson, Ed., *Sensor Technology Handbook*. Elsevier, 2005.
- [64] S. Tumanski, “Induction coil sensors—a review,” *MEASUREMENT SCIENCE AND TECHNOLOGY*, vol. 18, pp. R31–R46, 2007.
- [65] C. Cavoit, “Closed loop applied to magnetic measurements in the range of 0.1–50mhz,” *Review of Scientific Instruments*, 2006.
- [66] S.Yabukami, K.Kikichi, M. Yamaguchi, and K.Arai, “Magnetic flux sensor principle of microstrip pickup coil,” *IEEE Transactions on Magnetics*, vol. 33, no. 5, pp. 4044 – 4046, 1997.

- [67] S. Y. M. Yamaguchi and K. I. Arai, "Development of multilayer planar flux sensing coil and its application to 1 mhz–3.5 ghz thin film permeance meter," *Sensors and Actuator*, vol. 81, pp. 212–215, 2000.
- [68] M. Oberle, R. Reutemann, J. Hertle, and Q. Huang, "A 10-mw two-channel fully integrated system-on-chip for eddy-current position sensing," *IEEE JOURNAL OF SOLID-STATE CIRCUITS*, 2002.
- [69] Y. Lai, "Eddy current displacement sensor with ltcc technology," Ph.D. dissertation, Albert Ludwigs University of Freiburg, 2014.
- [70] *Application Note :Antenna Design for MLX90129*.
- [71] M. Misakian, "Equations for the magnetic field produced by one or more rectangular loops of wire in the same plane," *Journal of Research of the National Institute of Standards and Technology*, vol. 105, no. 4, p. 557, August 2000.
- [72] K. Cho and H. Itakura, "Input impedance characteristics of small rectangular loop antenna," in *Proceedings of ISAP Sapporo Japan*, 1992.
- [73] E. Weber, *Electromagnetic Theory*. Dover: New York, 1965.
- [74] P. May and E. Zhou, *Numerical Modelling*. InTech, 2012, ch. Numerical Modelling and Design of an Eddy Current Sensor, pp. 159–184.
- [75] W.-T. Chen and H.-R. Chuang, "Numerical computation of human interaction with arbitrarily oriented superquadric loop antennas in personal communications," *IEEE Transactions on Antennas and Propagation*, vol. 6, no. 6, pp. 821–828, June 1998.

- [76] L.-C. Kuo, W.-T. Chen, and H.-R. Chuang, "Numerical computation of human body effects on radiation characteristics of loop antennas for watch-type wrist radiophone application," in *Asia-Pacific Microwave Conference*, vol. 3, 2001, pp. 1307–1310.
- [77] K. Ito, I. Ida, and M.-S. Wu, "Body effect on characteristics of small loop antenna in pager systems," in *IEEE Antennas and Propagation Society International Symposium*, vol. 2, 1992, pp. 1081–1084.
- [78] W.-T. Chen and H. Chuang, "Human body coupling effects on radiation characteristics of superquadric loop antennas for pagers' application," in *Antennas and Propagation Society International Symposium*, 1997.
- [79] J. Kracek, M. Svanda, M. Mazanek, and J. Machac, "Semi-active 866 mhz rfid implantable tag fed by 6.78 mhz inductive wireless power transfer," in *46th European Microwave Conference (EuMC)*, 2016, pp. 620–622.
- [80] J. Kracek, M. Švanda, M. Mazanek, and J. Machac, "Implantable semi-active uhf rfid tag with inductive wireless power transfer," *IEEE Antennas and Wireless Propagation Letters*, vol. 15, pp. 1657–1660, 2016.
- [81] C. L. Harris and P. B. Siegel, "An implantable telemeter for determining body temperature and heart rate," *Journal of applied physiology*, 1967.
- [82] R. Jegadeesan, S. Nag, K. Agarwal, N. V. Thakor, and Y. X. Guo, "Enabling wireless powering and telemetry for peripheral nerve implants," *IEEE Journal of Biomedical and Health Informatics*, vol. 19, no. 3, pp. 958–970, May 2015.

- [83] U. M. Jow and M. Ghovanloo, "Optimization of a multiband wireless link for neuroprosthetic implantable devices," in *2008 IEEE Biomedical Circuits and Systems Conference*, Nov 2008, pp. 97–100.
- [84] U. Jow and Ghovanloo, "Optimization of data coils in a multiband wireless link for neuroprosthetic implantable devices," *IEEE Transactions on Biomedical Circuits and Systems*, vol. 4, no. 5, pp. 301–310, Oct 2010.
- [85] K. Y. Yazdandoost and R. Miura, "Miniaturized uwb implantable antenna for brain-machine-interface," in *2015 9th European Conference on Antennas and Propagation (EuCAP)*, May 2015, pp. 1–5.
- [86] S. M. Asif, J. Hansen, M. S. Khan, S. D. Walden, M. O. Jensen, B. D. Braaten, and D. L. Ewert, "Design and in vivo test of a batteryless and fully wireless implantable asynchronous pacing system," *IEEE Transactions on Biomedical Engineering*, vol. 63, no. 5, pp. 1070–1081, May 2016.
- [87] A. J. Johansson, "Performance of a radio link between a base station and a medical implant utilising the mics standard," in *The 26th Annual International Conference of the IEEE Engineering in Medicine and Biology Society*, vol. 1, Sept 2004, pp. 2113–2116.
- [88] D. Li, X. Huang, J. Chen, and W. Kainz, "A study of antenna efficiency and mri compatibility of cardiac stent," in *2014 IEEE International Symposium on Electromagnetic Compatibility (EMC)*, Aug 2014, pp. 165–170.
- [89] K. S. Nikita, *Stimulator Paradigm: Artificial Retina*. Wiley-IEEE Press, 2014, pp. 736–. [Online]. Available: <http://ieeexplore.ieee.org/xpl/articleDetails.jsp?arnumber=6880016>

- [90] S. C. DeMarco, G. Lazzi, W. Liu, J. D. Weiland, and M. S. Humayun, "Computed sar and thermal elevation in a 0.25-mm 2-d model of the human eye and head in response to an implanted retinal stimulator - part i: models and methods," *IEEE Transactions on Antennas and Propagation*, vol. 51, no. 9, pp. 2274–2285, Sept 2003.
- [91] S. Soora, K. Gosalia, M. S. Humayun, and G. Lazzi, "A comparison of two and three dimensional dipole antennas for an implantable retinal prosthesis," *IEEE Transactions on Antennas and Propagation*, vol. 56, no. 3, pp. 622–629, March 2008.
- [92] A. Qusba, A. K. RamRakhyani, J. H. So, G. J. Hayes, M. D. Dickey, and G. Lazzi, "On the design of microfluidic implant coil for flexible telemetry system," *IEEE Sensors Journal*, vol. 14, no. 4, pp. 1074–1080, April 2014.
- [93] S. H. Chen and C. L. Yang, "Implantable fractal dental antennas for low invasive biomedical devices," in *2010 IEEE Antennas and Propagation Society International Symposium*, July 2010, pp. 1–4.
- [94] Y. L. Yang, C. L. Tsai, and C. L. Yang, "Enhancement of output voltage for novel dental rectennas," in *2012 42nd European Microwave Conference*, Oct 2012, pp. 321–324.
- [95] C. L. Yang, C. L. Tsai, and S. H. Chen, "Implantable high-gain dental antennas for minimally invasive biomedical devices," *IEEE Transactions on Antennas and Propagation*, vol. 61, no. 5, pp. 2380–2387, May 2013.

- [96] S. Afroz, S. W. Thomas, G. Mumcu, and S. E. Saddow, "Implantable sic based rf antenna biosensor for continuous glucose monitoring," in *2013 IEEE SENSORS*, Nov 2013, pp. 1–4.
- [97] T. Karacolak, A. Z. Hood, and E. Topsakal, "Design of a dual-band implantable antenna and development of skin mimicking gels for continuous glucose monitoring," *IEEE Transactions on Microwave Theory and Techniques*, vol. 56, no. 4, pp. 1001–1008, April 2008.
- [98] X. Y. Liu, Z. T. Wu, Y. Fan, and E. M. Tentzeris, "A miniaturized csrr loaded wide-beamwidth circularly polarized implantable antenna for subcutaneous real-time glucose monitoring," *IEEE Antennas and Wireless Propagation Letters*, vol. 16, pp. 577–580, 2017.
- [99] Z. Xiao, X. Tan, X. Chen, S. Chen, Z. Zhang, H. Zhang, J. Wang, Y. Huang, P. Zhang, L. Zheng, and H. Min, "An implantable rfid sensor tag toward continuous glucose monitoring," *IEEE Journal of Biomedical and Health Informatics*, vol. 19, no. 3, pp. 910–919, May 2015.
- [100] C. Liu, Y. X. Guo, and S. Xiao, "Circularly polarized helical antenna for ism-band ingestible capsule endoscope systems," *IEEE Transactions on Antennas and Propagation*, vol. 62, no. 12, pp. 6027–6039, Dec 2014.
- [101] K. Fricke, R. Sobot, and C. Hodgson, "Design and evaluation of a 3d printed bio-compatible capsule for implantable telemetry systems," in *2014 IEEE Biomedical Circuits and Systems Conference (BioCAS) Proceedings*, Oct 2014, pp. 368–371.

- [102] S. Deutsch, "An implanted telemetry unit for ambulatory animals," *IEEE Transactions on Communications*, vol. 23, no. 9, pp. 983–987, Sep 1975.
- [103] L. Lizzi, P. Perrissol, F. Ferrero, P. L. Thuc, and R. Staraj, "Experimental validation of a miniature implantable rfid tag antenna for small animals monitoring," in *2014 IEEE Conference on Antenna Measurements Applications (CAMA)*, Nov 2014, pp. 1–3.
- [104] J. Lu, L. Zhang, S. Matsumoto, H. Hiroshima, K. Serizawa, M. Hayase, and T. Gotoh, "Miniaturization and packaging of implantable wireless sensor nodes for animals monitoring," in *2016 IEEE SENSORS*, Oct 2016, pp. 1–3.
- [105] M. N. Shakib, M. Moghavvemi, W. N. L. Mahadi, and M. R. Ahmed, "Design of a broadband implantable antenna in the rat for biotelemetry applications," in *2015 IEEE MTT-S 2015 International Microwave Workshop Series on RF and Wireless Technologies for Biomedical and Healthcare Applications (IMWS-BIO)*, Sept 2015, pp. 239–240.
- [106] B. Gupta, S. Sankaralingam, and S. Dhar, "Development of wearable and implantable antennas in the last decade: A review," in *2010 10th Mediterranean Microwave Symposium*, Aug 2010, pp. 251–267.
- [107] A. Kiourti and K. S. Nikita, "A review of implantable patch antennas for biomedical telemetry: Challenges and solutions [wireless corner]," *IEEE Antennas and Propagation Magazine*, vol. 54, no. 3, pp. 210–228, June 2012.
- [108] A. Valanarasi and R. Dhanasekaran, "A review on design considerations of implantable antennas," in *2016 International Conference on Advanced Com-*

- munication Control and Computing Technologies (ICACCCT)*, May 2016, pp. 207–211.
- [109] C. M. Furse, “Biomedical telemetry: Today’s opportunities and challenges,” in *2009 IEEE International Workshop on Antenna Technology*, March 2009, pp. 1–4.
- [110] S. Islam, K. P. Esselle, D. Bull, and P. M. Pilowsky, “Making a telemetry system implantable: Challenges and opportunities in antenna design,” in *2013 IEEE MTT-S International Microwave Workshop Series on RF and Wireless Technologies for Biomedical and Healthcare Applications (IMWS-BIO)*, Dec 2013, pp. 1–3.
- [111] A. K. Skrivervik, “Implantable antennas: The challenge of efficiency,” in *2013 7th European Conference on Antennas and Propagation (EuCAP)*, April 2013, pp. 3627–3631.
- [112] E. Topsakal, “Antennas for medical applications: Ongoing research and future challenges,” in *2009 International Conference on Electromagnetics in Advanced Applications*, Sept 2009, pp. 890–893.
- [113] A. Traille and M. M. Tentzeris, “Liquid rf antennas, electronics and sensors: A modeling challenge,” in *2011 XXXth URSI General Assembly and Scientific Symposium*, Aug 2011, pp. 1–4.
- [114] L. Marnat, M. H. Ouda, M. Arsalan, K. Salama, and A. Shamim, “On-chip implantable antennas for wireless power and data transfer in a glaucoma-monitoring soc,” *IEEE Antennas and Wireless Propagation Letters*, vol. 11, pp. 1671–1674, 2012.

- [115] E. Moradi, T. Björninen, L. Sydänheimo, L. Ukkonen, and J. M. Rabaey, “Antenna design for implanted tags in wireless brain machine interface system,” in *2013 IEEE Antennas and Propagation Society International Symposium (APSURSI)*, July 2013, pp. 2083–2084.
- [116] L. Song and Y. Rahmat-Samii, “Analysis of millimeter-size implanted loop antennas for brain-machine interface systems,” in *2016 United States National Committee of URSI National Radio Science Meeting (USNC-URSI NRSM)*, Jan 2016, pp. 1–2.
- [117] R. Alrawashdeh, Y. Huang, A. A. B. Sajak, L. Xing, and M. Kod, “Orientation effect of flexible implantable antennas on performance,” in *2014 IEEE Antennas and Propagation Society International Symposium (APSURSI)*, July 2014, pp. 973–974.
- [118] R. Alrawashdeh, Y. Huang, and A. A. B. Sajak, “A flexible loop antenna for biomedical bone implants,” in *The 8th European Conference on Antennas and Propagation (EuCAP 2014)*, April 2014, pp. 861–864.
- [119] R. S. Alrawashdeh, Y. Huang, M. Kod, and A. A. B. Sajak, “A broadband flexible implantable loop antenna with complementary split ring resonators,” *IEEE Antennas and Wireless Propagation Letters*, vol. 14, pp. 1506–1509, 2015.
- [120] R. Alrawashdeh, Y. Huang, and P. Cao, “A flexible loop antenna for total knee replacement implants in the medradio band,” in *2013 Loughborough Antennas Propagation Conference (LAPC)*, Nov 2013, pp. 225–228.

- [121] P. Zakavi, N. C. Karmakar, and I. Griggs, "Wireless orthopedic pin for bone healing and growth: Antenna development," *IEEE Transactions on Antennas and Propagation*, vol. 58, no. 12, pp. 4069–4074, Dec 2010.
- [122] R. Alrawashdeh, Y. Huang, and P. Cao, "Flexible meandered loop antenna for implants in medradio and ism bands," *Electronics Letters*, vol. 49, no. 24, pp. 1515–1517, November 2013.
- [123] —, "A conformal u-shaped loop antenna for biomedical applications," in *2013 7th European Conference on Antennas and Propagation (EuCAP)*, April 2013, pp. 157–160.
- [124] P.A.Hasgall, D. G. F., C.Baumgartner, E. Neufeld, M. Gosselin, D. Payne, A. Klingenbock, and N. Kuster, "It's database for thermal and electromagnetic parameters of biological tissues," [www.itis.ethz.ch/database.](http://www.itis.ethz.ch/database/), January 2015.
- [125] W. Wang and C. K. Poh, *Titanium Alloys - Advances in Properties Control*. InTech Open, 2013, ch. Titanium Alloys in Orthopaedics.
- [126] P. Fonda, Z. Wang, K. Yamazaki, and Y. Akutsu, "A fundamental study on ti-6al-4v's thermal and electrical properties and their relation to edm productivity," *Journal of Materials Processing Technology*, 2008.
- [127] R. Boyer, G. Welsch, and E. W. Collings, *Materials Properties Handbook: Titanium Alloys*. ASM International, 1994.

- [128] S. Gabriel, R. W. Lau, and C. Gabriel, "The dielectric properties of biological tissues: Ii. measurements in the frequency range 10 hz to 20 ghz," *Phys. Med. Biology*, vol. 41, p. 2251, 1996.
- [129] K. S. Cole and R. H. Cole, "Dispersion and absorption in dielectrics i. alternating current characteristics," *J. Chem. Phys.*, vol. 9, pp. 341–351, 1941.
- [130] E. Dagotto, *Nanoscale Phase Separation and Colossal Magnetoresistance.*, ser. Springer Series in Solid-State Sciences. Berlin Heidelberg: Springer, 2003, vol. 136, ch. Brief Introduction to Giant Magnetoresistance (GMR).
- [131] F. A. Cardoso, L. S. Rosado, F. Franco, R. Ferreira, E. Paz, S. Cardoso, P. M. Ramos, M. Piedade, and P. P. Freitas, "Improved magnetic tunnel junctions design for the detection of superficial defects by eddy currents test," *IEEE Transactions on Magnetism*, vol. 50, no. 11, 2014.
- [132] W. J. Gallagher, S. S. P. Parkin, Y. Lu, X. P. Bian, A. Marley, K. P. Roche, R. A. Altman, S. A. Rishton, C. Jahnes, T. M. Shaw, and G. Xiao, "Microstructured magnetic tunnel junctions (invited)," *Journal of Applied Physics*, 1997.
- [133] E. Paz, R. Ferreira, and P. Freitas, "Linearization of magnetic sensors with a weakly pinned free layer mtj stack using a three-step annealing process," *IEEE Transactions Magnetism*, 2016.
- [134] D. P. Kotler, S. Burastero, J. Wang, and R. N. P. Jr, "Prediction of body cell mass, fat-free mass, and total body water with bioelectrical impedance analysis: effects of race, sex, and disease," *The American Journal of Clinical Nutrition*, vol. 64, no. 3, pp. 4895–4975, 1996.

- [135] P. A. WILLIAMS and S. SAHA, “The electrical and dielectric properties of human bone tissue and their relationship with density and bone mineral content,” *Annals of Biomedical Engineering*, vol. 24, pp. 222–233, 1996.
- [136] N. A. Islam and F. Arifin, “Performance analysis of a miniaturized implantable pifa antenna for wban at ism band,” in *2016 3rd International Conference on Electrical Engineering and Information Communication Technology (ICEEICT)*, Sept 2016, pp. 1–5.
- [137] Z.-J. Yang and S.-Q. Xiao, “A single-fed miniaturized circularly polarized implantable antenna for ism band biomedical application,” in *2016 IEEE MTT-S International Microwave Workshop Series on Advanced Materials and Processes for RF and THz Applications (IMWS-AMP)*, July 2016, pp. 1–3.
- [138] C. Liu, Y. X. Guo, and S. Xiao, “Capacitively loaded circularly polarized implantable patch antenna for ism band biomedical applications,” *IEEE Transactions on Antennas and Propagation*, vol. 62, no. 5, pp. 2407–2417, May 2014.
- [139] Z. Duan, Y. X. Guo, M. Je, and D. L. Kwong, “Design and in vitro test of a differentially fed dual-band implantable antenna operating at mics and ism bands,” *IEEE Transactions on Antennas and Propagation*, vol. 62, no. 5, pp. 2430–2439, May 2014.
- [140] H. Y. Lin, M. Takahashi, K. Saito, and K. Ito, “Performance of implantable folded dipole antenna for in-body wireless communication,” *IEEE Transac-*

- tions on Antennas and Propagation*, vol. 61, no. 3, pp. 1363–1370, March 2013.
- [141] A. J. Blazevich, N. D. Gill, and S. Zhou, “Intra- and intermuscular variation in human quadriceps femoris architecture assessed in vivo,” *Journal of Anatomy*, 2006.
- [142] A. Kiourti, M. Christopoulou, and K. S. Nikita, “Performance of a novel miniature antenna implanted in the human head for wireless biotelemetry,” in *2011 IEEE International Symposium on Antennas and Propagation (AP-SURSI)*, July 2011, pp. 392–395.
- [143] A. Kiourti and K. S. Nikita, “Miniature scalp-implantable antennas for telemetry in the mics and ism bands: Design, safety considerations and link budget analysis,” *IEEE Transactions on Antennas and Propagation*, vol. 60, no. 8, pp. 3568–3575, Aug 2012.
- [144] P. Soontornpipit, C. M. Furse, and Y. C. Chung, “Design of implantable microstrip antenna for communication with medical implants,” *IEEE Transactions on Microwave Theory and Techniques*, vol. 52, no. 8, pp. 1944–1951, Aug 2004.
- [145] J. L. Volakis, C. Chen, and K. Fujimoto, *Small Antennas: Miniaturization Techniques and Applications*. McGraw Hill Publications, 2010.
- [146] D. H. Werner and S. Ganguly, “An overview of fractal antenna engineering research,” *IEEE Antennas and Propagation Magazine*, vol. 45, no. 1, pp. 38–57, 2003.

- [147] J. P. Gianvittorio and Y. Rahmat-Samii, "Fractal antennas: a novel antenna miniaturization technique, and applications," *IEEE Antennas and Propagation Magazine*, vol. 44, no. 1, pp. 20–36, 2002.
- [148] D.Li and J.Mao, "Sierpinskized koch like sided multifractal dipole antenna," *Progress in Electromagnetics Research*, 2012.
- [149] C. P. Baliarda, J. Romeu, and A. Cardama, "The koch monopole: a small fractal antenna," *IEEE Transactions on Antennas and Propagation*, vol. 48, no. 1, pp. 1773–1781, 2000.
- [150] S. Best, "A discussion on the significance of geometry in determining the resonant behavior of fractal and other non-euclidean wire antennas," *IEEE Antennas and Propagation Magazine*, 2003.
- [151] R. Azaro, F. D. N. ., M. Donelli, E. Zeni, and A. Massa, "Design of a prefractal monopolar antenna for 3.4-3.6 ghz wi-max band portable devices," *IEEE Antennas and Wireless Propagation Letters*, 2006.
- [152] R. Azaro, F. D. Natale, M. Donelli, E. Zeni, and A. Massa, "Synthesis of a prefractal dual-band monopolar antenna for gps applications," *IEEE Antennas and Wireless Propagation Letters*, 2006.
- [153] S. Dhar, K. Patra, R. Ghatak, B.Gupta, and D.R.Poddar, "A dielectric resonator-loaded minkowski fractal-shaped slot loop heptaband antenna," *IEEE Transactions on Antennas and Propagation*, 2015.

- [154] K.Sengupta and K.J.Vinoy, "A new measure of lacunarity for generalized fractals and its impact in the electromagnetic behaviour of koch dipole antennas," *Fractals*, 2006.
- [155] M. Comissio, "On the use of dimension and lacunarity for comparing the resonant behavior of convoluted wire antennas," *Progress in Electromagnetics Research*, 2009.
- [156] C. A. Balanis, *Antenna Theory: Analysis and Design*. Wiley Publications, 2016.
- [157] R. Khokle, "Design of horizontally polarized ultra wide band microstrip antenna," Ph.D. dissertation, Defence Institute of Advanced Technology, 2013.
- [158] R. Kumar, R. Khokle, and R. V. S. R. Krishna, "A horizontally polarized rectangular stepped slot antenna for ultra wide bandwidth with boresight radiation patterns," *IEEE Transactions on Antennas and Propagation*, 2014.
- [159] T. Dissanayake, "Prediction of the notch frequency of slot loaded printed uwb antennas," *IEEE Transactions on Antennas and Propagation*, vol. 55, no. 11, pp. 3320–3325, 2007.
- [160] S. Cohn, "Slot line on a dielectric substrate," *IEEE Transactions on Microwave Theory and Techniques*, 1969.
- [161] R. Janaswami and D. H. Schaubert, "Characteristic impedance of a wide slot line on low permittivity substrates," *IEEE Transactions on Microwave Theory and Techniques*, 1986.

- [162] N. G. Alexopoulos and D. R. Jackson, "Fundamental superstrate (cover) effects on printed circuit antennas," *IEEE Transactions on Antennas and Propagation*, vol. 32, no. 8, pp. 807–816, 1984.
- [163] M. Islam, "Implantable antennas for medical wireless telemetry systems operating in the 900 mhz ism band," Ph.D. dissertation, Macquarie University, 2014.
- [164] L. Vershney and J. Roy, "A broadband stepped slot antenna," *Microwave Review*, pp. 33–36, 2009.
- [165] C. Chulvanich, J. Nakasuwan, N. Songthanapitak, N. Anantrasirichai, and T. Wakabayashi, "Design of narrow slot antenna for dual frequency," *Progr. Electromagn. Res*, 2007.
- [166] K. Nithisopa, J. Nakasuwan, N. Songthanapitak, N. Anantrasirichai, , and T. Wakabayashi, "Design of cpw fed slot antenna for wideband applications," *Progr. Electromagn. Res.*, vol. 3, no. 7, pp. 1124–1127, 2007.
- [167] G. Khunead, J.Nakasuwan, N. Songthanapitak, and N.Anantrasirichai, "Investigate rectangular slot antenna with l-shaped strip," *Progress in Electromagnetics Research Online*, 2007.
- [168] X. Huang, C. H. Cheng, and L. Zhu, "An ultrawideband (uwb) slotline antenna under multiple-mode resonance," *IEEE Transactions on Antennas and Propagation*, 2012.